JORGE AUGUSTO VASCONCELOS ALVES

SAFETY-CRITICAL CONTROL METHODS FOR VEHICLE LATERAL STABILITY

São Paulo
2023

JORGE AUGUSTO VASCONCELOS ALVES

SAFETY-CRITICAL CONTROL METHODS FOR VEHICLE LATERAL STABILITY

Corrected Version

Thesis presented to the Escola Politécnica da Universidade de São Paulo to obtain the degree of Doctor in Science.

São Paulo
2023

JORGE AUGUSTO VASCONCELOS ALVES

SAFETY-CRITICAL CONTROL METHODS FOR VEHICLE LATERAL STABILITY

Corrected Version

Thesis presented to the Escola Politécnica da Universidade de São Paulo to obtain the degree of Doctor in Science.

Concentration Area:
Systems Engineering

Advisor:
Prof. Dr. Bruno Augusto Angélico

São Paulo
2023

Este exemplar foi revisado e corrigido em relação à versão original, sob responsabilidade única do autor e com a anuência de seu orientador.

São Paulo, 23 de outubro de 2023

Assinatura do autor: 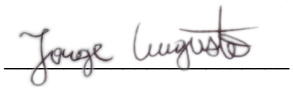

Assinatura do orientador: 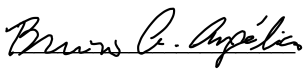

Catalogação-na-publicação

Alves, Jorge Augusto Vasconcelos
Safety-Critical Control Methods for Vehicle Lateral Stability / J. A. V. Alves -- versão corr. -- São Paulo, 2023.
186 p.

Tese (Doutorado) - Escola Politécnica da Universidade de São Paulo. Departamento de Engenharia de Telecomunicações e Controle.

1.Dinâmica veicular 2.Controle de estabilidade veicular 3.Controle eletrônico de estabilidade 4.Controle de estabilidade de guinada 5.Controle de segurança crítica I.Universidade de São Paulo. Escola Politécnica. Departamento de Engenharia de Telecomunicações e Controle II.t.

To my family and friends.

ACKNOWLEDGMENTS

Many thanks to my colleagues, with whom I have shared the laboratory for as much as the COVID-19 pandemic has allowed us. In particular, Fabio Yukio Toriumi, Gabriel Pereira Neves, Mateus Mussi Brugnolli, and Rafael Pereira Bachega composed our initial research group. Thanks to my advisor, Prof. Bruno Augusto Angélico, who has provided the necessary tools to develop this work. Thanks to Prof. Laganá for conducting the SegurAuto project with Prof. Bruno. Special thanks to Prof. Chinelato for assisting us with the safety-critical control algorithms implementation.

I also thank all the undergraduate students that were part of the SegurAuto Project at the Polytechnic School of the University of São Paulo: Fernando Zolubas Preto, Gad Alagia Ripari, Lucas Antonio Jardim Pontes. Moreover, I express my gratitude to the other graduate students of the project: Andrei Araújo Felix, Carlos Arronte, Henrique Caballeria Mesquita, and Nouriandres Liborio Silva. Finally, thanks to my family and girlfriend, Veridiane Martins, for supporting me throughout the work leave from UTFPR.

This work was partially supported by both the Fundação de Desenvolvimento da Pesquisa - Fundep Rota 2030 - Linha V, for the Grant SegurAuto - Projeto e Desenvolvimento Integrado de Funções de Segurança Assistida ao Condutor e Ambiente para Veículos Autônomos, and by the Coordenação de Aperfeiçoamento de Pessoal de Nível Superior - Brazil (CAPES) under Grant 001.

RESUMO

Alves, J. A. V. **Safety-Critical Control Methods for Vehicle Lateral Stability**. 2023. 186p. Tese (Doutorado em Ciências) – Escola Politécnica, Universidade de São Paulo, São Paulo, 2023.

Aplicamos controle de segurança crítica a controle eletrônico de estabilidade, com foco em estabilidade lateral. As vantagens inerentes de controle eletrônico de estabilidade de veículos automotores e as restrições intrínsecas de segurança presentes em sistemas de emergência justificam a proposta. Os fundamentos de dinâmica e estabilidade veicular são apresentados, subdivididos em dinâmica de pneus, corpo e chassi, e controle. Segue uma introdução à teoria de funções de controle de barreira, apresentando suas propriedades, vantagens, e limitações. Inicialmente, aprimoramos e corrigimos métodos de geração de regiões de estabilidade lateral. Após, estendemos teoria de controle de segurança crítica baseada em funções de barreira de controle para acomodar controle eletrônico de estabilidade usando esterçamento ativo e frenagem diferencial. Por fim, investigamos a viabilidade de funções de barreira de controle para estabilidade veicular após as referidas extensões, concluindo que os requisitos são satisfeitos. Validamos as propostas através de simulação usando modelos cada vez mais complexos, desde modelos de segunda ordem linearizados a softwares comerciais de simulação veicular.
Palavras-chave: Dinâmica veicular. Controle de estabilidade veicular. Controle eletrônico de estabilidade. Controle de estabilidade de guinada. Controle de segurança crítica. Funções de barreira de controle.

ABSTRACT

Alves, J. A. V. **Safety-Critical Control Methods for Vehicle Lateral Stability**. 2023. 186p. Thesis (Doctor in Science) – Escola Politécnica, Universidade de São Paulo, São Paulo, 2023.

We apply safety-critical control to electronic stability control, focusing on lateral stability. The inherent advantages of electronic stability control of road vehicles and the intrinsic safety restrictions that emergency systems such as electronic stability control require to maintain or reestablish vehicle control justify the proposal. The theoretical basis of vehicle dynamics and stability are presented: tire dynamics, body and chassis, and control. An introduction to control barrier function theory follows, with comments on its properties, advantages, and shortcomings. First, we improve and correct stability region generation methods. Next, we validate the steering-angle-dependent regions with electronic stability control systems with active steering, extending the safety-critical control theory based on control barrier functions. We then propose an electronic stability control system with differential braking as the input method, which demands another extension of the control barrier function theory. An inquiry on the viability of control barrier functions to vehicle stability finishes the text, where we show that the proposed control method should satisfy the control objectives. The results were validated through simulation using increasingly more complex models, from 2nd-order linearized lateral models to commercial vehicle simulation software.
Keywords: Vehicle dynamics. Vehicle stability control. Electronic stability control. Yaw stability control. Safety-critical control. Control barrier functions.

LIST OF FIGURES

LIST OF TABLES

LIST OF ACRONYMS

4WD	Four-wheel drive
ABS	*Antiblockier-Bremssystem* (anti-lock braking system)
ADAS	Advanced driver-assistance systems
AFS	Active front steering
ARC	Active roll control
ARS	Active rear steering
ASC	Active steering control
CBF	Control barrier function
CDBF	Control-dependent control barrier function
CDLF	Control-dependent control Lyapunov function
CDDBF	Control-disturbance-dependent control barrier function
CDDLF	Control-disturbance-dependent control Lyapunov function
CDDEBF	Control-disturbance-dependent exponential control barrier function
CDDELF	Control-disturbance-dependent exponential control Lyapunov function
CLF	Control Lyapunov function
DOF	Degree of freedom
DYC	Direct yaw moment control
ECBF	Exponential control barrier function
ESC	Electronic stability control
ESP	Electronic stability program
FMVSS	Federal Motor Vehicle Safety Standards
GVWR	Gross vehicle weight rating
HUD	Heads-up display
IMU	Inertial measurement unit
ISO	International Organization for Standardization
LFT	Linear fraction transformation
LMI	Linear matrix inequality
LOC	Loss of vehicle control
LPV	Linear parameter-varying
MF	Magic formula
MPC	Model predictive control
MPCA	Fast model predictive control allocation
NCAP	New car assessment program
PID	Proportional-integral-derivative
QP	Quadratic problem
SUV	Sport utility vehicle
UN/ECE	United Nations Economic Commission for Europe
USA	United States of America
VSC	Vehicle stability control
YSC	Yaw stability control

LIST OF SYMBOLS

a	contact patch half-length, inscribed circle radius
a_{gi}	vehicle acceleration in the direction of the Oi axis
$a_{y_{\max}}$	maximum lateral acceleration
A	sine with dwell maximum steering angle factor
$\mathbf{A}$	state-space system matrix
$\bar{\mathbf{A}}$	equivalent system state-space system matrix
$\mathbf{A}_{qp}$	quadratic problem standard form inequality constraint matrix
b_i	safe set barrier polynomial
$\mathbf{b}_{qp}$	quadratic problem standard form inequality constraint vector
B	magic formula stiffness factor
$\mathbf{B}$	state-space input matrix
$\bar{\mathbf{B}}$	equivalent system state-space input matrix
$\mathbf{B}_c$	linearized system control input matrix
$\mathbf{B}_e$	linearized system external input matrix
c	midpoint of the contact patch
c_a	drag coefficient
c_{p_x}	bristle longitudinal stiffness
c_{p_y}	bristle cornering stiffness
c_h	convergence rate factor of the barrier function
c_V	convergence rate factor of the Lyapunov function
C	magic formula shape factor
$\mathbf{C}$	state-space output matrix
$\bar{\mathbf{C}}$	equivalent system state-space output matrix
$\mathcal{C}$	safe set
$\mathrm{fr}(\mathcal{C})$	frontier (or boundary) safe set
$\mathrm{Int}(\mathcal{C})$	interior of the safe set
$C_{F\alpha}$	cornering stiffness
$C_{F\kappa}$	longitudinal slip stiffness
C_{M_α}	wheel aligning stiffness
C_{α_f}	front axle cornering stiffness
C_{α_r}	rear axle cornering stiffness
$C_{\bar{\alpha}_f}$	local front axle cornering stiffness
$C_{\bar{\alpha}_r}$	local rear axle cornering stiffness
$C_{\bar{\alpha}\,i}$	tire local cornering stiffness
d_θ	yaw control steering angle error
df_z	vertical load increment
dp_i	inflating pressure increment
d_ψ	yaw rate error
D	magic formula maximum value
$\mathbf{D}$	state-space direct transmission matrix
$\bar{\mathbf{D}}$	equivalent system state-space direct transmission matrix
$\mathcal{D}$	set of possible state vectors that contains the safe set

e	hindmost point of the contact patch
E	magic formula curvature factor
f	affine nonlinear system autonomous function
f_y	lateral force per unit of length
f_ψ	rolling resistance coefficient
$\mathbf{F}$	quadratic problem linear coefficient matrix
$\bar{\mathbf{F}}$	input-output linearized system state-space system matrix
F_i	force in the direction of the Oi axis
$\bar{F}_i$	normalized force in the direction of the Oi axis
F_{x_i}	longitudinal tire force on the i wheel
F_{y_i}	lateral tire force on the i wheel
g	acceleration of gravity, affine nonlinear system input factor
g_c	affine nonlinear system control input factor
g_e	affine nonlinear system external input factor
$\bar{\mathbf{G}}$	input-output linearized system state-space input matrix
h	(zeroing) barrier function, (zeroing) control barrier function
h_g	center of mass distance from the road
$\mathbf{H}$	quadratic problem weight matrix
I_{CR}	instantaneous center of rotation
I_x	vehicle roll moment of inertia
I_y	vehicle pitch moment of inertia
I_z	vehicle yaw moment of inertia
k_r	desired yaw rate barrier coefficient
k_{st}	stability factor
$k_{\gamma i}$	CDELF desired Hurwitz polynomial coefficient
$k_{\zeta i}$	CDEBF desired Hurwitz polynomial coefficient
$\mathbf{K}_\zeta$	ECBF pole placement coefficient vector
$\mathbf{K}_{\gamma r}$	CDELF pole placement coefficient vector
$\mathbf{K}_{\zeta r}$	CDEBF pole placement coefficient vector
l	wheel base
l_1	front wheel base
l_2	rear wheel base
l_w	half track width
L_w	track width
$L_X Y$	Lie derivative of Y with respect to X
m_b	vehicle mass
M_{a_z}	wheel restoring moment due to the non-slipping bristles
M_{s_z}	wheel restoring moment due to the slipping bristles
M_z	wheel restoring moment
M_ψ	correcting yaw moment
M_b	vehicle mass
p	quadratic problem linear term weight
p_u	quadratic problem input signal weight
p_δ	quadratic problem slack variable weight
p_{Aij}	jth magic formula parameter for the parameter A, axis Oi
P_i	inflating pressure, parallelogram vertex

$P_{\gamma r}$	CDELF desired Hurwitz polynomial
$P_{\zeta r}$	CDEBF desired Hurwitz polynomial
$\bar{\mathbf{P}}$	state-space change-of-basis matrix
$\mathbf{P}_i$	quadratic curve change-of-basis matrix
q_{b_x}	bristle pressure in the direction of the Oi axis
q_{f_x}	maximum bristle pressure in the direction of the Oi axis
q_z	parabolic contact patch pressure
r	relative degree
r_{me}	relative degree of the barrier function with respect to the external input vector
r_{mc}	relative degree of the barrier function with respect to the control input vector
$r_{\min}$	minimum wheel radius
r_e	effective rolling radius
R	curve radius
R_a	drag force
R_b	trailer force
R_{rf}	front axle rolling resistance
R_{rr}	read axle rolling resistance
$\mathbb{R}$	set of real numbers
$\Re$	real part
S_{Hi}	magic formula horizontal shift
S_{Vi}	magic formula vertical shift
t	time
t_M	pneumatic trail
u	input signal, control input
u_c	control system input signal
u_e	disturbance or external input signal
$\mathbf{u}$	input vector, control vector
$\mathbf{u}_c$	control system input vector
$\mathbf{u}_e$	external input vector
$\mathbf{u}_f$	control-dependent extended input vector
$\mathbf{u}_{ref}$	reference input vector
u_{b_i}	bristle deformation in the direction of the Oi axis
$\mathcal{U}$	set of possible input vectors
v_{gx}	vehicle longitudinal speed
v_{gy}	vehicle lateral speed
v_{ij}	wheel velocity
v_r	wheel nominal longitudinal speed
v_{u_i}	bristle deformation speed in the direction of the Oi axis
v_x	wheel actual longitudinal speed
$v_{x_{rr}}$	wheel longitudinal speed at zero acceleration
v_y	wheel lateral speed
V	Lyapunov function, control Lyapunov function
W	normal force
x	magic formula argument (κ, α, $\tan(\alpha)$)
$\mathbf{x}$	state vector

x_{eq}	equilibrium point
x_m	magic formula argument related to the maximum value D
x_s	slip distance
$\mathbf{y}$	state-space output vector
y_a	high slip magic formula asymptotic value
α	tire slip angle
$\bar{\alpha}$	normalized tire slip angle
β	vehicle side-slip angle
γ	camber angle, Lyapunov function class-κ function
δ	steering angle
δ_d	steering angle from the driver
$\delta_{d\max}$	sine with dwell maximum steering angle
δ_l	front-left wheel steering angle
δ_r	front-right wheel steering angle
δ_s	quadratic problem slack variable
δ_u	AFS steering angle intervention
ϵ_i	small quantity to avoid division-by-zero singularities
ζ	barrier function class-κ function
$\eta_b(\mathbf{x})$	input-output linearized system state vector
θ_s	slope angle, road grade
θ_x	theoretical longitudinal slip coefficient
θ_y	theoretical lateral slip coefficient
κ	longitudinal slip, slip ratio
$\bar{\kappa}$	normalized slip ratio
λ	no-slip contact patch ratio, system matrix eigenvalue
λ_i	magic formula scaling factor
μ	tire-road friction coefficient
μ_x	tire-road friction coefficient in the longitudinal direction
μ_y	tire-road friction coefficient in the lateral direction
μ_i	derivative of the control barrier function of rth order
σ	characteristic polynomial
σ_x	theoretical longitudinal slip
σ_y	theoretical lateral slip
τ_{G_z}	net moments around the Oz axis
ψ	vehicle yaw angle
$\dot{\psi}_d$	desired yaw rate
$\dot{\psi}_{\max}$	maximum yaw rate
ω	wheel angular speed
ω_{rr}	wheel angular speed at zero acceleration
ω_u	time derivative of the input signal
ω_y	vehicle pitch rate
Ω_C	region of attraction
Ω_u	set of admissible input signal time derivatives

CONTENTS

1 INTRODUCTION

This chapter presents the justification of this work and a brief description of the proposal itself and the employed methodology. The justification is divided into contextualization, that Section 1.1 presents, emphasizing road safety, and a specific tool for improving vehicle safety: electronic stability control, presented in Section 1.2.

1.1 Contextualization

Automobiles have been the most flexible personal mean of transport for over a century (GILLESPIE, 1992). Most sources agree that there are over 1.2 billion vehicles in the world today (STATISTA, 2020; CHESTERTON, 2018). By July 2019, there were 106 289 700 registered vehicles in Brazil (BRASIL, Ministério da Infraestrutura, 2020). Among these, 57 305 419 were automobiles and 1052 212 were utility vehicles, such as pick-up trucks or vans. By 2020, the total was 107 984 371 vehicles (IBGE, 2020) (see Figure 1). Hence, it can be said that road vehicles are a part of our lives, e.g., Figure 2.

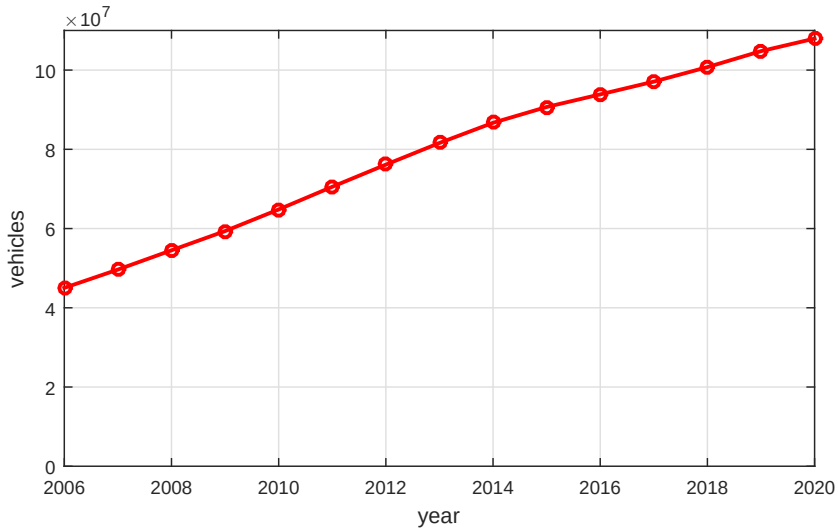

Figure 1: Vehicle fleet in Brazil.
SOURCE: (IBGE, 2020).

Figure 2: Heavy traffic at Pinheiros River expressway.
SOURCE: Marcos Santos/USP Imagens[1].

The widespread convenience of automobiles does not come without a cost, however. In 2016, 1.35 million people lost their lives in traffic accidents, being the 8th most common way of dying and the chief cause for people between 5 and 29 years old (LACERDA, 2019; WHO, 2018a, 2018b). In Brazil, it was the 10th leading cause of death in 2019, with 40 721 casualties. The country has the third most violent traffic in the world, only behind India and China, whose population is, of course, vastly superior (see Figure 3). The situation in other underdeveloped countries is similar: road accidents are the 7th cause of death in low-income countries, and 10th in both lower-middle-income and upper-middle-income countries (WHO, 2018b).

SOURCE: USP Imagens[2].
(a) Severe rear collision.

SOURCE: USP Imagens[3].
(b) Accident with a vehicle rollover.

Figure 3: Accidents in highways.

[1]Available at <https://imagens.usp.br/editorias/pessoas-categorias/transito-2/attachment/28112013transitofotomarcossantos016/>

Thus, ways of mitigating the loss of lives due to vehicle accidents are essential. Several methods of endeavoring this objective have already been attempted, from road conservation strategies to alcohol consumption control (WHO, 2018a). Legislation and technical advances have been responsible for improving road safety in the past. Most countries have legislation about speeding, driving under the influence of alcohol and other drugs, and using protective devices such as seatbelts and helmets. As for technical advances, motor vehicle manufacturers have provided cars with better energy-absorbing structures, shatter-resistant glass windshields, and airbags, called passive safety features; and automatic cruise control, lane keeping assist, anti-lock braking systems, and stability control systems, which are active safety systems (JARAŠŨNIENE; JAKUBAUSKAS, 2007).

1.2 Electronic stability control as a safety system

Traffic accidents that feature vehicle rollovers (e.g., Figure 3b) are among the ones with the highest death rates. According to the U.S. Department of Transportation, around 35 % of fatal accidents in that country in 2010 were a result of a mere 2.1 % of the total of crashes, precisely the ones which featured a vehicle rollover (U.S. DEPARTMENT OF TRANSPORTATION, 2020b). This happens because the upper part of the vehicle is usually more fragile than its chassis and main body. Moreover, when the vehicle overturns, occupants' vital parts such as heads, necks, and torsos are subject to additional impact hazards that, in turn, are increased by multiple rollovers or any security item failure. As a result, this type of accident must be avoided at all costs.

The lethality of rollover accidents is not necessarily related to a previous accident that may have caused it. In point of fact, most cases of vehicle overturns only involve the driver, the vehicle, and the terrain, that is to say, they are not a result of previous crashes with other vehicles. They are often caused by alcohol consumption and speeding, and are more common on 2-way roads at higher speeds and with vehicles with a higher center of mass (U.S. DEPARTMENT OF TRANSPORTATION, 2020a).

The most technically advanced strategy to reduce the number of accidents that is being developed throughout the last decades is to remove the human driver altogether, using fully automated cars instead (JOCHEM; POMERLEAU; THORPE, 1995; BUEHLER; IAGNEMMA; SINGH, 2008a, 2008b; IAGNEMMA; BUEHLER, 2006a, 2006b; GUIZZO,

[2]Available at <https://imagens.usp.br/editorias/lugares-categorias/estradas/attachment/estrada004/>

[3]Available at <https://imagens.usp.br/editorias/lugares-categorias/estradas/attachment/estrada001/>

2011; THRUN; BURGARD; FOX, 2005). Less daring strategies aim to supply the human driver with extra tools in order to maneuver the automobiles or other vehicles, such as heads-up displays (HUDs) presenting speed limit, current speed, pedestrians, cyclists, and any other important information on the windshield so that the human does not need to stop watching the road to access them. Other tools include adaptive cruise speed control, to avoid collision with vehicles ahead of the driver; or *electronic stability control* (ESC), so as to avoid roll-overs and slippages when the vehicle is maneuvered in harsh conditions, especially those with a higher center of mass. Such tools are collectively known as *advanced driver-assistance systems* (ADAS), and many of those are also part of what is necessary to implement a self-driving car, except the necessity of formatting information in a way a human operator can understand it.

The tool that is most closely related to reducing rollover accidents is ESC, and its effectiveness in preventing vehicle accidents has been demonstrated by several studies (ERKE, 2008; PAPELIS; WATSON; BROWN, 2010; HØYE, 2011), being that for sport utility vehicles (SUVs) this reduction may be extreme (GREEN; WOODROOFFE, 2006). This can be explained by both the avoidance of loss of vehicle control (LOC), which often leads to overcorrection by the driver, and the reduced chance of road departures, which can cause *tripped rollovers*, the most common type of such accidents (U.S. DEPARTMENT OF TRANSPORTATION, 2020c).

The first ESC systems prevented the driver from losing control of the vehicle by selectively braking individual wheels when it is about to spin out (more on that in Chapter 3). Applying individual braking pressures on each wheel's brake actuator is known as *differential braking*. This method is still the most common in the industry. An alternative technique—which, nonetheless, can be used simultaneously with differential braking—is *active steering*, which consists of interfering with the steering system and preventing the steerable wheels from excessively turning in case of overcorrection by the driver due to an emergency.

The primary objectives of this work are to develop safety-critical electronic stability control systems for low center-of-mass automobiles, using the steering and braking systems as input methods. As a consequence of the low center of mass, the respective research endeavor dealt only with yaw control, i.e., we have investigated lateral stability, but not roll stability. This is known as yaw stability control (YSC).

There are two possible approaches to ESC: preventing the vehicle from losing stability and recovering stability. To apply the first approach, we studied lateral stability regions,

with the ulterior objective of preventing the vehicle state from leaving them. We identified shortcomings in the literature, providing the contributions presented in Chapter 5 and published in (ALVES; CHINELATO; ANGELICO, 2022).

The stability regions from Chapter 5 have been used to design ESC systems with safety-critical control methods that consider those regions as safe sets. Such sets are dependent on the steering wheel angle. If the driver moves the steering wheel fast enough, it becomes impossible to keep the state in the aforementioned safe set. In order to accomplish that, it was necessary to extend the current safety-critical control theory (see Chapter 4 for a brief survey on the subject) and to use the steering system as the control input, i.e., active steering. The proposed methods are presented in Chapter 6.

Our second set of control contributions considers the more usual ESC system, which employs differential braking to generate a yaw moment on the vehicle. The driver can always cause vehicle instability if the control system does not interfere with the steering system. We propose a strategy to either maintain or recover stability in the face of two system inputs: the steering angle, provided by the driver, and the brake pressures, given by the ESC system. We again provided extensions to safety-critical control theory, this time to accommodate either known disturbances or external control inputs—they are indistinguishable from the point of view of the control system. The methodology for validating the closed-loop systems is presented in Section 1.3. Section 1.4 summarizes the chapter.

1.3 Methodology

Our first contribution is improving lateral stability region generation for road vehicles. We obtain higher-definition regions by using binary lattices and avoiding errors when analyzing stability conditions. In particular, we argue that such regions can be used to design electronic stability control systems. This is validated by properly implementing such systems using conservative stability regions to design an active steering ESC system.

At the same time, this text also proposes safety-critical control based on control barrier functions (CBFs) as a viable control method for ESC systems. Since the aforementioned closed-loop systems use safety-critical control, it is clear that the respective implementations validate that claim. The claim is further validated by alternative ESC system implementations that used differential braking in place of active steering.

This text proposes safety-critical ESC systems considering both active front steering

(AFS) and differential braking. Several standard maneuvers access the lateral stability of the vehicle, such as the Fishhook test (NHTSA, 2001), Double Lane Change (LNCAP, 2020), Steady-State Circle Series, J-Turn test (NHTSA, 2001, 2018), or the Sine with Dwell test (NHTSA, 2008, 2009; EUROPEAN UNION, 2015; ENCAP, 2020). However, most of them are also affected by other aspects, such as roll stability, driver skill, handling, and road conditions. The one focused on lateral stability, and used to access automobile ESC systems, is the Sine with Dwell test, which uses the 0.7-Hz Sine with Dwell maneuver.

On the other hand, the literature often employs distinct maneuvers. Some works use the standard Double Lane Change, which uses an expert driver to perform a path-following task, and induces lateral instability immediately after each lane change. Other studies also use a double lane change maneuver but not following a standard. A few of them use single lane change maneuvers, which are not part of any standards; J-turn maneuvers; and other open-loop steering inputs. Concisely, we do not verify a consensus in the scientific literature on methods to evaluate lateral stability.

When convenient, we used a non-standardized maneuver to more easily compare our results with the respective literature (in Section 6.2). However, for other cases, we adopted the Sine with Dwell test to better describe the effectiveness of the proposed ESC systems. Section 3.3 presents the procedure: we shall learn that the test uses two criteria: a responsiveness one, based on the ability to change the trajectory of the vehicle, and a lateral stability criterion, which considers how long the system takes to recover from the effects of oversteering.

Finally, we know that vehicles are complex systems composed of several moving parts, some of which are not necessarily rigid. This includes not only the tires but longer axles which are part of the transmission system. Hence the system is not lumped, i.e., it cannot be exactly modeled by a finite number of states. Moreover, the system has several nonlinear components, such as tires, suspension, and said moving parts—even the rigid ones—are modeled by nonlinear equations of disparate dynamics. Consequently, more comprehensive models are ill-posed, being difficult to simulate.

We used a 2nd-order linearized model to design the control systems we propose. The closed-loop systems were validated by linear and nonlinear models of order 2 or higher. In particular, CarSim provided the most extensive model, whose behavior is much closer to a real vehicle. In addition, we used the magic formula (MF) equation set to describe steady-state tire dynamics, either for the in-house models or CarSim vehicle models.

1.4 Concluding remarks

The work on ESC is justified by both its major role in accident prevention in general, with particular importance of its ability to considerably reduce the occurrence of vehicle rollovers.

ESCs have been a hot research topic for over a decade. Safety-critical control advances from the last decade have also called the attention of the control system academic community. This text introduces one of the first applications of safety-critical control based on control barrier and Lyapunov functions to ESCs based on active steering, the first application to ESC based on differential braking, and provides a few convenient extensions to the respective theory. Moreover, it solves problems from those first AFS implementations and contributes to lateral stability region generation.

This work presents the following contributions:

1. improves lateral stability region generation;
2. introduces conservative stability regions;
3. identifies necessary conditions for safe sets used in safety-critical control applied to lateral vehicle stability;
4. introduces control-dependent control Lyapunov functions;
5. presents the second safety-critical control ESC implementation based on control barrier functions that uses active front steering while solving latent problems from the previous entry in the literature;
6. validates the stability regions through safety-critical control applications based on CBFs that use active front steering;
7. identifies a limitation in the proposed safety-critical control ESC implementation;
8. introduces control-dependent exponential control barrier and Lyapunov functions;
9. presents a third safety-critical control ESC implementation based on CBFs that uses active front steering, this time using control-dependent exponential control barrier functions;
10. validates safety-critical control based on control-dependent exponential control barrier functions through the aforementioned implementation using CarSim;
11. identifies that lateral stability regions cannot be rendered safe by differential-braking ESC systems;
12. introduces control-disturbance-dependent exponential control barrier and Lyapunov functions;
13. presents the first safety-critical control ESC implementation based on CBFs that

uses differential braking;

14. validates safety-critical control based on control-disturbance-dependent exponential control barrier functions through the aforementioned implementation using CarSim.

The remainder of this document is structured as follows: Chapter 2 presents an introduction to vehicle dynamics, focused on the most important subsystems for stability control; Chapter 3 presents the electronic stability control problem and a review of the pertaining literature. Chapter 4 follows with an introduction to safety-critical control based on control barrier functions: its fundamentals and the elementary theory. The stability regions and the active steering safety-critical control methods are presented, in the respective order, in Chapters 5 and 6. The extensions to control Lyapunov functions and exponential barrier functions that depend on the control input are also presented in Chapter 6. Yaw stability control methods are shown in Chapter 7, together with the safety-critical control extensions that consider external control inputs and arbitrary-order exponential functions, while Chapter 8 presents the last remarks and future works.

2 VEHICLE DYNAMICS

Wheeled robots are often modeled as nonholonomic systems, where one assumes the wheels do not slip. Under this consideration, it is possible to prove that there are only five types of possible wheeled vehicles when it comes to the type of constraint which results from the wheels it uses (CAMPION; BASTIN; D'ANDRÉA-NOVEL, 1996). One of those types is vehicles with two fixed wheels along the same axis, and other orientable wheels in order to steer them. Of course, passenger cars are among such vehicles.

The problem is that the dynamic descriptions of vehicles under the aforementioned circumstances had simply failed to adequately describe their behavior, despite how complete the description of the vehicle's several moving parts would be (GILLESPIE, 1992). The notion that when a wheel turns, it moves itself forward proportionally to its angular position variation, and that it would not move sideways when turning was found not to be true. In other words, the assumptions which are often considered in mobile robotics simple kinematic models are, in truth, not valid for vehicles with pneumatic tires. This sparked the interest in the development and study of *tire dynamics*, whose study could be traced back to the 1930s.

The field of tire dynamics describes how rubber tires behave when attached to a vehicle and being used to move it. More precisely, it relates the torques and forces the tires can develop in relation to their orientation and movement. These forces cause the vehicle to move, which can then be described by increasingly complex models, depending on the amount of detail that is necessary for the problem at hand. The field of *vehicle dynamics* deals with such models combined with those of the remainder of the vehicle. It was mature since around the 1970s, with the appearance of the first books on the subject (GILLESPIE, 1992).

The equations which establish a vehicle model are related to how forces and torques are generated and, eventually, cause the vehicle to move. Hence, a comprehensive mathematical model includes the motor's ability to produce torque on its crankshaft, which depends primarily on the latter's angular speed and fuel injection on the first. The engine

is coupled to a transmission, which, in turn, is coupled to the rest of the drivetrain. The set will deliver torque to the wheels under a certain rotation ratio and at the expense of energy loss due to friction and kinetic energy variation of the moving parts (GILLESPIE, 1992).

The driver further changes the orientation of steerable wheels through the steering system and directly applies torque through the brakes. The relative movement of the wheels and the ground, in turn, together with the torque from the drivetrain, will generate forces and torques on the vehicle's body. Those are a function of the normal force on the tire, the wheel's longitudinal and lateral speed with respect to the ground, its angular speeds around the rolling and vertical axles, and the torque from the drivetrain (GILLESPIE, 1992; PACEJKA, 2012). The aforementioned efforts are applied both on the suspension system, which absorbs part of the energy with respect to the relative movement between the body and the wheels; and directly to the body. As the vehicle accelerates, so do the several moving parts inside it, and the normal forces on the tires are altered. Therefore, several internal feedback loops are present in the model, as depicted in Figure 4.

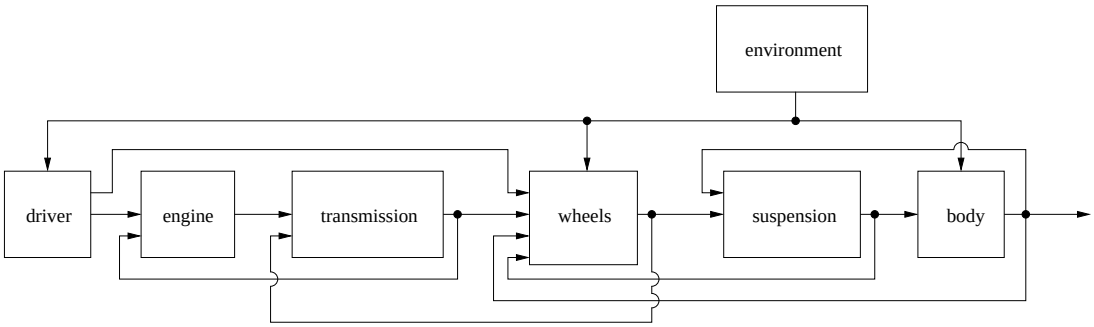

Figure 4: Block diagram of a vehicle model.

Every block from Figure 4 is a multivariate subsystem described by nonlinear equations. The resulting model, in which the signal quantities are omitted, is quite complex and cannot be expressed in closed form. Hence, simplifications and linearizations are often made in order to treat the related control problems. Since vehicle stability problems are grave, the control system must quickly dealt with them. So fast that the engine is unable to respond on such short notice in the case of internal-combustion engines. Thus, the ESC literature (see Chapter 3) often assumes the vehicle's speed will not be affected by the engine and the drivetrain. As a result, the subsystems that are necessary for stability control are the tires and the body. Suspension is either taken into account or not, depending on the level of detail and the specific control objective.

We first introduce the tire dynamics in Section 2.1 and follow with the different vehicle

models in Section 2.3, where the body is taken into account.

2.1 Tire Dynamics

Here we present the bases to understand how pneumatic rubber wheels traction vehicles. The differences from the aforementioned simplifications which are often considered in the field of robotics are related to the material from which pneumatic tires are made, that is to say, rubber. Of course, we know rubber is deformable, therefore it is not true that wheels would touch the ground through a single point, whereas common approximations are non-deformable wheels and punctual contact with the ground. For a more complete description of wheels, see (PACEJKA, 2012)—which will serve as the main source for this section—and the references therein.

As a wheel deforms, it forms an area of contact with the ground, which is referred to as *contact patch*. The forces which cause the movement of the vehicle's body come from the collection of such contact patches (four, in the case of an automobile), and are applied there. This is an unfortunate fact since such forces are as far away from the vehicle's center of mass as they can be, thus excerpting the maximum moment around that point. This is the cause of the phenomenon known as *load transfer*, which explains how a vehicle may roll over after overcorrection from the driver while the vehicle turns.

As torque is applied to traction wheels, they will accelerate the vehicle's body in the expected direction. However, as they are subject to such torques, one can not find a proportion between the wheel angle variation and the distance the wheel moves along. The higher the torque applied to it, the less it moves forward when compared to how much it turns. In other words, *wheels slip*. A similar phenomenon is observed when vehicles turn: unlike what one might expect, as a vehicle performs a turn, its wheels will slightly move sideways. Thus, there is an *angle* related to how wheels slip in turns.

In addition to the slip, rubber tires also oppose rolling through a phenomenon known as *rolling resistance*. As a tire sustains any weight through the structure it is attached to, its ability to roll is incrementally decreased. This happens regardless of any dry or viscous friction which might be verified on its pillow block, or friction between the tire and the soil. Therefore, it does not depend mainly on the wheel's angular speed, but on the weight it sustains, that is, the normal force.

The phenomena of slip and rolling resistance are related to the properties of rubber. Rubber is a *viscoelastic* material, which differs from elastic ones. For elastic materials,

there is a proportion between the force applied to them and the resulting deformation. The relation between force and deformation can be described by a function, i.e., there is a one-to-one relation between those two quantities. Viscoelastic materials, on the other hand, have this relation being dependent on time, and on previous loadings or unloadings. As a result, the typical loading and unloading curve for this type of material is as Figure 5 shows, where τ_v is the stress (either compression or decompression) and Δx_v is the resulting deformation. We see that after removing the load, the material does not immediately return to its original dimension, unlike elastic materials.

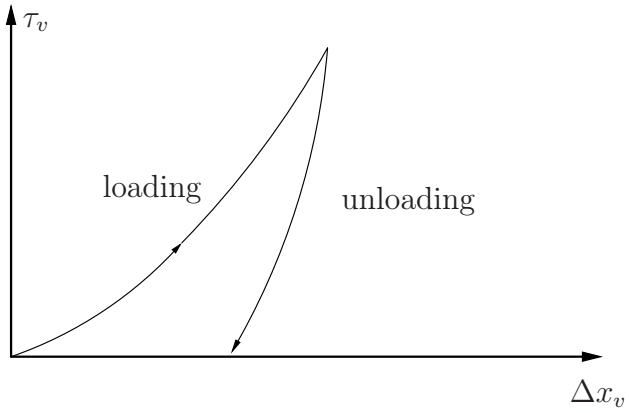

Figure 5: Viscoelastic material loading and unloading deformation.

We start with the rolling resistance since it is easier to explain. Assume the wheel sustains a weight W, from which results that the normal force between the wheel and the ground is also W and the lower part of the wheel deforms, as seen in Figure 6a. Assuming the deformation is highest near the center of the contact patch, where the minimum wheel radius $r_{\min}$ touches the ground, we can assume it will be symmetric around c, as the dashed line in Figure 6a shows. Since we are talking about dynamics, the wheel must be moving. As it rolls forward, the tread elements at the region between a and c are compressed and tend to decelerate it, while at the region between c and e they are decompressed, pulling it forward again. Would the material the tire is made of be elastic, the pressure on both these regions would be the same, and so would the acceleration and deceleration forces. However, this is not the case. Since rubber is a viscoelastic material, the compression region will generate a force that is slightly larger than that of the decompression one, which is shown as the continuous line in Figure 6b. Thus, there will be a decelerating moment against the tire's movement, which can be seen by the vehicle body as a force against the direction the vehicle moves to. The exact nature of this force depends on several variables which are a consequence of the highly nonlinear, time and temperature-dependent behavior of rubber. This rolling resistance force R_i is often simplified, however,

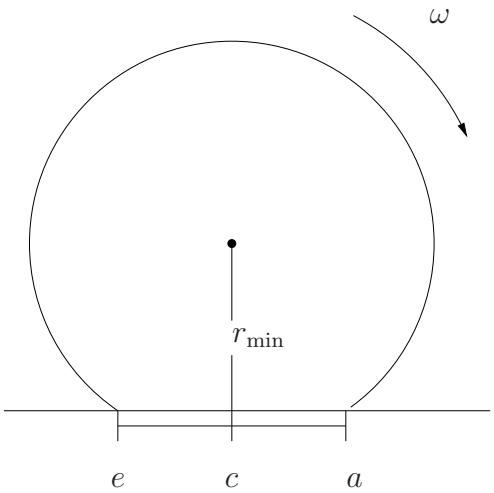

(a) Deformed wheel under loading.

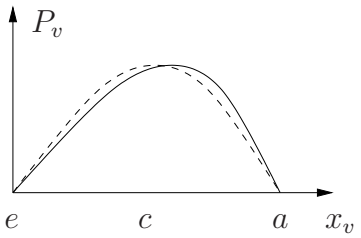

(b) Pressure throughout the contact patch.

Figure 6: Wheel carrying a load.

in most vehicle dynamics textbooks, software, and articles as being proportional to the vertical load W_i on the tire as

$$R_i = f_\psi W_i, \tag{2.1}$$

where f_ψ is the rolling resistance coefficient. We shall reference each wheel's rolling resistance and normal force through the index i, being fr for the front right wheel, fl for the front left wheel, rr for the rear right wheel, and rl for the rear left wheel. In other words, for instance, R_{rl} is the rolling resistance on the rear left wheel of the vehicle.

2.2 Tire models

The process of force generation on tires is also related to the properties of rubber. The aforementioned facts about tire slip are related to the use of a deformable material in order to manufacture them. As the driver moves the steering wheel and either accelerates or brakes the vehicle, the forces generated by the tires change, but not instantly, since such a vehicle is not rigidly attached to the ground. However, the dynamic behavior of the tires themselves is faster than that of the whole vehicle. Therefore, dynamic models of vehicles often consider only steady-state models for the tires. We will present two such models, one that is simpler to understand, and the other that is more descriptive of the actual tire behavior (PACEJKA, 2012).

2.2.1 Brush model

The brush model describes, in a simplified manner, wheels with deformable tires rolling over a plane. While not accurate for severe tire slip, it provides an important understanding of the tire dynamics fundamentals. The subject is introduced as presented in (PACEJKA, 2012). We consider that the plane the wheel rolls over is defined by Ox and Oy axes, as pictured in Figure 7, where the wheel points to the positive direction of Ox. However, due to sliding, the wheel moves with velocity v instead, which is at an angle α with Ox. We define a wheel's yaw angle ψ_w around Oz with respect to an inertial frame,

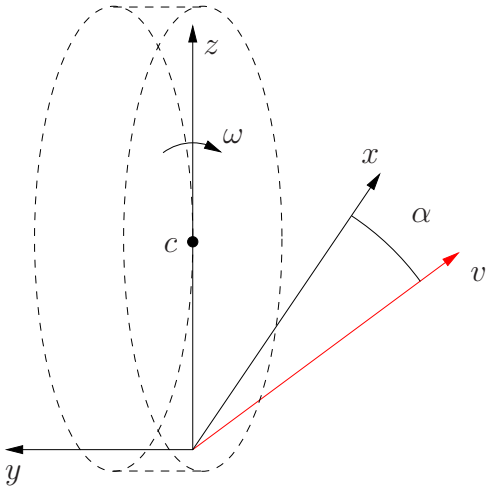

Figure 7: Wheel coordinates.

whose time derivative is the yaw rate $\dot{\psi}_w$. We first describe the longitudinal movement of the wheel, where α and ψ_w can be ignored, so that the wheel moves forward in the Ox direction, as expected.

Let us consider a tire whose tread elements are several bristles, as seen in Figure 8. To more easily display it, the number of bristles is reduced in Figure 8, but we assume there are several of them close to one another, whose effect is eventually integrated in order to obtain the model. We assume the bristles are so close to one another that they are not susceptible to buckling. In other words, they will not collapse when subject to compression, but instead simply deform vertically. When subject to shear stress, on the other hand, they will deform horizontally, but still, they shall not collapse.

The process which causes tread elements to slip is described in the brush model as a combination of vertical compression and horizontal stress. This is a simplification of the actual phenomenon of shear stress which the tread elements are subject to when the vehicle either brakes or accelerates. The bristles' compression is a result of the normal force on the tire. As a consequence, would we picture a tire at rest, holding its share of

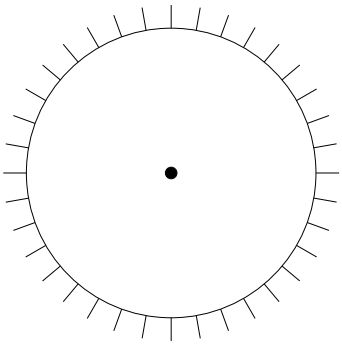

Figure 8: Wheel made of bristles (brush wheel).

the weight of the vehicle, the tire's bristles within the contact patch would all be subject to compression, and would therefore be vertically deformed (see Figure 9a). Now let the wheel be subject to an accelerating torque, but still not moving so as to properly pull the vehicle. Just before it turns, all bristles would be equally deformed, as seen in Figure 9b, in the horizontal direction, as the upper end of such bristles is attached to the rest of the wheel while the lower end is anchored to the ground through dry friction. This combination of horizontal traction due to accelerating or braking and the friction from the vertical load and the friction coefficient will explain the phenomenon of slipping. Assume, now, the wheel turns just so that the leftmost bristle in Figure 9b detaches from the ground, while another one touches and adheres to it at the rightmost part of the contact patch, which is shown in Figure 9c. If one assumes the torque is still the same as before, the sum of all the bristles' forces, together with the new one which has just touched the ground, should integrate to the same force previously provided by the bristles (Figure 9b). As a result, since the bristle which has just touched the ground is, at first, undeformed, and as one of such bristles has just lost contact with the ground, all others must become slightly more deformed, to compensate for the loss of traction. Therefore, the new bristle deformation will be very small, and the remaining ones must deform the same amount even more.

Proceeding by induction, each time a bristle loses adhesion at the leftmost part of the contact patch as another one touches the ground on the opposite end, the horizontal deformation increases from right to left, if the wheel rolls in the clockwise direction, as seen in Figure 9d. Therefore, we realize that the bristles' deformation increases from the point they adhere to the ground up until they are about to lose contact, that all bristles are subject to shear stress, and they adhere to the ground through static dry friction between the rubber and the ground. In addition to it, it is easy to understand that the larger the accelerating torque on the wheel is, the larger the shear stress and the resulting deformation will be. We are now ready to understand the principle of wheel slip.

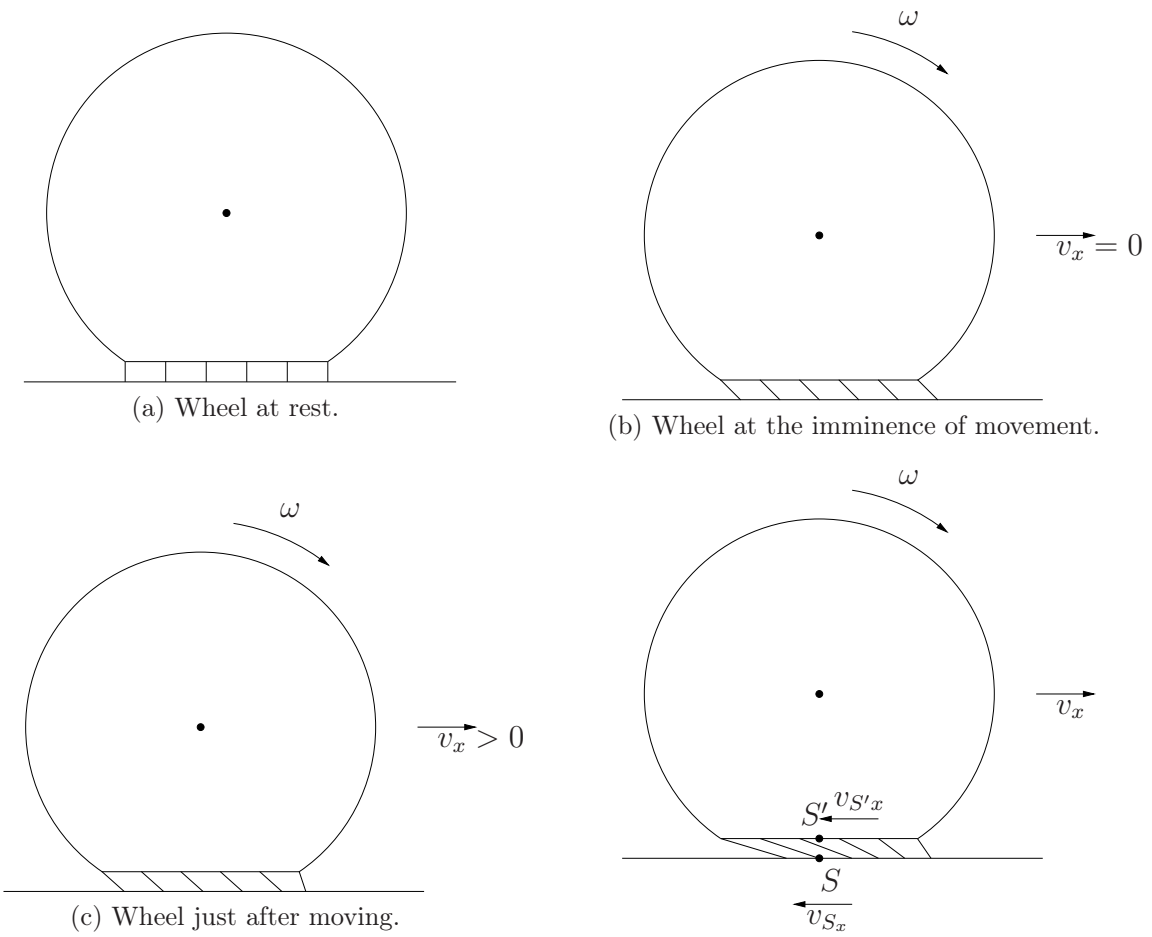

(a) Wheel at rest.

(b) Wheel at the imminence of movement.

(c) Wheel just after moving.

(d) Steady-state wheel under traction.

Figure 9: Moving wheel.

We know the bristles are held in place by the friction force. Friction forces, in turn, are always limited by the normal force between the adjacent surfaces, which are additionally factored by the friction coefficient. Therefore, there will be a maximum deformation that the bristles can withstand before they start slipping. As a consequence, if the torque on the wheel is large enough, those bristles which are deformed the most will start slipping. Also, the larger the torque is, the larger the region of the contact patch in which slipping takes place. Figure 10 illustrates this fact, in which the *slip distance* x_s is defined.

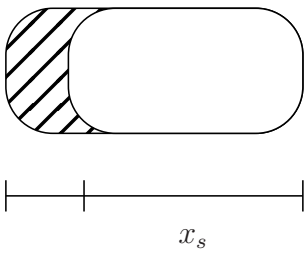

Figure 10: Contact patch and slip distance.

We conclude that there is a relation between the wheel torque and slip. We proceed to formally define wheel slip. We first define the *effective radius* as

$$r_e \triangleq \frac{v_{x_{rr}}}{\omega_{rr}}, \tag{2.2}$$

where $v_{x_{rr}}$ and ω_{rr} are, in the respective order, the longitudinal and angular speeds of the wheel when the applied torque is just enough to maintain its movement, that is to say, to cancel the effects of the rolling resistance. In that situation, the wheels generate no actual force on the vehicle body. The more we increase the torque, the higher the force on the vehicle gets, as expected. However, that increases the slip region. A consequence is that the wheel increases its angular speed, but it has to turn slightly more per unit of traveled length since there is slipping in an increasingly larger area of the contact patch. In this regard, the *longitudinal slip* or *slip ratio* (also called *practical slip*) is defined as

$$\kappa \triangleq -\frac{v_x - r_e\omega}{|v_x|}, \tag{2.3}$$

which will be positive when a positive torque is applied on the wheel, or, in other words, when it pulls the vehicle forward or brakes it while in reverse gear, whereas it will assume negative values when the vehicle brakes (or accelerates, when in reverse). By definition [(2.2) and (2.3)], when the vehicle maintains its longitudinal speed while traveling in a straight line, there is no slipping. Finally, a corollary is that when the wheel is blocked, $\kappa = \mp 1$ (PACEJKA, 2012) (negative in the case of forward gears).

Here, it is important to mention that what most people would associate with slipping (or *sliding*, which is not a synonym within vehicle dynamics) is either regions of slipping propagating themselves throughout the contact patch, or no region of adhesion at all within the tire's contact patch, whereas the definition in vehicle dynamics is merely a difference in longitudinal speed. It has been verified, moreover, that slipping needs to be taken into account in order to properly describe vehicles with pneumatic tires. When the vehicle is turning, this will be even more important, since not considering slipping in that situation would lead to very large position errors due to drifting within a short period, wrong direction of lateral forces, and incorrect yaw moments, as a consequence.

A longitudinal tire model must relate the longitudinal slip to the driving force the wheel generates. Within the ambit of the brush model, this will be achieved under the following assumptions:

1. the normal force per unit of length, throughout the contact patch, is a parabolic function that is null at the borders (a and e in Figure 6b) and has its peak below

the center of the wheel;

2. there is no difference between the dry friction coefficient and the kinetic friction coefficient;
3. the bristles are described by their longitudinal stiffness c_{p_x}, which is the ratio of the force needed to deform them and the longitudinal deformation itself;
4. the difference between the area of the contact patch and the corresponding area on the wheel rim (at the upper end of the thread elements) is negligible[1].

These assumptions are considered together with a fact: the driving forces, which cause the vehicle to alter its velocity, come from the contact patches. Each contact patch can be partitioned into two areas: one with bristle adhesion, and the other where there is slipping. The force provided by the area with adhesion is proportional to the bristles' deformation factored by the bristles' longitudinal stiffness. The force from the friction is the normal force multiplied by the friction coefficient. We start with the adhesion area.

In order to integrate the adhesion forces, one must first obtain the sliding distance, which is the length of the adhesion area (see Figure 10). This distance will be that of when the bristle deformation u_{b_x} causes a force that equals the friction force. Considering Figure 9d, let the reference point be the center of the wheel. In this reference, a point S in the road, which is within the contact patch, moves backward at speed v_{S_x} (the actual wheel longitudinal speed). A point S' on the upper end of the bristles moves at a slightly higher speed, namely that of the points at the effective wheel radius [2]. Thus, deformation increases over time and can be expressed as

$$u_{b_x} = \frac{\omega r_e - v_x}{v_r} \Delta t, \tag{2.4}$$

where Δt is the time since the bristle touched the ground.

Let $2a$ be the length of the contact patch, and let the origin of a real axis be positioned at the midpoint of it. Thus, points in the contact patch belong to $[-a, a]$. At a distance $x = a$, the bristle has just touched the ground, and there is no deformation, yet. As time goes by, the deformation increases according to

$$v_{u_x} \triangleq \frac{\mathrm{d}u_{b_x}}{\mathrm{d}t} = v_r - v_x, \tag{2.5}$$

with $v_r \triangleq \omega r_e$. The deformation of the bristles whose upper end are at a distance x from

[1] This is equivalent to considering that the bristles' deformation is much smaller than the contact patch length, which is a valid approximation for any passenger car tire.

[2] This assumption is equivalent to considering that the bristles' height is negligible so that they deform in the horizontal direction.

the origin is

$$u_{b_x} = v_{u_x} \Delta t. \tag{2.6}$$

Considering the point S', we have

$$\Delta t = \frac{a - x}{v_r}. \tag{2.7}$$

Substituting (2.7) in (2.4), we have

$$u_{b_x} = (a - x)\frac{v_r - v_x}{v_r}, \tag{2.8}$$

and using (2.3),

$$u_{b_x} = (a - x)\frac{\kappa}{1 + \kappa}. \tag{2.9}$$

In order to abridge later expressions, we define the *theoretical (longitudinal) slip* $\sigma_x \triangleq v_{u_x}/|v_r|$, so that (2.9) becomes

$$u_{b_x} = (a - x)\sigma_x. \tag{2.10}$$

The pressure q_{b_x} the bristles apply on the wheel (and, thus, the vehicle) is

$$q_{b_x} = c_x u_{b_x}. \tag{2.11}$$

The condition for the bristle slip to occur—which, thus, defines the slip distance x_s—is

$$q_{b_x} > q_{f_x}, \tag{2.12}$$

where q_{f_x} is the maximum friction pressure given by

$$q_{f_x} = \mu q_z, \tag{2.13}$$

where q_z is the normal pressure. As previously mentioned, we assume a parabolic pressure distribution along the contact patch (see Figure 11)

$$q_z = \frac{3W}{4a}\left(1 - \left(\frac{x}{a}\right)^2\right). \tag{2.14}$$

Substituting (2.13), (2.14), (2.11), (2.10) into (2.12) and turning it into an equality we have

$$c_{px}(a - x)\sigma_x = \mu\frac{3W}{4a}\left(\frac{a^2 - x^2}{a^2}\right), \tag{2.15}$$

and solving for σ_x we obtain

$$\sigma_x = \frac{3\mu W}{4c_{px}a^2}\frac{a + x_s}{a}. \tag{2.16}$$

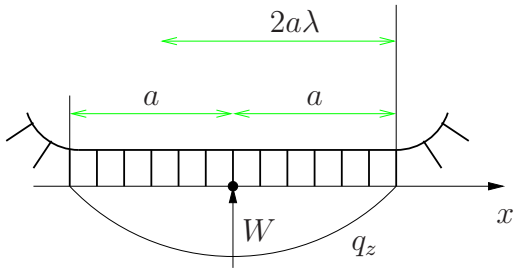

Figure 11: Contact patch pressure.
Source: (PACEJKA, 2012) (adapted).

For the sake of shortening the expressions, we define

$$\theta_x \triangleq \frac{2}{3}\frac{c_{px}a^2}{\mu W}, \tag{2.17}$$

and assume that the bristles lose adhesion to the ground at $x_s = 2a\lambda$ (see Figure 11)

$$\begin{aligned}\sigma_x &= \frac{3}{4}\frac{\mu W}{c_{px}a^2}\frac{a+x_s}{a}\\ &= \frac{1}{2\theta_x}\frac{2a-2a\lambda}{a}\\ &= \frac{1}{\theta_x}(1-\lambda)\\ \lambda &= 1-\theta_x\sigma_x. \end{aligned}\tag{2.18}$$

Knowing x_s, the longitudinal wheel force from the adhesion and slip regions can be found by integration. Let F_{a_x} be the longitudinal force addend that results from adhesion, and F_{s_x} the one that is due to sliding. Then we have

$$F_x = F_{a_x} + F_{s_x}, \tag{2.19}$$

with

$$\begin{aligned}F_{a_x} &= \int_{a-2a\lambda}^{a} c_{p_x}(a-x)\sigma_x \,\mathrm{d}x\\ &= c_{p_x}\sigma_x\left[ax - \frac{1}{2}x^2\right]_{a-2a\lambda}^{a}\\ &= 2c_{p_x}a^2\sigma_x\left[1-2\theta_x\sigma_x+(\theta_x\sigma_x)^2\right]\end{aligned}\tag{2.20}$$

and

$$\begin{aligned}F_{s_x} &= \int_{-a}^{a-2a\lambda} \mu q_z \,\mathrm{d}x\\ &= \int_{-a}^{a-2a\lambda} \frac{3\mu W}{4a^2}(a^2-x^2)\,\mathrm{d}x\end{aligned}$$

$$
\begin{aligned}
&= \int_{-a}^{a-2a\lambda} \frac{c_{p_x}}{2\theta_x} \frac{a^2 - x^2}{a} \, \mathrm{d}x \\
&= \frac{c_{p_x}}{2\theta_x} \left[ax - \frac{1}{3a} x^3 \right]_{-a}^{a-2a\lambda} \\
&= 2c_{p_x} a^2 \sigma_x \left[\theta_x \sigma_x - \frac{2}{3} (\theta_x \sigma_x)^2 \right]. \qquad (2.21)
\end{aligned}
$$

Substituting (2.20) and (2.21) in (2.19), we obtain

$$
F_x = C_{F\kappa} \sigma_x \left[1 - \theta_x \sigma_x + \frac{1}{3} (\theta_x \sigma_x)^2 \right], \qquad (2.22)
$$

where $C_{F\kappa} \triangleq 2c_{p_x} a^2$ is the *longitudinal slip stiffness*.

In case the wheel torque is low, (2.12) does not hold, and there is no slipping. Therefore, the slip distance is the contact patch length, or, in other words, $\lambda = 1$. As a result, (2.20) becomes

$$
\begin{aligned}
F_{a_x} &= \int_{-a}^{a} c_{p_x} (a - x) \sigma_x \, \mathrm{d}x \\
&= c_{p_x} \sigma_x \left[ax - \frac{1}{2} x^2 \right]_{-a}^{a} \\
&= C_{F\kappa} \sigma_x. \qquad (2.23)
\end{aligned}
$$

It is clear (2.23) is linear on σ_x. On the other hand, the higher order terms in (2.22) will already vanish for very low force values. Therefore, it is unnecessary to worry about (eventually) having no slip region inside the contact patch, so one can consider (2.22) exclusively. Still, since the definition of longitudinal slip does not depend on the existence of tread element slipping through dry friction, but on a difference between a nominal longitudinal speed (based on the wheel's angular speed) and the actual wheel speed which can result due to the viscoelastic material the tire is made of, it follows that there is a one-to-one relation between force generation and longitudinal slip.

The lateral force generation involves a similar mechanism to that of longitudinal slip, shown in Figure 12. Let a wheel under a vertical load W be subject to a lateral force. The immediate effect would be that all bristles in contact with the ground would be deformed sideways, that is to say, in the y direction. Now let it roll forward just so that a bristle loses contact with the ground and another one touches it. Since all bristles were previously deformed so as to withstand the lateral force, the remaining ones will be further deformed, while the one that touches the ground will deform only slightly. As a result, even if the lateral force which results from the collection of deformed bristles remains the same, it will

no longer be applied at the center of the contact patch, but slightly behind it, nearer to the hind region of the contact patch. Thus, the wheel tends to turn in the negative direction of its yaw angle. If we proceed by induction, similarly to the longitudinal case, the closer

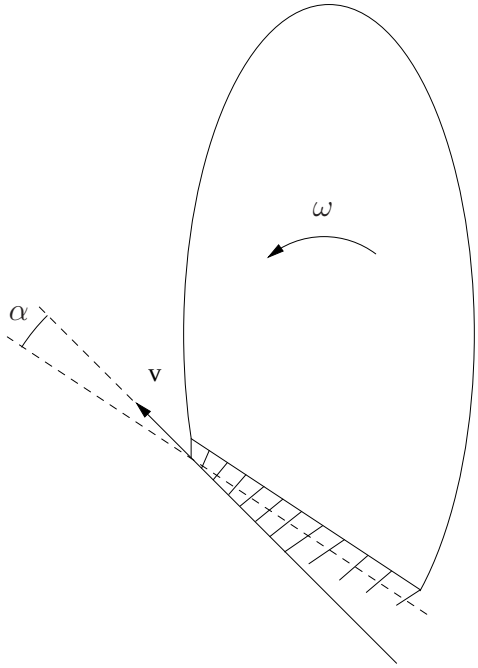

Figure 12: Brush wheel while turning.

the bristles are to the rear of the contact patch, the more deformed they become. That will increase the distance between the lateral force point of application and the center of the wheels, thus creating a moment. If we now assure the wheel is attached to a vehicle that turns with a positive yaw rate (that is to say, counterclockwise when viewed from above, see Figure 7), that moment will try to return the wheel to the straight position. This explains why this moment is called *aligning torque* or *restoring moment*.

The incremental bristle deformation that is verified in the first section of the contact patch is such that the bristles adhere to the ground. Therefore, they are aligned with the direction the tire moves, as in Figure 13. Thus, we define α as the slip angle, which describes the difference between the direction the wheel points to and the one in which it moves, and can be expressed as

$$\alpha = -\arctan\left(\frac{v_y}{v_x}\right), \tag{2.24}$$

v_x and v_y being the longitudinal and lateral components of the wheel velocity.

Similarly to the longitudinal slip, we will obtain the lateral force based on the forces

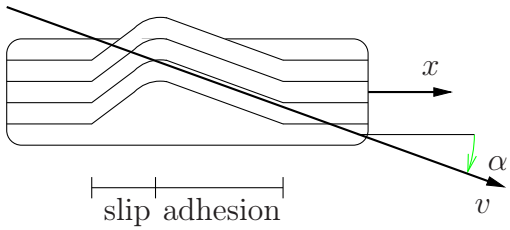

Figure 13: Deformed contact patch in turns.
Source: (GILLESPIE, 1992) (adapted).

applied at the contact patch. Also similar is the fact that as the bristles' tips adhere to the ground, their deformation increases linearly as the wheel turns, and the force is a result of that deformation. As the deformation increases, eventually the friction force is no longer enough to keep them in place, and bristle slipping occurs (see Figure 13). Thus, we obtain the lateral force and the aligning moment based on the sum of those two forces: the adhesion region force, and the slip region force.

We will again consider a parabolic pressure at the contact patch, given by (2.14). The deformation u_{b_y} is in accordance with Figure 14, given by

$$u_{b_y} = (a - x)\tan(\alpha), \tag{2.25}$$

which generates a lateral pressure

$$q_{b_y} = c_y u_{b_y}. \tag{2.26}$$

We consider an analogous condition for x_s to the longitudinal case,

$$q_{b_y} > q_{f_y}, \tag{2.27}$$

with q_{f_y} (the maximum friction pressure in the lateral direction) given by

$$q_{f_x} = \mu q_z. \tag{2.28}$$

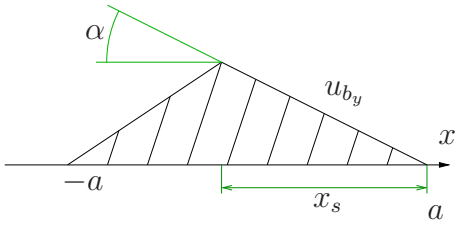

Figure 14: Lateral deformation.

Since the same contact patch pressure for the longitudinal slip has been considered,

and (2.25)–(2.28) are analogous to (2.10)–(2.13), it follows that the remaining force derivation is the same. Hence, the lateral force is given by

$$F_y = 2c_{p_y}a^2\sigma_y\left[\theta_y\sigma_y - \frac{2}{3}(\theta_y\sigma_y)^2\right] \tag{2.29}$$

$$= C_{F\alpha}\sigma_y\left[1 - \theta_y\sigma_y + \frac{1}{3}(\theta_y\sigma_y)^2\right], \tag{2.30}$$

where

$$\theta_y \triangleq \frac{2}{3}\frac{c_{py}a^2}{\mu W}, \tag{2.31}$$

$\sigma_y \triangleq \tan(\alpha)$, and $C_{F\alpha} \triangleq 2c_{p_y}a^2$ is the *cornering stiffness*. Similar linearization considerations follow, that is, $F_y \approx C_{F\alpha}\tan(\alpha)$ for sufficiently low slip angles.

A judicious observation of Figure 14 confirms that most of the lateral force is applied on the rear of the wheel. We can obtain the restoring moment M_z as

$$M_z = \int_{-a}^{a} f_y x \mathrm{d}x, \tag{2.32}$$

where f_y is the lateral force per unit of length. The restoring moment will have an addend due to the adhesion region, and another from the sliding region, i.e.,

$$M_z = M_{a_z} + M_{s_z}. \tag{2.33}$$

The adhesion part can be obtained as

$$\begin{aligned} M_{a_z} &= \int_{a-2a\lambda}^{a} c_{py}\sigma_y(a-x)x\mathrm{d}x \\ &= c_{py}\sigma_y\left[\frac{1}{2}ax^2 - \frac{1}{3}x^3\right]_{a-2a\lambda}^{a} \\ &= -\mu W a\theta_y\sigma_y\left[1 - 6\theta_y\sigma_y + 9(\theta_y\sigma_y)^2 - 4(\theta_y\sigma_y)^3\right], \end{aligned} \tag{2.34}$$

where we have used an analogous consideration to (2.17), that is,

$$\theta_y \triangleq \frac{2}{3}\frac{c_{py}a^2}{\mu W}. \tag{2.35}$$

The sliding portion can be found as

$$\begin{aligned} M_{s_z} &= \int_{-a}^{a-2a\lambda} \frac{3\mu W}{4a^2}(a^2 - x^2)x\mathrm{d}x \\ &= \frac{3\mu W}{4a}\left[\frac{2a^2x^2 - x^4}{4a^2}\right]_{-a}^{a-2a\lambda} \\ &= -\mu W a\theta_y\sigma_y[3\theta_y\sigma_y - 6(\theta_y\sigma_y)^2 + 3(\theta_y\sigma_y)^3]. \end{aligned} \tag{2.36}$$

Hence, defining the *aligning stiffness* $C_{M_\alpha} \triangleq \mu W a \theta_y$, and substituting (2.34) and (2.36) in (2.33), we have

$$M_z = -C_{M_\alpha}\sigma_y[1 - 3\theta_y\sigma_y + 3(\theta_y\sigma_y)^2 - (\theta_y\sigma_y)^3]. \tag{2.37}$$

Therefore, (2.37) is a 4th-order polynomial function on σ_x. The restoring moment is an odd function, which makes sense, since one would suppose that opposite curves would generate opposing moments. For positive slide angles, it has a maximum value of (2.37) is $27\mu W/256$, which occurs at $\sigma_y = 1/(4\theta_y)$.

Knowing both the lateral force and the restoring moment, we can obtain the *pneumatic trail* t_M as

$$t_M = -\frac{M_z}{F_y}, \tag{2.38}$$

which is the distance from the wheel center where F_y is applied. As the sliding angle increases, the sliding region increases up to when the whole contact patch loses adhesion. As it happens, the pneumatic trail and the restoring moment vanish, according to the brush model. This behavior does not reflect experimental data, however. Hence, in extreme situations, i.e., very high slide angles, another type of model is required. One such family of models, which better matches experiments, is presented in Section 2.2.2.

2.2.2 Magic Formula model

The brush model is very interesting in order to understand the basic mechanics behind pneumatic tire sliding. It is also accurate enough for most uses where the vehicle can still be controlled by either the driver or an automatic security system. Still, other types of models have been presented in the vehicle dynamics literature, one of which is known as the *magic formula model*, or *similarity method* (PACEJKA, 2012).

When the tire is subject to larger slip angles or longitudinal slips, it actually exhibits maximum lateral or longitudinal forces, for a particular value or α or κ. As slip increases, the maximum level decreases, in practice. Similarly, under high slip angles, the restoring moment not only vanishes but eventually switches its sign as α increases, i.e., it causes the wheel to turn even more, instead of returning it to its longitudinal position. These facts are not captured by the brush model.

The main idea behind the similarity method is that as soon as force and moment curves have been obtained by experiments under a given condition, say, normal force, tire-road friction coefficient, and inflation pressure (which is related to the contact patch

length $2a$), other curves—for different sets of conditions—can be obtained by horizontal and vertical factors and shifts of the original one.

The curves that are fit to the experimental data fall on a family of nested trigonometric functions with the same structure that can adjust a given (initial) linear growth, usually either the longitudinal slip stiffness, the cornering stiffness, or the aligning stiffness; a maximum value, which is the maximum force or moment the tire can generate; and a rate decrease, which would be slow for forces and faster for the restoring moment.

The process of obtaining functions to accommodate force and moment generation on tires can be described as an iterative process. A first attempt is to consider a sine function

$$F_i = D\sin(x) \tag{2.39}$$

where F_i is either F_x, F_y, or M_z, and x is κ or $\tan(\alpha)$. It is clear that D is the *maximum value* of the function. However, once this is set, its derivative cannot be adjusted. A second iteration would be

$$F_i = D\sin(Bx), \tag{2.40}$$

where B is called a *stiffness factor* (not to be confused with $C_{F\kappa}$, $C_{F\alpha}$ or C_{M_α}, more on that later on). The sinusoidal function at (2.40) would allow for the adjustment of the derivative—or, conversely, where the peak value occurs—but it iss impossible to adjust how the curve prolongs itself horizontally. This could, in turn, be achieved by a third attempt,

$$F_i = D\sin\big(C\arctan(Bx)\big), \tag{2.41}$$

with C being called the *shape factor*. Moreover, the result from $\arctan(\cdot)$ is bounded, effectively removing the periodicity from (2.40), as the argument of the sinusoidal function becomes bounded. On the other hand, this function prevents one from solving one particular problem: experimental data shows that force functions rise rather quickly, and then slowly decrease after the peak value, in practice. Moreover, it has been mentioned that the restoring moment not only decreases rather quickly but even changes its sign at higher slip angles. This could be accommodated by a fourth iteration,

$$F_i = D\sin\big[C\arctan(B\phi)\big] \tag{2.42}$$

$$\phi = (1-E)x + \frac{E}{B}\arctan(Bx), \tag{2.43}$$

where E is designated the *curvature factor*. Substituting (2.43) into (2.42) yields

$$F_i = D\sin\Big\{C\arctan\Big[Bx - E\big(Bx - \arctan(Bx)\big)\Big]\Big\}, \tag{2.44}$$

called the *magic formula* for tire models. Thus, in order to obtain a model for a given tire, one must find B, C, D, and E that cause (2.44) to match the experimental data obtained from it.

The general aspect of (2.44) can be seen in Figure 15. The curve is mostly linear for a relatively large neighborhood of the origin, with slope C_i; exhibits a maximum D at x_m, then decreases asymptotically to y_a. For the longitudinal and lateral forces, y_a has the same sign as D; for the restoring moment, they are opposite to one another. As (2.44) is an odd function, its values for $x < 0$ have been omitted since the curve is symmetric around the origin.

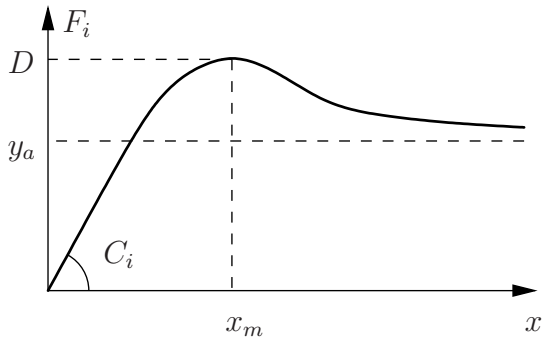

Figure 15: Magic formula curve.
Source: (PACEJKA, 2012) (adapted).

The parameters in Figure 15 can be chosen through B, C, D, and E. However, they are coupled. For instance, the first derivative of (2.44) is particularly important at $x = 0$, since that is the stiffness parameter for longitudinal or lateral motion, for either forces or the restoring moment, as introduced in Section 2.2.1. Because

$$\left.\frac{\mathrm{d}F_i}{\mathrm{d}x}\right|_{x=0} = C_i = BCD, \tag{2.45}$$

we have $BCD = C_{F\kappa}$, for $x = \kappa$, and $BCD = \{C_{F\alpha}, C_{M_\alpha}\}$, for $x = \tan(\alpha)$.

The peak value of (2.44), D, is limited by the normal force W on the wheel, and factored by the friction coefficient μ, or

$$D = \mu_x W \tag{2.46}$$

$$D = \mu_y W, \tag{2.47}$$

where, unlike in Section 2.2.1, we assume the coefficient might be different for the longitudinal and lateral directions, which depends on the construction of the tire itself. The peak value parameter for the restoring moment is related to that of the lateral force, being

given by

$$D = c_3 a \mu_y W, \tag{2.48}$$

where $c_3 > 0$ is to be found in practice (the brush model from Section 2.2.1 would give $c_3 > 27/256$, but it has been seen that it is not valid for high slip angles).

The value of C controls the limits of the argument of $\sin(\cdot)$. Therefore, it is related to the asymptotic value y_a. It is given by

$$C = 1 \pm \left(1 - \frac{2}{\pi} \arcsin\left(\frac{y_a}{D}\right)\right). \tag{2.49}$$

In case $C \leq 1$, the argument of $\sin(\cdot)$ in (2.44) does not reach past $\pi/2$. Hence, there shall be no maximum in (2.44). Since the curves to which the equation should be fitted do have a maximum value, either for forces or the restoring moment, this case can be ignored. The remaining parameter, E, controls how the curve varies before and after the maximum value. It can be obtained from B, C, and x_m as

$$E = \frac{Bx_m - \tan\left(\frac{\pi}{2C}\right)}{Bx_m - \arctan(Bx_m)}, \tag{2.50}$$

again, for $C > 1$.

So far, it has been shown how one can find the magic formula parameters to fit a curve whose parameters are clearly identifiable. Sadly, that is not a realistic situation: instead, it is more likely that either a number of points around such a curve, or even a family of such experiments are obtained. In addition to it, experimental data has identified that the parameters B, C, D and E can be obtained as functions of the normal force W. Therefore, practical parameter identification can use

$$D = a_1 W^2 + a_2 W \tag{2.51}$$

$$E = a_6 W^2 + a_7 W + a_8 \tag{2.52}$$

$$BCD = \frac{a_3 W^2 + a_4 W}{e^{a_6 W}} \tag{2.53}$$

$$C = \begin{cases} 1.30 & \text{for cornering,} \\ 1.65 & \text{for braking,} \\ 2.40 & \text{for the restoring moment.} \end{cases} \tag{2.54}$$

Hence, obtaining a magic formula model means obtaining a_1, a_2, …, a_8 for the experimental data, or, in other words, (2.51)–(2.54) are used instead of (2.45)–(2.50).

We recall that the values of C are related to a decreased force or moment under high

slip. The cornering value means that there is a loss of centripetal force of around 10 % in that situation. However, for braking, there can be a 40 % braking force loss, which greatly increases the braking distance. Finally, the value of C for the restoring moment is related to a value of 60 % maximum moment in the opposite direction, that is to say, the wheel's yaw angle tends to increase, instead of aligning itself naturally.

Moreover, it has been proposed (PACEJKA, 1958; HADT; PACEJKA, 1963) and shown (HADT; MILLIKEN, 1983) that such curves, for a known tire, can be normalized to describe its behavior in different conditions, that is to say, under different loads and surfaces. Strictly put, the similarity method is the act of doing such normalization or data extrapolation, while the magic formula model is the family of functions through which this is usually accomplished. This can be done considering a normalized horizontal slip

$$\bar{\kappa} = \frac{C_{F\kappa}(W)}{C_{F\kappa o}} \frac{\mu_o W_o}{\mu W} \kappa, \tag{2.55}$$

a normalized longitudinal force

$$\bar{F}_x = \frac{\mu W}{\mu_o W_o} F_{xo}(\bar{\kappa}), \tag{2.56}$$

a normalized slip angle

$$\bar{\alpha} = \frac{C_{F\alpha}(W)}{C_{F\alpha o}} \frac{\mu_o W_o}{\mu W} \left(\alpha + \frac{C_{F\gamma}(W)}{C_{F\alpha}(W)} \gamma \right), \tag{2.57}$$

a normalized lateral force

$$\bar{F}_y = \frac{\mu W}{\mu_o W_o} F_{yo}(\bar{\alpha}), \tag{2.58}$$

and a normalized restoring moment

$$\bar{M}_z = \frac{\mu W}{\mu_o W_o} \frac{C_{M\alpha}(W)}{C_{M\alpha 0}} \frac{C_{F\alpha 0}}{C_{F\alpha}(W)} M_{zo}(\bar{\alpha}) + M_{zr}, \tag{2.59}$$

with

$$M_{zr} = \frac{C_{M\gamma}(W) + t(W) C_{F\gamma}(W)}{1 + c_7 \alpha^2} \gamma \tag{2.60}$$

where the camber angle γ is included, $t(W)$ is the pneumatic trail under W, and c_7 is a parameter related to the vertical shift of the moment curve (omitted here).

With (2.55)–(2.59), a set of magic formula equations with nominal parameters can be used. These nominal parameters need not be the ones verified on the actual vehicle: most likely, they shall not. Rather, they will be the ones used to test the tire, e.g., with a flat-belt tire test rig. A set of equations for pure longitudinal slip, pure side slip, combined slip, overturning moment, and rolling resistance moment is available in (PACEJKA, 2012),

Chapter 4. We reproduce the ones which describe pure lateral force, which are used for lateral dynamics:

$$F_{yo} = D_y \sin\Big\{ C_y \arctan\Big[B_y\alpha_y - E_y\big(B_y\alpha_y - \arctan(B_y\alpha_y)\big)\Big]\Big\} + S_{Vy} \tag{2.61}$$

$$\alpha_y = \alpha^* + S_{Hy} \tag{2.62}$$

$$\alpha^* = -\tan(\alpha)\,\mathrm{sign}(v_x) = -\frac{v_y}{v_x} \tag{2.63}$$

$$C_y = p_{Cy1}\lambda_{Cy} \tag{2.64}$$

$$D_y = \mu_y W \zeta_2 \tag{2.65}$$

$$\mu_y = (p_{Dy1} + p_{Dy2}df_z)(1 + p_{py3}dp_i + p_{py4}dp_i^2)(1 - p_{Dy3}{\gamma^*}^2)\lambda^*_{\mu y} \tag{2.66}$$

$$E_y = (p_{Ey1} + p_{Ey2}df_z)\left[1 + p_{Ey5}{\gamma^*}^2 - (p_{Ey3} + p_{Ey4}\gamma^*)\,\mathrm{sign}(\alpha_y)\right]\lambda_{Ey} \tag{2.67}$$

$$B_y = \frac{K_{y\alpha}}{C_y D_y + \epsilon_y} \tag{2.68}$$

$$\begin{aligned} K_{y\alpha} &= p_{Ky1} W_o (1 + p_{py1})(1 - p_{Ky3}|\gamma^*|) \\ &\quad \sin\left\{ p_{Ky4} \arctan\left[\frac{W/W_o}{(p_{Ky2} + p_{Ky5}{\gamma^*}^2)(1 + p_{py2}dp_i)} \right] \right\} \\ &= C_{F\alpha} \end{aligned} \tag{2.69}$$

$$S_{Hy} = (p_{Hy1} + p_{Hy2}df_z)\lambda_{Hy} + \frac{K_{y\gamma 0}\gamma^* - S_{Vy\gamma}}{K_{y\alpha} + \epsilon_K}\zeta_o + \zeta_4 - 1 \tag{2.70}$$

$$S_{Vy} = W(p_{Vy1} + p_{Vy2}df_z)\lambda_{Vy}\lambda'_{\mu y}\zeta_2 + S_{Vy\gamma} \tag{2.71}$$

$$S_{Vy\gamma} = W(p_{Vy3} + p_{Vy4}df_z)\gamma^*\lambda_{Ky\gamma}\lambda'_{\mu y}\zeta_2 \tag{2.72}$$

$$\begin{aligned} K_{y\gamma o} &= W(p_{Ky6} + p_{Ky7}df_z)(1 + p_{py5}dp_i)\lambda_{Ky\gamma} \\ &= C_{F\gamma}, \end{aligned} \tag{2.73}$$

which can be used in the opposite order, i.e., from (2.73) to (2.61). In (2.61)–(2.73), the parameters on p (p_{Cyi}, p_{Dyi}, p_{pyi}, etc.) are obtained either from experimental data or from the manufacturer. Normal force and inflating pressure variation are weighted through $df_z \triangleq (W - W_o)/W_o$ and $dp_i \triangleq (P_i - P_{io})/P_{io}$. The scaling factors λ have a default value of one, with the sole exception of $\lambda_{\mu V}$, which is zero. These can be adapted to accommodate friction variations, in manners which are out of the scope of this text.

The full set of magic formula equations is often implemented in vehicle dynamics software, for both pure and combined slip.

2.3 Vehicle Models

Vehicles are complex systems. For instance, let us consider a rather common source of rollover accidents: a vehicle travels over the roadway of a highway at high speed—even if within the speed limit. Either by driver misbehavior or necessity, the vehicle suddenly leaves the roadway and enters the shoulder area, and then tries to get back. Since the asphalt pavement over the roadway is often thicker than that of the shoulder, the vehicle's roll angle is further tilted clockwise, assuming right-hand traffic. In order to provide a general description of a wheeled vehicle for such a situation, we not only have to model the mechanisms within it—more importantly, the suspension system—but also the surface it traverses over. This is not a trivial task. To better tackle different problems within vehicle dynamics, assumptions are made to obtain simpler, yet descriptive-enough models for a given situation.

A rather simple model can be considered to describe the phenomenon of load transfer while the vehicle accelerates. It can also be used to obtain the braking distance, design brake pressure distribution, or describe scalar speed changes. It is called the *longitudinal model*. Another model can be considered when a vehicle turns and slipping may cause the driver to lose control over it. In this situation, vehicles with a low center of mass could be safe from an immediate rollover but might depart from the road, when they would be subject to either rollovers or run-off-road collisions. The *lateral model* is often enough to describe that situation. In addition to it, and contrary to the previous case, vehicles with higher centers of mass often overturn immediately after sudden changes in their trajectories. In order to describe how a vehicle may roll over while on track, *roll models* can be used.

This work will restrict its extent to longitudinal and lateral models, focusing on the latter ones. Section 2.3.1 presents the longitudinal models, while Section 2.3.2 discusses pure lateral models and planar dynamics, i.e., models that describe longitudinal and lateral accelerations and the yaw angle as functions of the forces from the tires.

2.3.1 Longitudinal Model

A longitudinal model describes two important phenomena from wheeled vehicles: its speed change and load transfer. As the wheels develop torque or are subject to brake forces, the vehicle increases or decreases its speed, as limited by the wheels' dynamic behavior. Also, as it accelerates or brakes, the share of its weight which is supported by the rear

or front wheels changes from ones to others. The importance of this fact was described in Section 2.2, as a wheel's ability to to develop accelerating, braking or lateral forces is limited by its normal force.

Let a vehicle be at a road with constant slope θ_s, which is positive when it goes up while moving forward. The vehicle's wheels are distant l of each other, which is known as *wheel base*. Its center of mass is at a distance h from the ground, l_1 away from the front wheel and l_2 away from the rear one. The vehicle is subject to (at most) two traction forces, F_f from both front wheels—each wheel provides half the force—and F_r from the rear ones. Its movement is hindered by four different forces: the rolling resistance, which is composed of R_{rf} from the front wheels, and R_{rr} from the rear ones; the drag force R_a, which is applied h_a away from the ground; and a possible trailer force R_b from any cargo or utility trailers the vehicle might be pulling, applied h_b from the ground. Finally, the vehicle is subject to its own weight W_b, whose longitudinal projection W_{g_x} may help or hinder its movement, depending on the sign of θ_s. As the wheels support the whole machine, this weight is shared by the front and rear wheels through W_f and W_r, in the respective order.

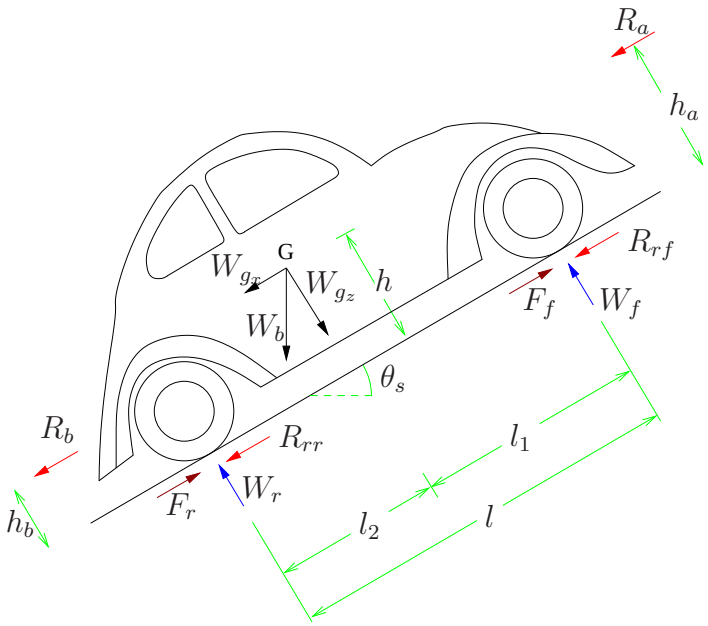

Figure 16: Longitudinal model parameters.

As with any other mechanical model, one can obtain a longitudinal model by considering the net forces and moments on the vehicle. Since the movement of the vehicle in Figure 16 is assumed to be restricted to a line on a vertical plane, one needs to obtain a movement equation along the direction the vehicle moves (longitudinal acceleration), and two equilibrium equations: one for the vertical movement, and another for the moments

around a point. Nonetheless, as the normal forces W_f and W_r on the tires are important, it is customary to obtain two moment equations, one around the center of each wheel, so as to obtain the normal force on the other.

It has just been mentioned that the reaction forces on the tires have to match the weight of the vehicle, that is to say,

$$W = W_f + W_r. \tag{2.74}$$

Moreover, we assume the drag force R_a is quadratic on the vehicle's speed, as in (PACEJKA, 2012; GILLESPIE, 1992)

$$R_a = c_a v_x^2, \tag{2.75}$$

where c_a is the drag coefficient and v_x is the vehicle's speed. The net force along the longitudinal direction is

$$F_r + F_f - R_{rr} - R_{rf} - R_a - R_b - W\sin\theta_s = m_b a_x, \tag{2.76}$$

with m_b as the body mass and a_x the longitudinal acceleration. Substituting (2.1), (2.74) and (2.75) into (2.76):

$$a_x = \dot{v}_x = \frac{1}{m_b}\left(-c_a v_x^2 - W\sin\theta_s - f_r W + F_r + F_f\right). \tag{2.77}$$

Therefore, the right-hand side of(2.77) describes the longitudinal acceleration of vehicle—which we integrate to obtain its longitudinal speed. It can be seen that the rolling resistance is irrespective of the normal force distribution among W_f and W_r. However, the ability to modify the vehicle's speed does depend on it, since this is accomplished through F_r, for front-wheel drive; F_r, for rear-wheel drive; or both, for either a four-wheel drive or a all-wheel drive vehicle [see (2.22) and (2.46)].

The moments around the rear and forward wheels, in the respective order, are given by

$$R_a h_a + R_b h_b + Wh\sin\theta_s - Wl_2\cos\theta_s + W_f l + \frac{W}{g}ha = I_{yr}\dot{\omega}_y, \tag{2.78}$$

$$R_a h_a + R_b h_b + Wh\sin\theta_s + Wl_1\cos\theta_s - W_r l + \frac{W}{g}ha = I_{yf}\dot{\omega}_y, \tag{2.79}$$

where g is the gravitational acceleration and ω_y is the pitch rate of the vehicle. For the sake of simplicity, let $h_a = h_b = h$. Isolate the normal forces W_f and W_r:

$$W_f = \frac{l_2}{l}W\cos\theta_s - \frac{h}{l}\left(R_a + W\sin\theta_s + \frac{W}{g}a\right) \tag{2.80}$$

$$W_r = \frac{l_1}{l} W \cos\theta_s + \frac{h}{l}\left(R_a + W \sin\theta_s + \frac{W}{g} a\right). \tag{2.81}$$

Substituting (2.76) into (2.80) and (2.81), we obtain

$$W_f = \frac{l_2}{l} W \cos\theta_s - \frac{h}{l}\left(F_r + F_f - F_r W\right) \tag{2.82}$$

$$W_r = \frac{l_1}{l} W \cos\theta_s + \frac{h}{l}\left(F_r + F_f - F_r W\right), \tag{2.83}$$

which show how the weight of the vehicle is moved from the front to the rear wheels as it accelerates, and the other way around when it brakes. The same effect can be observed in lateral models, where the weight of the vehicle is increasingly supported by the outer wheels the shorter the curve radius is. The phenomenon of normal force moving from one or more wheels to others as a vehicle changes its velocity is called *load transfer*.

2.3.2 Lateral Models

The longitudinal model can be employed to estimate speed changes as the driver brakes or accelerates the vehicle. This can lead to bicycle and motorcycle rollovers through excessive pitch angle rate, but for almost any automobile such maneuvers are safe in that regard. These vehicles risk overturning, however, in curves, when they cannot compensate lateral load transfer by changing the camber angle of the whole structure, aside from the road bank, of course. The lateral load transfer effectively moves the vehicle's center of mass sideways, and given enough tire grip, it can eventually fall outside the area between its wheels, causing a rollover.

When one mentions curves as a cause of rollover, this naturally does not restrict danger to road curves. Any change of direction by the driver will cause lateral load transfer, for instance, overtaking, shifting lanes, or moving to the shoulder area of a road. Nonetheless, we have seen that vehicles with a low center of mass might be safe from instantly rolling over, but some of its wheels might lose grip and allow the vehicle to leave the road, where tripped rollovers are both more frequent and serious. As the vehicle changes its direction of movement, its wheels' slip angles can dramatically change, be it a set of those wheels—say, for instance, the rear wheels—or even all of them. This situation can prevent the driver from controlling, or regaining control of the vehicle, generating oversteers, understeers, spin outs, or side slips, with eventual road departures.

The simplest lateral model which can be used for a vehicle is the bicycle model. It considers both front and rear wheels as one—as done for the longitudinal model—but now the steering angle is taken into account. The speed is assumed constant, but the velocity

changes since the steer angle δ is nonzero. Figure 17 shows the model parameters for it. As for the longitudinal model, the wheel base is l, being the distance between the center

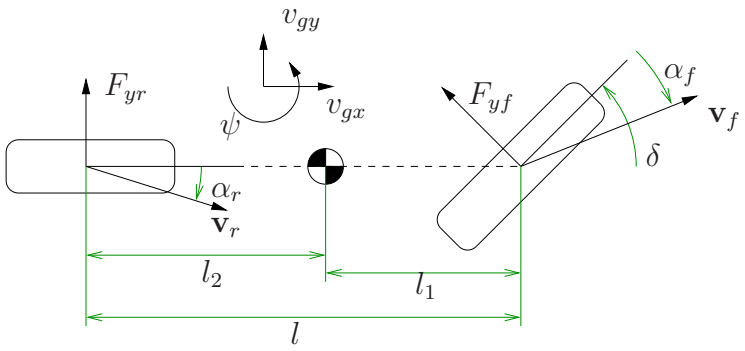

Figure 17: Bicycle model parameters.

of mass and the front and rear wheels, in the respective order, is l_1 and l_2. A wheel that is equivalent to both front wheels is steered by an angle δ, moves with velocity $\mathbf{v}_f$ and slip angle α_f, and generates a lateral force F_{yf}. The rear wheels are also condensed, move with velocity $\mathbf{v}_r$ and equivalent slip angle α_r, and provide a lateral force F_{yr}. A frame on the vehicle considers the longitudinal and lateral velocities of the center of mass v_{gx} and v_{gy}, respectively—the vector sum of both being v_g—and yaw angle ψ. The objective is to describe the yaw rate $\dot{\psi}$.

The yaw rate is a result of the net moment τ_{G_z} around the vehicle's center of mass, or, in other words,

$$\tau_{G_z} = I_z\ddot{\psi} = l_1 F_{yf}\cos(\delta) - l_2 F_{yr}. \tag{2.84}$$

To obtain (2.84), pneumatic trails have not been considered, even though they might not be negligible. See (PACEJKA, 2012). The forces along v_{gy} are responsible for the lateral acceleration of the vehicle, which is the sum of the lateral speed rate and the centripetal force which maintains it in a curve:

$$m_b(\dot{v}_{gy} + \dot{\psi}v_{gx}) = F_{yf}\cos(\delta) + F_{yr}. \tag{2.85}$$

Therefore, we can isolate $\dot{\psi}$ and $\dot{v}_{gy}$ in (2.84) and (2.85), respectively, for a simple nonlinear lateral model:

$$\ddot{\psi} = l_1 I_z^{-1} F_{yf}\cos(\delta) - l_2 I_z^{-1} F_{yr} \tag{2.86}$$

$$\dot{v}_{gy} = \dot{\psi}v_{gx} + m_b^{-1} F_{yf}\cos(\delta) + m_b^{-1} F_{yr}. \tag{2.87}$$

A linearized model is often considered for the bicycle model of the vehicle. We first consider the fact that most road curves have a relatively large radius, of several dozens

of meters. Therefore, δ is small, and $\cos(\delta) \approx 1$. We define the *side-slip angle* (or *vehicle slip angle*) β as

$$\tan(\beta) = \frac{v_{gy}}{v_{gx}}. \tag{2.88}$$

Also, for the rear wheel slip angle,

$$\tan(\alpha_r) = -\frac{v_{gy} - l_2\dot{\psi}}{v_{gx}} \tag{2.89}$$

holds. Assuming $\tan(\alpha_r) \approx \alpha_r$ and a curve radius R:

$$\begin{aligned} \alpha_r &= \frac{l_2\dot{\psi}}{v_{gx}} - \frac{v_{gy}}{v_{gx}} \\ &= \frac{l_2}{R} - \beta. \end{aligned} \tag{2.90}$$

For the front wheel, again assuming $\tan(\alpha_f) \approx \alpha_f$,

$$\alpha_f = -\left(\frac{l_1\dot{\psi} + v_{gy}}{v_{gx}} - \delta\right). \tag{2.91}$$

Rearranging (2.91) and proceeding as before:

$$\delta = \frac{l}{R} - \alpha_f + \alpha_r. \tag{2.92}$$

Assuming the tires operate on the linear region, we can use the simplified model

$$F_{yf} = C_{\alpha_f}\alpha_f \tag{2.93}$$

$$F_{yr} = C_{\alpha_r}\alpha_r. \tag{2.94}$$

Therefore, the lateral force is given by

$$\begin{aligned} F_y &= F_{yf} + F_{yr} \\ &= C_{\alpha_f}\alpha_f + C_{\alpha_r}\alpha_r \\ &= \left(-\frac{l_1}{v_{gx}}C_{\alpha_f} + \frac{l_2}{v_{gx}}C_{\alpha_r}\right)\dot{\psi} - (C_{\alpha_f} + C_{\alpha_r})\beta + C_{\alpha_f}\delta, \end{aligned} \tag{2.95}$$

while the vertical moment is

$$\begin{aligned} \tau_z &= l_1F_{yf} - l_2F_{yr} \\ &= \left(-\frac{l_1^2}{v_{gx}}C_{\alpha_f} - \frac{l_2^2}{v_{gx}}C_{\alpha_r}\right)\dot{\psi} - (l_1C_{\alpha_f} - l_2C_{\alpha_r})\beta + l_1C_{\alpha_f}\delta. \end{aligned} \tag{2.96}$$

By substituting (2.95) and (2.96) in (2.86) and (2.87), we can write

$$\begin{bmatrix} \dot{v}_{gy} \\ \ddot{\psi} \end{bmatrix} = \mathbf{A} \begin{bmatrix} v_{gy} \\ \dot{\psi} \end{bmatrix} + \mathbf{B}\delta \tag{2.97}$$

$$\begin{bmatrix} a_{gy} \\ \dot{\psi} \\ \beta \end{bmatrix} = \mathbf{C} \begin{bmatrix} v_{gy} \\ \dot{\psi} \end{bmatrix} + \mathbf{D}\delta, \tag{2.98}$$

with

$$\mathbf{A} = \begin{bmatrix} -\frac{C_{\alpha_f}+C_{\alpha_r}}{m_b v_{gx}} & -\frac{C_{\alpha_f} l_1 - C_{\alpha_r} l_2}{m_b v_{gx}} - v_{gx} \\ -\frac{C_{\alpha_f} l_1 - C_{\alpha_r} l_2}{I_z v_{gx}} & -\frac{C_{\alpha_f} l_1^2 + C_{\alpha_r} l_2^2}{I_z v_{gx}} \end{bmatrix} \qquad \mathbf{B} = \begin{bmatrix} \frac{C_{\alpha_f}}{m_b} \\ \frac{C_{\alpha_f} l_1}{I_z} \end{bmatrix} \tag{2.99}$$

$$\mathbf{C} = \begin{bmatrix} -\frac{C_{\alpha_f}+C_{\alpha_r}}{m_b v_{gx}} & -\frac{C_{\alpha_f} l_1 - C_{\alpha_r} l_2}{m_b v_{gx}} \\ 0 & 1 \\ \frac{1}{v_{gx}} & 0 \end{bmatrix} \qquad \mathbf{D} = \begin{bmatrix} \frac{C_{\alpha_f}}{m_b} \\ 0 \\ 0 \end{bmatrix}. \tag{2.100}$$

Another linear model is often used for the bicycle model, considering the different state vector $\mathbf{x} \triangleq [\beta \;\; \dot{\psi}]^{\mathrm{T}}$. Such a model is convenient for stability control applications (see Chapter 3). It can be easily obtained from (2.97) and (2.98) by approximating (2.88) as $\tan(\beta) \approx \beta$. Hence, we write the new state as

$$\begin{bmatrix} \beta \\ \dot{\psi} \end{bmatrix} = \begin{bmatrix} v_{gx}^{-1} & 0 \\ 0 & 1 \end{bmatrix} \begin{bmatrix} v_{gy} \\ \dot{\psi} \end{bmatrix} = \bar{\mathbf{P}} \begin{bmatrix} v_{gy} \\ \dot{\psi} \end{bmatrix} \tag{2.101}$$

and apply the equivalence transformation

$$\begin{bmatrix} \dot{\beta} \\ \ddot{\psi} \end{bmatrix} = \bar{\mathbf{A}} \begin{bmatrix} \beta \\ \dot{\psi} \end{bmatrix} + \bar{\mathbf{B}}\delta \tag{2.102}$$

$$\begin{bmatrix} a_{gy} \\ \dot{\psi} \\ \beta \end{bmatrix} = \bar{\mathbf{C}} \begin{bmatrix} \beta \\ \dot{\psi} \end{bmatrix} + \bar{\mathbf{D}}\delta, \tag{2.103}$$

with

$$\bar{\mathbf{A}} = \bar{\mathbf{P}}\mathbf{A}\bar{\mathbf{P}}^{-1} = \begin{bmatrix} -\frac{C_{\alpha_f}+C_{\alpha_r}}{m_b v_{gx}} & -\frac{C_{\alpha_f} l_1 - C_{\alpha_r} l_2}{m_b v_{gx}^2} - 1 \\ -\frac{C_{\alpha_f} l_1 - C_{\alpha_r} l_2}{I_z} & -\frac{C_{\alpha_f} l_1^2 C_{\alpha_r} l_2^2}{I_z v_{gx}} \end{bmatrix} \qquad \bar{\mathbf{B}} = \bar{\mathbf{P}}\mathbf{B} = \begin{bmatrix} \frac{C_{\alpha_f}}{m_b v_{gx}} \\ \frac{C_{\alpha_f} l_1}{I_z} \end{bmatrix} \tag{2.104}$$

$$\mathbf{C} = \mathbf{C}\bar{\mathbf{P}}^{-1} = \begin{bmatrix} -\frac{C_{\alpha_f}+C_{\alpha_r}}{m_b} & -\frac{C_{\alpha_f} l_1 - C_{\alpha_r} l_2}{m_b v_{gx}} \\ 0 & 1 \\ 1 & 0 \end{bmatrix} \qquad \bar{\mathbf{D}} = \mathbf{D}. \tag{2.105}$$

The models given by (2.97), (2.98) and (2.102), (2.103) do not take differential braking into account. A more descriptive lateral model considers each wheel separately. Both front wheels can be steered, but not independently. More specifically, the steering angles δ_l and δ_r of the left and right wheels, in the respective order, can be related to an equivalent steering angle δ of the front wheel of a tricycle. Since this work is related to a passenger car—in the sense that it is not a race car—the most common steering system will be considered, which is the *Ackermann steering system*, depicted in Figure 18.

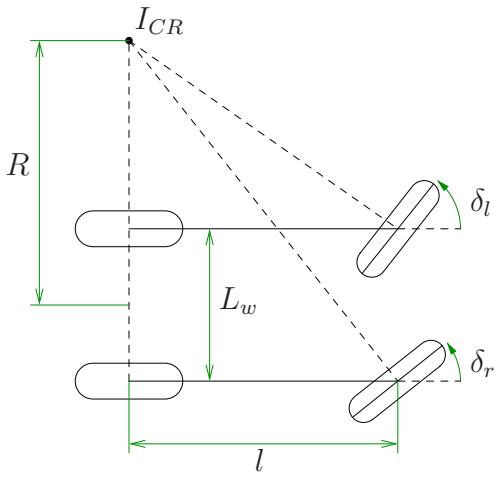

Figure 18: Ackermann steering system.

Ackermann steering means that the presumed instantaneous center of rotation of the vehicle, under negligible wheel slip, is the same for all wheels. This is equivalent to saying that the rotation axles of all wheels meet at a single point. The distance between the fixed wheels L_w is known as *track width*. For convenience, let $L_w = 2l_w$, i.e., l_w is half the track width. Assuming the vehicle performs a curve with radius R, which is measured from the instantaneous center of rotation I_{CR} to the midpoint between both fixed wheels, we can obtain

$$\tan(\delta_l) = \frac{l}{R - l_w}, \tag{2.106}$$

for the left orientable wheel, and

$$\tan(\delta_r) = \frac{l}{R + l_w}, \tag{2.107}$$

for the right one. Let an imaginary wheel be placed at the midpoint between both steering wheels. We would have

$$\tan(\delta) = \frac{l}{R}. \tag{2.108}$$

Substituting (2.108) into (2.106) and (2.107) and taking the inverse of both sides, we

obtain

$$\cot(\delta_l) = \cot(\delta) - l_w \tag{2.109}$$

$$\cot(\delta_r) = \cot(\delta) + l_w. \tag{2.110}$$

Finally, subtracting (2.109) and (2.109) yields

$$\cot(\delta_r) - \cot(\delta_l) = \frac{L_w}{l}. \tag{2.111}$$

Therefore, δ_r and δ_l are related by (2.111), and both are related to δ according to (2.109) and (2.110). The imaginary wheel steering angle δ is a function of the steering wheel angle, provided by the driver.

Now that the steering system for most four-wheel vehicles has been introduced, a more complete lateral model can be obtained. In that regard, we consider a four-wheel vehicle whose every wheel is subject to slipping, as shown in Figure 19. The velocity of each wheel is noted as $\mathbf{v}_{ij}$, with ij being rr, for the rear right wheel; rl, for the rear left one; fr, for the front right one; and fl, for the front left wheel. Likewise, the slip angles are α_{ij}, and the steering angles are δ_r, for the front right wheel; and δ_l for the front left wheel.

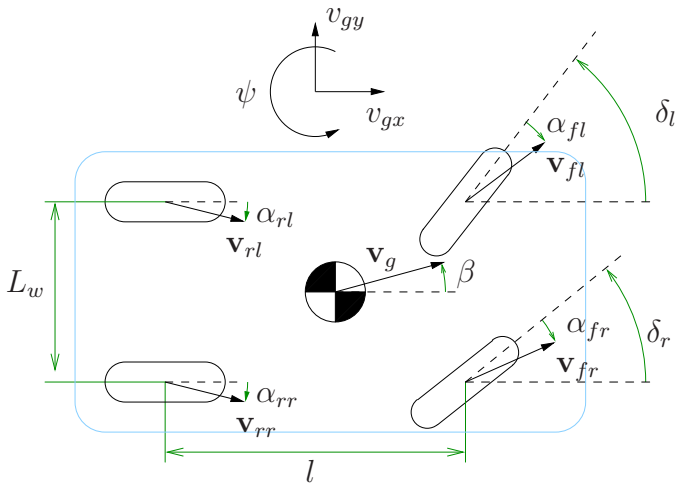

Figure 19: 4-wheel lateral model parameters.

The tile slip angles can be obtained from $\mathbf{v}_f$ and $\dot{\psi}$ by assuming the vehicle chassis is rigid as

$$\alpha_{fl} = \delta_l - \arctan\left(\frac{v_{gy} + l_1\dot{\psi}}{v_{gx} - l_{w1}\dot{\psi}}\right), \tag{2.112}$$

$$\alpha_{fr} = \delta_r - \arctan\left(\frac{v_{gy} + l_1\dot{\psi}}{v_{gx} + l_{w1}\dot{\psi}}\right), \tag{2.113}$$

$$\alpha_{rl} = -\arctan\left(\frac{v_{gy} - l_2\dot{\psi}}{v_{gx} - l_{w2}\dot{\psi}}\right), \tag{2.114}$$

$$\alpha_{rr} = -\arctan\left(\frac{v_{gy} - l_2\dot{\psi}}{v_{gx} + l_{w2}\dot{\psi}}\right), \tag{2.115}$$

where we assume the track witdh (L_w) might be different for the front and rear wheels (l_{w1} and l_{w2}, in the respective order).

As with the longitudinal and bicycle models, we can obtain movement equations by considering the longitudinal and lateral net forces, and the moments around the vehicle's center of mass. For the forces along the longitudinal axis, we obtain

$$m_b\dot{v}_{gx} - m_b v_{gy}\dot{\psi} = F_{x_{rr}} + F_{x_{rl}} + \cos(\delta_r)F_{x_{fr}} - \sin(\delta_r)F_{y_{fr}} + \cos(\delta_l)F_{x_{fl}} - \sin(\delta_l)F_{y_{fl}}. \tag{2.116}$$

In turn, for the lateral forces, we obtain

$$m_b\dot{v}_{gy} + m_b v_{gx}\dot{\psi} = F_{y_{rr}} + F_{y_{rl}} + \cos(\delta_r)F_{y_{fr}} + \sin(\delta_r)F_{x_{fr}} + \cos(\delta_l)F_{y_{fl}} + \sin(\delta_l)F_{x_{fl}}. \tag{2.117}$$

Therefore, it can be seen from (2.116) that the longitudinal tire forces propel the vehicle forward, but when there is a steering angle, part of the forces is lost due to the vehicle turning (the term on $v_{gy}\dot{\psi}$). In addition to it, the lateral forces slightly decrease the vehicle's acceleration. These phenomena could not be observed in the simpler longitudinal model expressed by (2.77) (Section 2.3.1).

Similarly, from (2.116) we have a similar conclusion to that of (2.85). In other words, the wheel's forces both keep the vehicle turning (the term on $v_{gx}\dot{\psi}$) and prevent it from side-slipping (the term on $\dot{v}_{gy}$). In the latter conclusion, we note that such a term is negative, in practice, since the vehicle's slip angle β is positive for positive steering angles α_r and α_l.

The vehicle's yaw angle can be described by considering the moments provided by the tire forces. By considering the net moment around the vehicle's center of mass, we obtain

$$\begin{aligned} I_z\ddot{\psi} = &-l_2(F_{y_{rr}} + F_{y_{rl}}) + l_w(F_{x_{rr}} - F_{x_{rl}}) + (l_1\sin(\delta_l) - l_w\cos(\delta_l))F_{x_{fl}} \\ &+ (l_1\sin(\delta_r) + l_w\cos(\delta_r))F_{x_{fr}} + (l_1\cos(\delta_l) + l_w\sin(\delta_l))F_{y_{fl}} \\ &+ (l_1\cos(\delta_r) - l_w\sin(\delta_r))F_{y_{fr}}. \end{aligned} \tag{2.118}$$

Now we recall this work aims to provide an electronic stability control scheme for an actual vehicle. In this regard, let us restrict our attention to the yaw angle. The force terms contribute or go against increasing the yaw rate; assuming positive δ_l and δ_r, the ones that

contribute the most are the term on $F_{x_{fr}}$, for the longitudinal tire forces; and the term on $F_{y_{fr}}$, for the lateral forces. Between those, the latter is largely uncontrollable, since the lateral force is a function of the slip angle, which, in turn, is a function of the steering angle and the normal force, and the steering angle comes from the driver. Assuming the system has an electric steering wheel to control it, still, it cannot be changed instantly, and even if it could, there is a dynamic description between changing the steering angle and altering the lateral forces being applied on the tires—a description which has not been presented in this text, as it is rather complex, but is known to be equivalent to a lag from around half to a full wheel roll over its axis. On the other hand, the term on $F_{x_{fr}}$ can be controlled in a much easier way. Since brakes are mounted on the wheel itself, they can be used to apply a negative longitudinal force very quickly. As a result, braking the left wheels is an efficient way to provide a negative yaw rate acceleration. In case the vehicle has a motor mounted on the wheel itself—that is to say, an electric car—it can also be used to provide a positive acceleration. Finally, outer wheels have increased normal forces due to weight transfer, so the respective brake forces do not saturate the tire's ability to move the vehicle through circles of friction as much (PACEJKA, 2012).

Seldom is the model provided by (2.116), (2.117), (2.118), and whatever tire dynamics model used without simplifications. As with the bicycle model, one often considers small steering angles. In this situation, the curve radius R is large, and $\delta \approx \delta_l \approx \delta_r$. Moreover, if δ is small, then (2.116), (2.117) and (2.118) reduce to

$$m\dot{v}_{gx} = mv_{gy}\dot{\psi} + F_{x_{rr}} + F_{x_{rl}} + F_{x_{fr}} + F_{x_{fl}} \tag{2.119}$$

$$m\dot{v}_{gy} = -mv_{gx}\dot{\psi} + F_{y_{rr}} + F_{y_{rl}} + F_{y_{fr}} + F_{y_{fl}} \tag{2.120}$$

$$I_z\ddot{\psi} = -l_2(F_{y_{rr}} + F_{y_{rl}}) + l_w(F_{x_{rr}} - F_{x_{rl}}) + l_w(-F_{x_{fl}} + F_{x_{fr}}) + l_1(F_{y_{fl}} + F_{y_{fr}}). \tag{2.121}$$

If we again drop the effects on the longitudinal acceleration expressed by (2.119), we are left with equations that are equivalent to using the bicycle model, with the addition of an extra input, which we can define as the *correcting yaw moment* M_ψ, expressed by

$$M_\psi \triangleq l_w(F_{x_{rr}} - F_{x_{rl}}) + l_w(-F_{x_{fl}} + F_{x_{fr}}). \tag{2.122}$$

If the actuation is restricted to differential braking, longitudinal forces are of course negative, and one can rewrite (2.122) as a function of the braking forces T_{fl}, T_{fr}, T_{rr}, and T_{rl} as

$$M_\psi \triangleq l_w(T_{rl} - T_{rr}) + l_w(-T_{fr} + T_{fl}). \tag{2.123}$$

The most common dynamic model simplification employed in ESC design is the ex-

tension of the bicycle models with the correcting yaw moment, yielding the state equation

$$\begin{bmatrix} \dot{\beta} \\ \ddot{\psi} \end{bmatrix} = \bar{\mathbf{A}} \begin{bmatrix} \beta \\ \dot{\psi} \end{bmatrix} + \bar{\mathbf{B}}_{ex} \begin{bmatrix} \delta \\ M_\psi \end{bmatrix}, \tag{2.124}$$

where

$$\bar{\mathbf{B}}_{ex} = \begin{bmatrix} \frac{C_{\alpha_f}}{m_b v_{gx}} & 0 \\ \frac{C_{\alpha_f} l_1}{I_z} & \frac{1}{I_z} \end{bmatrix}. \tag{2.125}$$

Therefore, (2.125) can be used in case both active front steering and differential braking are available. On the other hand, in case only differential braking is used, δ is known and only M_ψ is employed as control input.

2.4 Last remarks

This chapter has presented both the fundamentals of tire dynamics and the most basic vehicle body dynamic equations, which are essential for describing the vehicle's longitudinal and lateral dynamics. It has been shown that tires can only generate forces on the vehicle body if they slip, which explains why the usual nonholonomic wheel kinematic equations are not used in vehicle dynamics.

We presented two tire models, to better explain the principles behind slip (brush model) and introduce the model that most studies use (magic formula). The introduction to this area is often not too intuitive in textbooks. Combined slip, on the other hand, is not trivial to be explained, at least not briefly. As a result, presenting that subject has not been attempted.

Moreover, the aforementioned tire models describe steady-state behavior. This means the equations are valid for constant normal force, slip ratio, and slip angle. When the steering angle changes, so do the slip angles. The tread elements will take time to adapt to it, which delays the lateral force update. Similarly, when the vehicle starts moving, the tread elements are at rest, so it takes a certain rotation angle for them to apply force. These transient phenomena are related to the distributed aspect of tires. Deformable objects are not lumped systems: they demand an infinite number of variables to be perfectly described. This behavior can be approximated by either transient model extensions or more descriptive models.

Finally, the dynamic effects for every part of the vehicle have not been covered. Motor, driveline, hydraulics, and suspension dynamics have not been presented, since the scope

of this work is to deal with ESC, which is most affected by tire and body dynamics. Also, the subject would take a whole course to present, as seen in several mechanical engineering undergraduate and graduate degrees.

The reader who is interested in the remaining magic formula equations (pure longitudinal slip, combined slip, pneumatic trail, and aligning moment) and alternative tire models can refer to (PACEJKA, 2012). The dynamics of motors, transmissions, and the different types of suspension systems are covered in depth in (GILLESPIE, 1992; JAZAR, 2008). They are implemented in most vehicle dynamics software, such as DYNA4, CarSim, or MATLAB Vehicle Dynamics Blockset.

3 ELECTRONIC STABILITY CONTROL

Electronic stability control is the use of automatic control in order to keep the vehicle stable in the intended trajectory. The intended trajectory is that from the driver, in most vehicles, or from a trajectory planner, in automated ones. As the vehicle tracks the desired trajectory, it may become unstable, i.e., either skidding or overturning.

Assuming the vehicle does not overturn, it may leave the intended trajectory in two ways: its front or rear wheels can slide more than the others (understeer and oversteer, in the respective order), or it may slide laterally. In the first case, the vehicle's yaw rate becomes different from the intended one. In the latter, the side-slip angle becomes increasingly negative, and the curve radius increases. Thus, the problem can be solved by controlling both $\dot{\psi}$ and β (from Section 2.3.2), which is the YSC problem.

In case the vehicle overturns without colliding or leaving the roadway, its roll angle changes. This can be caused by side wind, inappropriate road bank, excessive speed while turning at a specific turning radius, or overcorrection by the driver while making successive turns (such as when changing lanes). Possible control variables are lateral acceleration, normal force on tires, and roll angle and its acceleration.

Section 3.1 presents a literature review of ESC. Next, Section 3.2 presents a general, abridged description of an ESC system, describing its inherent subproblems or design steps. The standard automobile ESC test is presented in Section 3.3. Lastly, the chapter is summarized in Section 3.4.

3.1 On Electronic Stability Control Systems

While ESC had been in development since the 1980s, the first commercial vehicles to include it were presented in 1995. The S600 Coupé, by Mercedes-Benz, and the Crown Majesta, by Toyota, featured ESC systems produced independently by Bosch and Toyota (ZANTEN; ERHARDT; PFAFF, 1995). Those were luxury cars. However, the avail-

ability of ESC on current commercial models is quickly becoming widespread. All automobiles, utility vehicles, trucks, and buses with less than 4536 kg are obligated to have ESC in the United States since 2012 (NHTSA, 2008). Electronic stability control is mandatory, in Europe, since November 2011 (EUROPEAN UNION, 2009, 2015). In Brazil, Honda and Toyota would only sell automobiles and pick-up trucks with ESC, while GM would sell vehicles with ESC on every model that would not have a 1.0 motor, in 2020. The ESC requirement on all vehicles has been postponed to January 2024 (CONTRAN, 2020).

Since ESC has been available in industry for a few decades already, it is often mentioned in several other ways, such as electronic stability program (ESP), by Bosch; vehicle stability control (VSC), by Toyota; dynamic stability control, as referred to by BMW or Mazda; of even brand names such as StabiliTrak or AdvanceTrac, by GM and Ford, respectively (ROBERT BOSCH GMBH, 2020; TOYOTA MOTOR CORPORATION, 2022; CADILLAC MOTOR CAR DIVISION, 2020; FORD, 2018). In this text, on the other hand, we will restrict the naming convention to ESC, for the sake of clarity and simplicity.

Electronic stability control can encompass a few different strategies and objectives when it comes to keeping the vehicle in a stable trajectory. The objectives can be to control the vehicle's yaw speed, to control the vehicle's roll speed, to control overall tire slipping—which can be lumped into the vehicle's side-slip angle—or any combination of those. As for how to achieve such objectives, the vehicle can use the braking system, only; it can also use the motor's throttle; it may also use the steering system; and finally, it may be equipped with some sort of active suspension system. Naturally, the more control inputs the vehicle has at its disposal, the better it can react in extreme situations, should they arise, and the more control objectives can be simultaneously achieved. As a consequence, ESC means a system that achieves the aforementioned goals, which can be different both in the goals at hand and in the available inputs of the underlying control system.

The ESC system developed by Bosch was presented in (ZANTEN; ERHARDT; PFAFF, 1995). It would originally control the yaw moment, as most ESC systems, and as proposed by most articles on the subject. The system takes the steering angle, the accelerator pedal position, and the brake pressures as measured variables in order to estimate the vehicle's nominal behavior through a lateral dynamics model. Then, the measured behavior is obtained by calculating the yaw rate and lateral acceleration from sensors. The estimated yaw rate is compared to the measured one, and a PID controller is employed to obtain the engine torque and the individual wheel brake pressures, which are the control inputs of the whole system—an approach known as *differential braking*. The idea of estimating

the system state through the driver's inputs, comparing it with the estimate from sensors, and obtaining the control inputs is the most common strategy presented in the literature. The act of controlling the yaw rate is known as *yaw stability control* (YSC).

Since brakes, engine, power drive, and steering system are mounted on the chassis, the use of such devices as control tools is collectively known as *active chassis control* (ARIPIN et al., 2014). For the scope of this study, systems that act on the vehicle's vertical dynamics shall not be employed, even if they are, too, mounted on the chassis. Classes of control methods among active chassis control are *direct yaw moment control* (DYC), *active steering control* (ASC), or an integration of both. By DYC we mean explicitly obtaining a correcting yaw moment (i.e., around the vertical axis), which then must be realized by accelerating or braking wheels (SHIBAHATA; SHIMADA; TOMARI, 1993). On the other hand, ASC uses the steering system as input to vary the lateral force on the steerable wheels, which can be the front ones, or *active front steering* (AFS); the rear ones, which is known as *active rear steering* (ARS); or even have every wheel as steerable, which is called *active four-wheel steering*.

Active steering control and differential braking are also used to avoid rollovers, that is to say, to control the vehicle's roll angle and speed. The act of controlling the roll angle (and any of its time derivatives) is known as *active roll control* (ARC) or *active rollover protection*. Those differ from passive protection systems such as anti-roll bars in the sense that there is a control input to the system. Further methods of ARC are active anti-roll bars, and active suspensions such as continuous damping control—which shall not be considered as possible control methods for this study, by design.

Differential braking accomplishes yaw control by braking opposite wheels to manipulate the yaw moment. By braking the left front and rear wheels, a counter-clockwise moment is generated. On the other hand, a clockwise moment is obtained by braking the right front and rear wheels. The brake pressure on such wheels will not necessarily be equal—in general, it shall not. Therefore, the control system must have the ability to separately apply any brake pressure to each wheel. The device used by most manufacturers consists of an extended version of the hydraulic system employed in ABS systems. An alternative has been proposed, which uses electric motors and signals to brake each wheel, called *brake-by-wire*. One such system has been presented in (XIANG et al., 2008), where the authors list the advantages and disadvantages of the architecture, and then consider a 3-degree-of-freedom (3-DOF) four-wheel chassis with parallel steering together with a Dugoff tire model (DUGOFF; FANCHER; SEGEL, 1970) as vehicle dynamics. A brief literature review up until 2005 follows, and a fuzzy-logic controller is presented afterward,

for both lateral deviation and yaw rate control. However, the objective is not stability during curves, but something akin to lane keeping, that is to say, keeping the vehicle in a straight line with minimum deviation from a set point and minimum yaw rate (i.e., straight-line trajectory tracking).

Active differentials and multiple motors can be used to extend the actuation provided by brakes. Active differentials allow for a reduction in the torque on a wheel through a corresponding increase on the one beside it (WHEALS et al., 2006). This way, the vehicle is not forced to lose speed while the ESC system is active. While this can be improved by having motors on both driven axles, a more flexible approach is available on electric cars with motors on each wheel, that is, *independent-drive* electric cars. In such vehicles, acceleration or braking can be applied at will on each wheel, provided that the motor is able to output the needed torque and the normal force on the wheel allows for it (see "load transfer", Section 2.3.1).

The first academic mention of differential braking was in (PILUTTI; ULSOY; HROVAT, 1995). Nonetheless, it was used to help the driver maintain the desired course at all times, whereas common practice in ESC has the controller only intervening when the vehicle is about to lose stability. It was, however, already in use in the industry. DRAKUNOV; ASHRAFI; ROSIGLIONI (2000) used differential braking with a sliding-mode controller for the yaw rate. The (conference) article is brief and only presents the control strategy: no experiments or simulations are presented. The authors had previously used sliding mode with braking systems for ABS (DRAKUNOV et al., 1995).

A simple ESC system with both yaw and roll stability was implemented in (KINJAWADEKA, 2009). A commercial vehicle was modeled in MATLAB with CarSim, and then such a model has been validated with actual vehicle data. A switched controller for the yaw and roll control problems has been presented, using lookup tables to generate the individual wheel braking pressures, considering two different standard maneuvers. Simulation results followed.

ZHOU; LIU (2010) used a sliding-mode observer to estimate the tire forces, and then a sliding-mode controller is used to restrict the yaw rate by braking a single wheel. The closed-loop system is validated with simulation results based on a standard double lane-change maneuver. In (SUBROTO; WANG; LIAN, 2020), a sliding-mode strategy is also employed to deal with the yaw rate problem, but with a vehicle with more control inputs. A four-wheel independent drive electric vehicle is considered, so both positive and negative torques are possible on every wheel. Moreover, both the front and rear

wheels can be steered, unlike most vehicles, which only have a pair of steerable wheels. A dual-layer controller is proposed: a sliding-mode one for the outer loop, and dynamic control allocation for the inner one. Actuator fault was considered by assuming each of the control inputs might either decrease in amplitude, be stuck at a given value, or be disturbed by an additive value. The stability of the control loop system was demonstrated and simulation results illustrated its application.

Another multi-layer sliding-mode strategy was proposed in (XU; WANG; LI, 2014). A lateral dynamics controller is proposed at the lowest level to track the slip ratio with a sliding-mode technique. A mid-level layer relates a reference yaw moment, which comes from a higher-level controller, with the slip ratio the aforementioned controller has to track, considering a 3-DOF vehicle chassis model combined with an assumed-linear tire dynamics model. This high-level controller also employs a sliding-mode strategy which takes the yaw rate error as input to obtain the required yaw moment. Simulation results are presented in order to validate the proposed control system, using the ISO-standard double-lane change maneuver as the scenario.

A model predictive control (MPC) ESC considering a bicycle model is presented in (CHOI; CHOI, 2014). However, some sort of dynamic model of the transient state was taken into account in the form of a time delay, whereas most works only consider the steady-state tire models (see Section 2.1). This is convenient in MPC, assuming one approximates time delays to an integer number of sampling periods. Moreover, instead of the more usual quadratic cost function from the control deviation which is often used in linearized MPC, it considers an absolute-value one. The strategy was validated through simulation, considering a sinusoidal steering angle input over both high and low friction surfaces, and presenting the difference between considering delay or not.

In (JALALI et al., 2017) the authors propose an MPC ESC with active front steering, in addition to individual tire brakes. The feedback system controls the vehicle's yaw rate and its lateral speed. A quadratic function on the control input was used together with a soft constraint on the lateral speed, where a bicycle model was considered. The authors used simulations based on the CarSim model from MATLAB with the parameters of a commercial electrical vehicle to validate the closed-loop system. Finally, experimental results have been presented with the vehicle moving over a wet road.

The computing power is often an issue for MPC when the system is not linear and time-invariant. An ESC based on model predictive control with particular care on the computational complexity is proposed in (MAGALHÃES JÚNIOR, 2019; MAGALHÃES

JÚNIOR; MURILO; LOPES, 2022). Lateral and rolling models have been considered, with linearized or magic formula models for tires, and simulation results are presented. Another study that dealt with the computing time while using MPC was (GUO et al., 2020). The authors considered a four-wheel 2DOF model and aimed at reducing the tire slip energy. A fast model predictive control allocation (MPCA) method was presented and tested through simulation for high and average (which they have called "low") friction coefficients for the road.

Other control strategies are also found in the literature. For instance, in (ZHAI; SUN; WANG, 2016) an ESC for a four in-wheel motor independent-drive electric vehicle (4MIDEV) is presented. However, the vehicle which was considered differs from the one in (SUBROTO; WANG; LIAN, 2020) in that it only has front steering. A multi-layer controller is used for the yaw moment, which is implicitly restricted through the side-slip angle and side-slip angle rate. Ultimately, a quadratic problem is rewritten as a weighted least-squares problem to obtain the motor torques. The system is shown in operation through simulations for three different maneuvers under wet surface conditions.

Another article that considers a vehicle with more inputs than ordinary internal-combustion vehicles is (FENG; CHEN; QI, 2020). The vehicle has a single motor, but it is equipped with an electronically controlled real-time four-wheel drive (4WD) so that all wheels can provide torque. It also uses differential braking and active front steering. The study proposes a coordinated chassis control (CCC), that is to say, an embedded control system that monitors more than one variable, namely the yaw rate and the individual wheel slip angles. It considers a bicycle model and uses a hierarchical structure, with supervisory, upper-level, and lower-level controllers. Simulation results were presented for a given maneuver and a handling course road.

In (VU et al., 2019), the roll stability problem is approached with a Linear Parameter-Varying (LPV) Model and an H_∞ controller that maximizes roll stability by restricting the load transfer from the left wheels to the right ones and vice-versa. The models on the H_∞ structure are parameterized by a variable that depends on the load transfer, the problem is solved through a linear matrix inequality (LMI) approach, and simulation results are presented.

Another use of H_∞ control is presented in (ZHANG; SUN; FENG, 2018), which would control the yaw rate considering both mass and moment of inertia uncertainties, which are used as scheduled variables. The authors used a bicycle model, from which a linear fraction transformation (LFT) model is obtained and used in standard H_∞ form. The

proposed method was validated with simulations with a CarSim MATLAB model for the simulated vehicle.

3.2 Control problem

A general ESC scheme is depicted in Figure 20, showing a simplified diagram of the general feedback system. The driver's commands are directly applied on the vehicle most of the time. The vehicle's behavior is a result of those commands as the vehicle interacts with the environment. This response, as measured by sensors, is compared to a reference behavior, which is obtained from the driver's commands. Vehicle data might be used to improve the reference. If the reference behavior, sometimes called *desired behavior*, is close enough to the measured one, the ESC system does not intervene, and the vehicle operates without any assistance from it. Else, the control system takes the error and vehicle data to obtain the control signals, which override the driver's commands. The dashed line indicates the implicit feedback the driver obtains from the vehicle (acceleration, vibration, trajectory) together with the explicit one (senses, panel instruments).

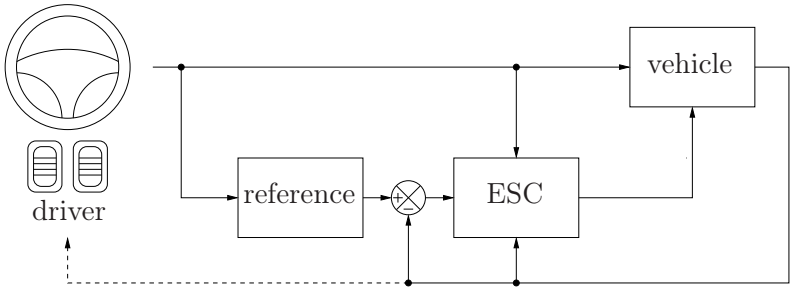

Figure 20: General ESC system.

The signals considered on the reference depend on the ESC problem. Naturally, roll control adds the roll angle, while yaw control takes the yaw rate error as input. We focus on the YSC problem, which often takes a side-slip angle error too, to detect side-slip, i.e., lateral slide under very low yaw rates. A common criterion is the desired yaw rate as described by the linearized bicycle model (XU; WANG; LI, 2014; MAGALHÃES JÚNIOR, 2019; MIRZAEI, 2010; MIRZAEINEJAD; MIRZAEI; RAFATNIA, 2018; BASLAMISLI; KÖSE; ANLAÇ, 2011; CHO et al., 2008), considering a null side-slip angle, given by:

$$\dot{\psi}_d = \frac{v_{gx}\delta}{l + k_{st}v_{gx}^2}, \qquad k_{st} \triangleq \frac{m_b(l_2 C_{\alpha_r} - l_1 C_{\alpha_f})}{l C_{\alpha_f} C_{\alpha_r}}, \tag{3.1}$$

where k_{st} is called the *stability factor*. This criterion is not unique, however: (TSENG et al., 1999; LENZO et al., 2021; VAN PUTEN, 2008; CHOI; CHOI, 2014) use a different

desired yaw rate, with a non-zero side-slip angle reference. Moreover, (3.1) may not be possible in case the curve is excessively sharp—or, likewise, the longitudinal speed is too high for a given curve. In this regard, it is clear that the maximum lateral force the wheels can sustain is limited by friction and the normal force on them. On a non-cambered road, this means

$$F_{y_{\max},i} = \mu W_i \tag{3.2}$$

for the i^{th} wheel. For all wheels, this yields

$$m_b a_{y_{\max}} = \mu \sum^{i} W_i = \mu W = \mu m_b g, \tag{3.3}$$

where $a_{y_{\max}}$ is the maximum centripetal acceleration. Since $a_{y_{\max}}$ is a centripetal acceleration, it is also given by $\dot{\psi} v_{gy}$. Hence, (3.3) can be rewritten as

$$\dot{\psi}_{\max} = \frac{\mu g}{v_{gx}}, \tag{3.4}$$

assuming $v_{gx} > 0$.

Since the desired yaw rate from the neutral side-slip angle is limited by the maximum lateral acceleration, it is often extended as

$$\dot{\psi}_d = \min \left\{ \left| \frac{v_{gx}\delta}{l + k_{sf} v_{gx}^2} \right|, \left| \frac{\mu g}{v_{gx}} \right| \right\} \operatorname{sign}(\delta) \tag{3.5}$$

which in essence limits (3.1) by the maximum feasible lateral force on the tires.

Finally, it is important to mention that a null side-slip angle is not a steady-state condition for automobiles at low speeds. The slower the vehicle is, the closer its trajectory gets to that expected by pure Ackermann kinematics, where the side-slip angle always points inwards to the curve. As the vehicle gains speed, the wheels' slip angles increase, and β tends to point outwards to curves. For this reason, the use of YSC together with (3.1) is often perceived to be invasive to the driver's commands.

In case there is a discrepancy between the desired and actual vehicle behavior, the ESC system interferes with whatever input commands it has at its disposal, from brakes (most common), steering angle, and individual wheel throttle. In order to obtain the desired behavior, the system measures the driver's input: steering wheel angle, throttle, brake pedal, clutch, and so on. The control signal is obtained by estimating the vehicle state variables through accelerometers, gyroscopes, wheel angular speeds, steering system angles, etc. Again, this discrepancy is usually on yaw rate and side-slip angle (e.g., (XU; WANG; LI, 2014; MAGALHÃES JÚNIOR, 2019)), but it can be the yaw

rate, alone (MIRZAEINEJAD; MIRZAEI; RAFATNIA, 2018). One advantage of taking both errors to monitor the vehicle is that a constant small yaw rate error (which might not trigger the ESC system) will cause the side-slip angle error to increase.

At this point, an analysis of the linearized models from Section 2.3.2 can be insightful. Since equivalence transformations do not affect controllability, we can consider either $[v_{gy} \;\; \dot{\psi}]^{\mathrm{T}}$ or $[\beta \;\; \dot{\psi}]^{\mathrm{T}}$ as the state. Using the latter, it turns out that (2.124) is controllable. Moreover, if we consider only δ or only M_ψ as input, by verifying the controllability of the pairs $\{\bar{\mathbf{A}}, \bar{\mathbf{B}}_{ex1}\}$ and $\{\bar{\mathbf{A}}, \bar{\mathbf{B}}_{ex2}\}$, in the order, $\bar{\mathbf{B}}_{ex} = [\bar{\mathbf{B}}_{ex1} \;\; \bar{\mathbf{B}}_{ex2}]$, both systems remain controllable.

Even though the linearized system is controllable, it does not mean the desired state can be easily reached or any trajectory easily tracked. The steering angle δ input direction ($\bar{\mathbf{B}}_{ex1}$) does affect both β and $\dot{\psi}$, but in practice, this input variable has a delayed effect on the system that is only modeled by dynamic tire models (GILLESPIE, 1992; PACEJKA, 2012). This means the system cannot be immediately influenced by active steering, which is an issue since ESC is fundamentally an emergency control system. Moreover, a sudden loss of traction while in a curve means that both effects on the lateral speed and yaw moment become reduced, especially in the event of understeering.

On the other hand, the input delay is much shorter on longitudinal tire forces (CHOI; CHOI, 2014), hence, on M_ψ. However, the correcting yaw moment only directly affects $\dot{\psi}$, which means its effect on β is delayed. In addition to it, the use of M_ψ alone (DYC) cannot promptly reduce both yaw rate and side-slip angle errors, since those are competing objectives. In other words: assume the vehicle has a side-slip angle error, but negligible yaw rate error. The side-slip angle correction will demand a yaw rate change, which will increase the respective error. This fact must be weighted in optimal control tuning: not favoring one controlled variable over another may lead to overly low input signals, especially with short prediction horizons. In addition to it, it explains why some YSC systems with no active steering will control the yaw rate, only (MIRZAEI, 2010; XIANG et al., 2008; ZHOU; LIU, 2010). Finally, the shorter delay on τ_{G_z} justifies the prevalence of differential braking systems as input variables for YSC in the industry.

Recalling the control design problem, the criterion is often to reduce the yaw rate error as fast as possible, but different choices have been discussed. These are dependent on the available input variables—which, in this work, shall be restricted to differential braking and active steering. Derivatives of input or system variables can be used to improve passenger comfort (MAGALHÃES JÚNIOR, 2019). The input and output error

can be reduced or minimized through MPC (CHOI; CHOI, 2014; JALALI et al., 2017; MAGALHÃES JÚNIOR, 2019; GUO et al., 2020), LQ (MIRZAEI, 2010; NAGAI; SHINO; GAO, 2002), H_∞ (ZHANG; SUN; FENG, 2018; LENZO et al., 2021; GÜVENÇ et al., 2004), or fuzzy programming (XIANG et al., 2008; ZHAI; SUN; WANG, 2016; MIRZAEINEJAD; MIRZAEI; RAFATNIA, 2018). In (DRAKUNOV; ASHRAFI; ROSIGLIONI, 2000; ZHOU; LIU, 2010; SUBROTO; WANG; LIAN, 2020; XU; WANG; LI, 2014; CHO et al., 2008), sliding-mode control is used to stabilize the system. Finally, it should be mentioned that other strategies exist, e.g., (YAMAKADO; TAKAHASHI; SAITO, 2012).

Whatever control method is used in YSC, the control scheme is often separated into two layers: one for obtaining the correcting yaw moment, and another for applying brake pressures on tires. The yaw moment is obtained by changing the steering angle, braking individual wheels, or both. Braking wheels is a more complex procedure, which demands control loops for each controlled wheel.

The yaw moment control layer will return a desired correcting moment. Since this is based on a vehicle model, this model's parameters must first be obtained. In practice, several parameters are time-variant, such as the vehicle's center of mass while accelerating or curving. Notwithstanding, simpler models demand, at least, the longitudinal speed and the tire's longitudinal and cornering stiffnesses. Assuming the longitudinal speed is available, the stiffnesses remain, which are dependent on the normal force on the tires (Section 2.1).

The normal forces on the tires are a result of vehicle mass distribution, weight transfer, and the suspension system. How much vertical load each tire has to support at constant speeds can be obtained offline. Weight transfer, however, demands the vehicle's body accelerations. The most common strategy is to consider a mass suspended by springs and damped by dashpots, dubbed *sprung mass*, and assume it has a roll (and maybe a pitch) axis of rotation (MAGALHÃES JÚNIOR, 2019; MIRZAEINEJAD; MIRZAEI; RAFATNIA, 2018; CHO et al., 2008). Another strategy is to consider no suspension system, obtaining the normal forces from static load transfer, e.g., as in (NAGAI; SHINO; GAO, 2002; YAMAKADO; TAKAHASHI; SAITO, 2012). The latter strategy is not a good description of sudden steering angle changes.

The longitudinal forces from the brakes can be obtained from the correcting yaw moment, the tire longitudinal stiffness, and the slip ratio. These forces are to satisfy the correcting moment, and this is the task of the low-level control loop. The first task is to determine which wheels will be used. The original ESC systems would brake the outer

front wheel in case of oversteering, and the inner rear wheel in the event of understeering. Other studies suggested different force distributions among outer and inner tires (CHOI; CHOI, 2014).

Given the desired longitudinal braking force on a tire, it can be obtained by controlling the tire's slip ratio, which is done through its brake pressure. The brake pressure, in turn, is proportional to the braking moment on that tire. This problem demands descriptive tire models and accurate longitudinal speed measurements since the slip ratio is a function of both the longitudinal and angular speeds. An alternative to estimating slip ratio is to estimate the longitudinal force, directly, e.g., (ZHOU; LIU, 2010).

Thus, the general control procedure is:

1. obtain the outputs of all sensors [inertial measurement unit (IMU), tire speeds, axle speeds];
2. measure or estimate the vehicle's lateral and longitudinal speeds;
3. obtain the normal force on all tires;
4. obtain the parameters for the models which are used in the control loop;
5. obtain the desired (reference) vehicle behavior;
6. obtain the correcting yaw moment;
7. obtain the equivalent force distribution on the tires;
8. control the equivalent longitudinal force on every tire;
9. apply the respective braking pressures.

There are several standard tests to access electronic stability control effectiveness. The Fishhook and J-Turn tests induce rollover (NHTSA, 2001, 2018). The Double Lane Change induces rollover and oversteering while testing handling (LNCAP, 2020). The Steady-State Circle Series, in turn, can be used to obtain steady-state cornering parameters, which although related to lateral stability, cannot be used to validate an ESC system (STEADY-STATE..., 1998; PASSENGER..., 2021). Finally, standard FMVSS № 126/UN/ECE Regulation № 13-H Sine with Dwell test consists of a set of instability-inducing maneuvers during which stability requisites are to be satisfied (NHTSA, 2009; EUROPEAN UNION, 2015). We used the latter to validate yaw stability control proposals. Section 3.3 describes the procedure.

3.3 Sine with Dwell test

The Sine with Dwell test is used to validate commercial ESC systems for passenger cars, as prescribed by the standards FMVSS № 126, for the USA, and UN/ECE Regulation № 13-H, in Europe (NHTSA, 2009; EUROPEAN UNION, 2015). Before ESC became mandatory in Europe, it was part of the Euro NCAP as ESC Dynamic Test Protocol, which is now part of the Latin NCAP (EURO..., 2011). The idea of the test is to induce vehicle instability and measure the ESC system's ability to recover from it.

The test consists of a set of open-loop steering wheel movements with increasingly larger amplitude, performed at an initial longitudinal speed of 80 km/h. These maneuvers are guaranteed to induce lateral instability on a vehicle that is not equipped with ESC. As the vehicle performs the maneuver, the closed-loop ESC system must react to the loss or near loss of vehicle control. More clearly, the effects of vehicle instability are then to be limited by lateral stability criteria and a responsiveness criterion.

Figure 21 shows the steering wheel maneuver and the stability criteria. The steering wheel is attached to a piece of equipment that performs open-loop movements in accordance with Figure 21, which is a 0.7 Hz sine function that is halted at its negative peak for 0.5 s, which is the dwell time.

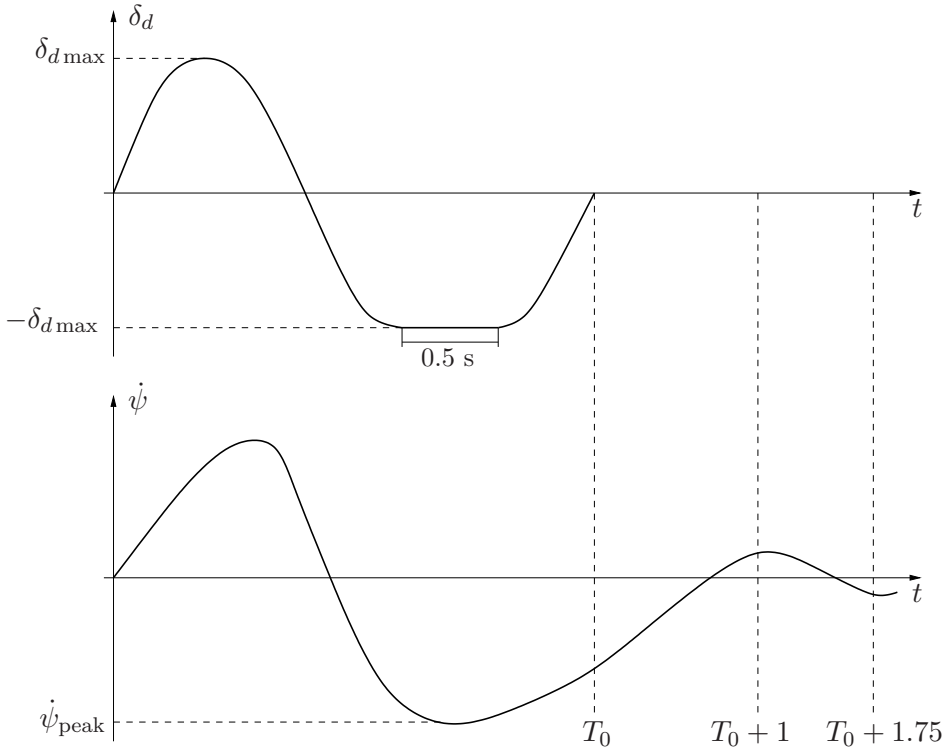

Figure 21: Sine with Dwell test steering wheel input and yaw rate stability requirements. SOURCE: (NHTSA, 2008, 2009; EUROPEAN UNION, 2015) (Adapted).

The amplitudes $\delta_{d\max}$ of the 0.7-Hz Sine with Dwell steering wheel movements are factors of A, defined as the (constant) steering wheel angle which causes a lateral acceleration of $0.3g$. In particular, the test procedure starts with $\delta_{d\max} = 1.5A$, and after each successful maneuver, $\delta_{d\max}$ is incremented by $0.5A$. This amplitude is incremented until either $6.5A$ or 270°, whichever is greater. In case $6.5A > 300°$, the final amplitude is set to 300°. If all maneuvers are successful, negative (i.e., clockwise) steering wheel angle amplitudes are employed (NHTSA, 2008, 2009; EUROPEAN UNION, 2015).

The lateral stability criteria are related to the peak value $\dot{\psi}_{\text{peak}}$ of the yaw rate, measured after the steering wheel angle changes sign (see Figure 21). One second after the open-loop steering wheel movement is completed ($T_0 = 1.93$ s), the yaw rate is again measured, and must not exceed 35 % of $\dot{\psi}_{\text{peak}}$. After that, at $t = T_0 + 1.75$ s, $\dot{\psi}$ must be equal or less than 20 % of $\dot{\psi}_{\text{peak}}$, in magnitude. As a consequence, the lateral stability criteria are (NHTSA, 2008, 2009; EUROPEAN UNION, 2015)

$$|\dot{\psi}(T_0 + 1.00)| \leq 0.35|\dot{\psi}_{\text{peak}}| \qquad |\dot{\psi}(T_0 + 1.75)| \leq 0.20|\dot{\psi}_{\text{peak}}|. \tag{3.6}$$

The vehicle is also expected to move sideways, as the first part of the maneuver moves the vehicle either to the left, for $\delta_d > 0$, or right, for $\delta_d < 0$. Else, the vehicle would be side-slipping, as if the vehicle were moving on a highly slippery surface, with $\mu \approx 0$. This aspect is verified by the responsiveness criterion, which is exerted for $\delta_d \geq 5A$. The lateral movement Δy_g of the center of mass of the vehicle is measured at the beginning of the dwell time, at $t = 1.07$ s after the steering wheel movement begins, or $\Delta y_g \triangleq y_g(1.07) - y_g(0)$. This lateral movement must be at least 1.83 m for vehicles with up to 3500 kg of gross vehicle weight rating (GVWR). The GVWR is the maximum mass the vehicle can operate with, safely. It is the sum of its mass, the occupants' mass, and any other payload it was designed to carry, e.g., luggage (NHTSA, 2008, 2009; EUROPEAN UNION, 2015).

We are now able to understand why a passenger car that does not have ESC is incapable of completing the Sine with Dwell test. We recall that A is the common factor used for the steering wheel angle δ_d maximum amplitude, related to a lateral acceleration of $0.3g$. We also recall from Section 5.1.2 that the typical friction coefficient of dry asphalt is 0.85. It can reach values around 0.9 for exceptionally clean roads with no humidity. So the maximum lateral acceleration we would expect from a passenger car, which we assume is unable to generate downforce, is $0.9g$, in ideal conditions. Should we admit that the lateral acceleration is proportional to the steering wheel angle, we can expect the first test ($\delta_d = 1.5A$) to generate $0.45g$; the second test ($2A$) to produce $0.6g$; the third,

$0.75g$ from $\delta_d = 2.5A$; and the fourth test, when $\delta_d = 3A$, already puts the vehicle on the verge of losing stability at $0.9g$. Consequently, a vehicle that is not designed to generate downforce shall not be stable in its trajectory for $\delta_{d\,\max} \geq 3.5A$.

Moreover, the Sine with Dwell maneuver first induces a yaw rate with the opposite magnitude of that which would one verifies during the dwell time. Thus, it makes it even harder for the wheels to provide both the needed longitudinal force to invert the yaw rate sign and the lateral force that would keep the vehicle stable. Most vehicles with no ESC systems will oversteer—or even spin out—during and after the dwell time, in which the steering wheel is maintained at the highest magnitude after the vehicle was induced to move laterally to the opposite side.

3.4 Remarks on ESC

Section 3.2 presents the structure of ESC systems, emphasizing YSC. Most systems will take the wheels' speeds and IMU signals as inputs, together with the driver commands. The IMU signals are used to estimate or directly measure yaw rate, longitudinal and lateral acceleration, longitudinal and lateral speed, tires' slip ratio and slip angle, tires' normal forces, tires' stiffnesses, and longitudinal and lateral forces. The information from the driver is used to obtain an expected or desired behavior, most often expressed by a desired yaw rate and a desired side-slip angle.

The yaw rate and side-slip angle errors are used to trigger the ESC system so that it does not become exceedingly intrusive and obtain the system input signals, which are the brake pressures on each wheel for differential braking; and steering angle correction for active steering.

Yaw stability control systems are often implemented in layers. First, an upper-layer control loop obtains a correcting yaw moment that, if applied, would adequately control the yaw rate or side-slip angle of the vehicle. Second, a lower-level control loop obtains this moment as a sum of longitudinal and lateral forces from the tires, factored by the respective lever arm distances to the vehicle center of mass. Finally, the longitudinal or lateral forces are obtained by controlling the slip ratios and angles on the individual tires, as described in Section 2.2. In particular, the brakes and throttle control the slip ratio whereas the steering angle controls the slip angle.

It has been noted that the main difficulties arise from the ability—or lack thereof—to properly describe the vehicle during aggressive driving or emergency maneuvers and

to maintain it in a controllable state. Those are related to inherent uncertainties and nonlinearities which are present in both the vehicle and the environment. Tire conditions, road type, obstacles, vehicle load, load distribution, and wind intensity all affect the vehicle's behavior in ways that can be very hard or impossible to quantify. The ultimate purpose of the system is to keep the vehicle in a controllable state on the road while interfering as little as possible with the behavior that is expected from the driver's actions. Hence, a control structure that is lenient on a given operating region, but also prevents the system from ever leaving it would be highly desirable. In case the system does become unstable, we wish the driver recovers control as fast as possible.

ESC systems are validated in both Europe and the United States by the Sine with Dwell test (NHTSA, 2009; EUROPEAN UNION, 2015). The test is focused on the ability of the vehicle to recover from lateral instability but also verifies the responsiveness to steering wheel commands.

This text will leave the difficulties related to estimating the several important variables and parameters out of its scope, focusing on the control problem. We assume vehicle velocity and yaw rate are perfectly measured; vehicle mass and mass distribution, friction coefficient, and tire parameters are known, and road grade and bank are null. Such problems, consequently, as left as future works or research suggestions (see Chapter 8).

4 SAFETY-CRITICAL CONTROL BASED ON CONTROL BARRIER FUNCTIONS

Safety-critical control assumes safety takes precedence over other automatic control properties or objectives, e.g., performance (GURRIET et al., 2020). Safety, in this field, is understood as the invariability of an arbitrary set where the state is constrained to. This set can be related to keeping the system stable or controllable. Or maintaining it within a linear region of operation, within a differentiable nonlinear region of operation, or constrained to whatever manner that should prevent it from ever harming nearby people, animals, or other equipment. The set which satisfies the safety criteria is called a *safe set*. For instance, assume we are dealing with a trajectory tracking problem for a road vehicle operating within city limits. We may want to prevent it from ever invading sidewalks. Consequently, we would want to restrict it to paved roads, which the safe set for the given problem would be comprised of.

There are different approaches to safety-critical control. Among them, we mention set invariance (MITCHELL; BAYEN; TOMLIN, 2005; GILLULA; KAYNAMA; TOMLIN, 2014) and backup trajectory tracking (HO et al., 2017; LOPEZ; HOW, 2017). In this text, we employ Control barrier functions, as presented in the literature from 2017 onwards (GURRIET et al., 2020; AMES et al., 2017, 2019). Safety-critical control based on CBFs can be understood as an extension to set invariance control theory, where instead of establishing asymptotic stability to a specified equilibrium state, one aims for convergence to a set in the state space. Thus, the most important property is not asymptotic stability (that is to say, to close in on a given state), but set invariance itself.

An introduction to invariance set control is presented in the form of Lyapunov theory, as presented in any nonlinear systems textbook, e.g., (SLOTINE; LI, 1990; KHALIL, 2002). The advances in invariance control, from its inception until the end of the 20th century, are summarized in (BLANCHINI, 1999). Control barrier functions—based on barrier functions, also known as barrier certificates—have been proposed in two ways, first by (WIELAND; ALLGÖWER, 2007), and then by (AMES et al., 2017). We introduce

the subject as presented by (AMES et al., 2017, 2019), focusing only on *zeroing* control barrier functions, as opposed to *reciprocal* ones [see (AMES et al., 2017)], previously used in optimization, e.g., (BOYD; VANDENBERGHE, 2004). First, the fundamentals of invariance control are presented, in Section 4.1, and then those of control barrier functions, in Section 4.3. Since it is clear that the following is not a contribution of this work, and for the sake of brevity, readers are referred to the appropriate sources for theorem proofs. We summarize the subject in Section 4.4, before presenting the proposals, in Chapters 6 and 7.

Before proceeding to the remainder of the chapter, it is convenient to mention that, in order to shorten notation, we will employ usual dynamic systems general notation, for example, $\mathbf{x}(t)$ is any dynamic system state vector, not necessarily the ones seen in Section 2.3, and so on. We shall also drop the time dependency on all state and input vectors, unless we want to emphasize it, again to simplify notation, i.e., the input vector $\mathbf{u}$ denotes $\mathbf{u}(t)$.

4.1 Invariance Control Basics

The most fundamental set invariance concept is Lyapunov stability, which, in essence, means that the states around a certain equilibrium point $\mathbf{x}_{eq}$ remain close to it, or, in other words, remain within a neighborhood of it. As such, the state will be restricted to some set $\mathcal{C}$, called an *invariant set*. The main result in Lyapunov theory is expressed in Theorem 1.

Theorem 1 (Lyapunov stability (SLOTINE; LI, 1990; KHALIL, 2002))**.** *Consider the system* $\dot{\mathbf{x}} = f(\mathbf{x})$*. An equilibrium point* $\mathbf{x}_{eq}$ *is* Lyapunov stable*, or* stable in the Lyapunov sense*, if there exists*

$$V(\mathbf{x}) > 0, \quad \mathbf{x} \neq \mathbf{x}_{eq}, \quad V(\mathbf{x}_{eq}) = 0 \tag{4.1}$$

$$\dot{V}(\mathbf{x}) \leq 0, \quad \mathbf{x} \neq \mathbf{x}_{eq}, \quad \dot{V}(\mathbf{x}_{eq}) = 0. \tag{4.2}$$

If $V(\mathbf{x})$ satisfies (4.1) and (4.2), it is called a *Lyapunov function*. Moreover, if $\dot{V}(\mathbf{x}) < 0$, $\mathbf{x}_{eq}$ is *asymptotic stable*. Finally, if (4.1) and (4.2) hold for any $\mathbf{x} \in \mathcal{C}$, then $\mathcal{C}$ is invariant[1]. Figure 22 depicts the result.

[1]Negatively invariant sets are of little importance in engineering; hence, we refer to positively invariant sets, or forward invariant sets, as simply invariant sets.

[2]Also known as boundary of $\mathcal{C}$.

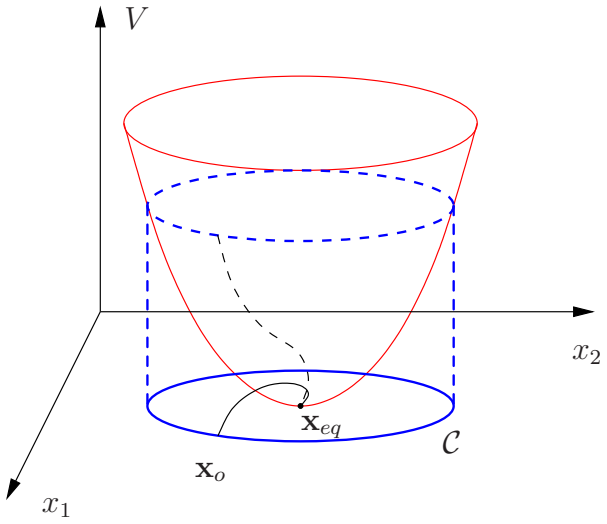

Figure 22: Set invariance under Lyapunov theory for a 2nd-order system. Continuous red lines: parabolic Lyapunov function. Continuous blue line: invariant set frontier[2]. Continuous black line: state trajectory. Dashed black line: $V(\mathbf{x})$ trajectory.

In Figure 22, an initial state $\mathbf{x}_o \triangleq \mathbf{x}(0)$ from a 2nd-order system evolves towards the equilibrium point $\mathbf{x}_{eq}$ as its respective Lyapunov function value decreases over time. The set invariance, here, is a consequence of asymptotical stability.

As one is often interested in convergence time restrictions, the Lyapunov exponential stability theorem is often employed.

Theorem 2 (Lyapunov exponential stability (SLOTINE; LI, 1990; KHALIL, 2002)). *Consider the system* $\dot{\mathbf{x}} = f(\mathbf{x})$. *An equilibrium point* $\mathbf{x}_{eq}$ *is* Lyapunov exponentially stable, *if there exists*

$$V(\mathbf{x}) > 0, \quad \mathbf{x} \neq \mathbf{x}_{eq}, \quad V(\mathbf{x}_{eq}) = 0 \tag{4.3}$$

$$\dot{V}(\mathbf{x}) < -\lambda V(\mathbf{x}), \quad \mathbf{x} \neq \mathbf{x}_{eq}, \quad \dot{V}(\mathbf{x}_{eq}) = 0. \tag{4.4}$$

If (4.3) and (4.4) hold, then there exists $K \in \mathbb{R}$ such that $|\mathbf{x}(t) - \mathbf{x}(0)| < Ke^{-\frac{\lambda t}{2}}|\mathbf{x}(0) - \mathbf{x}_{eq}|$.

A related result is given by Nagumo's invariance principle (NAGUMO, 1942), which uses a function h that has a maximum, instead of V, which has a minimum at $\mathbf{x}_{eq}$.

Theorem 3 (Nagumo's invariance principle (NAGUMO, 1942; AMES et al., 2017, 2019)). *Let* $h(\mathbf{x})$ *be a concave function over a set* $\mathcal{C} = \{\mathbf{x} \mid h((x)) \geq 0\}$, *with*

$$\dot{\mathbf{x}} = f(\mathbf{x}).$$

Then, if $\dot{h}(\mathbf{x}) \geq 0, \forall \mathbf{x} \in \text{fr}(\mathcal{C})$, $\text{fr}(\mathcal{C})$ *being the frontier of* $\mathcal{C}$, $\mathcal{C}$ *is invariant.*

Figure 23 depicts the result from Theorem 3 for a 2nd-order system and a parabolic h function. If Theorem 3 holds, h is called a *zeroing barrier function*, in contrast to a *reciprocal barrier function*, which is neither explained nor employed in this text. As a result, we henceforth refer to zeroing barrier functions as simply "barrier functions".

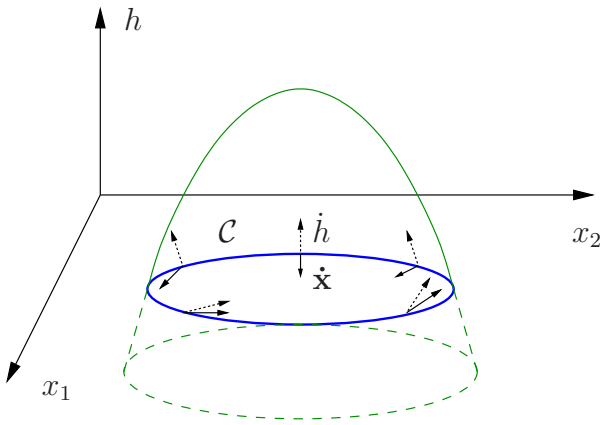

Figure 23: Set invariance under Nagumo' principle. Continuous green lines: parabolic barrier function. Continuous blue line: invariant set frontier. Continuous black lines: state derivatives. Dashed black lines: barrier function derivatives.

Figure 23 shows (five) different initial conditions, where the state derivatives are shown in continuous black lines and the respective h derivatives are shown in dashed black lines. Positive values of h are depicted in continuous green lines, while negative ones are in dashed green lines. Whenever the state approaches the frontier of the invariant set, $\dot{h}$ is positive, so $\dot{x}$ points inward. No asymptotic stability is implied.

While in Lyapunov theory the invariant set is guaranteed to converge to a neighborhood of $\mathbf{x}_{eq}$, Nagumo's principle only establishes that points in $\mathcal{C}$ remain constrained to it. These will be analogously extended as, in the respective order, control Lyapunov functions and control barrier functions.

4.2 Control Lyapunov functions

Theorems 1–3 can be adapted to feedback systems by adding a control input to $f(\cdot)$. Let us consider the subclass of nonlinear systems expressed by

$$\dot{\mathbf{x}} = f(\mathbf{x}) + g(\mathbf{x})\mathbf{u}, \tag{4.5}$$

or *control-affine systems*, where $\mathbf{x} \in \mathcal{D} \subset \mathbb{R}^n$, $\mathcal{D}$ the set of possible state vectors; $\mathbf{u} \in \mathcal{U} \subset \mathbb{R}^m$, $\mathcal{U}$ containing the admissible input vectors; and both $f(\cdot)$ and $g(\cdot)$ are Lipschitz

continuous, i.e., there exists $K \in \mathbb{R}$ such that

$$|f(\mathbf{x}_1) - f(\mathbf{x}_2)| \leq K|\mathbf{x}_1 - \mathbf{x}_2|, \tag{4.6}$$

for any $\mathbf{x}_1$, $\mathbf{x}_1$, and the same to $g(\cdot)$. In other words, the absolute value of the derivative of $f(\cdot)$ and $g(\cdot)$ with respect to $\mathbf{x}$ is bounded in any direction.

Now, if $\mathbf{u}$ is a function of $\mathbf{x}$, Theorems 1–3 can be used to assess the stability and invariability of closed-loop systems. Recall that in order to apply Lyapunov theory, time derivatives of Lyapunov functions are needed. Let us assume $\mathbf{u} = k(\mathbf{x})$, $V(\mathbf{x}) > 0$, $V(\mathbf{x}_{eq}) = 0$ and

$$V(\mathbf{x}, k(\mathbf{x})) > 0, \quad \mathbf{x} \neq \mathbf{x}_{eq}, \quad V(\mathbf{x}_{eq}, k(\mathbf{x}_{eq})) = 0. \tag{4.7}$$

As the time derivative of $\mathbf{x}$ is given by (4.5), we have

$$\begin{aligned} \dot{V}(\mathbf{x}) &= \frac{\partial V(\mathbf{x})}{\partial \mathbf{x}} \dot{\mathbf{x}} \\ &= \frac{\partial V(\mathbf{x})}{\partial \mathbf{x}} (f(\mathbf{x}) + g(\mathbf{x})\mathbf{u}) \\ &= \frac{\partial V(\mathbf{x})}{\partial \mathbf{x}} f(\mathbf{x}) + \frac{\partial V(\mathbf{x})}{\partial \mathbf{x}} g(\mathbf{x})\mathbf{u} \\ &= L_f V(\mathbf{x}) + L_g V(\mathbf{x})\mathbf{u}, \end{aligned} \tag{4.8}$$

where $L_f V(\mathbf{x})$ and $L_g V(\mathbf{x})$ are the *Lie derivatives* of $\mathbf{x}$ with respect to f and g, in the respective order. Now control Lyapunov functions can be defined. They are closely related to the concept of stabilizability of control-affine systems.

Definition 1 (Stabilizability (SLOTINE; LI, 1990; KHALIL, 2002; AMES et al., 2019))**.** *Let $\gamma\colon \mathbb{R}_{0+} \to \mathbb{R}_{0+}$ be a class κ function, i.e., $\gamma(0) = 0$ and $\gamma(\cdot)$ is monotonically increasing. Then if*

$$\exists \mathbf{u} = k(\mathbf{x}) \quad s.t. \quad \dot{V}(\mathbf{x}, k(\mathbf{x})) \leq -\gamma(V(\mathbf{x})), \tag{4.9}$$

then the system is stabilizable *to $\mathbf{x}_{eq}$.*

Also, if a *sublevel set* of $V(\mathbf{x})$, $\Omega_c \triangleq \{\mathbf{x} \in \mathbb{R}^n : V(\mathbf{x}) \leq c\}$, is bounded, then Ω_c is a region of attraction of $\mathbf{x}_{eq}$.

Definition 2 (control Lyapunov function (AMES et al., 2017, 2019))**.** *If $V(\cdot)$ is positive definite and*

$$\inf_{\mathbf{u} \in U} (L_f V(\mathbf{x}) + L_g V(\mathbf{x})\mathbf{u}) \leq -\gamma(V(\mathbf{x})) \tag{4.10}$$

holds, then $V(\cdot)$ is a control Lyapunov function *(CLF).*

Control Lyapunov functions make it possible to examine all possible stabilizing con-

trollers for any state vector in D. Such set is written as

$$k_{clf}(\mathbf{x}) \triangleq \{\mathbf{u} \in \mathcal{U} : L_f V(\mathbf{x}) + L_g V(\mathbf{x})\mathbf{u} \leq -\gamma(V(\mathbf{x}))\}\,. \tag{4.11}$$

The control problem for CLF can be written as a quadratic programming (QP) problem, which shall be referred to as the CLF-QP problem, given by (AMES et al., 2019)

$$\arg\min_{\mathbf{u}\in\mathcal{U}} \frac{1}{2}(\mathbf{u} - \mathbf{u}_{ref})^{\mathrm{T}}\mathbf{H}(\mathbf{u} - \mathbf{u}_{ref}) + p\delta_s \tag{4.12}$$

$$\text{subject to} \quad L_f V(\mathbf{x}) + L_g V(\mathbf{x})\mathbf{u} + \gamma(V(\mathbf{x})) \leq \delta_s, \tag{4.13}$$

with $\mathbf{H}$ positive definite. Note that the inequality constraints are affine in $\mathbf{u}$; keeping only $L_g V(\mathbf{x})\mathbf{u}$ on the left-hand side of (4.13) turns it into a linear constraint. In order to more easily solve the CLF-QP problem, a relaxation or slack variable δ_s can be introduced, weighted by a positive parameter p. The CLF-QP problem will be extended in Section 4.3, so as to accommodate CBFs.

4.3 Control Barrier Functions Theory

Lyapunov stability restricts states in the region of attraction to some neighborhood of $\mathbf{x}_{eq}$. Usually, this is the intended behavior when the system operates in a safe condition. However, in the case dangerous situations occur, it would be of major importance that the closed-loop system operates in a way that prevents any hazardous or catastrophic situations, returning to the safe condition. That is to say, the system would temporarily forgo its default objective of steering $\mathbf{x}$ to $\mathbf{x}_{eq}$, in favor of avoiding unsafe conditions.

In case such unsafe conditions can be mapped to the frontier of a safe set, control barrier functions can be used to prevent the system from leaving that set. One advantage of the method is that the restrictions from the control barrier functions take precedence over the default behavior near the frontier, but do not affect the system's behavior otherwise. This can be accomplished by set invariance conditions that do not force asymptotic stability to arbitrary points in the state space, rather pushing the states away from the frontier of the specified safe set.

Definition 3 (Safe set (AMES et al., 2017, 2019)). *Let $\mathcal{C}$ satisfy*

$$\mathcal{C} = \{\mathbf{x} \in \mathcal{D} \subset \mathbb{R}^n : h((x)) \geq 0\} \tag{4.14}$$

$$\mathrm{fr}(\mathcal{C}) = \{\mathbf{x} \in \mathcal{D} \subset \mathbb{R}^n : h(\mathbf{x}) = 0\} \tag{4.15}$$

$$\mathrm{Int}(\mathcal{C}) = \{\mathbf{x} \in \mathcal{D} \subset \mathbb{R}^n : h(\mathbf{x}) > 0\}. \tag{4.16}$$

Then $\mathcal{C}$ *is the* safe set.

In other words, $\mathcal{C}$ is the superlevel set of $h(\mathbf{x})$, composed of its interior $\text{Int}(\mathcal{C})$ and frontier $\text{fr}(\mathcal{C})$. If $\mathcal{C}$ is safe for (4.5), with $u = k(\mathbf{x})$, then (4.5) is *safe with respect to* $\mathcal{C}$.

The control barrier functions are defined as:

Definition 4 (Control barrier function (AMES et al., 2017; XU et al., 2015; AMES et al., 2019))**.** *Let*

$$\mathcal{C} = \{\mathbf{x} \in \mathcal{D} \subset \mathbb{R}^n : h((x)) \geq 0\},$$

with $h \colon \mathcal{D} \to \mathbb{R}$*. If*

$$\exists \alpha(\mathbf{x}) \mid \sup_{\mathbf{u} \in \mathcal{U}} \left(L_f h(\mathbf{x}) + L_g h(\mathbf{x})\mathbf{u}\right) \geq -\zeta(h(\mathbf{x})) \tag{4.17}$$

holds, with $\zeta(\cdot)$ *an extended class* κ_∞ *function,* $\forall \mathbf{x} \in \mathcal{D}$*,* $h(\mathbf{x})$ *is a* control barrier function*.*

In Definition 4, an extended class κ_∞ function satisfies $\zeta \colon \mathbb{R} \to \mathbb{R}$, $\zeta(0) = 0$, $\mathrm{d}\zeta/\mathrm{d}x > 0$, $x \in \mathbb{R}^3$.

Analogously to (4.11), the set of all possible safe control values can be obtained from a CBF,

$$k_{cbf}(\mathbf{x}) \triangleq \{\mathbf{u} \in \mathcal{U} : L_f h(\mathbf{x}) + L_g h(\mathbf{x})\mathbf{u} + \zeta(h(\mathbf{x})) \geq 0\} \tag{4.18}$$

i.e., all input values that make $\mathcal{C}$ safe for (4.5).

As with CLF, the CBF control problem can also be written as a quadratic programming problem. This shall be referred to as the CBF-QP problem, expressed as (AMES et al., 2017, 2019)

$$\mathbf{u} = \arg\min_{\mathbf{u} \in \mathcal{U}} \frac{1}{2}\|\mathbf{u} - \mathbf{u}_{ref}\|^2 \tag{4.19}$$

$$\text{subject to} \quad L_f h(\mathbf{x}) + L_g h(\mathbf{x})\mathbf{u} \geq -\zeta(h(\mathbf{x})). \tag{4.20}$$

The CBF-QP problem has a closed-form solution, due to having a single inequality constraint (AMES et al., 2014; BOYD; VANDENBERGHE, 2004; AMES et al., 2019).

Moreover, the asymptotic stability and the safety constraints can be combined, with the objective of assembling a single quadratic problem, extending (4.12) and (4.13) with (4.20), as (AMES et al., 2017, 2019)

$$\arg\min_{\substack{\mathbf{u} \in \mathcal{U} \\ \delta \in \mathbb{R}}} \frac{1}{2}(\mathbf{u} - \mathbf{u}_{ref})^{\mathrm{T}}\mathbf{H}(\mathbf{u} - \mathbf{u}_{ref}) + p\delta_s \tag{4.21}$$

[3]That is to say, a class κ function with $(-\infty, \infty)$ as domain.

$$\begin{aligned} \text{subject to} \quad & L_f V(\mathbf{x}) + L_g V(\mathbf{x})\mathbf{u} + \zeta(V(\mathbf{x})) \leq \delta_s \\ & L_f h(\mathbf{x}) + L_g h(\mathbf{x})\mathbf{u} + \zeta(h(\mathbf{x})) \geq 0, \end{aligned}$$

called the CLF-CBF-QP problem. Hence, the stability and safety problems can be combined in a single QP problem with affine constraints on $\mathbf{u}$.

We remark that in case $\gamma(V(\mathbf{x})) = \gamma V(\mathbf{x})$ and $\zeta(h(\mathbf{x})) = \zeta h(\mathbf{x})$, $\gamma, \zeta \in \mathbb{R}^+$, the equilibrium point $\mathbf{x}_{eq}$ and the safe set $\mathcal{C}$ are exponentially stable. Finally, this result, and the relative degree of 1 restriction on h, implied by (4.17), are extended to higher relative degree reciprocal barrier functions in (AMES et al., 2017), and zeroing CBFs in (AMES et al., 2019).

4.3.1 Exponential control barrier functions

The CBF-QP and CLF-CBF-QP problems presented so far can have exponential stability, provided that $\gamma(V(\mathbf{x})) = \gamma V(\mathbf{x})$ and $\alpha(h(\mathbf{x})) = \alpha h(\mathbf{x})$, for positive real γ and α. However, the relative degree of h remains restricted to 1. This can be extended to arbitrarily high relative degree barrier functions while guaranteeing exponential stability.

The procedure is analogous to input-output linearization, but instead of taking the derivatives over the output variable, they are taken over the barrier function. More specifically, we have the rth time derivative of $h(\mathbf{x})$ given by (AMES et al., 2019)

$$h^{(r)}(\mathbf{x}) = L_f^r h(\mathbf{x}) + L_g L_f^{r-1} h(\mathbf{x})\mathbf{u}. \tag{4.22}$$

If the relative degree of $h(\mathbf{x})$ is r, then $L_g L_f^{r-1} h(\mathbf{x}) \neq 0$. Now, defining a linearized state vector

$$\eta_b(\mathbf{x}) \triangleq \begin{bmatrix} h(\mathbf{x}) \\ \dot{h}(\mathbf{x}) \\ L_f^2 h(\mathbf{x}) \\ \vdots \\ L_f^{(r-1)} h(\mathbf{x}) \end{bmatrix} = \begin{bmatrix} h(\mathbf{x}) \\ L_f h(\mathbf{x}) \\ \ddot{h}(\mathbf{x}) \\ \vdots \\ h^{(r-1)}(\mathbf{x}) \end{bmatrix} \tag{4.23}$$

we can write the linearized system (AMES et al., 2019)

$$\dot{\eta}_b(\mathbf{x}) = \bar{\mathbf{F}}\eta_b(\mathbf{x}) + \bar{\mathbf{G}}\mu_i \tag{4.24}$$

$$h(\mathbf{x}) = \bar{\mathbf{C}}\eta_b(\mathbf{x}), \tag{4.25}$$

with

$$\bar{\mathbf{F}} = \begin{bmatrix} \mathbf{0}_{(r-1)\times 1} & \mathbf{I}_{r-1} \\ 0 & \mathbf{0}_{1\times(r-1)} \end{bmatrix} \qquad \bar{\mathbf{G}} = \begin{bmatrix} \mathbf{0}_{(r-1)\times 1} \\ 1 \end{bmatrix}$$
$$\bar{\mathbf{C}} = \begin{bmatrix} 1 & \mathbf{0}_{1\times(r-1)} \end{bmatrix} \qquad \mu_i = h^{(r)}(\mathbf{x}).$$

Then, general exponential control barrier functions can be defined as

Definition 5 (Exponential control barrier functions (AMES et al., 2019)). *Let $\mathcal{C} \in \mathcal{D} \subset \mathbb{R}^n$ be a superlevel set of a r-times differentiable function $h\colon \mathcal{D} \to \mathbb{R}$. Then $h(\mathbf{x})$ is an* exponential control barrier function *(ECBF) if there exists $\mathbf{K}_\zeta$, $\Re\{\sigma(\bar{\mathbf{F}} - \bar{\mathbf{G}}\mathbf{K}_\zeta)\} < 0$, such that for $\dot{\mathbf{x}} = f(\mathbf{x}) + g(\mathbf{x})\mathbf{u}$,*

$$\sup_{\mathbf{u}\in\mathcal{U}} \left(L_f^r h(\mathbf{x}) + L_g L_f^{r-1} h(\mathbf{x})\mathbf{u} \right) \geq \mathbf{K}_\zeta \eta_b(\mathbf{x}), \tag{4.26}$$

any $\mathbf{x} \in \operatorname{Int} \mathcal{C}$ results in $h(\mathbf{x}(t)) \geq \bar{\mathbf{C}} e^{(\bar{\mathbf{F}} - \bar{\mathbf{G}}\mathbf{K}_\zeta)t} \eta_b(\mathbf{x}) \geq 0$ if $h(\mathbf{x}(0)) \geq 0$.

Then the ECBF can be incorporated into the CLF-QP problem, resulting in the CLF-ECBF-QP problem, given by (AMES et al., 2019)

$$\arg\min_{\substack{\mathbf{u}\in\mathcal{U} \\ \delta\in\mathbb{R} \\ \mu_i\in\mathbb{R}}} \frac{1}{2}(\mathbf{u} - \mathbf{u}_{ref})^{\mathrm{T}} \mathbf{H} (\mathbf{u} - \mathbf{u}_{ref}) + p\delta_s \tag{4.27}$$

subject to

$$\begin{aligned} L_f V(\mathbf{x}) + L_g V(\mathbf{x})\mathbf{u} + \gamma(V(\mathbf{x})) &\leq \delta_s \\ L_f^r h(\mathbf{x}) + L_g L_f^{r-1} h(\mathbf{x})\mathbf{u} &= \mu_i \\ \mu_i + \mathbf{K}_\zeta \eta_b(\mathbf{x}) &\geq 0. \end{aligned}$$

The CLF-ECBF-QP allows us to consider a barrier function of any relative degree so as to synthesize a safety control system with stability constraints in the interior of the safe set while guaranteeing the invariance of the whole set.

4.4 Last remarks

There are very important characteristics of safety-critical control based on CBF. Namely, the liveness property of a large portion of the invariant set, its suitability to safety systems in the form of preventing emergency situations, and its applicability to multivariate nonlinear systems.

Liveness means the control barrier function restriction is not present for states in the safe set but not at a neighborhood of its boundary so that the closed-loop system behaves as designed by the usual or default controller. This default controller takes the reference input, often related to the operating point, and the stability condition. Safety means that the safe restrictions always take precedence over the stability or tracking conditions, guaranteeing the invariance of the safe set.

Finally, the existence of closed-form solutions allows us to synthesize CBF controllers without using quadratic programming algorithms online. Thus, more processing power can be made available to the safe set controller.

5 LATERAL STABILITY REGIONS

We are concerned with the main problem of electronic stability control when applied to automobiles or passenger cars, which is lateral stability. In this regard, we mention the shortcomings of the state-of-the-art in order to contextualize the contributions of this study. These are related to lateral stability region generation, design and implementation of active front steering ESC with CBF-based safety-critical control, and design and implementation of differential-braking ESC with CBF-based safety-critical control.

A stability region of a (nonlinear) system is a region around either a stable equilibrium point or limit cycle that is positively invariant (CHIANG; HIRSCH; WU, 1988). In other words, we know the state variables shall not leave that region. For the lateral model of a vehicle, this means that its yaw rate and lateral speed (or side-slip angle) will remain bounded and in a set that contains the desired yaw rate that results from the steering angle. As a consequence, we shall not be interested in invariant sets around equilibrium points that result from exaggerated steering angles, with yaw rate or lateral speed values that are incompatible with public roads, passenger cars, and road traffic legislation. In addition to it, we shall also assume there is only one stability region for each steering angle value since we are only interested in the equilibrium point around the desired state.

Lateral stability regions are important in the analysis and design of ESC systems because their operation principle is either keeping the vehicle in a stable region or bringing its state back to that region. Lateral stability regions are presented in (HUANG; LIANG; CHEN, 2017; SAVA; COPAE, 2021; HUANG; CHEN, 2017; ZHANG et al., 2020), based on the linearized system characteristic equation, and in (CHEN et al., 2016; INAGAKI; KUSHIRO; YAMAMOTO, 1994; ZHANG et al., 2011; HUANG; LIANG; CHEN, 2017; LIU; CHEN; LI, 2016; SUN et al., 2013), from the phase portrait obtained a simplified nonlinear model.

Let us consider the latter method, i.e., lateral regions from the characteristic equation. Now when one analyses the resulting regions from (HUANG; LIANG; CHEN, 2017) and (ZHANG et al., 2020), their shapes are different from one another, even if the generation

criteria are the same. Hence, we have further investigated the subject. The results are presented in Chapter 5.

After working out the lateral stability region problem, we investigated an existing active front steering ESC based on safety-critical control (HUANG; YONG; CHEN, 2019). After reproducing the results from the article, we realized it had important shortcomings. Those are identified and addressed in Chapter 6.

By the time we started this study, there were no implementations of YSC using safety-critical control. Our proposals on the subject are discussed in Chapter 7.

5.1 Lateral Stability Regions Review

There are discrepancies in lateral regions from different sources in the literature (HUANG; LIANG; CHEN, 2017; SAVA; COPAE, 2021; HUANG; CHEN, 2017; ZHANG et al., 2020). We would expect some differences due to different vehicle parameters, such as mass, track width, or center of mass distance from the axles, even when the same criterion is used to obtain the regions. We would expect, however, similar regions, but of different dimensions. Nevertheless, the shapes are often different, e.g., Figure 24.

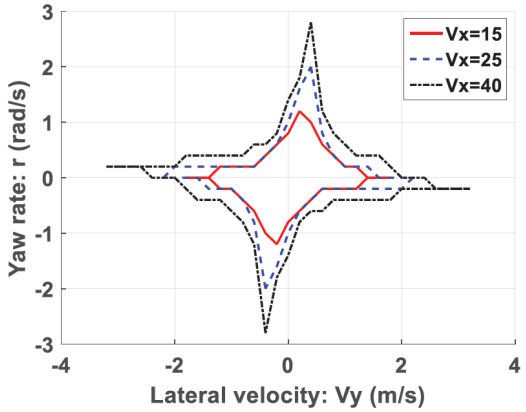

SOURCE: (HUANG; LIANG; CHEN, 2017).

(a)

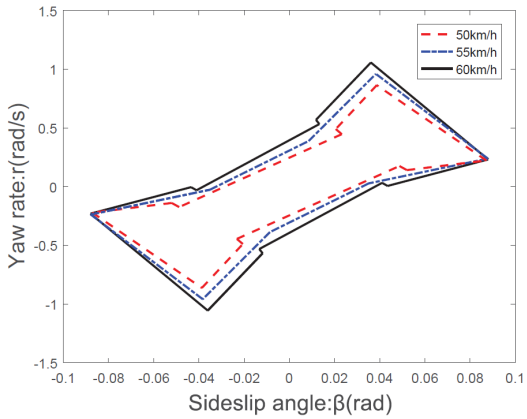

SOURCE: (ZHANG et al., 2020).

(b)

Figure 24: Lateral stability regions as a function of the longitudinal speed from different sources.

Figure 24a shows lateral stability regions for three different longitudinal speed values. The regions are different from one another not only in size but in shape. At first glance, one is unsure whether this is a result of low resolution, simplifications, or the actual result of the underlying stability equations. Two inequalities have been used: one

which results from the characteristic equation and yields two stability boundaries, and one controllability equation, which generates two controllability boundaries.

Figure 24b also presents lateral regions for different longitudinal speeds. The controllability inequality is the same. It also arises from the linearized system. The model used in (ZHANG et al., 2020) has the vehicle slip angle β instead of the lateral speed v_{gy}, but we have seen both models are equivalent in Section 2.3.2. Hence they have the same characteristic equation. The same controllability inequality is used, and while it is not mentioned that only positive values of front lateral stiffness are used, the images indicate so, else the regions would be unbounded.

It is clear that the regions in Figures 24a and 24b are different in shape. Figure 24b depicts details that appear and disappear as the longitudinal speed increases. Consequently, it is difficult to use them as ESC design tools. That aside, both sources make a mistake when obtaining an unnecessary alternate inequality when applying the Routh–Hurwitz stability criterion. The contribution presented in this section is based on these problems.

More specifically, our first contribution was the obtention of lateral stability regions based on the characteristic equation of a linearized system based on as few simplifications as possible. We also use the coefficients of the equation directly, instead of trying to solve the inequalities for one of their parameters. Moreover, we present a method that allows for arbitrarily high-quality images, and we generate those for more parameters than previous studies, and for a wider range of those previously published, e.g., in (HUANG; LIANG; CHEN, 2017; SAVA; COPAE, 2021; HUANG; CHEN, 2017; ZHANG et al., 2020).

This step was not planned when this study was being designed, but it proved necessary in order to obtain stability regions that would be useful for electronic stability control system design with safety-critical control, as we had planned to use such regions as safe sets. See Sections 6.2 and 6.3.

The system model for lateral stability analysis is presented in Section 5.1.1. The region generation algorithm and the regions themselves are shown in Section 5.1.2.

5.1.1 System model for stability analisys

Linear models have already been presented in Section 2.3.2 in the form of (2.97)–(2.98) and (2.102)–(2.103), with the front steering angle as the input; and (2.124), with an external moment as an additional input signal. These models describe the vehicle behavior when

subject to small slip angles. It is implicit, with respect to (2.29) or (2.61), that by "small slip angles" we mean values that cause a lateral force

$$F_y \approx C_{F\alpha}\alpha.$$

Under these circumstances, the vehicle will be stable and will have a steady-state value of $\dot{\psi}$, v_{gy}, and β, which depends on the steering angle δ.

Vehicle instability results from exaggerated wheel slip angles with respect to the tire-road friction coefficient, which causesoversteers, understeers, side slips, or loss of steering angle responsiveness. Consequently, the aforementioned models are invalid for these LOC or near-LOC situations. One possible solution is elementary: we linearize the system around the current operating condition, i.e., the current state, instead of around the equilibrium point. This means the linearization considers the current wheel slip angles, instead of null ones.

A nonlinear system

$$\dot{\mathbf{x}}_o = f(\mathbf{x}_o, u) = \begin{bmatrix} f_1(\mathbf{x}_o, u) \\ f_2(\mathbf{x}_o, u) \end{bmatrix}. \tag{5.1}$$

is linearized around the current state $\mathbf{x}_o = [v_{gy}(t) \;\; \dot{\psi}(t)]^{\mathrm{T}}$ by

$$\dot{\mathbf{x}} \approx \mathbf{A}\mathbf{x} + \mathbf{B}u, \tag{5.2}$$

where we choose the change in $\mathbf{x}_o$, i.e., $\mathbf{x} = [\Delta v_{gy} \;\; \Delta\dot{\psi}]^{\mathrm{T}}$ as the state vector and the steering angle as the input signal, i.e., $u = \delta = \delta_l = \delta_r$, with

$$\mathbf{A} \triangleq \frac{\partial f}{\partial \mathbf{x}_o} = \begin{bmatrix} \frac{\partial f}{\partial v_{gy}} & \frac{\partial f}{\partial \dot{\psi}} \end{bmatrix}, \qquad \mathbf{B} \triangleq \frac{\partial f}{\partial u}, \tag{5.3}$$

as explained in (KHALIL, 2002) and done in (HUANG; LIANG; CHEN, 2017; SAVA; COPAE, 2021; HUANG; CHEN, 2017). Let us consider the vehicle depicted in Figure 19 (Section 2.3.2), described by (2.116)–(2.118). If we restrict the study to the lateral model, (2.116) can be ignored, and there remain (2.117) and (2.118), which can be rewritten as

$$\dot{v}_{gy} = -v_{gx}\dot{\psi} + \frac{F_{y_{rr}}}{m_b} + \frac{F_{y_{rl}}}{m_b} + \frac{\cos(\delta_r)}{m_b}F_{y_{fr}} + \frac{\cos(\delta_l)}{m_b}F_{y_{fl}}, \tag{5.4a}$$

$$\ddot{\psi} = -\frac{l_2}{I_z}(F_{y_{rr}} + F_{y_{rl}}) + \left(\frac{l_1}{I_z}\cos(\delta_l) + \frac{l_w}{I_z}\sin(\delta_l)\right)F_{y_{fl}} + \left(\frac{l_1}{I_z}\cos(\delta_r) - \frac{l_w}{I_z}\sin(\delta_r)\right)F_{y_{fr}}, \tag{5.4b}$$

In (HUANG; LIANG; CHEN, 2017; HUANG; CHEN, 2017), a 2D LuGre tire model

was used to obtain the lateral forces F_{y_i}. In (ZHANG et al., 2020), a Fiala model was used, instead. Here, we employ a pure side-slip magic formula model, given by (2.61)–(2.73) (see Section 2.2.2), from (PACEJKA, 2012). As a consequence, the longitudinal forces (F_{y_i}) are ignored, i.e., assumed to be zero, so the longitudinal speed is assumed to be constant.

To obtain the linearized system (5.3) we must obtain the derivatives of the right-hand side of (5.4) with respect to v_{gy} and $\dot{\psi}$. Nonetheless, most of those terms are not explicit functions of either state variable. We can rewrite (5.1) as

$$\begin{aligned} f(\mathbf{x}_o, u) &= f_e(\mathbf{x}_o, u) + f_{ne}(\mathbf{x}_o, u) \\ &= \begin{bmatrix} -v_{gx}\dot{\psi} \\ 0 \end{bmatrix} + \begin{bmatrix} f_{ne1}(\mathbf{x}_o, u) \\ f_2(\mathbf{x}_o, u) \end{bmatrix} \end{aligned} \tag{5.5}$$

where $f_e(\mathbf{x}_o, u)$ is explicit on $\mathbf{x}$ and $f_{ne}(\mathbf{x}_o, u)$ is not. Hence $\mathbf{A}$ must be obtained by chain rule as

$$\mathbf{A} = \begin{bmatrix} 0 & -v_{gx} \\ 0 & 0 \end{bmatrix} + \frac{\partial f_{ne}}{\partial F_y}\frac{\partial F_y}{\partial \mathbf{x}_o}. \tag{5.6}$$

The second term from the right-hand side of (5.6) can be obtained from

$$\begin{aligned} \frac{\partial f_{ne}}{\partial F_y} &\triangleq \begin{bmatrix} \frac{\partial f_{ne}}{\partial F_{y_{fl}}} & \frac{\partial f_{ne}}{\partial F_{y_{fr}}} & \frac{\partial f_{ne}}{\partial F_{y_{rl}}} & \frac{\partial f_{ne}}{\partial F_{y_{rr}}} \end{bmatrix} \\ &= \begin{bmatrix} \frac{\partial f_{ne1}}{\partial F_{y_{fl}}} & \frac{\partial f_{ne1}}{\partial F_{y_{fr}}} & \frac{\partial f_{ne1}}{\partial F_{y_{rl}}} & \frac{\partial f_{ne1}}{\partial F_{y_{rr}}} \\ \frac{\partial f_2}{\partial F_{y_{fl}}} & \frac{\partial f_2}{\partial F_{y_{fr}}} & \frac{\partial f_2}{\partial F_{y_{rl}}} & \frac{\partial f_2}{\partial F_{y_{rr}}} \end{bmatrix} \end{aligned} \tag{5.7}$$

and

$$\frac{\partial F_y}{\partial \mathbf{x}_o} \triangleq \begin{bmatrix} \frac{\partial F_y}{\partial v_{gy}} & \frac{\partial F_y}{\partial \dot{\psi}} \end{bmatrix} = \begin{bmatrix} \frac{\partial F_{y_{fl}}}{\partial v_{gy}} & \frac{\partial F_{y_{fl}}}{\partial \dot{\psi}} \\ \frac{\partial F_{y_{fr}}}{\partial v_{gy}} & \frac{\partial F_{y_{fr}}}{\partial \dot{\psi}} \\ \frac{\partial F_{y_{rl}}}{\partial v_{gy}} & \frac{\partial F_{y_{rl}}}{\partial \dot{\psi}} \\ \frac{\partial F_{y_{rr}}}{\partial v_{gy}} & \frac{\partial F_{y_{rr}}}{\partial \dot{\psi}} \end{bmatrix}. \tag{5.8}$$

The derivatives of the tire forces are given by

$$\frac{\partial F_{y_i}}{\partial v_{gy}} = \frac{\partial F_{y_i}}{\partial \alpha_i}\frac{\partial \alpha_i}{\partial v_{gy}}, \tag{5.9}$$

$$\frac{\partial F_{y_i}}{\partial \dot{\psi}} = \frac{\partial F_{y_i}}{\partial \alpha_i}\frac{\partial \alpha_i}{\partial \dot{\psi}}, \tag{5.10}$$

where $C_{\bar{\alpha}\,i} \triangleq \frac{\partial F_{y_i}}{\partial \alpha_i}$ are the local cornering stiffness.

The derivatives of f_{ne} with respect to the lateral tire forces are given by

$$\frac{\partial f_{ne}}{\partial F_y} = \begin{bmatrix} \frac{\cos(\delta)}{m_b} & \frac{\cos(\delta)}{m_b} & \frac{1}{m_b} & \frac{1}{m_b} \\ \frac{l_1\cos(\delta)+l_{w1}\sin(\delta)}{I_z} & \frac{l_1\cos(\delta)-l_{w1}\sin(\delta)}{I_z} & -\frac{l_2}{I_z} & -\frac{l_2}{I_z} \end{bmatrix}. \tag{5.11}$$

The tire slip angle derivatives with respect to v_{gy} and $\dot{\psi}$, which are necessary for (5.9) and (5.10), are obtained as

$$\frac{\partial \alpha_{fl}}{\partial v_{gy}} = -\frac{1}{(v_{gx} - l_{w1}\dot{\psi})\left[\left(\frac{v_{gy}+l_1\dot{\psi}}{v_{gx}-l_{w1}\dot{\psi}}\right)^2 + 1\right]}, \tag{5.12}$$

$$\frac{\partial \alpha_{fr}}{\partial v_{gy}} = -\frac{1}{(v_{gx} + l_{w1}\dot{\psi})\left[\left(\frac{v_{gy}+l_1\dot{\psi}}{v_{gx}+l_{w1}\dot{\psi}}\right)^2 + 1\right]}, \tag{5.13}$$

$$\frac{\partial \alpha_{rl}}{\partial v_{gy}} = -\frac{1}{(v_{gx} - l_{w2}\dot{\psi})\left[\left(\frac{v_{gy}-l_2\dot{\psi}}{v_{gx}-l_{w2}\dot{\psi}}\right)^2 + 1\right]}, \tag{5.14}$$

$$\frac{\partial \alpha_{rr}}{\partial v_{gy}} = -\frac{1}{(v_{gx} + l_{w2}\dot{\psi})\left[\left(\frac{v_{gy}+l_2\dot{\psi}}{v_{gx}+l_{w2}\dot{\psi}}\right)^2 + 1\right]}, \tag{5.15}$$

$$\frac{\partial \alpha_{fl}}{\partial \dot{\psi}} = -\frac{\frac{l_1}{v_{gx}-l_{w1}\dot{\psi}} + \frac{l_{w1}(v_{gy}+l_1\dot{\psi})}{(v_{gx}-l_{w1}\dot{\psi})^2}}{\left(\frac{v_{gy}+l_1\dot{\psi}}{v_{gx}-l_{w1}\dot{\psi}}\right)^2 + 1}, \tag{5.16}$$

$$\frac{\partial \alpha_{fr}}{\partial \dot{\psi}} = -\frac{\frac{l_1}{v_{gx}+l_{w1}\dot{\psi}} - \frac{l_{w1}(v_{gy}+l_1\dot{\psi})}{(v_{gx}+l_{w1}\dot{\psi})^2}}{\left(\frac{v_{gy}+l_1\dot{\psi}}{v_{gx}+l_{w1}\dot{\psi}}\right)^2 + 1}, \tag{5.17}$$

$$\frac{\partial \alpha_{rl}}{\partial \dot{\psi}} = \frac{\frac{l_2}{v_{gx}-l_{w2}\dot{\psi}} - \frac{l_{w2}(v_{gy}-l_2\dot{\psi})}{(v_{gx}-l_{w2}\dot{\psi})^2}}{\left(\frac{v_{gy}-l_2\dot{\psi}}{v_{gx}-l_{w2}\dot{\psi}}\right)^2 + 1}, \tag{5.18}$$

$$\frac{\partial \alpha_{rr}}{\partial \dot{\psi}} = \frac{\frac{l_2}{v_{gx}+l_{w2}\dot{\psi}} + \frac{l_{w2}(v_{gy}-l_2\dot{\psi})}{(v_{gx}+l_{w2}\dot{\psi})^2}}{\left(\frac{v_{gy}-l_2\dot{\psi}}{v_{gx}+l_{w2}\dot{\psi}}\right)^2 + 1}, \tag{5.19}$$

where $L_{w1} = 2l_{w1}$ is the front track width and $L_{w2} = 2l_{w2}$ is the rear track width.

The local cornering stiffnesses $C_{\bar{\alpha}\,i}$ in (5.9) and (5.10) are the derivatives of (2.61) with respect to α_i,

$$C_{\bar{\alpha}\,i} = \frac{C_y D_y \cos\left[C_y \arctan(\bar{\phi})\right]\left[B_y - E_y\left(B_y - \frac{B_y}{B_y^2\alpha^2+1}\right)\right]}{\bar{\phi}^2 + 1}, \tag{5.20}$$

with

$$\bar{\phi} = B_y\alpha + E_y(\arctan(B_y\alpha) - B_y\alpha), \tag{5.21}$$

are evaluated for nominal tire inflating pressure, null camber angle, and the normal tire force from the steady-state operation, and where B_y, C_y, D_y, and E_y are obtained from (2.64)–(2.73) (Section 2.2.2).

It is now convenient to mention that many of those expressions are often simplified, both for steady-state and current-state linearized models. For instance, let us consider the state vector derivatives, given by (5.4). It is common to consider that the vehicle is at a sufficiently high speed so that the feasible steering angles are small, i.e., $\sin(\delta) \approx \delta$. Alternatively, it is also customary to admit that the front and rear trackwidths are small. The resulting state descriptions would read as

$$\dot{v}_{gy} = \frac{1}{m_b}\left(-m_b v_{gx}\dot{\psi} + F_{y_{rr}} + F_{y_{rl}} + F_{y_{fr}} + F_{y_{fl}}\right) \tag{5.22a}$$

$$\ddot{\psi} = \frac{1}{I_z}(l_1 F_{y_{fl}} + l_1 F_{y_{fr}} - l_2 F_{y_{rl}} - l_2 F_{y_{rt}}) \tag{5.22b}$$

Moreover, the tire slip angle derivatives are also simplified. Let us admit the side-slip angle is small ($\beta \approx 0$), or, equivalently, $|v_{gx}| \gg |v_{gy}|$. Then (5.12)–(5.19) are rewritten as

$$\frac{\partial \alpha_{fl}}{\partial v_{gy}} = -\frac{1}{v_{gx} - l_{w1}\dot{\psi}}, \tag{5.23}$$

$$\frac{\partial \alpha_{fr}}{\partial v_{gy}} = -\frac{1}{v_{gx} + l_{w1}\dot{\psi}}, \tag{5.24}$$

$$\frac{\partial \alpha_{rl}}{\partial v_{gy}} = -\frac{1}{v_{gx} - l_{w2}\dot{\psi}}, \tag{5.25}$$

$$\frac{\partial \alpha_{rr}}{\partial v_{gy}} = -\frac{1}{v_{gx} + l_{w2}\dot{\psi}}, \tag{5.26}$$

$$\frac{\partial \alpha_{fl}}{\partial \dot{\psi}} = -\frac{l_1}{v_{gx} - l_{w1}\dot{\psi}}, \tag{5.27}$$

$$\frac{\partial \alpha_{fr}}{\partial \dot{\psi}} = -\frac{l_1}{v_{gx} + l_{w1}\dot{\psi}}, \tag{5.28}$$

$$\frac{\partial \alpha_{rl}}{\partial \dot{\psi}} = \frac{l_2}{v_{gx} - l_{w2}\dot{\psi}}, \tag{5.29}$$

$$\frac{\partial \alpha_{rr}}{\partial \dot{\psi}} = \frac{l_2}{v_{gx} + l_{w2}\dot{\psi}}. \tag{5.30}$$

Furthermore, if we assume that either the yaw rate is numerically small compared to the longitudinal speed or the front and read trackwidths are small (i.e., the bicycle model assumption $l_{w1}, l_{w2} \approx 0$), (5.23)–(5.30) are reduced to

$$\frac{\partial \alpha_{fl}}{\partial v_{gy}} = -\frac{1}{v_{gx}}, \tag{5.31}$$

$$\frac{\partial \alpha_{fr}}{\partial v_{gy}} = -\frac{1}{v_{gx}}, \tag{5.32}$$

$$\frac{\partial \alpha_{rl}}{\partial v_{gy}} = -\frac{1}{v_{gx}}, \tag{5.33}$$

$$\frac{\partial \alpha_{rr}}{\partial v_{gy}} = -\frac{1}{v_{gx}}, \tag{5.34}$$

$$\frac{\partial \alpha_{fl}}{\partial \dot{\psi}} = -\frac{l_1}{v_{gx}}, \tag{5.35}$$

$$\frac{\partial \alpha_{fr}}{\partial \dot{\psi}} = -\frac{l_1}{v_{gx}}, \tag{5.36}$$

$$\frac{\partial \alpha_{rl}}{\partial \dot{\psi}} = \frac{l_2}{v_{gx}}, \tag{5.37}$$

$$\frac{\partial \alpha_{rr}}{\partial \dot{\psi}} = \frac{l_2}{v_{gx}}. \tag{5.38}$$

For instance, in case one assumes all those simplifications, one obtains

$$\dot{\mathbf{x}} = \mathbf{A}\mathbf{x} + \mathbf{B}u \tag{5.39}$$

with

$$\mathbf{A} = \begin{bmatrix} -\frac{C_{\bar{\alpha}_f} + C_{\bar{\alpha}_r}}{m_b v_{gx}} & -\frac{C_{\bar{\alpha}_f} l_1 - C_{\bar{\alpha}_r} l_2}{m_b v_{gx}} - v_{gx} \\ -\frac{C_{\bar{\alpha}_f} l_1 - C_{\bar{\alpha}_r} l_2}{I_z v_{gx}} & -\frac{C_{\bar{\alpha}_f} l_1^2 + C_{\bar{\alpha}_r} l_2^2}{I_z v_{gx}} \end{bmatrix} \qquad \mathbf{B} = \begin{bmatrix} \frac{C_{\bar{\alpha}_f}}{m_b} \\ \frac{C_{\bar{\alpha}_f} l_1}{I_z} \end{bmatrix} \tag{5.40}$$

where $C_{\bar{\alpha}_f} \triangleq C_{\bar{\alpha}\, fl} + C_{\bar{\alpha}\, fr}$ and $C_{\bar{\alpha}_r} \triangleq C_{\bar{\alpha}\, rl} + C_{\bar{\alpha}\, rr}$ are the local front and rear axles cornering stiffnesses. It can be observed that (5.39) is very similar to (2.97), where the local cornering stiffnesses are substituted for the cornering stiffnesses. Hence that model assumes all the aforementioned substitutions have been considered. These models have been used in (HUANG; LIANG; CHEN, 2017; SAVA; COPAE, 2021; HUANG; CHEN, 2017; ZHANG et al., 2020). In this study, instead, *none* of the aforementioned simplifications have been considered. As a result, the terms of the dynamic matrix $\mathbf{A}$ are too lengthy to be expressed here.

5.1.2 Stability region generation

The method of obtaining the linearized system dynamic matrix was described in Section 5.1.1. First, all local cornering stiffnesses are obtained from the current state and (5.20). After that, the derivatives of the tire forces are calculated by substituting the local cornering stiffnesses and (5.12)–(5.19) in (5.9) and (5.10), and then these in (5.8). Finally, $\mathbf{A}$ is evaluated by substituting (5.11) and (5.8) in (5.6).

The characteristic polynomial $p(\mathbf{A})$ is given by

$$p(\mathbf{A}) = |\lambda\mathbf{I} - \mathbf{A}| = \lambda^2 + a_1\lambda + a_2. \tag{5.41}$$

The system is stable, according to the Routh–Hurwitz stability criterion, if $a_1, a_2 > 0$. This condition can be made simpler, as a_1 is always positive for practical vehicle parameters, e.g., vehicle mass is positive and the vehicle's center of mass lies between both axles, or $l_1, l_2 > 0$. Hence we can consider only $a_2 > 0$ as the stability criterion.

In (HUANG; LIANG; CHEN, 2017; ZHANG et al., 2020), the simplifications presented in Section 5.1.1 have all been considered, and the stability criterion has been rewritten with respect to the vehicle's local lateral stiffness ($C_{\bar{\alpha}f} + C_{\bar{\alpha}r}$). However, since the condition is an inequality, proper algebra must be carried out, but this was not the case in said studies. As this was an unnecessary step, and since we have not used such simplifications, we have simply used the stability condition as-is, as it is simple enough to obtain the independent term a_2 of the characteristic equation out of a 2×2 matrix whose numerical values are known.

Therefore, at any instant, we assume $v_{gx}(t)$, $v_{gy}(t)$, and $\dot{\psi}(t)$ are known. Hence we can obtain the wheel slip angles from (2.112)–(2.115), and then, from those, the local lateral stiffness of each tire. Hence $\mathbf{A}$ is known, and the stability at $v_{gx}(t)$, $v_{gy}(t)$ can be assessed.

It is, however, not enough that the vehicle is stable in its trajectory. Since we assume a driver is operating it, said vehicle must be subject to hiscommands and must behave accordingly. A wheel can influence the trajectory of the vehicle if its local cornering stiffness is nonzero. Even so, at high slip angles, the influence is opposite of what the driver would expect, i.e., the lateral force absolute value decreases as the magnitude of the slip angle increases. Consequently, we shall assume a wheel is controllable when $C_{\bar{\alpha},i} > 0$, $i = \{fl, fr, rl, rr\}$.

A less conservative controllability condition would be restricted to the steerable axle. As a consequence, for a vehicle with front steering, the controllability condition would be $C_{\bar{\alpha}f} > 0$. We have considered more conservative conditions, which are to have every wheel contributing to the lateral force on the vehicle, i.e., $C_{\bar{\alpha},i} > 0$, as previously stated. This assumes the vehicle is not considered to be controllable when oversteering, which, when applied to control applications (see Section 6.2), means we wish to avoid such situations. This makes sense since drifting maneuvers are illegal on public roads in almost every country, but might be relaxed for race or off-road applications, which are beyond the scope of this text.

As a consequence, a stability region generation procedure is proposed.

Procedure 1 (Lateral stability region generation).

1. Generate four lattices on the $v_{gy} \times \dot{\psi}$ plane, one for the stability condition, one for the front axle controllability, one for the rear axle controllability, and one for the effective stability
2. For each point on the lattice, verify
   (a) the stability condition $a_2 > 0$,
   (b) the front wheels controllability conditions $C_{\bar{\alpha},i} > 0$, $i = \{fl, fr\}$
   (c) the rear wheels controllability conditions $C_{\bar{\alpha},i} > 0$, $i = \{rl, rr\}$
3. in case the previous conditions are satisfied, the lattice point is part of the effective stability region.

The lattices can be stored in logical or Boolean matrices to save memory.

We consider a vehicle with the parameters listed in Table 1 in this section. The tire and wheel parameters have the default values from MATLAB Vehicle Dynamics Blockset (VDB) (MATHWORKS, 2020), listed in Table 2. In this regard, the scaling factors λ and the ζ_i parameters in (2.64)–(2.73) have the default value of 1, except for $\lambda'_{\mu y}$, which is 0. In other words, we have not considered the effects of camber and turn slip.

Table 1: Vehicle parameters

Parameter	Value
m_b	1181 kg
I_z	2066 kg·m^2
l_1	1.515 m
l_2	1.504 m
L_w	1.922 m

Table 2: Lateral force parameters.

Parameter	Value	Parameter	Value	Parameter	Value
p_{Cy1}	1.343000	p_{Ky2}	1.731265	p_{Vy3}	-0.163544
p_{Dy1}	0.878268	p_{Ky3}	0.365350	p_{Vy4}	-0.491003
p_{Dy2}	-0.064460	p_{Ky4}	1.981768	p_{py1}	-0.620596
p_{Dy3}	0	p_{Ky5}	0	p_{py2}	-0.064782
p_{Ey1}	-0.809776	p_{Ky6}	-0.884005	p_{py3}	-0.164649
p_{Ey2}	-0.600181	p_{Ky7}	-0.237260	p_{py4}	0.283194
p_{Ey3}	0.099173	p_{Hy1}	-0.001834	p_{py5}	0
p_{Ey4}	-6.557797	p_{Hy2}	0.003464	W_0	4000
p_{Ey5}	0	p_{Vy1}	-0.006754		
p_{Ky1}	-15.57147	p_{Vy2}	0.036379		

Seldom does the literature present stability regions as a function of several different parameters. Alternatively, we present them as a function of the steering angle, longitudinal speed, road-tire friction coefficient, and longitudinal center of mass displacement.

The stability regions obtained from Procedure 1 with respect to the steering angle are shown in Figure 25, for a longitudinal speed of 60 km/h ($v_{gx} = 16.67$ m/s) and dry asphalt road ($\mu = 0.8$). In pursuance of obtaining them, the lattices have been transformed into bitmaps where the pixels are colored black for stable points and white for unstable ones.

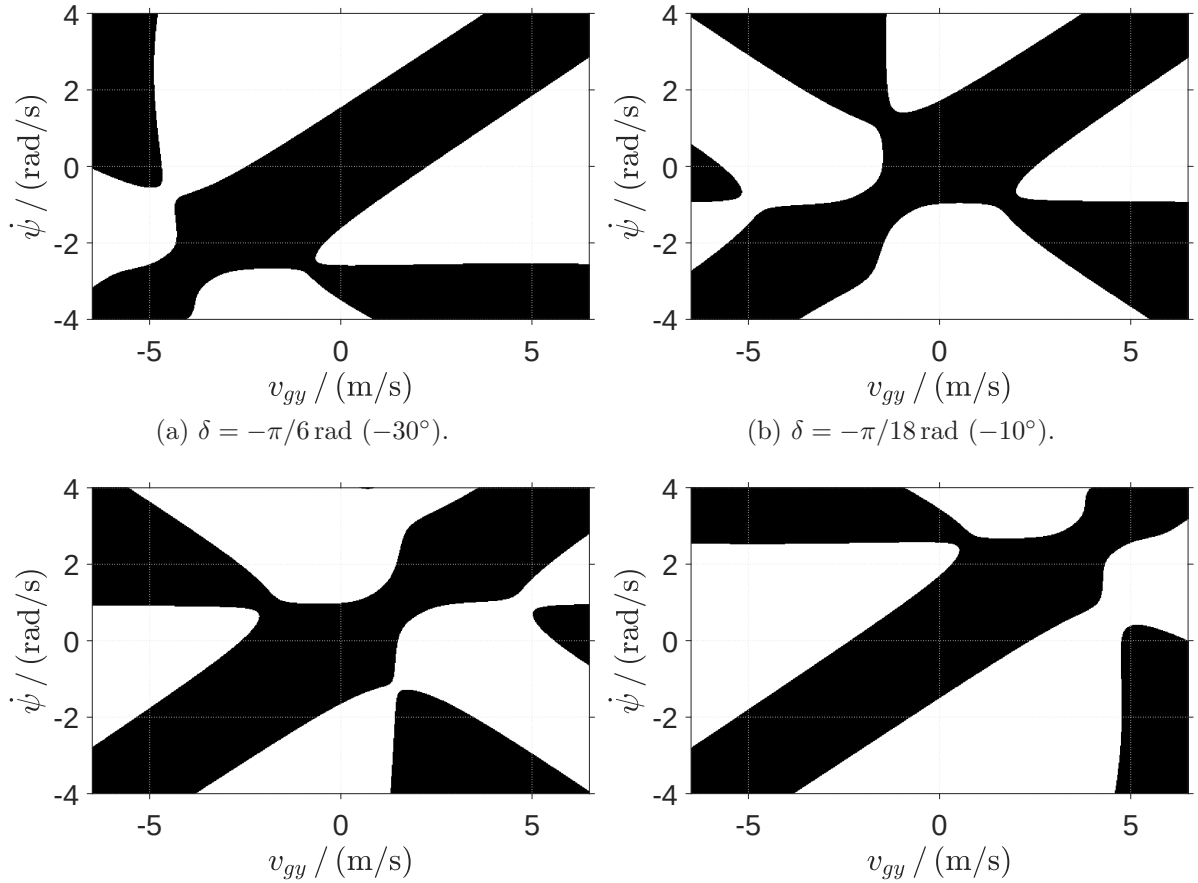

(a) $\delta = -\pi/6$ rad ($-30°$).

(b) $\delta = -\pi/18$ rad ($-10°$).

(c) $\delta = \pi/18$ rad ($10°$).

(d) $\delta = \pi/6$ rad ($30°$).

Figure 25: Stability case for $v_{gx} = 60$ km/h, $\mu = 0.8$, and varying δ.

Our procedure was able to detect shape changes with respect to steering angles. This dependency was not well documented in the pertaining literature (HUANG; LIANG; CHEN, 2017; HUANG; CHEN, 2017; ZHANG et al., 2020; HUANG; YONG; CHEN, 2019, 2021), which shows regions that maintain their shape as the steering angle changes. In particular, we observe that this dependency is more pronounced for large steering angles. As emergency maneuvers often call for near-limit steering and there is a possibility of overcorrection from the driver, this dependency will be considered for control applications, e.g., Sections 6.2 and 6.3.

The controllability regions for $v_{gx} = 16.67$ m/s (or 60 km/h) are depicted in Figure 26. In this figure, the controllability region boundaries are coded by different line styles for steering angle increments of 20°. The regions are the intersection of both front and rear wheels under positive local lateral stiffness. The larger the steering angle, the more deformed the controllability region becomes. For small values, they have a diamond-like shape.

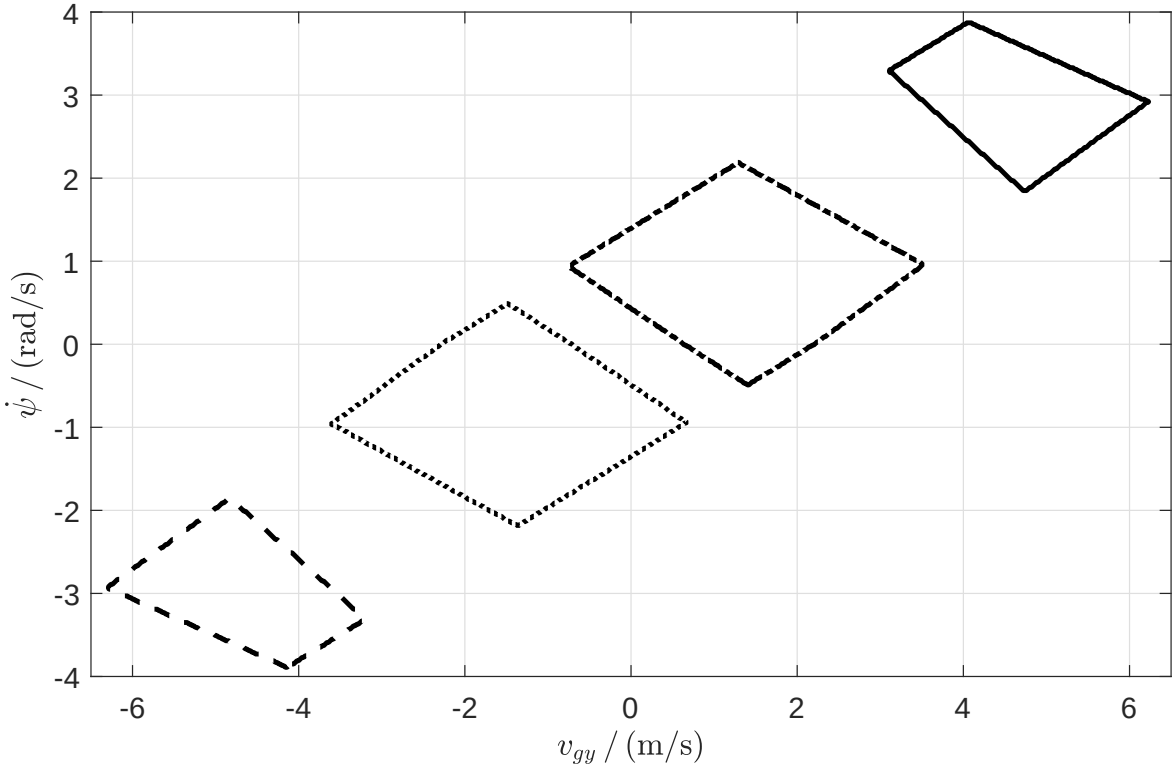

Figure 26: Controllability case for $v_{gx} = 60$ km/h, $\mu = 0.8$, and varying δ. Dashed line: $\delta = -\pi/6$ rad ($-30°$). Dotted line: $\delta = -\pi/18$ rad ($-10°$). Dash-dot line: $\delta = \pi/18$ rad ($10°$). Continuous line: $\delta = \pi/6$ rad ($30°$).

The intersection of the regions from Figures 25 and 26 yields the effective controllability regions, depicted in Figure 27. These are the regions that will be used for control applications since ESC aims to keep the vehicle both stable and controllable. The regions for low steering angles do bear a resemblance to some of the ones seen in the literature, but they are presented here in much greater detail. As the steering angle magnitude increases, they get deformed due to the combined effects of stability and controllability as functions of that variable.

The longitudinal speed also has a noticeable impact on the stability regions. We present them for a wide range of speeds that is compatible with public roads. More specifically, for v_{gx} ranging from 10 km/h (2.778 m/s) to 100 km/h (27.78 m/s), which

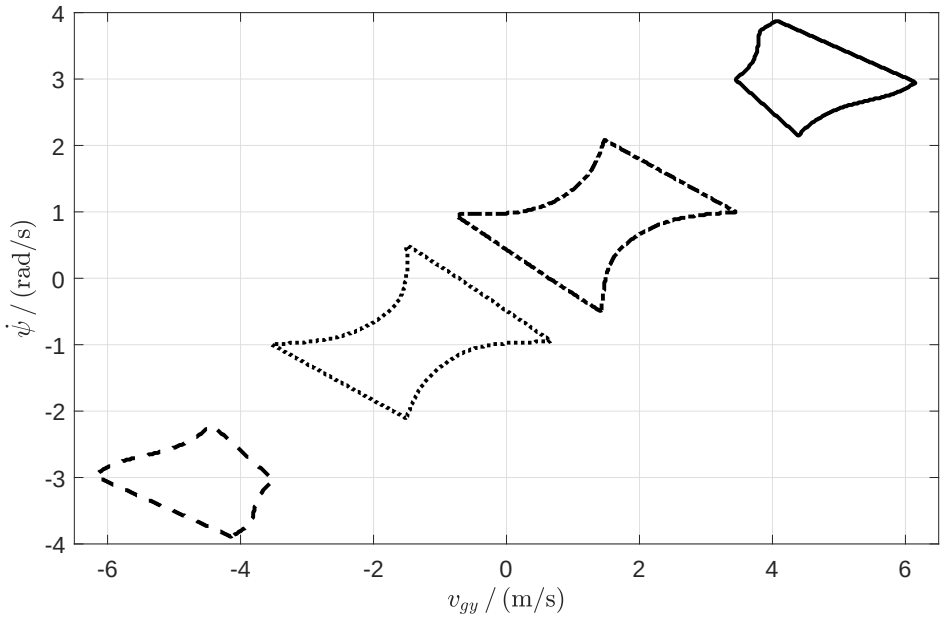

Figure 27: Effective stability regions for $v_{gx} = 60$ km/h, $\mu = 0.8$, and varying δ. Dashed line: $\delta = -\pi/6$ rad ($-30°$). Dotted line: $\delta = -\pi/18$ rad ($-10°$). Dash-dot line: $\delta = \pi/18$ rad ($10°$). Continuous line: $\delta = \pi/6$ rad ($30°$).

can accommodate maneuvers from parking lots to controlled-access highways.

The stability condition regions for a null steering angle and $\mu = 0.8$ are shown in Figure 28. We observe that the neighborhood around the origin increases with the longitudinal speed.

The controllability regions for null steering angle and $\mu = 0.8$ for different longitudinal speeds are presented in Figure 29. The low-speed regions are shown in Figure 29a, whereas the high-speed ones are in Figure 29b. They increase with speed, the reason being that slip angles are not changed if v_{gy} and $\dot{\psi}$ are proportional to v_{gx}.

The effective stability region as a function of the longitudinal speed, which results from Figures 28 and 29, is depicted in Figure 30. The resulting region is similar to the controllability one for low-speed values. For higher longitudinal speeds, it becomes closer to an hourglass-like shape that becomes thinner as the speed increases. This phenomenon occurs because the narrower stability region at high speeds is restricted by the larger controllability region.

The tire-road friction coefficient is one of the main sources of uncertainty in vehicle dynamics, and the most influential for vehicle stability. The stability regions with respect to the friction coefficient are depicted in Figure 31. The regions appear to be proportional to μ, which would be expected in case we were considering (5.39), as most terms in $\mathbf{A}$ from

(5.40) have cornering stiffnesses as factors. And it can be observed from (2.46) or (2.47) that the friction coefficient is a factor of both longitudinal and lateral stiffnesses—and hence also a factor of their derivatives, which are the local cornering stiffnesses.

Figure 32 presents the controllability regions for varying friction coefficients, while Figure 33 shows the effective stability regions from Figures 31 and 32. Since the forces on the wheels have the cornering stiffnesses as a factor, and the friction coefficient, in turn, has μ as a factor, the controllability regions are also proportional.

We can see that a friction coefficient reduction causes an immediate reduction in the stable region of operation. Since friction depends on several road aspects (pavement type, debris, rain, or oil), this is a largely unpredictable parameter.

At last, we present the effect on the stability regions from another varying parameter: the center of mass. As the vehicle is loaded with passengers and luggage, its center of mass may be shifted from the front to the rear, or the other way around. Here, we portray the effect of longitudinal displacement of the center of mass on lateral stability. To accomplish this, instead of considering all the dimensions from Table 1, we keep the same wheel base, $l = l_1 + l_2$, and consider increments of $0.2l$ for l_1. Hence we present stability regions for $l_1 = \{0.2l, 0.4l, 0.6l, 0.8l\}$.

The stability regions are presented in Figure 34. It can be observed that the stability region around the origin is slightly reduced as the center of mass approaches the rear axle.

Figure 35 shows the controllability condition. As in Figure 34, the deformation in the respective region is not pronounced.

The effective stability region for a varying center of mass is presented in Figure 36. It is perceived that the longitudinal displacement of the center of mass has a minor influence. More specifically, the region shrinks in the direction of the shifting vector, as l_1 increases, and expands in the perpendicular direction. Both deformations are modest, as expected from Figures 34 and 35.

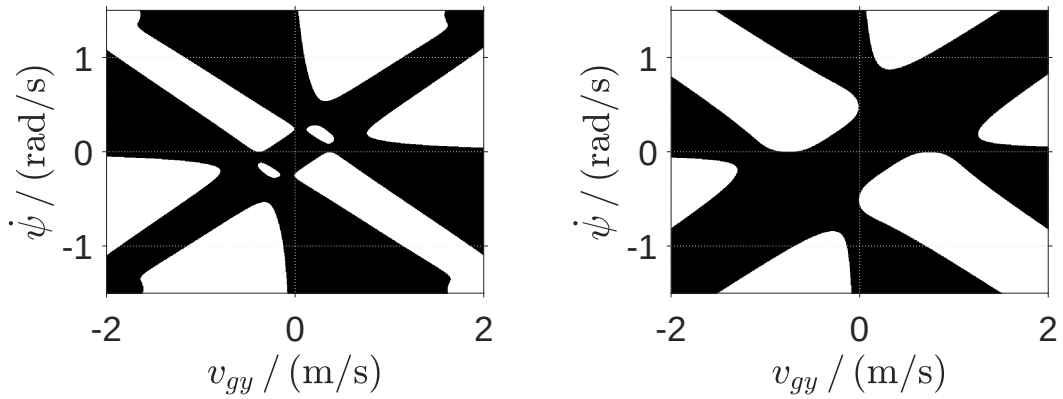

(a) $v_{gx} = 2.778$ m/s (10 km/h).

(b) $v_{gx} = 5.556$ m/s (20 km/h).

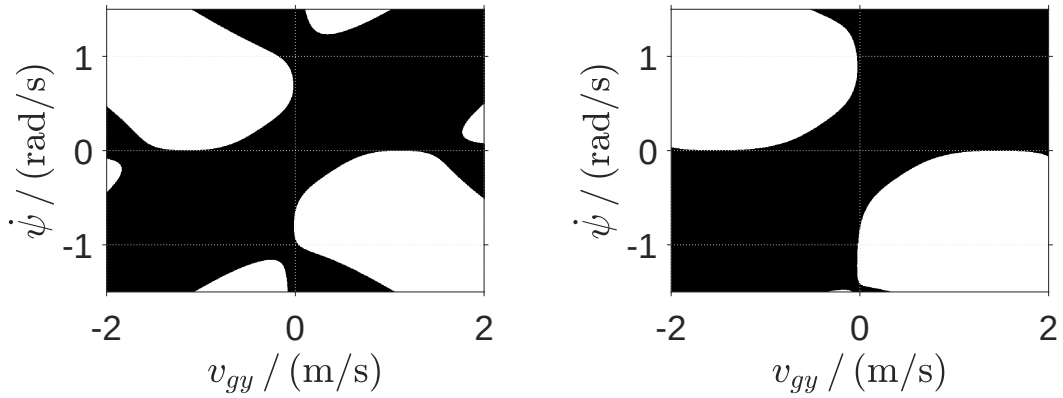

(c) $v_{gx} = 8.333$ m/s (30 km/h).

(d) $v_{gx} = 11.11$ m/s (40 km/h).

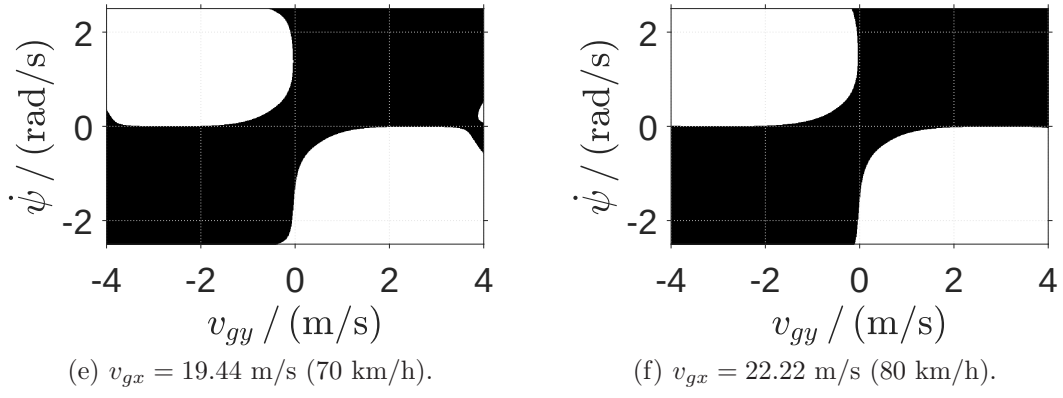

(e) $v_{gx} = 19.44$ m/s (70 km/h).

(f) $v_{gx} = 22.22$ m/s (80 km/h).

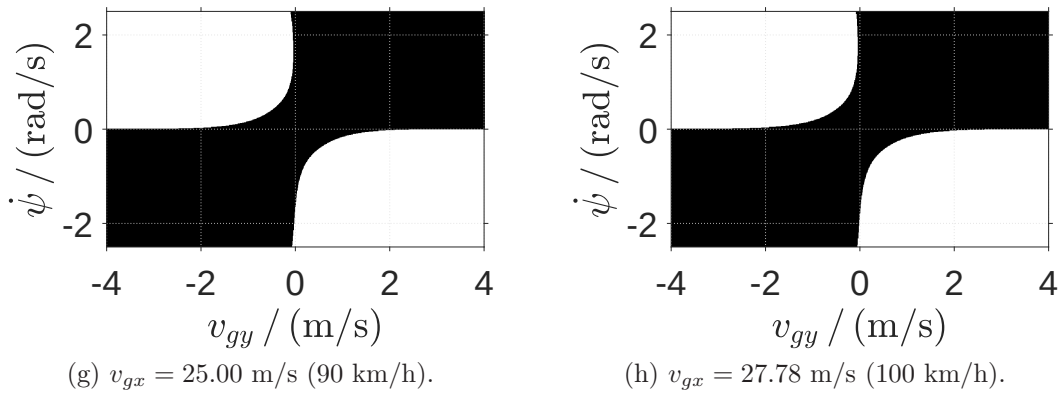

(g) $v_{gx} = 25.00$ m/s (90 km/h).

(h) $v_{gx} = 27.78$ m/s (100 km/h).

Figure 28: Stability case for $\delta = 0$ rad, $\mu = 0.8$, and varying v_{gx}.

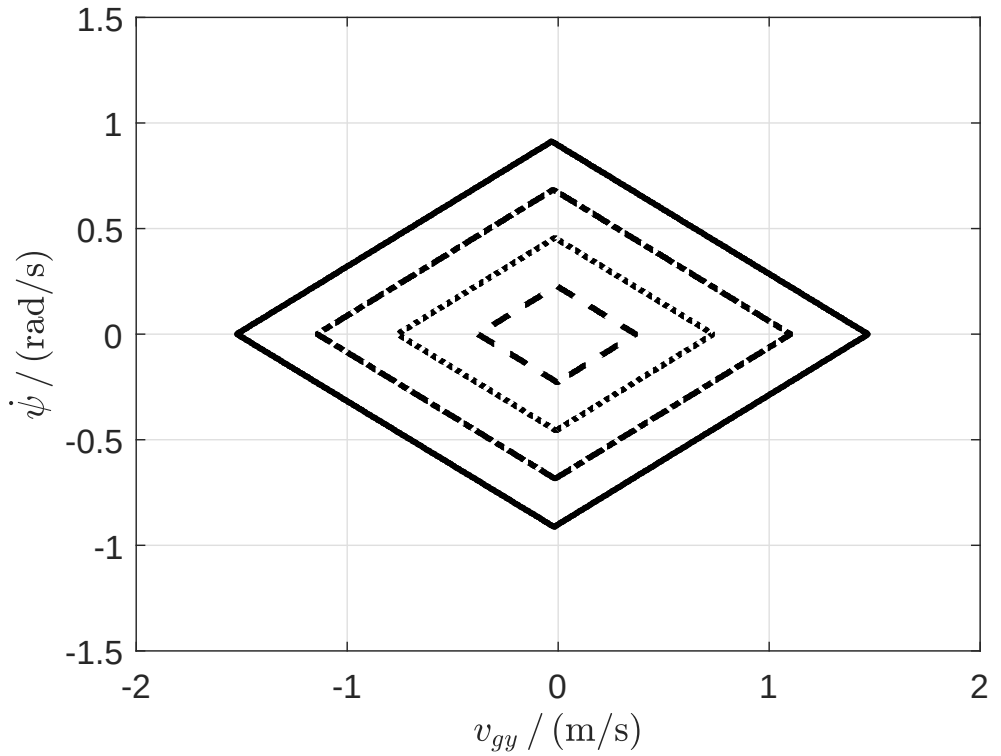

(a) Dashed line: $v_{gx} = 2.778$ m/s (10 km/h). Dotted line: $v_{gx} = 5.556$ m/s (20 km/h). Dash-dot line: $v_{gx} = 8.333$ m/s (30 km/h). Continuous line: $v_{gx} = 11.11$ m/s (40 km/h).

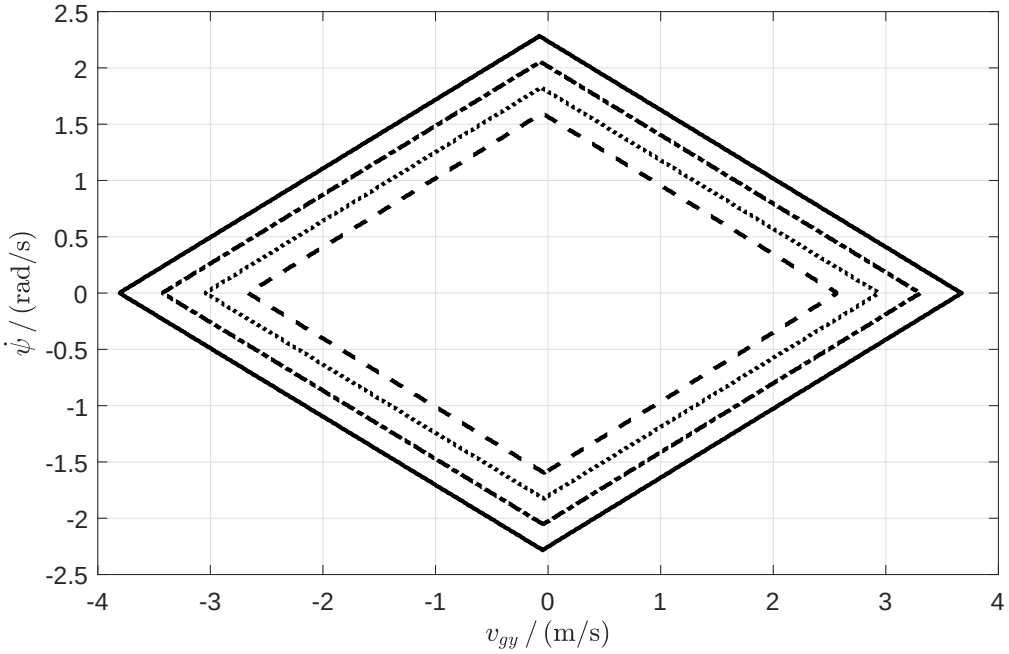

(b) Dashed line: $v_{gx} = 19.44$ m/s (70 km/h). Dotted line: $v_{gx} = 22.22$ m/s (80 km/h). Dash-dot line: $v_{gx} = 25.00$ m/s (90 km/h). Continuous line: $v_{gx} = 27.78$ m/s (100 km/h).

Figure 29: Controllability conditions for $\delta = 0$ rad, $\mu = 0.8$, and varying v_{gx}.

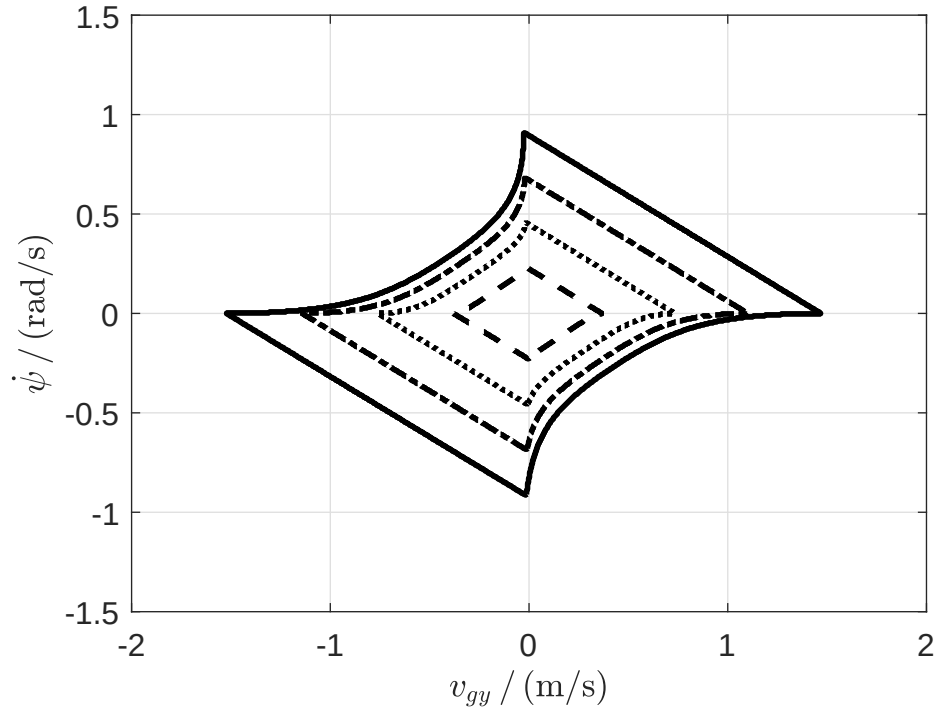

(a) Dashed line: $v_{gx} = 2.778$ m/s (10 km/h). Dotted line: $v_{gx} = 5.556$ m/s (20 km/h). Dash-dot line: $v_{gx} = 8.333$ m/s (30 km/h). Continuous line: $v_{gx} = 11.11$ m/s (40 km/h).

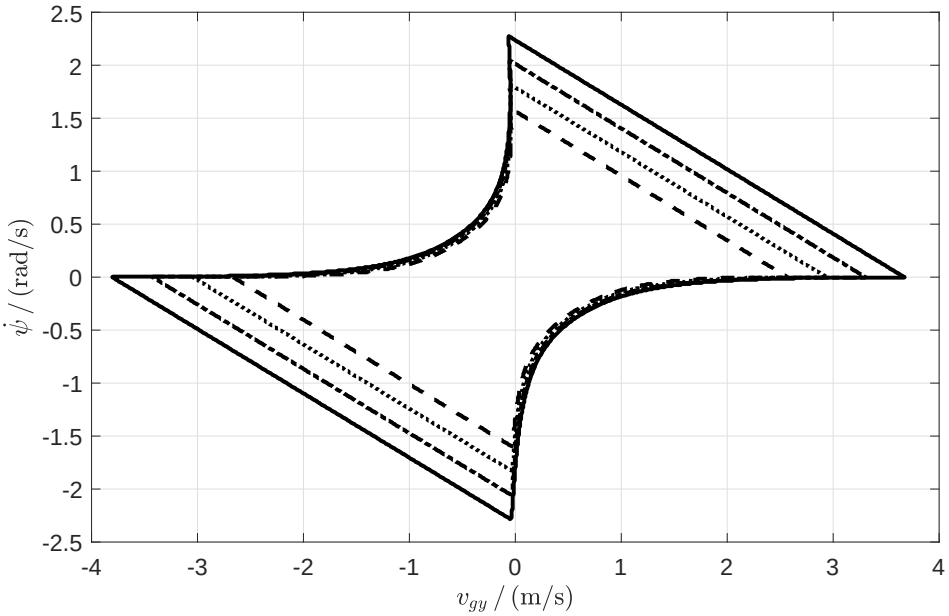

(b) Dashed line: $v_{gx} = 19.44$ m/s (70 km/h). Dotted line: $v_{gx} = 22.22$ m/s (80 km/h). Dash-dot line: $v_{gx} = 25.00$ m/s (90 km/h). Continuous line: $v_{gx} = 27.78$ m/s (100 km/h).

Figure 30: Effective stability regions for $\delta = 0$ rad, $\mu = 0.8$, and varying v_{gx}.

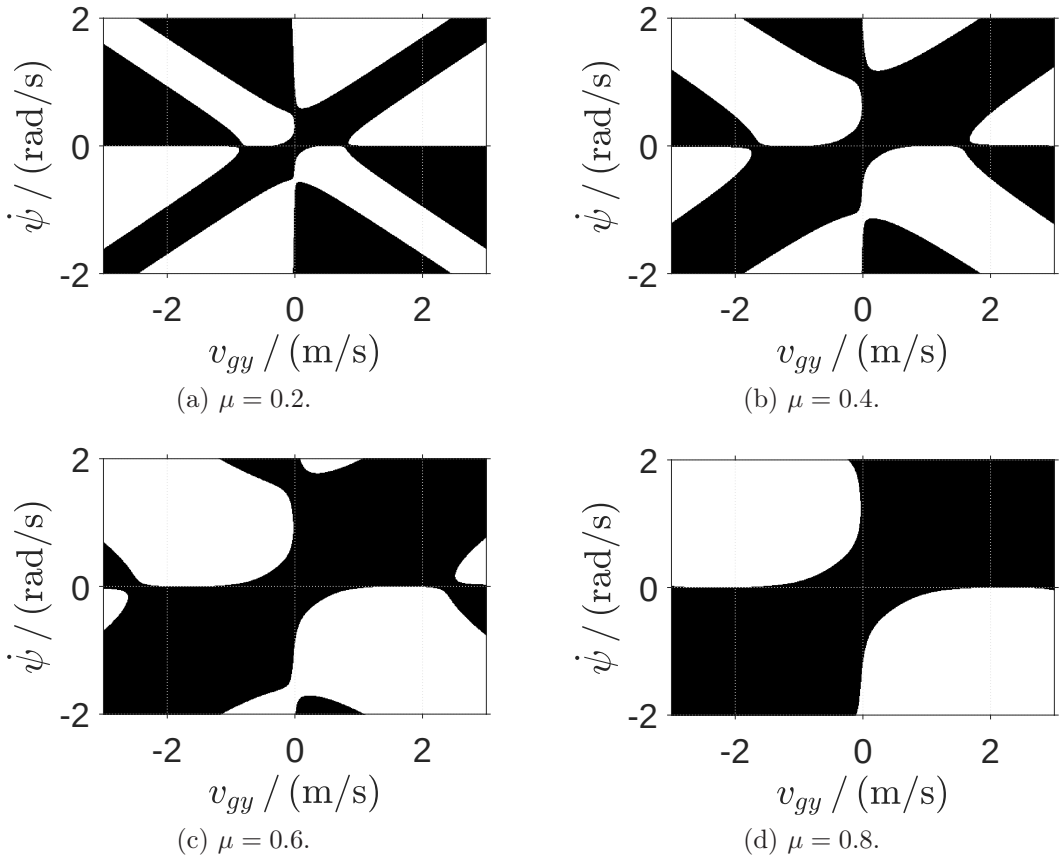

(a) $\mu = 0.2$. (b) $\mu = 0.4$.

(c) $\mu = 0.6$. (d) $\mu = 0.8$.

Figure 31: Stability case for $v_{gx} = 60$ km/h, $\delta = 0$ rad, and varying μ.

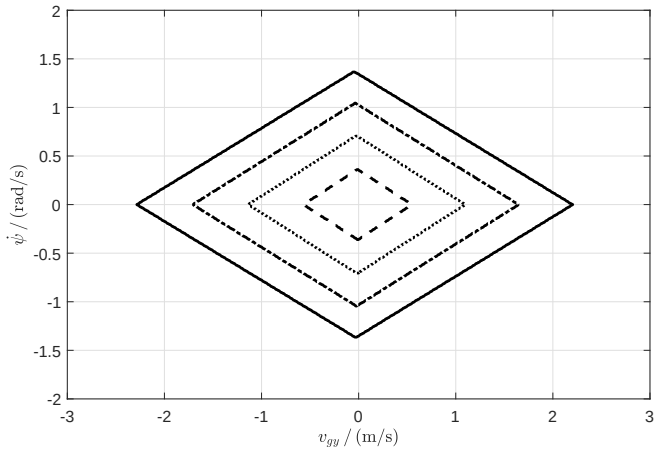

Figure 32: Controllability case for $v_{gx} = 60$ km/h, $\delta = 0$ rad, and varying μ. Dashed line: $\mu = 0.2$. Dotted line: $\mu = 0.4$. Dash-dot line: $\mu = 0.6$. Continuous line: $\mu = 0.8$.

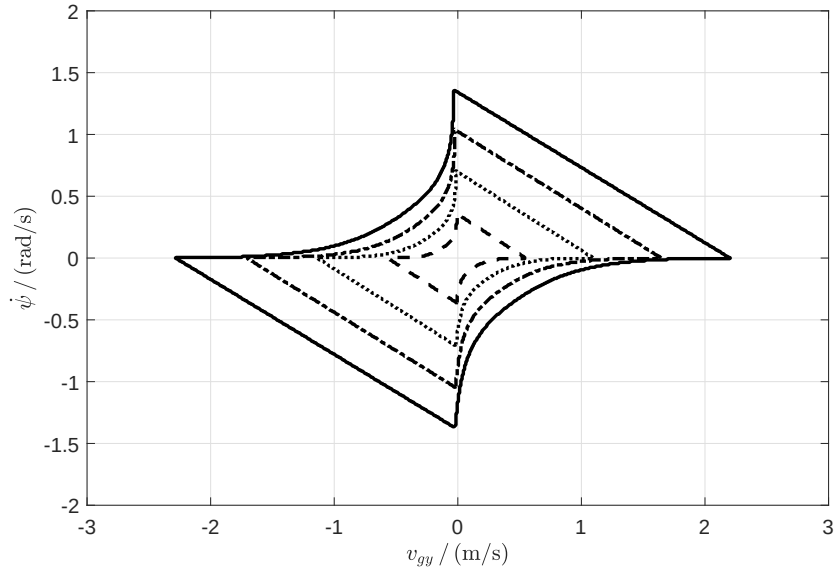

Figure 33: Effective stability regions for $v_{gx} = 60$ km/h, $\delta = 0$ rad, and varying μ. Dashed line: $\mu = 0.2$. Dotted line: $\mu = 0.4$. Dash-dot line: $\mu = 0.6$. Continuous line: $\mu = 0.8$.

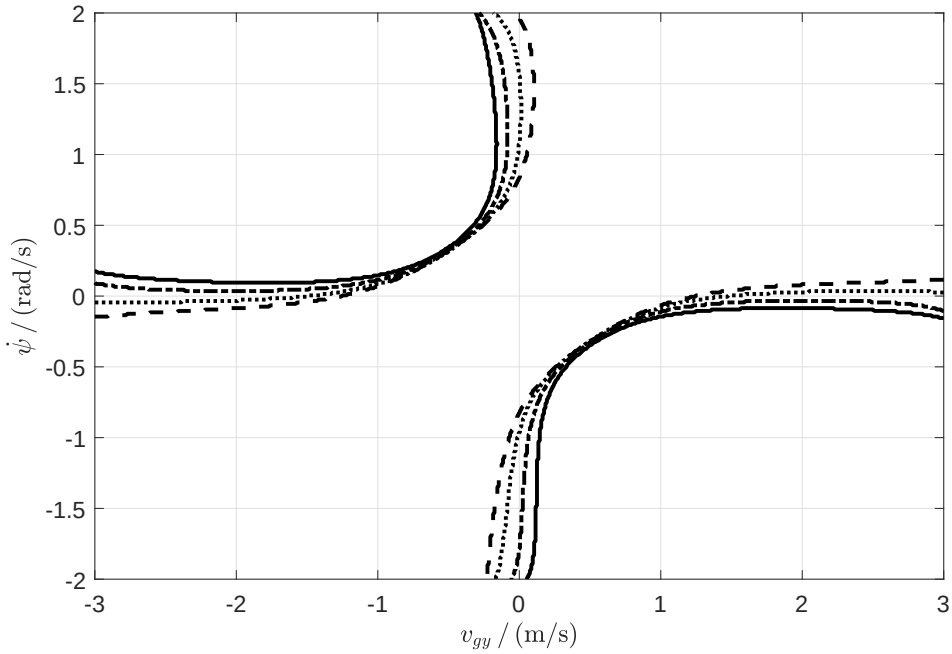

Figure 34: Stability case for $v_{gx} = 60$ km/h, $\mu = 0.8$, $\delta = 0$ rad, and varying longitudinal center of mass. Dashed line: $l_1 = 0.2l$. Dotted line: $l_1 = 0.4l$. Dash-dot line: $l_1 = 0.6l$. Continuous line: $l_1 = 0.8l$.

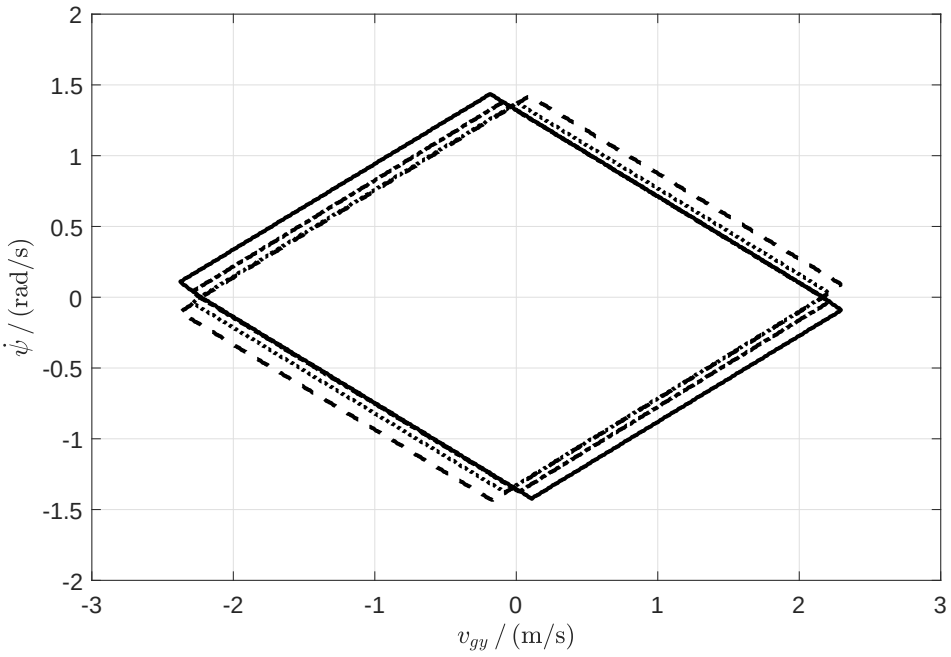

Figure 35: Controllability case for $v_{gx} = 60$ km/h, $\mu = 0.8$, $\delta = 0$ rad, and varying longitudinal center of mass. Dashed line: $l_1 = 0.2l$. Dotted line: $l_1 = 0.4l$. Dash-dot line: $l_1 = 0.6l$. Continuous line: $l_1 = 0.8l$.

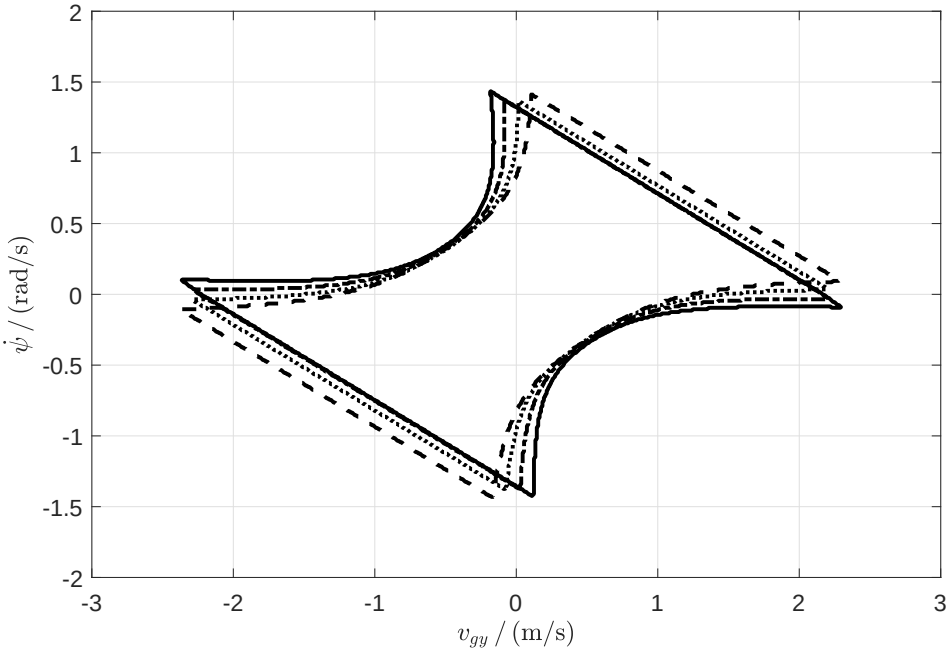

Figure 36: Effective stability regions for $v_{gx} = 60$ km/h, $\mu = 0.8$, $\delta = 0$ rad, and varying longitudinal center of mass. Dashed line: $l_1 = 0.2l$. Dotted line: $l_1 = 0.4l$. Dash-dot line: $l_1 = 0.6l$. Continuous line: $l_1 = 0.8l$.

5.1.2.1 Conservative regions

In Chapter 6, the control design will consider some degree of conservativeness with respect to ranges of values for some parameters. As seen, the stability regions are a function of several vehicle parameters. If they are time-variant, we can consider the controllability and stability criteria for the range of values that is expected for the interval of time that is under consideration. We refer to stability regions that are valid over a range of parameters as *conservative stability regions*.

We initially consider the steering angle. Let us admit that the steering angle will change as the vehicle performs a class of maneuvers that demands a maximum value to be performed. It was seen in Figure 27 that the stability regions are shifted when the steering angle changes. In order to account for this effect, we will consider the *shifting vector* from (HUANG; CHEN, 2017). The shifting vector is defined as the change $\mathbf{s}$ in the state vector $[v_{gy} \quad \dot{\psi}]^{\mathrm{T}}$ from (2.97)–(2.98) such that the wheel slip angles are unchanged when the steering angle changes from zero to δ and is given by

$$\mathbf{s} = \begin{bmatrix} s_1 \\ s_2 \end{bmatrix} = \begin{bmatrix} \frac{v_{gx} l_2 \delta}{l} \\ \frac{v_{gx} \delta}{l} \end{bmatrix}. \tag{5.42}$$

When the shifting vector is used, the $v_{gy} \times \dot{\psi}$ plane is transformed into the $(v_{gy} - s_1) \times (\dot{\psi} - s_2)$ plane, where the stability regions are centered at the origin. For instance, let the maximum value be $\pi/18$ rad, $\pi/9$ rad, and $\pi/6$ rad (10°, 20°, and 30°, respectively). Then the conservative stability regions are depicted in Figure 37.

We recall from Figure 27 that the shapes of lateral stability regions change as the steering angle increases. For large steering angles, this change is pronounced. Hence the conservative stability region dramatically shrinks as the maximum steering angle increases. This reduction is related to the larger tire slip angles which result from a given longitudinal speed and large steering angles.

The realization of conservative stability regions for a range of longitudinal speeds is, in turn, trivial. We have observed in Figure 30 that the regions that result from larger longitudinal speeds are also larger, and contain the regions for lower speeds. Hence the effective stability regions for the range of speeds from Figures 30a and 30b are those that result from the lowest values, viz., 2.778 m/s and 19.44 m/s (10 km/h and 70 km/h), in the respective order, which are the regions whose frontiers are depicted in dashed lines.

The generation of conservative stability regions for varying tire-road friction coef-

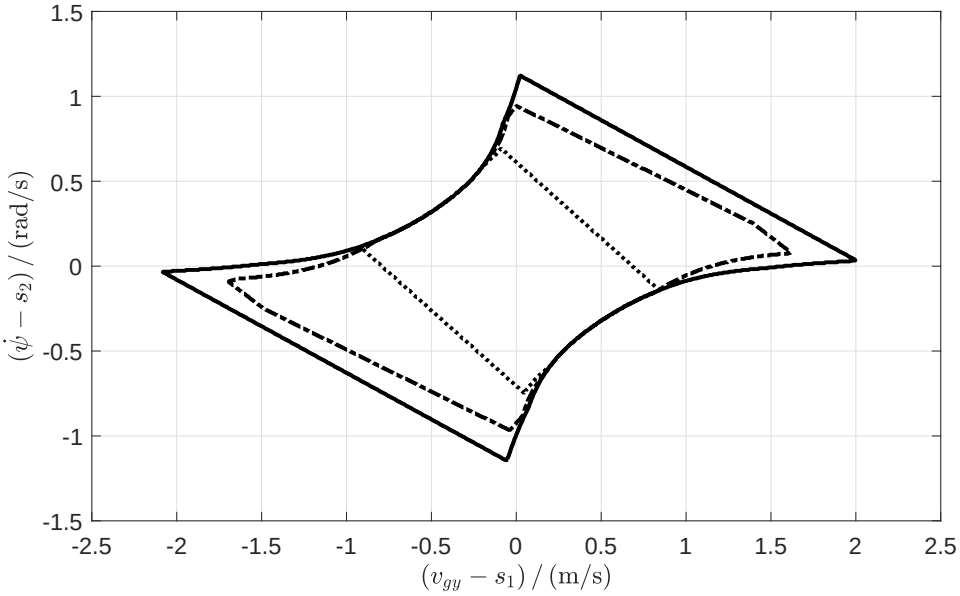

Figure 37: Conservative stability regions for $v_{gx} = 60$ km/h, $\mu = 0.8$, and different δ amplitude. Continuous line: $\delta \in \{-\pi/18 \text{ rad}, \pi/18 \text{ rad}\}$ ($\{-10°, 10°\}$). Dash-dot line: $\delta \in \{-\pi/9 \text{ rad}, \pi/9 \text{ rad}\}$ ($\{-20°, 20°\}$). Dotted line: $\delta \in \{-\pi/6 \text{ rad}, \pi/6 \text{ rad}\}$ ($\{-30°, 30°\}$).

ficients is analogous to varying longitudinal speeds, i.e., they reduce as the respective variable decreases. As a consequence, for instance, the conservative stability region for $\mu \in \{0.2, 0.8\}$ is that in dashed line, in Figure 33; and for $\mu \in \{0.6, 0.8\}$, in dash-dot line.

We also mention that we can generate conservative stability regions for more than one varying parameter. For instance, varying steering angle and friction coefficient. In that case, in accordance with what has been observed, we would obtain the region by considering the lowest friction coefficient and the maximum steering angle amplitude.

For the sake of brevity, we will present a last conservative stability region example in Figure 38, for the same additional parameter that was previously considered for stability regions, i.e., longitudinal center of mass shift. In particular, Figure 38 presents the effective stability region for $l_1 = \{0.02l, 0.98l\}$. Of course, these extreme values of l_1 of either just 2 % or 98 % of the wheel base of the vehicle would be a major problem for longitudinal stability. However, it can be observed, by comparing Figures 38 and 36, that the effect on lateral stability is relatively small.

5.2 Stability Region Conclusions

This chapter presented an improved method of generating lateral stability regions. The method considers a magic formula model for the steady-state tire dynamics and a four-

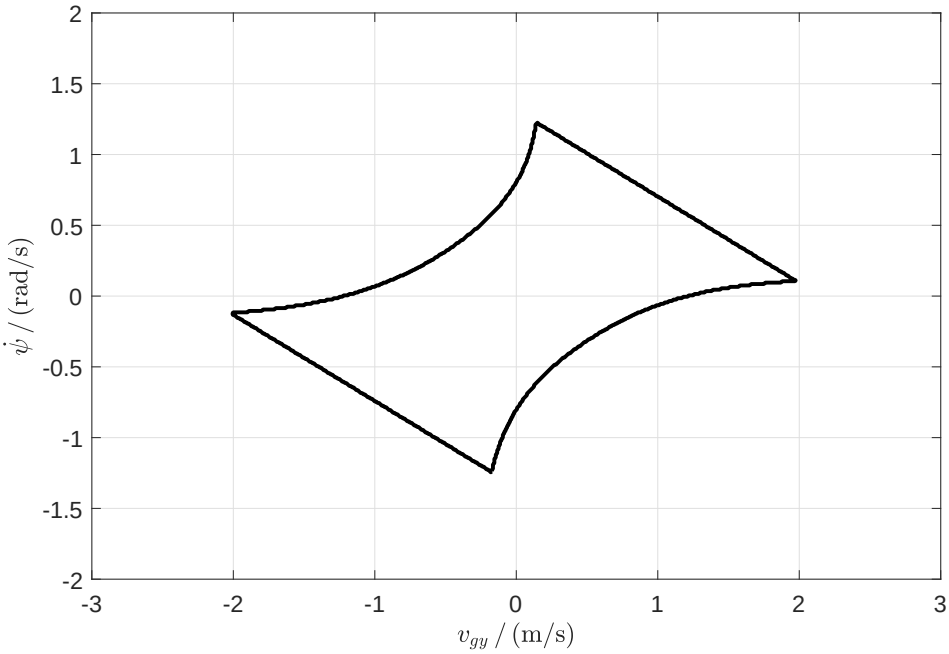

Figure 38: Conservative stability region for $v_{gx} = 60$ km/h, $\mu = 0.8$, $\delta = 0$ rad, and $l_1 = \{0.02l, 0.98l\}$.

wheel vehicle model. Methods of obtaining stability regions for varying parameters were presented, along with several examples. As instances, we presented regions for varying longitudinal speeds, steering angles, tire-road friction coefficients, and longitudinal center of mass displacements. Finally, we introduced a method of obtaining conservative stability regions. These remain valid for a range of different parameters and can be considered for control design when dealing with varying or unknown model parameters.

6 ACTIVE FRONT STEERING

The vast majority of road vehicles use front steering wheels. Hence the strategy of installing active steering systems on those vehicles is known as *active front steering*. When applied to ESC, AFS systems read the steering angles from the driver and change the resulting steering angles of the front wheels so as to maintain or recover lateral stability. The resulting control scheme is very similar to what is depicted in Figure 20 but uses steering angles and control inputs, instead of braking pressures.

When we started our review of safety-critical control ESC systems, the only proposed implementations for ESC used active steering (HUANG; YONG; CHEN, 2019, 2021). We reimplemented those and found shortcomings in the proposed control methods. In particular, the stability regions used in the design process had low definition, the maneuver used to validate the proposal was not enough to induce vehicle instability, the safe set employed in the control design had regions where it was impossible to guarantee invariance, and there was a nonzero steady-state value for the steering angle input.

The first problem was dealt with in Chapter 5. We now present electronic stability control systems that eliminate the remaining problems observed in (HUANG; YONG; CHEN, 2019) and improve the design criterion by employing the effective stability regions shown in Section 5.1.2. Before we present our contribution, we first recall the safety-critical implementation from (HUANG; YONG; CHEN, 2019) in Section 6.1. After that, Section 6.2 presents solutions to the previously described problems. Following, Section 6.3 introduces an alternative formulation that is less conservative. Finally, Section 6.4 summarizes the chapter.

6.1 A first active front steering safety critical ESC

Let us consider the safety-critical control formulation from Section 4.3, which considers the invariance theory from Section 4.2, given by the CLF-CBF-QP problem, expressed by

(4.21) (AMES et al., 2017, 2019). We repeat it here, for ease of reference:

$$\arg\min_{\substack{\mathbf{u}\in\mathcal{U}\\ \delta\in\mathbb{R}}} \frac{1}{2}(\mathbf{u}-\mathbf{u}_{ref})^{\mathrm{T}}\mathbf{H}(\mathbf{u}-\mathbf{u}_{ref}) + p\delta_s \tag{6.1}$$

$$\text{subject to} \quad L_fV(\mathbf{x}) + L_gV(\mathbf{x})\mathbf{u} + \gamma(V(\mathbf{x})) \leq \delta_s \tag{6.2}$$

$$L_fh(\mathbf{x}) + L_gh(\mathbf{x})\mathbf{u} + \alpha(h(\mathbf{x})) \geq 0. \tag{6.3}$$

Despite being a flexible formulation, it has the limitation of not allowing barrier functions that depend on the control input. However, an ESC system that uses AFS has the front steering wheels angle δ_f as the control input, and as seen in Figure 27, the effective stability region is heavily dependent on the said variable. As a consequence, an extension of control barrier functions has been presented in (HUANG; YONG; CHEN, 2019) to accommodate this dependency.

More specifically, a control-dependent barrier function $h(\mathbf{x},\mathbf{u})$ is proposed by (HUANG; YONG; CHEN, 2019) to deal with the problem of having safe sets that depend on the control input. This extra functionality comes at the expense of restricting $\mathbf{u}$ to be differentiable, however. In particular, an augmented system is defined by adding $\mathbf{u}$ as a state

$$\dot{\hat{\mathbf{x}}} = \begin{bmatrix}\dot{\mathbf{x}}\\ \mathbf{u}\end{bmatrix} = \begin{bmatrix}f(\mathbf{x},\mathbf{u})\\ \omega_u\end{bmatrix} = \hat{f}(\hat{\mathbf{x}},\omega_u), \tag{6.4}$$

with $\hat{\mathbf{x}} \triangleq [\mathbf{x}\ \ \mathbf{u}]^{\mathrm{T}}$. In other words, (6.4) defines a new system where $\mathbf{u}$ is part of the state and its derivative is the new input. Consequently, the safe set is defined with the aid of $h(\mathbf{x},\mathbf{u})$ in terms of the new state $\hat{\mathbf{x}}$ as

Definition 6 (Control-dependent barrier function (HUANG; YONG; CHEN, 2019))**.** *Let h satisfy*

$$h(\mathbf{x},\mathbf{u}) \geq 0, \forall \mathbf{x} \in \mathcal{C}(\mathbf{x},\mathbf{u}) \tag{6.5}$$

$$h(\mathbf{x},\mathbf{u}) = 0, \forall \mathbf{x} \in \mathrm{fr}\left(\mathcal{C}(\mathbf{x},\mathbf{u})\right) \tag{6.6}$$

$$h(\mathbf{x},\mathbf{u}) > 0, \forall \mathbf{x} \in \mathrm{Int}\left(\mathcal{C}(\mathbf{x},\mathbf{u})\right). \tag{6.7}$$

If there exists a control input $\mathbf{u} \in \mathcal{U}$, $\omega_u \in \Omega_u$ and an extended class κ function α such that

$$L_{\hat{f}}h(\mathbf{x},\mathbf{u}) + \alpha(h(\mathbf{x},\mathbf{u})) \geq 0, \tag{6.8}$$

then h is a control-dependent barrier function *and $\mathcal{C}$ is a* control-dependent safe set*.*

The proposal in (HUANG; YONG; CHEN, 2019) is to use a stability region from

(HUANG; LIANG; CHEN, 2017), adjust four polynomials as its boundaries, adapt them to barrier functions, and use (6.8) in place of (6.3) in (6.1) to close the loop, using the steering wheel as control input in (2.97)–(2.98). Then the (linearized) model of the vehicle is written as

$$\dot{\mathbf{x}} = \mathbf{A}\mathbf{x} + \mathbf{B}\delta \tag{6.9}$$

with $\mathbf{x} = [v_{gy} \;\; \dot{\psi}]^{\mathrm{T}}$ and $\delta = \delta_d + \delta_u$, where δ_d is the front steering angle which is due to the driver and δ_u is an addend from the ESC system that is supposed to be null whenever the vehicle is stable. As a consequence, $\mathbf{u} = u = \delta_u$ in the referred proposal.

As explained in Chapter 5, the images from (HUANG; LIANG; CHEN, 2017) lack detail, making it difficult to adjust polynomials to their frontier. As a result, we will use the regions presented in this text instead, namely the conservative effective stability regions, to account for longitudinal speed losses which would happen with a real vehicle and steering angle changes.

Let b_1, b_2, b_3, and b_4 be the polynomials that describe the frontier of the safe set, as depicted in Figure 39, for $\delta = 0$ rad. Next, we can obtain control barrier function candidates as (HUANG; YONG; CHEN, 2019)

$$h_1(\mathbf{x}, \mathbf{u}) = b_1(v_{gy} - s_1) - (\dot{\psi} - s_2), \tag{6.10}$$

$$h_2(\mathbf{x}, \mathbf{u}) = b_2(v_{gy} - s_1) - (\dot{\psi} - s_2), \tag{6.11}$$

$$h_3(\mathbf{x}, \mathbf{u}) = \dot{\psi} - s_2 - b_3(v_{gy} - s_1), \tag{6.12}$$

$$h_4(\mathbf{x}, \mathbf{u}) = \dot{\psi} - s_2 - b_4(v_{gy} - s_1), \tag{6.13}$$

which satisfy $h_{1,2,3,4} > 0$, $\mathbf{x} \in \mathcal{C}$, with $\mathcal{C}$ as in Figure 39.

The control signal can be obtained by solving the CBF-QP problem given by

$$\dot{\mathbf{u}}^{\star} = \arg\min_{\dot{\mathbf{u}} \in \mathbb{R}^m} \frac{1}{2}\dot{\mathbf{u}}^{\mathrm{T}}\mathbf{H}\dot{\mathbf{u}} + \mathbf{F}^{\mathrm{T}}\dot{\mathbf{u}}, \tag{6.14}$$

subject to

$$\frac{\partial h_i(\mathbf{x}, \mathbf{u})}{\partial \mathbf{x}} f(\mathbf{x}, \mathbf{u}) + \frac{\partial h_i(\mathbf{x}, \mathbf{u})}{\partial \mathbf{u}} \dot{\mathbf{u}} + \zeta(h_i(\mathbf{x}, \mathbf{u})) \geq 0, \tag{6.15}$$

where $\mathbf{H} \in \mathbb{R}^{m \times m}$ is postive-definite and $\mathbf{F} \in \mathbb{R}^m$. Then $\mathbf{u}$ can be obtained by integrating $\dot{\mathbf{u}}^{\star}$.

The closed-loop system that was just described can maintain the state in the safe set for some classes of driver inputs $\delta_d(t)$. But not all. For instance, let us consider the driver input given in Figure 40. The state vector trajectory in the shifted plane

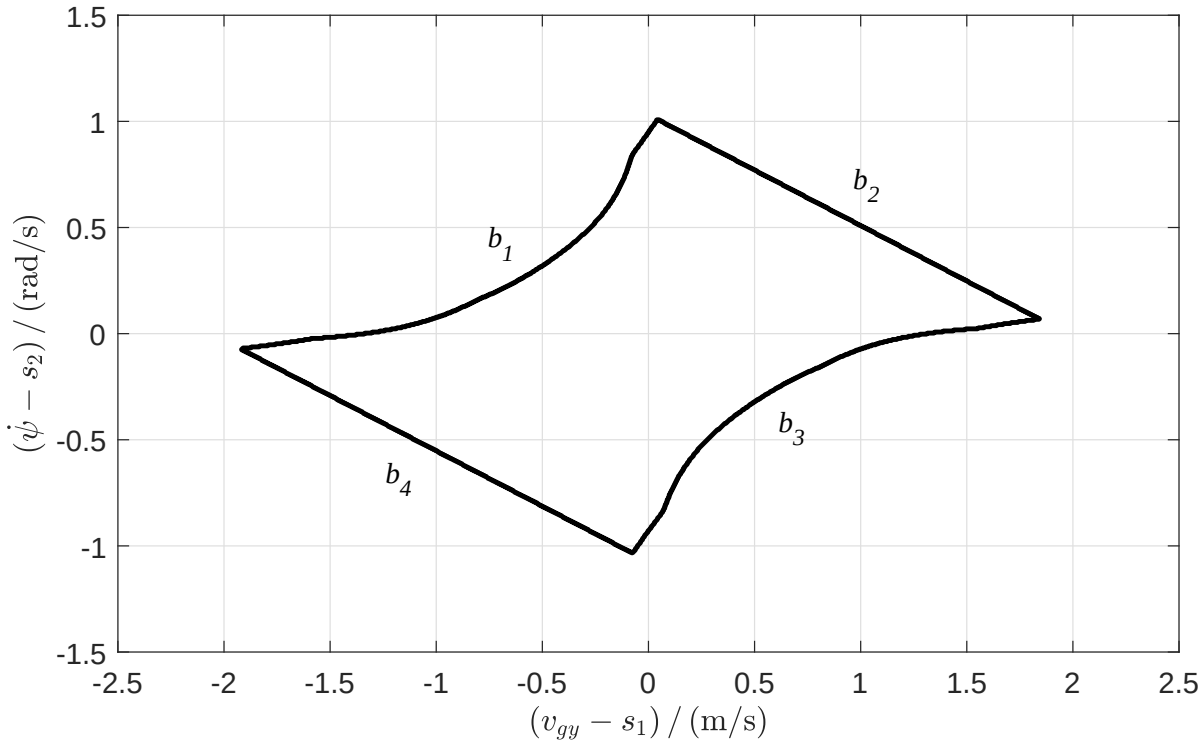

Figure 39: Conservative stability region for $\delta \in \{-\pi/12 \text{ rad}, \pi/12 \text{ rad}\}$ ($\{-15°, 15°\}$). The functions b_1, b_2, b_3, and b_4 describe the limits of the region.

$(v_{gy} - s_1) \times (\dot{\psi} - s_2)$ is presented in Figure 41.

Before we proceed, we mention that it is possible to adjust the safe set—and the respective CDBF candidates—by bringing h_2 and h_4 closer to one another. By proceeding in this manner, we obtain the shifted state trajectory depicted in Figure 42. However, the respective input signal is as shown in Figure 43. In particular, it is important to observe that the steady-state value of the control signal δ_u is nonzero (Figure 43a). This has an undesirable effect: the steady-state value of the effective front steering angle, which is the sum of the angles from the driver and the ESC system, is nonzero, as shown in Figure 43b. After the driver performs the maneuver from Figure 40, he moves the steering wheel to a neutral angle, which means he wants the vehicle to move in a straight line. However, if a barrier ever becomes active, the steady-state value of the input signal does not return to zero—only its derivative does—which leaves the driver with a modified steering system that looks twisted.

As a result, we notice two problems in this proposal from the literature. The first problem is that the ability of the safety-critical control system to effectively guarantee the safety conditions depends on which barrier becomes active. In particular, h_2 and h_4 are responsive barriers, which generate a proper control input in terms of preventing the

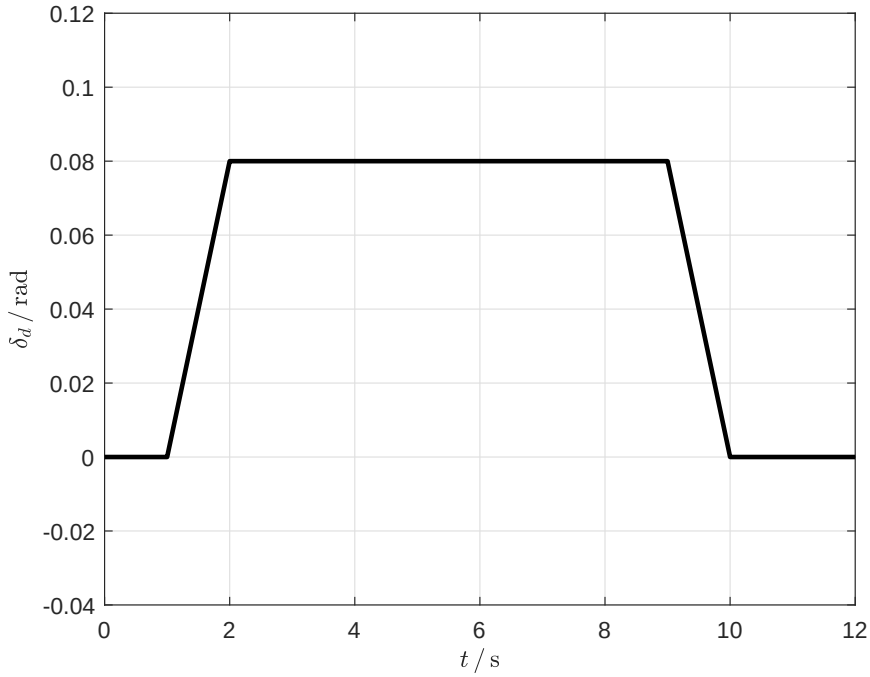

Figure 40: Possible front wheel steering angles for a driver input.

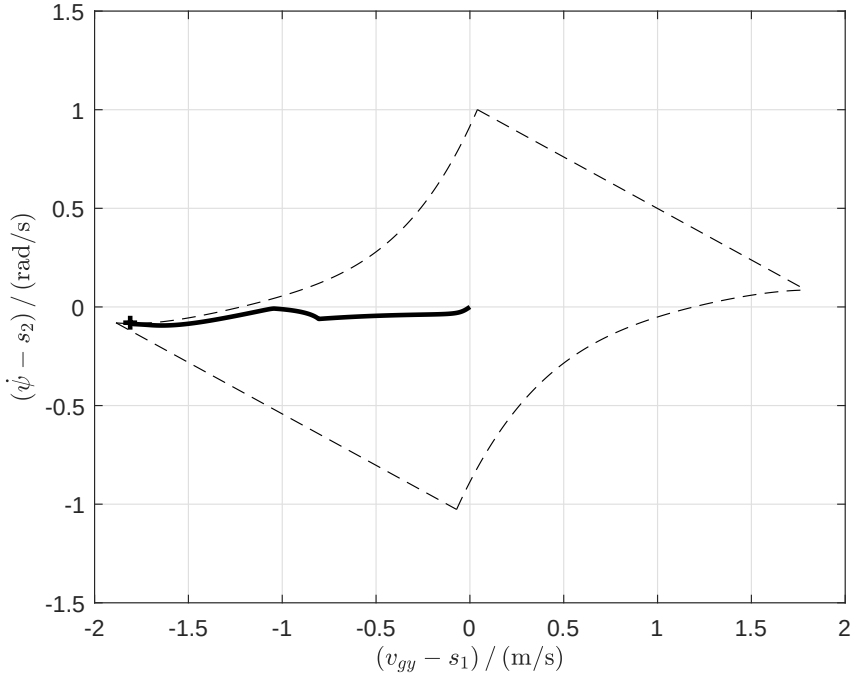

Figure 41: Shifted system state with respect to the centered safe set. Continuous line: shifted system trajectory. Dashed line: safe set frontier.

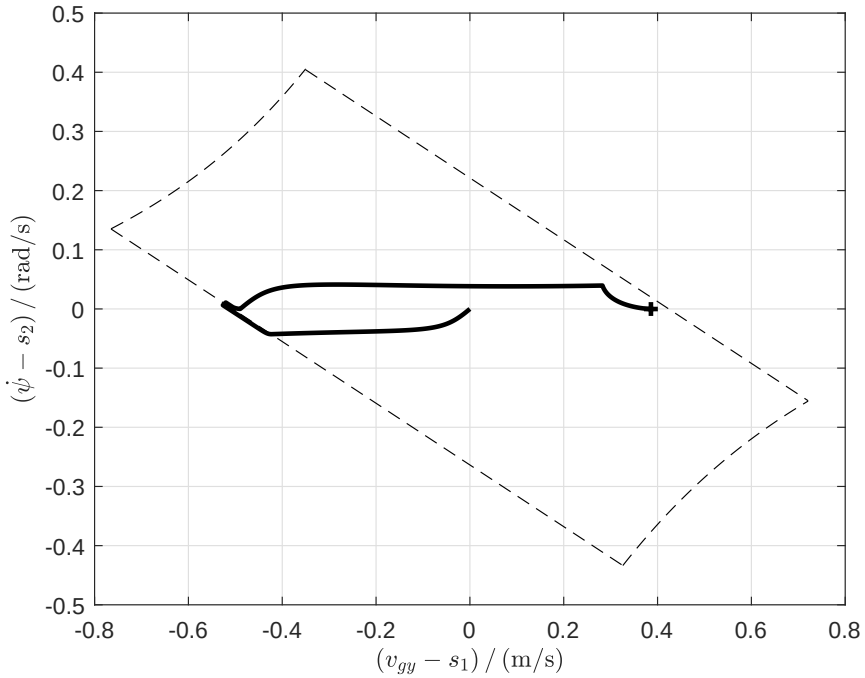

Figure 42: Shifted system state with respect to the modified centered safe set with h_2 and h_4 closer to one another. Continuous line: shifted system trajectory. Dashed line: safe set frontier.

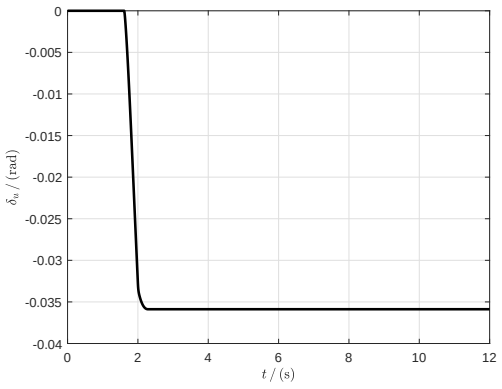

(a) Input signal δ_u.

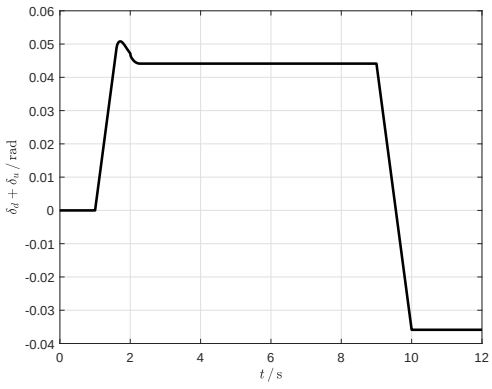

(b) Final front wheels steering angle.

Figure 43: Control input and effective front steering angle for the modified centered safe set with h_2 and h_4 closer to one another.

safety condition to be disrespected. The other problem is the steady-state behavior of the steering system, which changes after the ESC system responds to harsh maneuvers, i.e., after it intervenes to compensate for the driver's inputs.

In Section 6.2 we further clarify the reasons behind the aforementioned problems and propose an AFS ESC system based on safety-critical control that solves them.

6.2 Active front steering with control-dependent Lyapunov function

In Section 6.1 we presented an AFS system that may fail to maintain the state inside the safe set at all times, for any possible maneuver. Also, if it ever becomes active, this AFS system leaves a systematic error in the steering system, so the driver has to compensate for a deviation to either side of the road, permanently.

We show that the ability of the safety-critical control system to satisfy the safety restrictions is related to the dimension of the control input being less than the dimension of the safe set. Moreover, the safe set in (HUANG; YONG; CHEN, 2019) is concave, which makes it possible for the state to reach areas where the input is unable to steer the safe set and the state so that the safety restriction is satisfied.

Assume the driver moves the steering wheel in a counter-clockwise direction ($\delta_d > 0$). This moves the safe set in the direction of the shifting vector $\mathbf{s}$ while inducing a state derivative such that the yaw rate increases while the lateral speed becomes negative, i.e., $\dot{\psi} > 0$, $v_{gy} < 0$. These three phenomena, combined, may steer the state to the intersection of h_1 and h_4, as depicted in Figure 44. Let $\mathbf{x}_b$ be the state in that situation. The time derivative of the state vector is such that it shall leave the safe set if no control action is performed. However, assume a small change $\Delta\delta_u$ in the steering angle, either positive or negative. No matter what direction is used, the safe set moves away from the state, as shown in greater detail in Figure 44b. Hence it is impossible to satisfy the safety restrictions.

We have now established that concave safe sets cannot have their invariance guaranteed by scalar inputs, at least not in general. Consequently, we might assume that considering any convex set, together with the control method from Section 6.1, should solve the problem. Thus, let us consider a safe set candidate with the shape of a parallelogram, as presented in Figure 45a.

Especially, let us consider b_1, b_2, b_3, and b_4 as straight lines, i.e., first-order polyno-

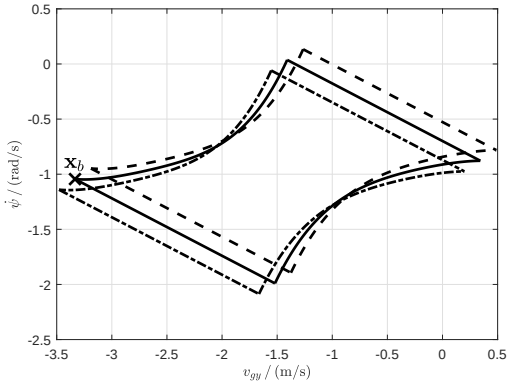

(a) Variation of the control-dependent safe sets for $\delta = 0.1745$ rad (10°), considering a change of ±1°.

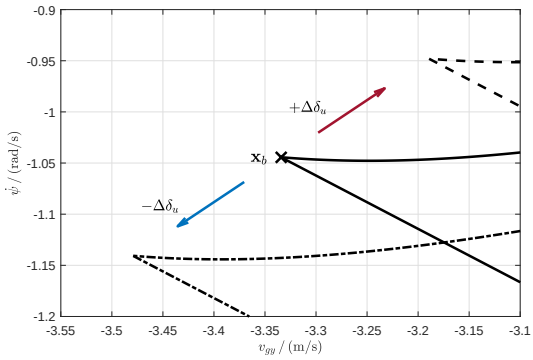

(b) Detail of the effect of changing δ for $\mathbf{x}_b$ at the boundary of the safe set for positive and negative steering angle changes.

Figure 44: Control-dependent safe sets for $\mu = 0.8$, $v_{gx} = 60$ km/h, and a maximum $\delta = 0.2618$ rad (15°), for different steering angles. Dash-dot line: $\delta = 0.1571$ rad (9°). Continuous line: $\delta = 0.1745$ rad (10°). Dashed line: $\delta = 0.1920$ rad (11°).

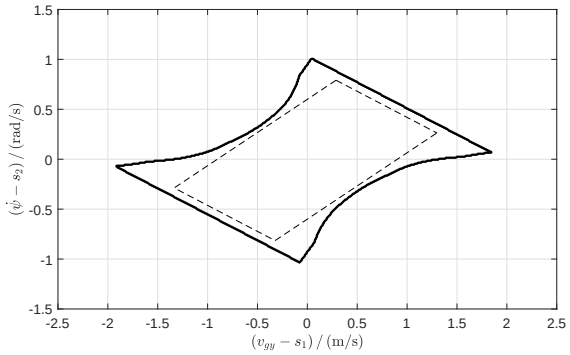

(a) Parallelogram-shaped control-dependent safe set candidate for maximum $\delta = \pi/12$ rad (15°).

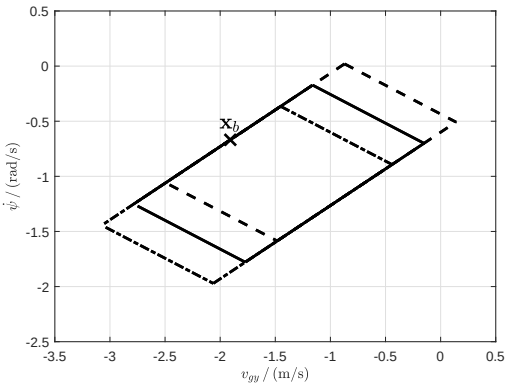

(b) Detail of the effect of changing δ for $\mathbf{x}_b$ at the boundary of the safe set for positive and negative steering angle changes.

Figure 45: Parallelogram-shaped control-dependent safe set candidate for $\mu = 0.8$, $v_{gx} = 60$ km/h, and a maximum $\delta = \pi/12$ rad (15°), for different steering angles. Dash-dot line: $\delta = 0.1571$ rad (8°). Continuous line: $\delta = 0.1745$ rad (10°). Dashed line: $\delta = 0.1920$ rad (12°).

mials, with b_1 and b_3 in the direction of $\mathbf{s}$, as depicted in Figure 45b. This causes h_2 and h_4 to be dependent on the control input δ_u, and h_1 and h_3 to be independent of it. The consequence is that when a state $\mathbf{x}_b$ is about to leave the safe set, e.g., through h_1 as in Figure 45b, the control input has no effect, and the state does trespass the barrier.

An investigation into the subject concludes that h_1 and h_3, as previously described, are in fact not control barrier functions, since they do not satisfy the condition expressed by (6.8) at the frontier. This is why we have used the expression "control barrier function candidate" when referring to them. There are two possible solutions for this problem: to use relative-degree-2 control barrier functions, as in Section 4.3.1, and to use a convex safe set that does not have a frontier that is parallel to $\mathbf{s}$.

Let us pursue the last solution. We propose a systematic procedure to obtain a parabolic control-dependent barrier function inscribed in any conservative stability region. This would result in an ellipsoidal control-dependent safe set, as presented in Figure 46. The CDBF which establishes the region from Figure 46 is obtained from successive lin-

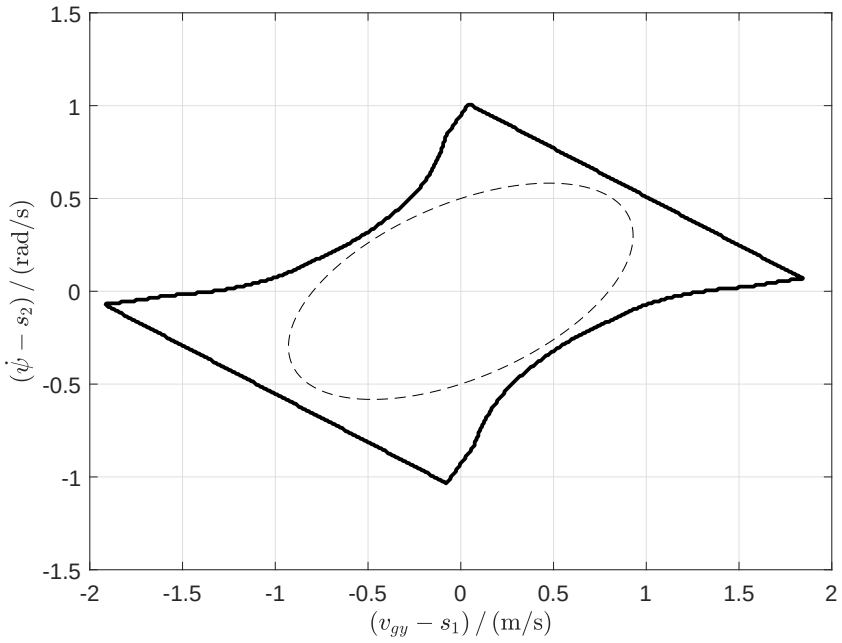

Figure 46: Ellipse-shaped safe set for a conservative stability region with $v_{gx} = 60$ km/h, $\mu = 0.8$, and varying δ.

ear transformations from the parallelogram inscribed in the conservative stability region (e.g., Figure 45a). To obtain further conservativeness, a margin between the inscribed parallelogram and the stability region may be specified.

First, the parallelogram is obtained from a conservative stability region. Let its sides be b_i, $i \in \{1, 2, 3, 4\}$, as in Figure 47a, and its vertices be P_1, P_2, P_3, P_4, defined, in the

respective order, as the coordinates of the intersections of b_1 and b_2, b_2 and b_3, b_3 and b_4 and b_1 and b_4. We can transform the parallelogram from Figure 47a into the rhombus

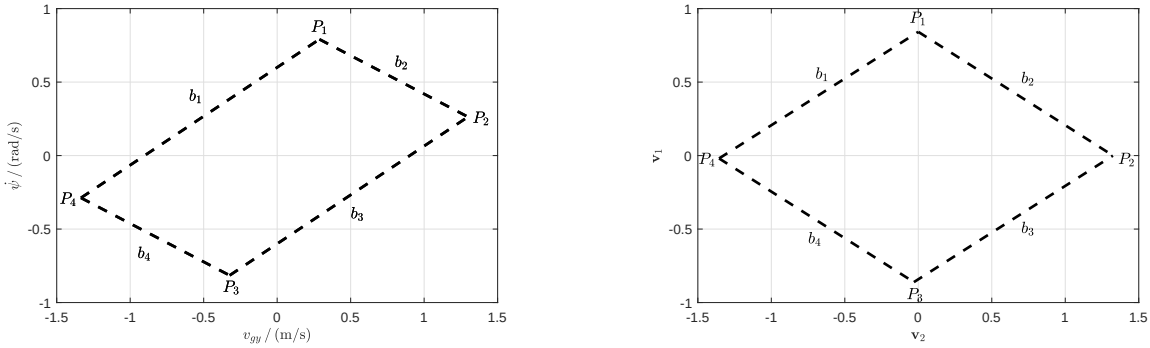

(a) Parallelogramic region where the elliptic safe set shall be inscribed.

(b) Rhombic region which results from the first linear transformation.

Figure 47: Safe set linear transformation.

from Figure 47b by applying a base change to v_{gy}, $\dot{\psi}$ defined by the base-change matrix

$$\mathbf{P}_1 \triangleq [\mathbf{v}_2 \;\; \mathbf{v}_1]^{-1}, \quad \mathbf{v}_1 = P_1, \quad \mathbf{v}_2 = P_2. \tag{6.16}$$

Subsequently, we can change the rhombus into an inclined square through another base change, described by

$$\mathbf{P}_2 \triangleq \operatorname{diag}\left\{\frac{v_1}{v_2}, 1\right\}. \tag{6.17}$$

In (6.17), v_1 and v_2 are obtained from the coordinates of the vertices of the rhombus, which are $[0 \;\; \pm v_1]$ and $[\pm v_2 \;\; 0]$. Subsequently, the inclined square is transformed into an upright one by a 45° rotation matrix given by

$$\mathbf{P}_3 \triangleq \begin{bmatrix} \cos(\frac{\pi}{4}) & \sin(\frac{\pi}{4}) \\ -\sin(\frac{\pi}{4}) & \cos(\frac{\pi}{4}) \end{bmatrix}. \tag{6.18}$$

The transformations that result from $\mathbf{P}_1$, $\mathbf{P}_2$ and $\mathbf{P}_3$ are depicted in Figure 48a. The next steps are to inscribe a circle into the upright square, and then gradually change it into an ellipse that is inscribed into the parallelogram from Figures 45a or 47a.

We then inscribe a circle with radius a equal to half the side of the upright square in it, described by

$$\frac{x^2}{a^2} + \frac{y^2}{a^2} - 1 = 0, \tag{6.19}$$

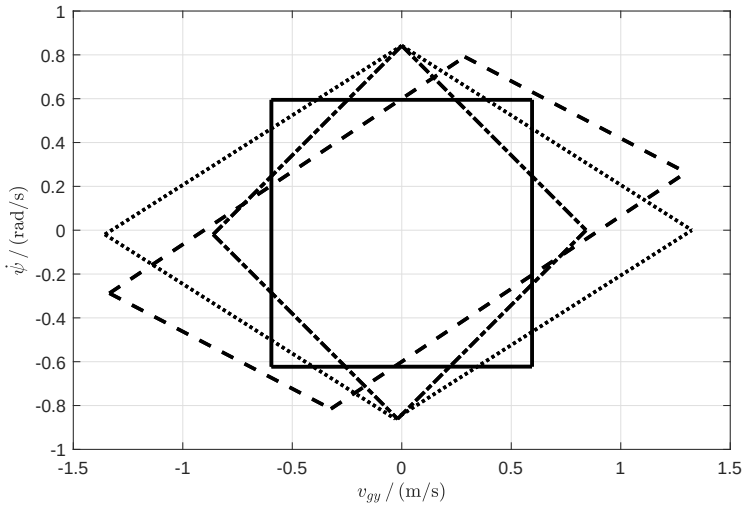

(a) Linear transformations from a parallelogram to an upright square. Dashed line: original parallelogram. Dotted line: first transformation, rhombus. Dash-dot line: second transformation, inclined square. Continuos line: third transformation, upright square.

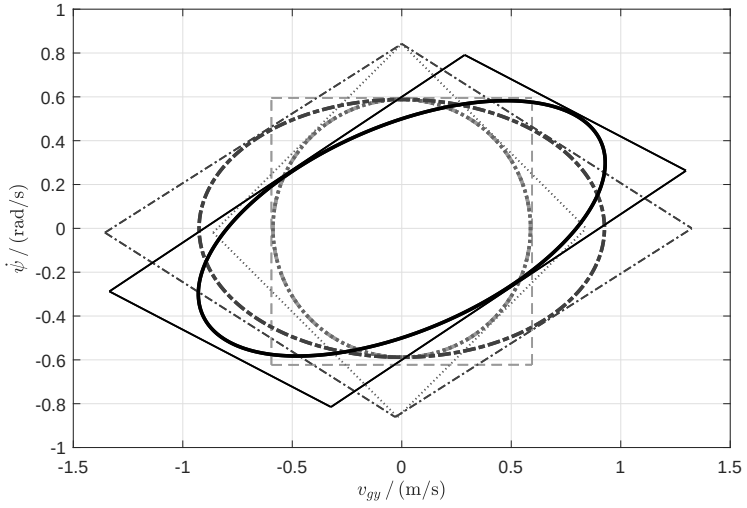

(b) Relative transformations from an inscribed circle to an inscribed ellipse. Dashed line: inscription in the upright square. Dotted line: inscription in the inclined square. Dash-dot line: inscription in the rhombus. Continuos line: inscription in the parallelogram.

Figure 48: Iterative transformations for obtaining a parabolic CDBF.

or

$$\begin{bmatrix} v_{gy} \\ \dot{\psi} \end{bmatrix}^{\mathrm{T}} \begin{bmatrix} \frac{1}{a^2} & 0 \\ 0 & \frac{1}{a^2} \end{bmatrix} \begin{bmatrix} v_{gy} \\ \dot{\psi} \end{bmatrix} - 1 = 0, \tag{6.20}$$

in matrix form.

The circle can be inscribed into the inclined square by using

$$\left(\mathbf{P}_3 \begin{bmatrix} v_{gy} \\ \dot{\psi} \end{bmatrix} \right)^{\mathrm{T}} \begin{bmatrix} \frac{1}{a^2} & 0 \\ 0 & \frac{1}{a^2} \end{bmatrix} \mathbf{P}_3 \begin{bmatrix} v_{gy} \\ \dot{\psi} \end{bmatrix} - 1 = 0, \tag{6.21}$$

into the rhombus by

$$\left(\mathbf{P}_3\mathbf{P}_2 \begin{bmatrix} v_{gy} \\ \dot{\psi} \end{bmatrix} \right)^{\mathrm{T}} \begin{bmatrix} \frac{1}{a^2} & 0 \\ 0 & \frac{1}{a^2} \end{bmatrix} \mathbf{P}_3\mathbf{P}_2 \begin{bmatrix} v_{gy} \\ \dot{\psi} \end{bmatrix} - 1 = 0, \tag{6.22}$$

and into the parallelogram by

$$\left(\mathbf{P}_3\mathbf{P}_2\mathbf{P}_1 \begin{bmatrix} v_{gy} \\ \dot{\psi} \end{bmatrix} \right)^{\mathrm{T}} \begin{bmatrix} \frac{1}{a^2} & 0 \\ 0 & \frac{1}{a^2} \end{bmatrix} \mathbf{P}_3\mathbf{P}_2\mathbf{P}_1 \begin{bmatrix} v_{gy} \\ \dot{\psi} \end{bmatrix} - 1 = 0. \tag{6.23}$$

The successive transformations from (6.21)–(6.23) are shown in Figure 48b. Then $h(\mathbf{x}, u)$ can be obtained as

$$h(\mathbf{x}, u) = \left(\mathbf{P}_3\mathbf{P}_2\mathbf{P}_1 \begin{bmatrix} v_{gy} - s_1 \\ \dot{\psi} - s_2 \end{bmatrix} \right)^{\mathrm{T}} \begin{bmatrix} \frac{1}{a^2} & 0 \\ 0 & \frac{1}{a^2} \end{bmatrix} \mathbf{P}_3\mathbf{P}_2\mathbf{P}_1 \begin{bmatrix} v_{gy} - s_1 \\ \dot{\psi} - s_2 \end{bmatrix} + 1. \tag{6.24}$$

Before applying (6.24), we recall that there remains a problem, the steady-state value of δ_u in Section 6.1. The control input does not return to zero because the CDBF extension substitutes its derivate for it in the respective quadratic programming problem. The derivative is minimized instead, as a consequence.

We introduce an analogous extension to control Lyapunov functions to deal with this difficulty. We wish to also minimize the absolute value of u, which we accomplish by minimizing u^2. However, u does not depend on the state, but on the control input. Hence it is natural that we introduce a control-dependent Lyapunov function, defined as

Definition 7 (Control-dependent Lyapunov function)**.** *If $V(\mathbf{x}, \mathbf{u})$ is positive-definite, with the control input $\mathbf{u} \in \mathcal{U}$, $\omega_u \in \Omega_u$ and an extended class κ function γ such that*

$$\inf_{\omega_u \in \Omega_u} \left(L_{\hat{f}} V(\mathbf{x}, \mathbf{u}) \right) + \gamma(V(\mathbf{x}, \mathbf{u})) \leq 0, \tag{6.25}$$

then V is a control-dependent Lyapunov function*.*

We recall, based on (6.4), that

$$L_{\hat{f}}V(\mathbf{x},\mathbf{u}) = \frac{\partial V(\mathbf{x},\mathbf{u})}{\partial \mathbf{x}} f(\mathbf{x},\mathbf{u}) + \frac{\partial V(\mathbf{x},\mathbf{u})}{\partial \mathbf{u}} \omega_u. \tag{6.26}$$

Control-dependent Lyapunov functions (Definition 7) are much more general than the specific use we have just considered. Instead of simply minimizing the control input, they can be used to track a reference that depends on the control input.

Then we can adapt the CDBF-QP problem, including the CDLF condition as a soft constraint, and enunciate the CDLF-CDBF-QP problem as

$$\dot{\mathbf{u}}^\star = \underset{\dot{\mathbf{u}}_f \in \mathbb{R}^{m+1}}{\arg\min} \frac{1}{2} \dot{\mathbf{u}}_f^{\mathrm{T}} \mathbf{H} \dot{\mathbf{u}}_f + \mathbf{F}^{\mathrm{T}} \dot{\mathbf{u}}_f, \tag{6.27}$$

subject to

$$\begin{aligned} \frac{\partial V(\mathbf{x},\mathbf{u})}{\partial \mathbf{x}} f(\mathbf{x},\mathbf{u}) + \frac{\partial V(\mathbf{x},\mathbf{u})}{\partial \mathbf{u}} \dot{\mathbf{u}} + \gamma(V(\mathbf{x},\mathbf{u})) - \delta_s \leq 0, \\ \frac{\partial h(\mathbf{x},\mathbf{u})}{\partial \mathbf{x}} f(\mathbf{x},\mathbf{u}) + \frac{\partial h(\mathbf{x},\mathbf{u})}{\partial \mathbf{u}} \dot{\mathbf{u}} + \zeta(h(\mathbf{x},\mathbf{u})) \geq 0, \end{aligned}$$

where $\dot{\mathbf{u}}_f \triangleq [\dot{\mathbf{u}} \;\; \delta_s]^{\mathrm{T}}$. Similarly to the CLF-CBF-QP problem, expressed in (4.21), δ_s is a relaxation variable used to make the stability or tracking objectives a soft constraint. The safety restriction, which uses h, remains a hard constraint.

The desirable tracking condition for the AFS application is that the steering angle change from the ESC system, given by δ_u, is null whenever possible. This can be achieved by a trivial quadratic CDLF written as

$$V(\mathbf{x}, u) = V(u) = u^2. \tag{6.28}$$

We are now able to fully specify the CDLF-CDBF-QP problem for the AFS application in study. We have

$$\mathbf{H} = \begin{bmatrix} p_u & 0 \\ 0 & p_\delta \end{bmatrix}, \qquad \mathbf{F} = \begin{bmatrix} 0 \\ 0 \end{bmatrix}, \tag{6.29}$$

with p_u and p_δ as the penalty weights for ω_u and δ_s, respectively; $h(\mathbf{x},\mathbf{u})$ given by (6.24); and $V(\mathbf{x}, u)$ given by (6.28).

Third-party optimization software is likely to require problems to be expressed in standard form. The QP in (6.27) satisfies this requirement, but the restrictions that follow do not. With this objective in mind, we can rewrite them as

$$\mathbf{A}_{qp} \dot{\mathbf{u}}_f \leq \mathbf{b}_{qp}, \tag{6.30}$$

with

$$\mathbf{A}_{qp} \triangleq \begin{bmatrix} \frac{\partial V(\mathbf{x},\mathbf{u})}{\partial \mathbf{u}} & -1 \\ -\frac{\partial h(\mathbf{x},\mathbf{u})}{\partial \mathbf{u}} & 0 \end{bmatrix}, \tag{6.31}$$

$$\mathbf{b}_{qp} \triangleq \begin{bmatrix} -\frac{\partial V(\mathbf{x},\mathbf{u})}{\partial \mathbf{x}} f(\mathbf{x},\mathbf{u}) - \gamma(V(\mathbf{x},\mathbf{u})) \\ \frac{\partial h(\mathbf{x},\mathbf{u})}{\partial \mathbf{x}} f(\mathbf{x},\mathbf{u}) + \zeta(h(\mathbf{x},\mathbf{u})) \end{bmatrix}. \tag{6.32}$$

The class-κ functions $\gamma(\cdot)$ and $\zeta(\cdot)$ are defined as

$$\gamma(V(\mathbf{x},\mathbf{u})) = c_V V(\mathbf{x},\mathbf{u}) \qquad \zeta(h(\mathbf{x},\mathbf{u})) = c_h h(\mathbf{x},\mathbf{u}), \tag{6.33}$$

where c_V is related to the convergence rate of u to zero when the safety requirements are not at risk and c_h is related to how fast the state is pulled away by the barrier function.

The present the implementation details and results in Section 6.2.0.1.

6.2.0.1 Active Front Steering Implementation with Control-Dependent Barrier Functions

We consider a vehicle described by (2.117)–(2.118), at first. This means we consider only the lateral movement of the vehicle, disregarding (2.116) entirely and ignoring the longitudinal projection of the lateral tire forces. The vehicle parameters are those from Table 1.

The tire dynamics dictates the remaining forces in (2.117)–(2.118), i.e., the lateral forces generated by the tires. They are described by the pure side-slip equation set from (PACEJKA, 2012), expressed by (2.61)–(2.73). The parameters are presented in Table 2 (see Section 5.1.2).

The control design considered a conservative stability region for $\delta \in \{-\pi/12 \text{ rad}, \pi/12 \text{ rad}\}$ ($\{-15°, 15°\}$), $v_{gx} \in \{60 \text{ km/s}, 80 \text{ km/s}\}$, and $\mu \in \{0.8, 1.0\}$.

Table 3: Controller parameters

Parameter	Value
p_u	0.1
p_δ	200
c_V	50
c_h	100

The block diagram of the closed-loop system is shown in Figure 49. Since the CDLF-CDBF-QP problem has the derivative of the input as its decision variable, it is necessary to integrate the control system output $\dot{\delta}_u$. Since the control-dependent barrier functions

depend on the input, their Lie derivatives depend on derivative of the steering angle. Hence δ_d must be differentiable and $\dot{\delta}_d$ is also needed by the QP.

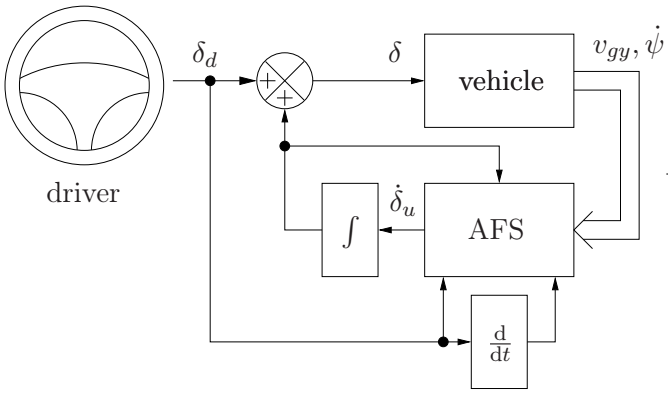

Figure 49: Block diagram of the AFS based on the CDLF-CDBF-QP problem.

A J-turn maneuver was considered, with its respective driver input presented in Figure 50. The maneuver has the front steering wheels move in a counter-clockwise direction for 1 s, maintain an angle of 0.2 rad for 7 s, and then return forward within 1 s, while keeping a longitudinal speed of 60 km/h (16.67 m/s). This steering angle magnitude is beyond the stability limits of the vehicle.

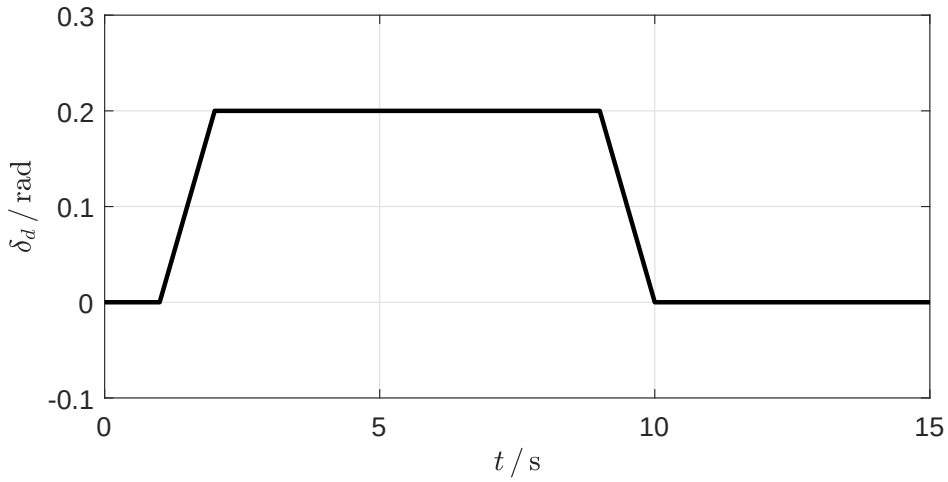

Figure 50: J-turn driver input.

The quadratic programming algorithm from (HILDRETH, 1957) solves the standard-form CDLF-CDBF-QP problem in our implementation, which was adapted from (WANG, 2009). The results matched those from the default interior-point algorithm for convex problems from the MATLAB function `quadprog`.

As with ordinary zeroing barrier functions, control-dependent barrier functions are a measure of system safety. Positive values are related to states that belong in the safe

set; null values are associated with the frontier of the safe set; while negative values show that the safety restrictions were disrespected. In particular, Figure 51 presents the CDBF expressed by (6.24) as a function of time for the J-turn maneuver from Figure 50. We observe that it does not assume negative values. When the driver maintains the steering angle at 0.2 rad, the CDBF approaches zero but remains positive. When the steering angle returns to zero, the CDBF increases.

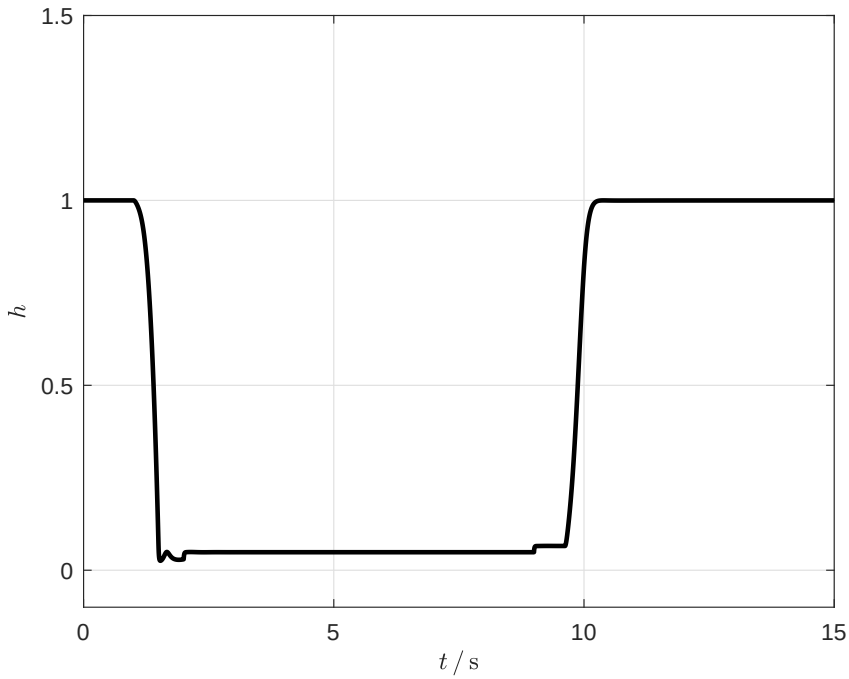

Figure 51: Control-dependent barrier function.

The safety restrictions can also be observed from the perspective of the safe set. However, since it depends on the steering input, the safe set and the state move with δ_d. This can be easily seen through an animation. In printed material, the alternative is to use the shifting vector s—as Figure 52 depicts—so the the sate moves as a function of time and δ_d while the safe set remains fixed. As expected from Figure 51, the shifted state is inside the safe set at all times, during the maneuver.

The way the active front steering system maintains stability is intuitive: it reduces the steering angle, which is exaggerated for the vehicle's speed. Figure 53 shows that the AFS ESC system counteracts more than half of the driver's input. As a consequence, the steady-state value of the steering angle is around 0.063 rad, or 3.6°.

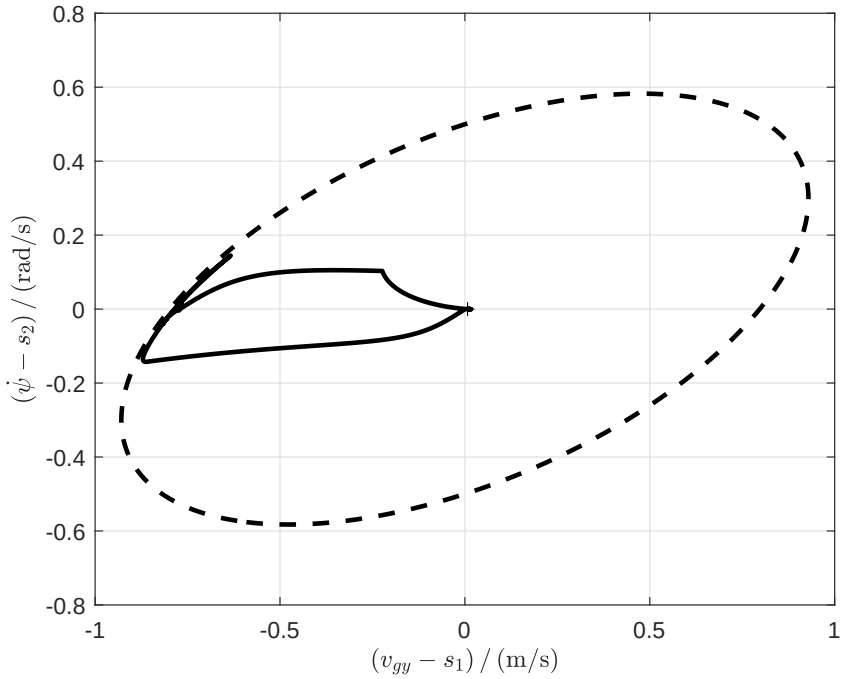

Figure 52: System state shifted by $\mathbf{s}$ and the centered safe set. Dashed line: safe set. Continuous line: shifted state.

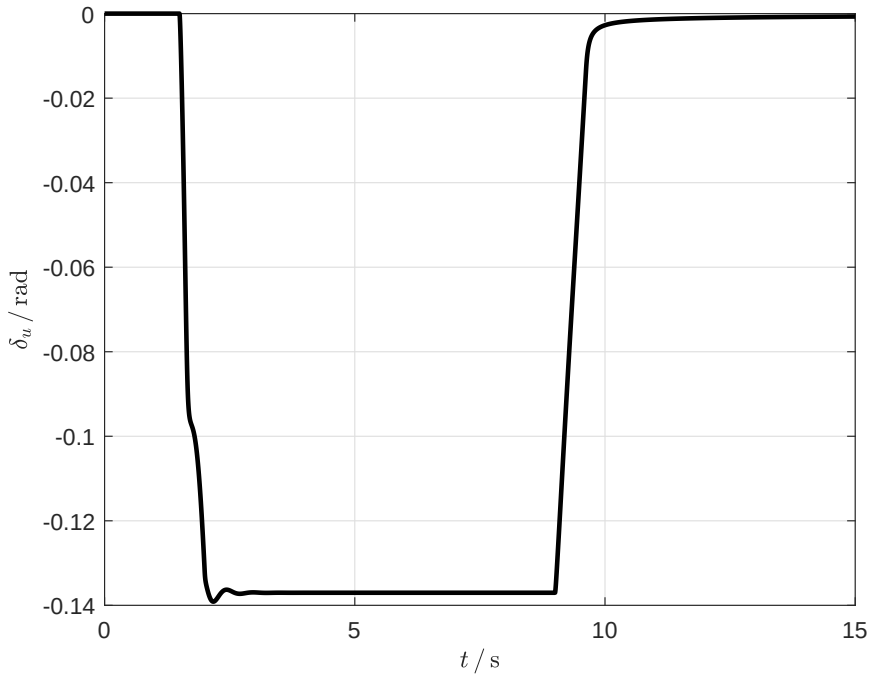

Figure 53: Control input for the J-turn maneuver.

6.2.1 Conclusions from this AFS implementation

This section presented an effective AFS ESC system that keeps the simplified vehicle state (lateral speed and yaw rate) within a subset of a lateral stability region. When the ESC system is not active, the steering wheels behave as if the ESC system did not exist. In particular, there is no steady-state error between the actual steering angles of the front wheels and the expected angle from the steering wheel movements from the driver.

The vehicle cannot leave the safe set, which is an ellipse that is a strictly proper subset of the stability regions presented in Chapter 5. Therefore, the closed-loop system is conservative in the sense that larger safe sets would allow the vehicle to move more freely, before the ESC system intervention.

The aforementioned contributions have been accomplished by extending the CDBF-QP problem to include CDLFs, and by avoiding situations when the CDBF conditions are not respected, namely when the derivatives of the control barrier functions are zero with respect to the control input.

Our proposal, however, as presented here, has a few shortcomings. The first one results from the studies we have used as a reference, which hadn't used a standard test to validate the system (HUANG; YONG; CHEN, 2019, 2021). While the J-turn is a standard maneuver, the one used therein does not follow the standard. Moreover, this test is applied to large vehicles such as buses, not passenger cars, and is more related to roll instability (NHTSA, 2001).

A second limitation is the allowed set of states the vehicle can reach before triggering an intervention from the ESC system. A larger safe set might be used, but the current safety-critical control theory would not allow for that. Consequently, a strictly convex set was selected as the safe set, instead of a parallelogram such as in Figure 45a.

Another conservative aspect of the proposed control system does not result from the control method itself but from the stability criteria. More specifically, the controllability criterion. In Chapter 5, we have chosen the individual tire stiffnesses as criteria. However, we have proposed an AFS system, not an all-wheel steering system, where every wheel steering angle is an input. Thus, the front and rear axles' stiffness could be used instead.

Finally, the simulated vehicle had a quite simplified model. While we did model tire lateral forces more thoroughly than most studies, we ignored longitudinal tire forces. In fact, the longitudinal forces were generally not described, nor were the suspension (roll, pitch, vertical movements) and compliance effects. These aspects have been considered

in Section 6.3.

6.3 Active front steering with control barrier fuctions of higher relative degree

Section 6.2 presented an active front steering ESC that uses a systematic method for obtaining appropriate control barrier functions so that the closed-loop system can guarantee safety, i.e., safety set invariance. This comes at the cost of reducing the safety set from the hourglass-like shapes from Chapter 5 to an inclined ellipse [$h(\mathbf{x}, u) = 0$ in (6.24)]. Hence the control system is conservative. The proposed solution avoids the areas that make the stability regions concave—those that are related to situations when invariance cannot be guaranteed, as seen in Figure 44—but also avoids other areas from the parallelogram-shaped set (Figure 45a) where the ellipse is inscribed.

We did mention that choosing b_1, b_2, b_3, and b_4 as straight lines (Figure 45b) and defining h_1, h_2, h_3, and h_4 as in (6.10)–(6.13) would result in h_1 and h_2 not being control barrier functions due to not satisfying (6.8). We propose to once-again extend the safety-critical control theory, this time to incorporate control-dependent high-relative-degree barrier or Lyapunov functions. Control barrier functions of higher relative degrees have been reviewed in Section 4.3.1. Section 6.3.1 presents the extension.

6.3.1 Control-dependent exponential barrier functions

Let $h(\mathbf{x}, \mathbf{u})$ be a concave function with respect to $\mathbf{x}$ and related to a safe set defined by $\forall \mathbf{x}\colon h(\mathbf{x}, \mathbf{u}) \geq 0$. Let $\partial h(\mathbf{x}, \mathbf{u})/\partial \mathbf{u} = 0$. Then, by definition, the relative degree of h is not one, and it is impossible to use $\mathbf{u}$ as the decision variable in the QP (6.14) since its coefficient in (6.15) is null. We wish to extend the QP problem to include control-dependent exponential barrier functions of an arbitrary relative degree r.

Let $\mathbf{u} \in \mathcal{U} \subset \mathbb{R}^m$ be an rth time differentiable input vector. Then we can extend the state from (6.4) as

$$\hat{\mathbf{x}} \triangleq \begin{bmatrix} \mathbf{x} \\ \mathbf{u} \\ \dot{\mathbf{u}} \\ \vdots \\ \mathbf{u}^{(r-1)} \end{bmatrix}. \tag{6.34}$$

Let the linearized state η_b be defined as

$$\eta_b(\mathbf{x},\mathbf{u}) \triangleq \begin{bmatrix} h(\mathbf{x},\mathbf{u}) \\ \dot{h}(\mathbf{x},\mathbf{u}) \\ \vdots \\ \mathbf{h}^{(r-1)}(\mathbf{x},\mathbf{u}) \end{bmatrix}. \tag{6.35}$$

Then we can write the linearized system as in Section 4.3.1, (4.24) i.e.,

$$\dot{\eta}_b(\mathbf{x},\mathbf{u}) = \bar{\mathbf{F}}\eta_b(\mathbf{x},\mathbf{u}) + \bar{\mathbf{G}}\mu_i \tag{6.36}$$

$$h(\mathbf{x},\mathbf{u}) = \bar{\mathbf{C}}\eta_b(\mathbf{x},\mathbf{u}), \tag{6.37}$$

with

$$\bar{\mathbf{F}} = \begin{bmatrix} \mathbf{0}_{(r-1)\times 1} & \mathbf{I}_{r-1} \\ 0 & \mathbf{0}_{1\times(r-1)} \end{bmatrix} \qquad \bar{\mathbf{G}} = \begin{bmatrix} \mathbf{0}_{(r-1)\times 1} \\ 1 \end{bmatrix}$$

$$\bar{\mathbf{C}} = \begin{bmatrix} 1 & \mathbf{0}_{1\times(r-1)} \end{bmatrix} \qquad \mu_i = h^{(r)}(\mathbf{x},\mathbf{u}),$$

but now with h also depending on the input vector.

The extension to higher relative-degree control-dependent Lyapunov functions is analogous to (6.35)–(6.36). First, let $P_{\gamma r}$ and $P_{\zeta r}$ be two r-degree Hurwitz polynomials on V and h, in the respective order, given by

$$P_{\gamma r} = \lambda^r + k_{\gamma 1}\lambda^{r-1} + k_{\gamma 2}\lambda^{r-2} + \cdots + k_{\gamma r} \tag{6.38}$$

$$P_{\zeta r} = \lambda^r + k_{\zeta 1}\lambda^{r-1} + k_{\zeta 2}\lambda^{r-2} + \cdots + k_{\zeta r}. \tag{6.39}$$

Next, let $\mathbf{K}_{\gamma r}$, $\mathbf{K}_{\zeta r}$ be the coefficient matrices

$$\mathbf{K}_{\gamma r} = [k_{\gamma r} \quad k_{\gamma r-1} \quad \dots \quad k_{\gamma 1}] \tag{6.40}$$

$$\mathbf{K}_{\zeta r} = [k_{\zeta r} \quad k_{\zeta r-1} \quad \dots \quad k_{\zeta 1}] \tag{6.41}$$

with respect to $P_{\gamma r}$ and $P_{\zeta r}$. Consequently, defining $\dot{\mathbf{u}}_f \triangleq [\dot{\mathbf{u}} \;\; \delta_s]$, we can write the QP as

$$\dot{\mathbf{u}}_\mathbf{f}^\star = \underset{\dot{\mathbf{u}}_f \in \mathbb{R}^{m+1}}{\arg\min} \frac{1}{2}\dot{\mathbf{u}}_f^{\mathrm{T}}\mathbf{H}\dot{\mathbf{u}}_f + \mathbf{F}^{\mathrm{T}}\dot{\mathbf{u}}_f, \tag{6.42}$$

subject to

$$V^{(r)}(\mathbf{x},\mathbf{u}) + \mathbf{K}_{\gamma r}\eta_v(\mathbf{x},\mathbf{u}) - \delta_s \leq 0,$$

$$h^{(r)}(\mathbf{x},\mathbf{u}) + \mathbf{K}_{\zeta r}\eta_b(\mathbf{x},\mathbf{u}) \geq 0,$$

where $\eta_b \triangleq [V(\mathbf{x},\mathbf{u}) \quad \dot{V}(\mathbf{x},\mathbf{u}) \quad \dots \quad V^{(r-1)}(\mathbf{x},\mathbf{u})]$. We dub (6.42) the CDELF-CDEBF quadratic problem, from control-dependent exponential control Lyapunov function (CDELF) and the analogous control-dependent exponential control barrier function (CDELF) that are used in the restrictions.

For instance, let $\mathbf{u} = u$ be a scalar and $r = 2$. Then

$$\dot{h}(\mathbf{x},u) = \frac{\partial h}{\partial \mathbf{x}}\dot{\mathbf{x}} + \frac{\partial h}{\partial u}\dot{u} = \frac{\partial h}{\partial \mathbf{x}}\dot{\mathbf{x}} = L_f h(\mathbf{x},u), \tag{6.43}$$

since $\partial h/\partial u = 0$. The 2nd-order derivative of h is

$$\ddot{h}(\mathbf{x},u) = \frac{\partial L_f h}{\partial \mathbf{x}}\dot{\mathbf{x}} + \frac{\partial L_f h}{\partial u}\dot{u}. \tag{6.44}$$

If we substitute (4.5) and $\omega_u = u$ [see (6.4)] in (6.44), then

$$\begin{aligned}\ddot{h}(\mathbf{x},u) &= \frac{\partial L_f h}{\partial \mathbf{x}} f(\mathbf{x}) + \frac{\partial L_f h}{\partial u}\omega_u \\ &= L_f L_f h + L_g L_f h \omega_u.\end{aligned} \tag{6.45}$$

Hence the relative-degree-two CDELF-CDEBF quadratic problem is written as (6.42), but subject to

$$\begin{aligned}\frac{\partial L_f V}{\partial \mathbf{x}} f(\mathbf{x}) + \frac{\partial L_f V}{\partial u}\omega_u + k_{\gamma 2} V(\mathbf{x},\mathbf{u}) + k_{\gamma 1}\dot{V}(\mathbf{x},\mathbf{u}) - \delta_s \leq 0, \\ \frac{\partial L_f h}{\partial \mathbf{x}} f(\mathbf{x}) + \frac{\partial L_f h}{\partial u}\omega_u + k_{\zeta 2} h(\mathbf{x},\mathbf{u}) + k_{\zeta 1}\dot{h}(\mathbf{x},\mathbf{u}) \geq 0,\end{aligned}$$

or, in standard form,

$$\begin{bmatrix}\omega_u^\star \\ \delta_s^\star\end{bmatrix} = \underset{\omega_u,\delta_s\in\mathbb{R}}{\arg\min} \begin{bmatrix}\omega_u & \delta_s\end{bmatrix} \begin{bmatrix}p_u & 0 \\ 0 & p_\delta\end{bmatrix} \begin{bmatrix}\omega_u \\ \delta_s\end{bmatrix} \tag{6.46}$$

subject to

$$\begin{bmatrix}\frac{\partial L_f V}{\partial u} & -1 \\ -\frac{\partial L_f h}{\partial u} & 0\end{bmatrix} \leq \begin{bmatrix}-\frac{\partial L_f V}{\partial \mathbf{x}} f(\mathbf{x}) - k_{\gamma 2} V(\mathbf{x},\mathbf{u}) - k_{\gamma 1}\dot{V}(\mathbf{x},\mathbf{u}) + \delta_s \\ \frac{\partial L_f h}{\partial \mathbf{x}} f(\mathbf{x}) + k_{\zeta 2} h(\mathbf{x},\mathbf{u}) + k_{\zeta 1}\dot{h}(\mathbf{x},\mathbf{u})\end{bmatrix}. \tag{6.47}$$

6.3.1.1 Control-dependent exponential barrier function Implementation

We are now able to consider a slightly less conservative safe set than the one used in Section 6.2. More specifically, we shall avoid the stability region areas that make them concave—since reaching them may lead to situations when it is impossible to guarantee the safe set invariance—and nothing else. As a consequence, we shall try and use a safe set like the one from Figure 45.

We recall from Section 6.2 that the parallelogram-shaped set from Figure 45 cannot be rendered safe by using the current control-dependent CBF theory (HUANG; YONG; CHEN, 2019, 2021) using a single steering axle. The theory from Section 6.3.1 is used to solve this problem.

Before applying the theory here, we mention that the steering input from (HUANG; YONG; CHEN, 2019) and Section 6.2 cannot be considered a reliable test for lateral stability, and we shall henceforth use the Sine with Dwell test instead, as justified in Section 3.3.

In addition, since the longitudinal speed loss which results from both AFS or differential braking also helps regain lateral stability, we shall employ models that can explain this phenomenon.

The loss of longitudinal speed during the actuation of an ESC system has a benefic impact on the stability recovery of the vehicle (NHTSA, 2009). This is not directly observable from the stability regions seen in Chapter 5, however. The stability regions do become larger as the longitudinal speed increases (see Figure 30). Still, while it is true that the stability region reduction due to friction coefficient is related to vehicle instability, the opposite is untrue for longitudinal speed, the reason being that larger longitudinal speeds are related to larger lateral accelerations through quadratic functions, i.e., for a fixed nonzero steering angle, doubling the longitudinal speed means increasing the lateral acceleration by a factor of 4, whereas the stability region becomes twice as large, only.

The vehicle model used in Sections 6.2 and 6.2.0.1 does not account for the longitudinal forces generated by the steering wheels. Accurate tire models that account for both longitudinal and lateral forces are much more complicated than the one used so far [Section 2.2.2, (2.55)–(2.59)]. Consequently, we use a combined slip magic formula model to describe the loss of longitudinal speed in this section. This allows us to employ (2.116) in the model, and also consider the longitudinal forces in (2.117) and (2.118). The description of such a model is more complex than the ones previously described and is out of the scope of this text. The equation set is presented in Appendix A. For further details, see (PACEJKA, 2012).

The other model that shall be used in this study is much more comprehensive than the one that has just been explained, i.e., simply adding combined slip to the body mass equations (2.116)–(2.118). The aforementioned model still lacks descriptions for vertical and roll movements, suspension, and powertrain. These, and many other aspects, are modeled in the CarSim software, which implements the Sine with Dwell test and presents

a plethora of realistic vehicle models.

Since this study is restricted to lateral stability, we selected a vehicle model that does not suffer from roll instability when moving over a horizontal plane. In particular, the C-class Hatchback vehicle. The Volkswagen Golf, Ford Focus, and Toyota Corolla Hatch are examples from this class.

In addition to it, since we are using the Magic Formula tire model, we have changed the default tire from the model to the one that has listed MF parameters. The original model tire is a 215/55 R17 one, described by the default software equations; we changed it to a 225/60 R18, simulated by MF-tyre. Hence we had access to the list of parameters needed by the set of equations listed in Appendix A. This modification aside, the default vehicle model was unchanged.

The parameters from the CarSim C-class Hatchback model have been used to generate stability regions, according to Chapter 5. Table 4 presents set of the parameters. In particular, we obtained a conservative effective stability region for $v_{gx} \geq 80$ km/h, $\mu \geq 0.85$, and $|\delta_d| \leq 5\pi/36$ rad (25°), but using the front and rear axle cornering stiffnesses as controllability criteria, instead of individual wheel cornering stiffnesses. This also made the stability region less conservative but does not make the system less safe, provided that the road grade bank is either null or towards the inside of the turn. The stability region and the inscribed safe set are depicted in Figure 54a, where the effect of relaxing the controllability criterion is clearly visible when comparing it with Figure 45a.

Table 4: C-class vehicle parameters

Parameter	Value
m_b	1413 kg
I_z	1536.7 kg·m^2
I_y	1536.7 kg·m^2
I_x	536.6 kg·m^2
l_1	1.015 m
l_2	1.895 m
L_w	1.675 m
h_g	0.54 m

We define h_1, h_2, h_3, and h_4 as (6.10)–(6.13). Hence they depend on $u \triangleq \delta_u$. Since h_2 and h_4 satisfy the ordinary control-dependent CBF conditions, they can be incorporated in the same manner as in Section 6.2. For h_1 and h_3, we have

$$L_g h_1(\mathbf{x}, u) = \frac{\partial h_1(\mathbf{x}, u)}{\partial u} = 0 \qquad L_g h_3(\mathbf{x}, u) = \frac{\partial h_3(\mathbf{x}, u)}{\partial u} = 0 \tag{6.48}$$

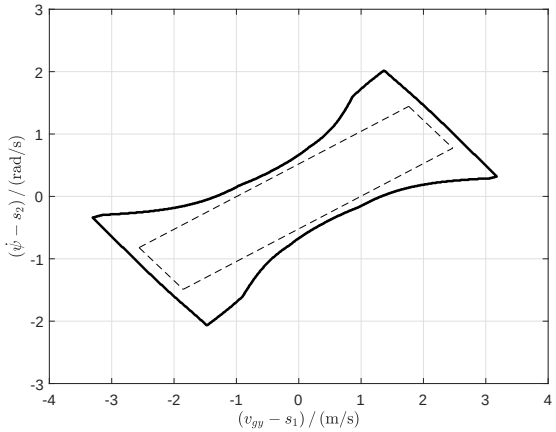

(a) Parallelogram-shaped control-dependent safe set inscribed in the conservative effective stability region.

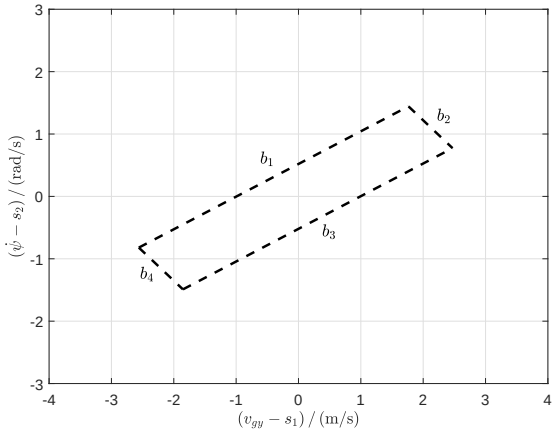

(b) First-order polynomials that define the control-dependent safe set.

Figure 54: Parallelogram-shaped control-dependent safe set for minimum $v_{gx} = 80$ km/h, minimum $\mu \geq 0.85$, and maximum $\delta = 5\pi/36$ rad (25°).

and

$$L_g L_f h_1(\mathbf{x}, u) = \frac{\partial L_g h_1(\mathbf{x}, u)}{\partial u} \neq 0 \qquad L_g L_f h_3(\mathbf{x}, u) = \frac{\partial L_g h_3(\mathbf{x}, u)}{\partial u} \neq 0. \tag{6.49}$$

Thus the relative degree of h_1 and h_3 is $r = 2$, and we can use the formulation from (6.45)–(6.47).

Since the default quadratic problems and (6.42) do not minimize the control input, we use (6.28), i.e., the same CDLF from Section 6.2,

$$V(\mathbf{x}, u) = V(u) = u^2. \tag{6.50}$$

We state the resulting quadratic problem as

$$\begin{bmatrix} \omega_u^\star \\ \delta_s^\star \end{bmatrix} = \underset{\omega_u, \delta_s \in \mathbb{R}}{\arg\min} \begin{bmatrix} \omega_u & \delta_s \end{bmatrix} \begin{bmatrix} p_u & 0 \\ 0 & p_\delta \end{bmatrix} \begin{bmatrix} \omega_u \\ \delta_s \end{bmatrix} \tag{6.51}$$

subject to

$$\begin{aligned} L_f V(\mathbf{x}, u) + L_g V(\mathbf{x}, u)\omega_u + \gamma(V(\mathbf{x}, \mathbf{u})) - \delta_s \leq 0, \\ L_f L_f h_1(\mathbf{x}, u) + L_g L_f h_1(\mathbf{x}, u)\omega_u + k_{\zeta 21} h_1(\mathbf{x}, u) + k_{\zeta 11} \dot{h}_1(\mathbf{x}, u) \geq 0 \\ L_f h_2(\mathbf{x}, u) + L_g h_2(\mathbf{x}, u)\omega_u + \zeta_2(h_2(\mathbf{x}, u)) \geq 0 \\ L_f L_f h_3(\mathbf{x}, u) + L_g L_f h_3(\mathbf{x}, u)\omega_u + k_{\zeta 23} h_3(\mathbf{x}, u) + k_{\zeta 13} \dot{h}_3(\mathbf{x}, u) \geq 0 \\ L_f h_4(\mathbf{x}, u) + L_g h_4(\mathbf{x}, u)\omega_u + \zeta_4(h_4(\mathbf{x}, u)) \geq 0 \end{aligned}$$

or, in standard form,

$$\begin{bmatrix} L_gV(\mathbf{x},u) & -1 \\ -L_gL_fh_1(\mathbf{x},u) & 0 \\ -L_gh_2(\mathbf{x},u) & 0 \\ -L_gL_fh_3(\mathbf{x},u) & 0 \\ -L_gh_2(\mathbf{x},u) & 0 \end{bmatrix} \leq \begin{bmatrix} -L_fV(\mathbf{x},u) - \gamma(V(\mathbf{x},\mathbf{u})) + \delta_s \\ L_fL_fh_1(\mathbf{x},u) + k_{\zeta 21}h_1(\mathbf{x},u) + k_{\zeta 11}\dot{h}_1(\mathbf{x},u) \\ L_fh_2(\mathbf{x},u) + \zeta_2(h_2(\mathbf{x},u)) \\ L_fL_fh_3(\mathbf{x},u) + k_{\zeta 23}h_3(\mathbf{x},u) + k_{\zeta 13}\dot{h}_3(\mathbf{x},u) \\ L_fh_4(\mathbf{x},u) + \zeta_4(h_4(\mathbf{x},u)) \end{bmatrix}. \tag{6.52}$$

The closed-loop system was initially validated through simulation, using increasingly more complex system models. For the sake of brevity, we briefly present two of them: the linearized model (2.124)–(2.125) and the nonlinear model (2.116)–(2.118) extended with a combined slip tire model (Appendix A). More comprehensive results are presented later on when a (much) more detailed vehicle simulator is employed using commercial software. Table 5 lists the controller parameters, where $\bar{v} \triangleq 9\mu v_{gx}/170$, whereas the block diagram remains the one for first-order control-dependent barrier and Lyapunov functions, i.e., Figure 49.

Table 5: CDEBF AFS controller parameters

Parameter	Value	Parameter	Value
p_u	1	b_{42}	$-3.243\bar{v}$
p_δ	100	γ	200
b_{11}	$1/l_2$	$k_{\zeta 21}$	900
b_{12}	$13/25\bar{v}$	$k_{\zeta 11}$	60
b_{21}	-0.9475	ζ_2	40
b_{22}	$3.115\bar{v}$	$k_{\zeta 23}$	900
b_{31}	$1/l_2$	$k_{\zeta 13}$	60
b_{32}	$-13/25\bar{v}$	ζ_4	40
b_{41}	-0.9460		

The linear model has no model error concerning the simple model used in the derivation of (6.52). Hence the safety restrictions are always satisfied, as shown in Figures 55 and 56.

Figure 57 shows the control input related to Figures 55 and 56. The input signal has opposite sign to the driver input, limiting the effective steering angle of the wheels and preventing the yaw rate and lateral speed from ever leaving the safe set.

The yaw rate satisfies the test requirements by large margins, as seen in Figure 58. The reductions of 65 % and 80 % at $T_0 + 1 = 2.93$ s and $T_0 + 1.75 = 3.68$ s, in the order, are already satisfied before $t = 1.82$ s, i.e., more than a full second before what the standard determines.

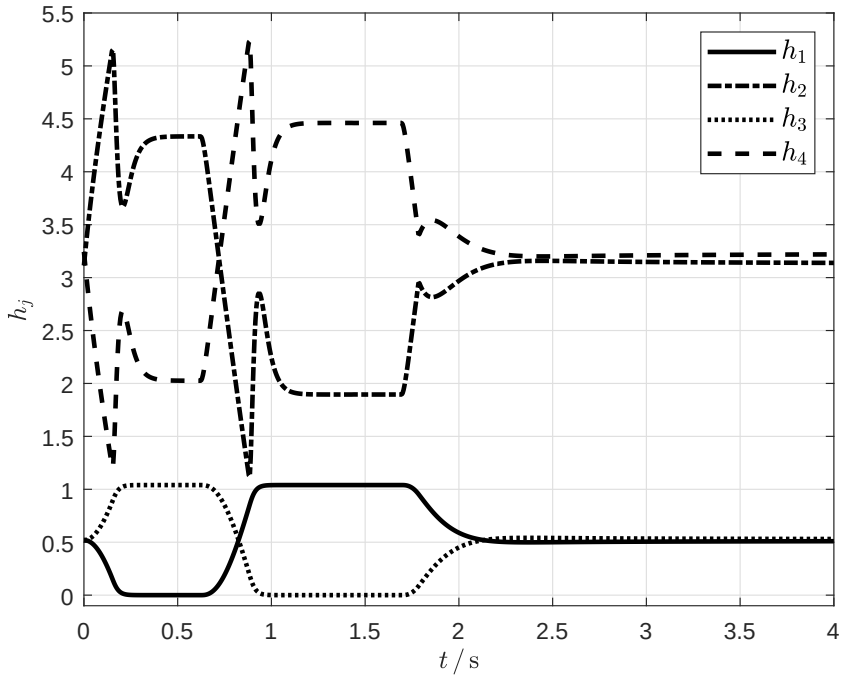

Figure 55: Barrier functions for the Sine with Dwell test, AFS with CDEBF, linearized system model, $\delta_{d\max} = 6.5A$. Continuous line: h_1. Dash-dot line: h_2. Dotted line: h_3. Dashed line: h_4.

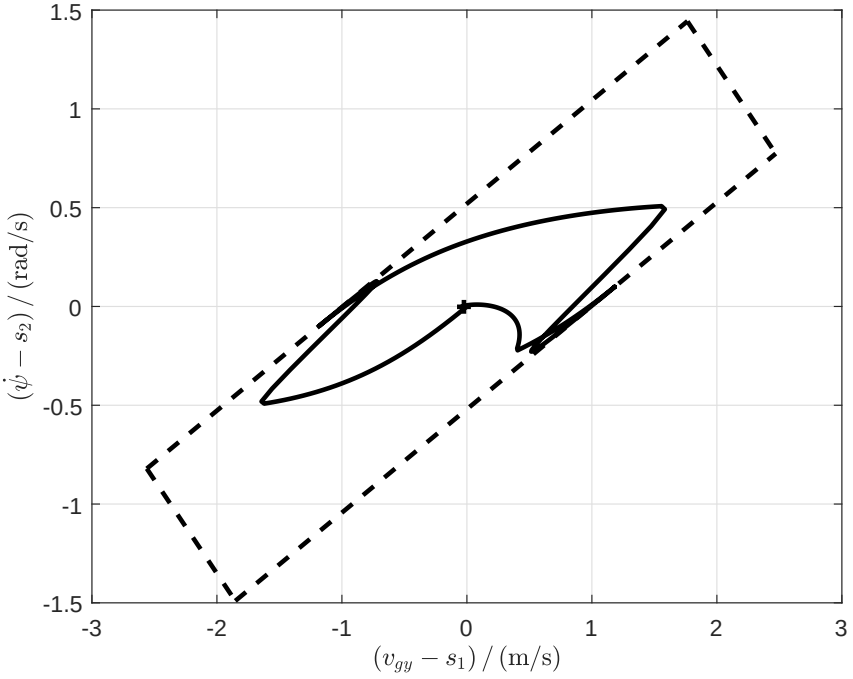

Figure 56: Control-dependent safe set for the Sine with Dwell test, AFS with CDEBF, linearized system model, $\delta_{d\max} = 6.5A$. Continuous line: shifted state trajectory. Dashed line: centered safe set.

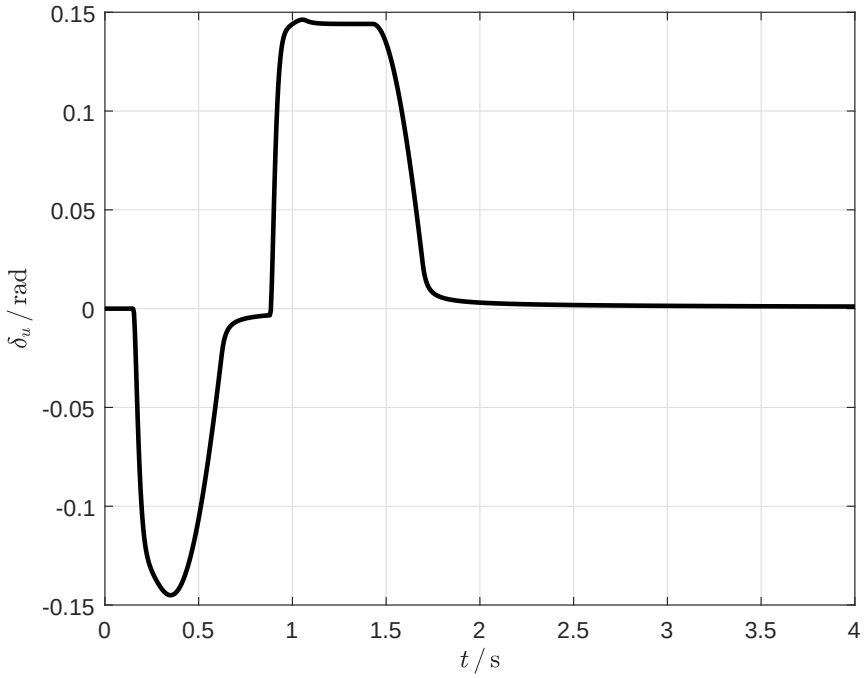

Figure 57: Control input δ_u for the Sine with Dwell test, AFS with CDEBF, linearized system model, $\delta_{d\max} = 6.5A$.

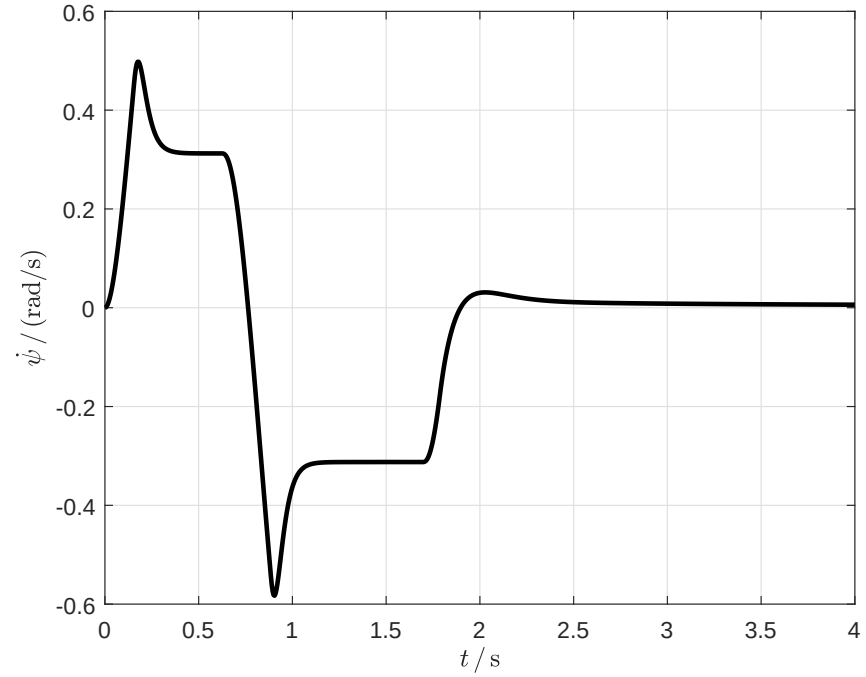

Figure 58: Yaw rate for the Sine with Dwell test, AFS with CDEBF, linearized system model, $\delta_{d\max} = 6.5A$.

Actual vehicles, however, are not perfectly described by linear models. They have many more state variables and saturation on the tire forces, among other aspects. More descriptive models, on the other hand, are more complex and more difficult to write in closed form, making it more difficult to use them in the control design stage. As a consequence, we tested the proposed AFS system, when using the linearized system for computing the Lie derivatives in (6.47), with further complex models. One of them was the nonlinear model considering the longitudinal dynamics for the body motion and combined slip for the wheel dynamics, i.e., (2.116)–(2.118) and the equation set from AppendixA.

One consequence of the impossibility of finding perfect models is shown in Figure 59, being hard to notice in Figure 60. The barrier functions h_1 and h_3 go slightly before zero: -0.0282, more precisely. This effect can easily be accommodated by being more conservative when selecting h_1 and h_3, or using the robust safety-critical control theory in the current literature (XU et al., 2015; CHINELATO; ANGÉLICO, 2021). The original safe set, shown in Figure 54a (continuous line), is not violated.

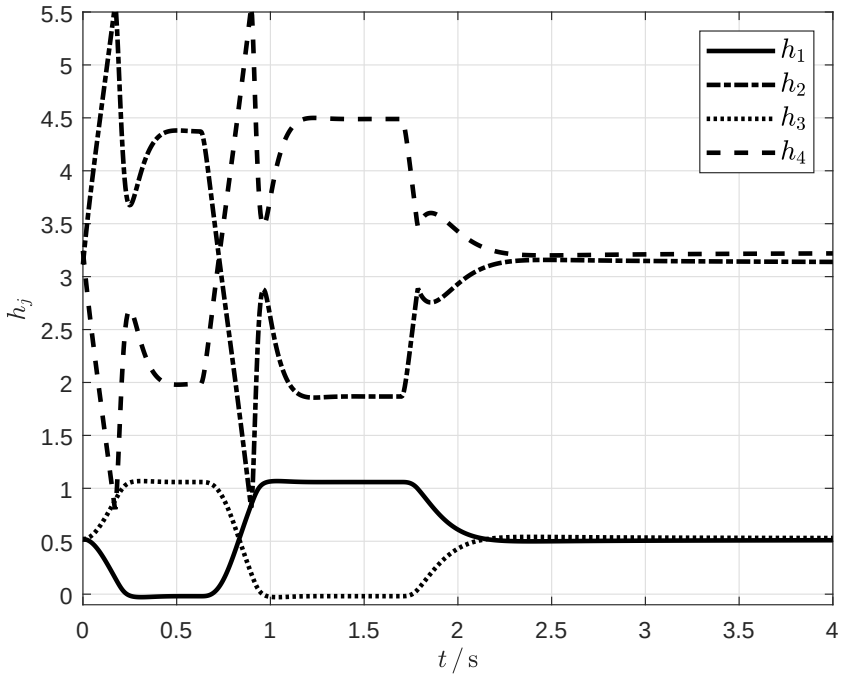

Figure 59: Barrier functions for the Sine with Dwell test, AFS with CDEBF, nonlinear model with combined slip, $\delta_{d\max} = 6.5A$. Continuous line: h_1. Dash-dot line: h_2. Dotted line: h_3. Dashed line: h_4.

Figure 61 presents the control input when using the nonlinear model. The signal is similar to the one from Figure 57: the respective comments still apply.

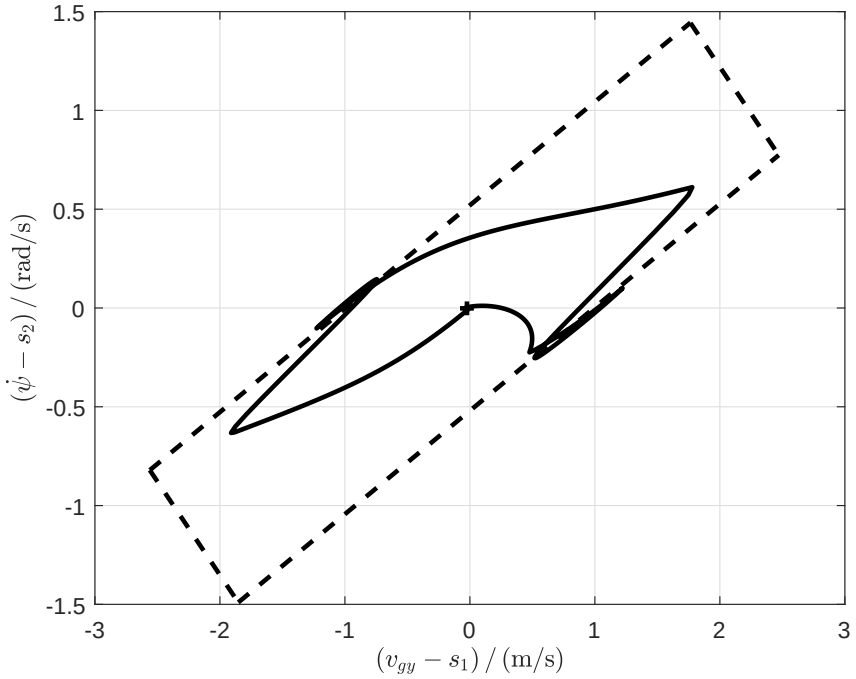

Figure 60: Control-dependent safe set for the Sine with Dwell test, AFS with CDEBF, nonlinear model with combined slip, $\delta_{d\max} = 6.5A$. Continuous line: shifted state trajectory. Dashed line: centered safe set.

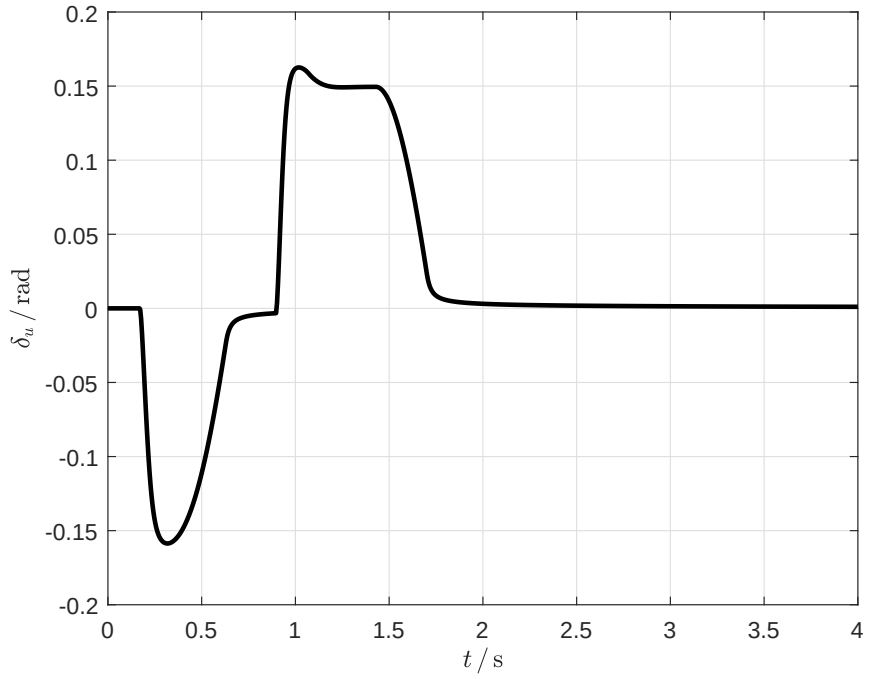

Figure 61: Control input δ_u for the Sine with Dwell test, AFS with CDEBF, nonlinear model with combined slip, $\delta_{d\max} = 6.5A$.

Despite small safe set violations, the yaw rate still satisfies the test requirements, by similar margins. Figure 62 shows the yaw rate with respect to time, where we can see that peaks are reduced by around 40 % in 200 ms or less, and the yaw rate is close to zero 500 ms after the end of steering. The reductions of 65 % and 80 % at $T_0 + 1 = 2.93$ s and $T_0 + 1.75 = 3.68$ s, in the order, are already satisfied before $t = 1.82$ s, i.e., more than a full second before what the standard determines.

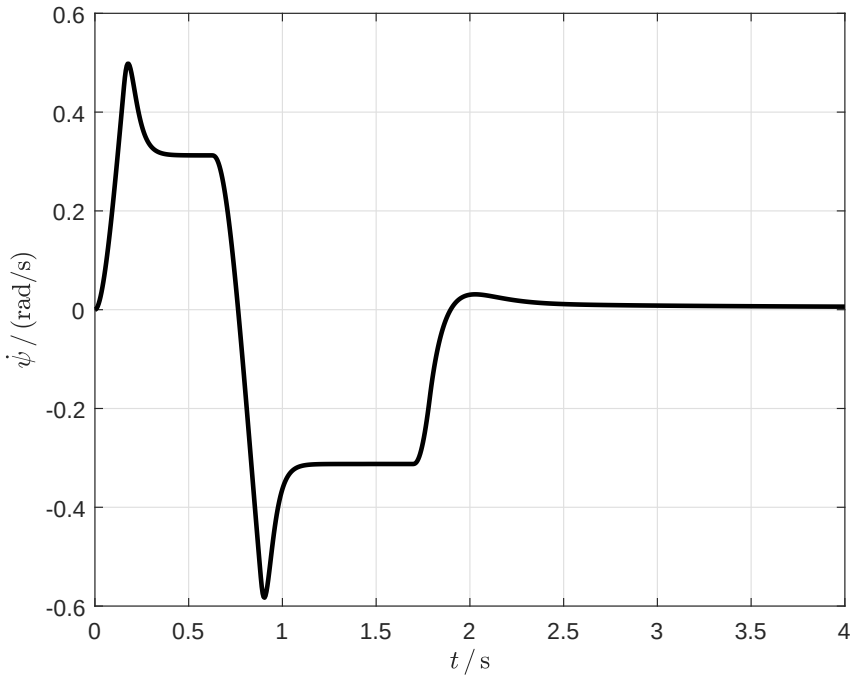

Figure 62: Yaw rate for the Sine with Dwell test, AFS with CDEBF, nonlinear model with combined slip, $\delta_{d\max} = 6.5A$.

The feedback system was further validated with CarSim, using the built-in Sine with Dwell test procedure, for the C-class Hatchback vehicle model. The vehicle has successfully completed the test, being subject to the steering wheel inputs presented in Figure 63.

The C-class Hatchback has a steering ratio of 20, which means the steering wheel angle is 20 times greater than the correspondent front wheel Ackermann steering angle, i.e., an equivalent wheel located in front of the vehicle, as if it was a tricycle. The $6.5A$ threshold is the 11th-largest steering wheel amplitude in Figure 63. The test goes on, however, since the correspondent steering wheel angle is not greater than 270°, for three more maneuvers—$7.0A$, $7.5A$ and 270°—for each steering direction.

Figure 64 presents the yaw rate response to the Sine with Dwell test, for the proposed CDEBF AFS system. The vehicle passes the test by a considerable margin, whatever the

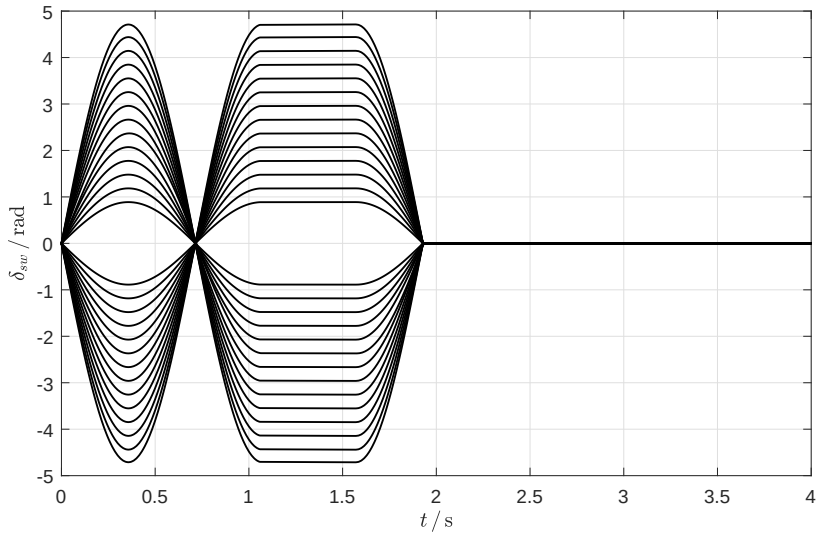

Figure 63: Steering wheel input ensemble for a succesfull Sine with Dwell test.

steering wheel amplitude is employed. We recall from Section 3.3 that the time thresholds when the yaw rate is verified are $T_0 + 1 = 2.93$ s and $T_0 + 1.75 = 3.68$ s, for reductions of 65 % and 80 %, in the respective order. Nevertheless, by $t = 2.5$ s the vehicle yaw rate has largely vanished, even for high steering angle amplitudes.

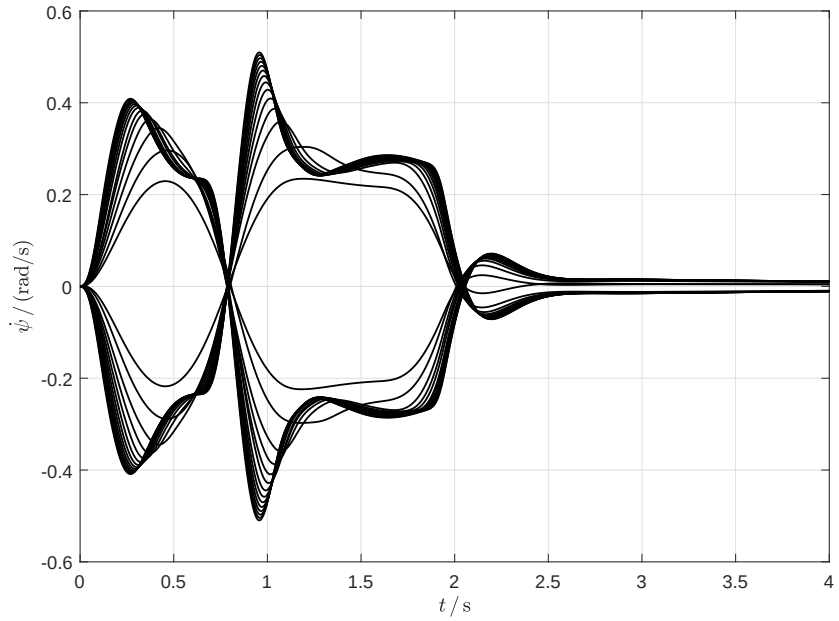

Figure 64: Yaw rate for the Sine with Dwell test, AFS with CDEBF.

The responsiveness criterion is based on the lateral displacement of the vehicle during the maneuver, which is depicted in Figure 65. The standard requires that this change in the lateral position is at least 1.83 m at 1.07 s after the steering input begins—which

is when the dwell time starts. However, this requirement only takes place for a steering amplitude of $\delta_{d\max} = 5.0A$ or larger. We can notice in Figure 65 that the responsiveness criterion is already satisfied at the 3rd maneuver when $\delta_{d\max} = 2.5A$. Hence the proposed method satisfies the requirement well in advance.

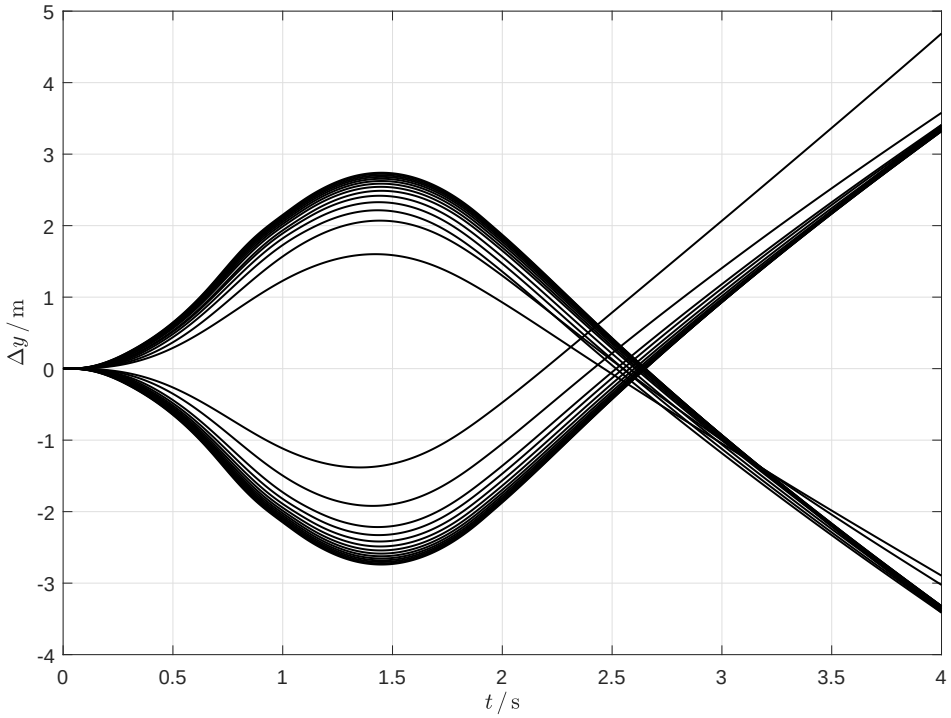

Figure 65: Lateral movement with respect to the track for the Sine with Dwell test, AFS with CDEBF.

The control input δ_u is presented in Figure 66. It has the effect of reducing the magnitude of the effective front steering angle, keeping the system state in the safe set. When the state is not at a neighborhood of the safe set frontier, the control input smoothly returns to zero.

Since the system model used by CarSim is much more complex than the simpler ones we presented, it can describe commercial vehicles with much greater detail. One consequence is that we can not employ all the equations in the controller design, i.e., (6.52). The model accuracy determines how well the state derivatives can be assessed when the restrictions are active, hence how well the safe set restrictions are respected in practice. Still, the safe set was mostly satisfied, as seen in Figure 67. A detailed observation of Figure 67 shows that the active restrictions are the CDECBFs related to h_1 and h_3. Due to the relaxation of the controllability criterion, h_2 and h_4 are no longer active, in any scenario we observed.

The safe set presented in Figure 54a considers the yaw rate $\dot{\psi}$ and the lateral speed v_{gx}

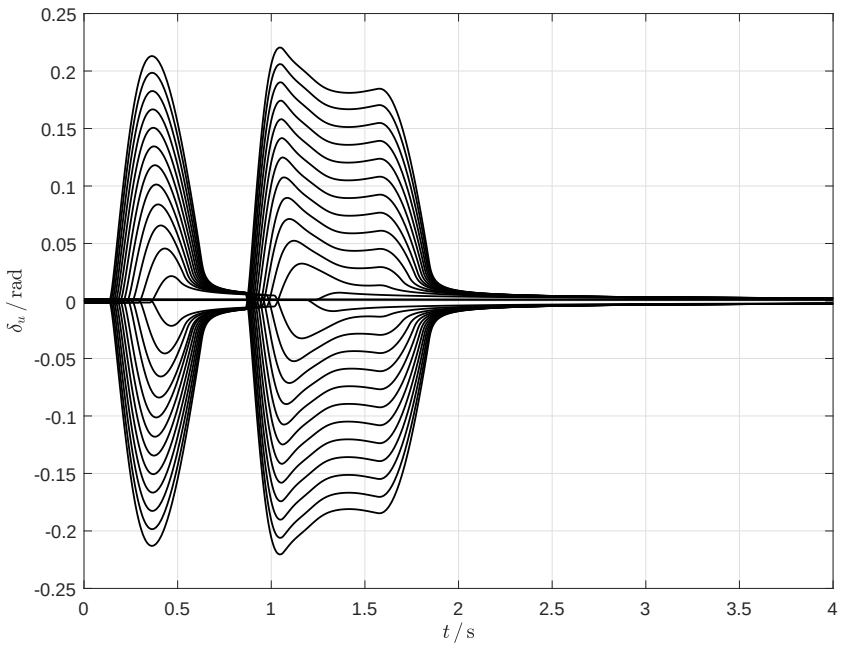

Figure 66: Control input δ_u for the Sine with Dwell test, AFS with CDEBF.

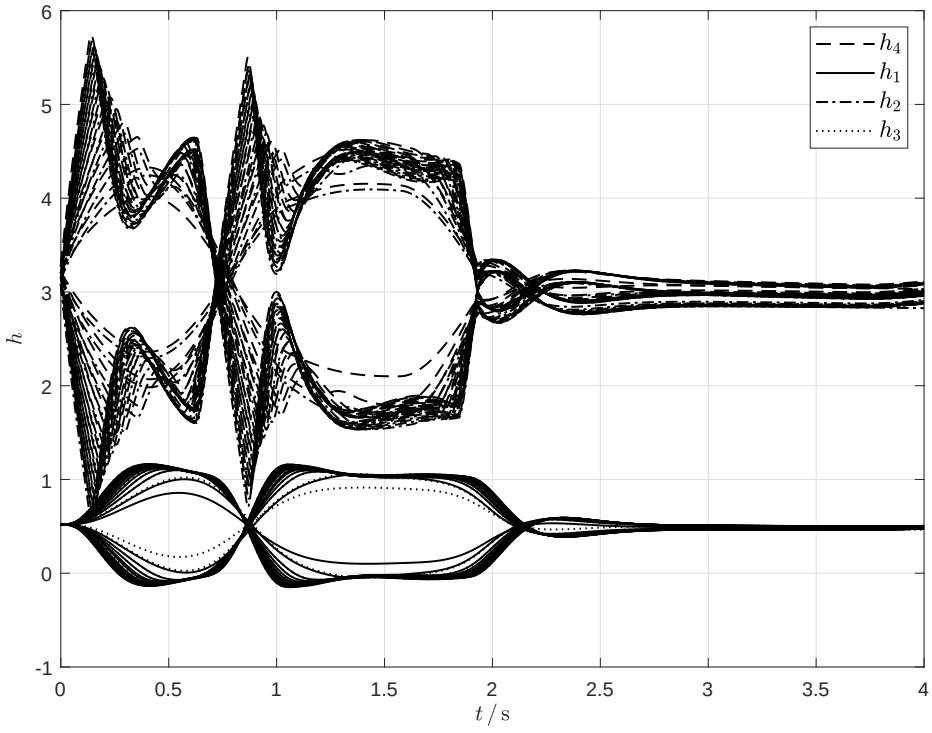

Figure 67: Barrier functions for the Sine with Dwell test, AFS with CDEBF. Continuous line: h_1. Dash-dot line: h_2. Dotted line: h_3. Dashed line: h_4.

as the lateral model state variables. Therefore, the side-slip angle is implicitly controlled, since v_{gx} and β are closely related. The side-slip angle is depicted in Figure 68.

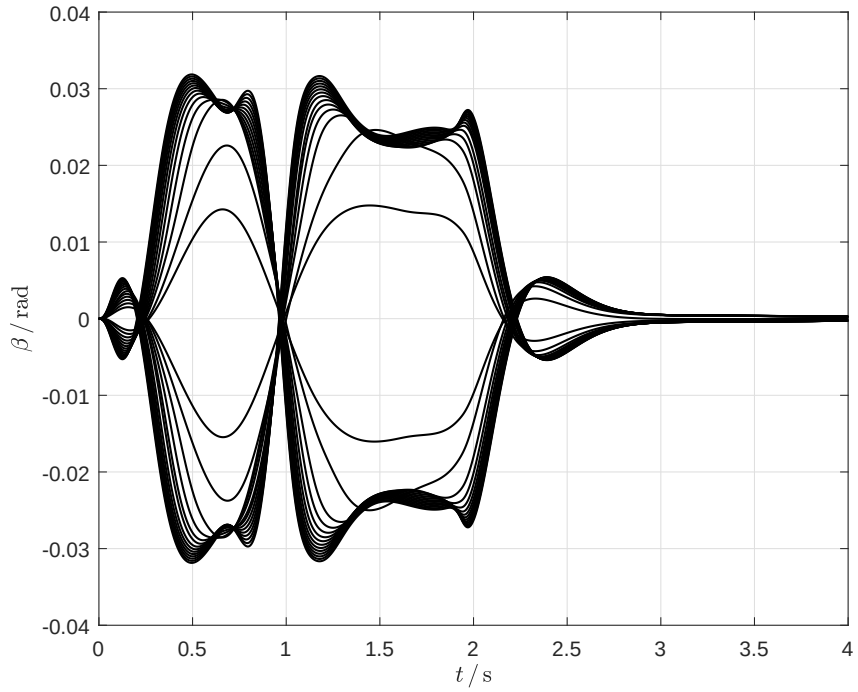

Figure 68: Vehicle side-slip angle for the Sine with Dwell test, AFS with CDEBF.

6.4 Conclusions from the AFS Proposals

Both AFS proposals proved to be efficient when applied to lateral stability. The state of the vehicle is restricted by implicitly limiting the wheel steering angles, from which results that the vehicle is kept in a controllable state at all times. Hence we can state that safety-critical control can be applied to electronic stability control, when considering stability regions as safe sets and using active steering as the control input.

Nonetheless, the default safety-critical control theory was not readily applicable to the problems presented herein. The first AFS proposal demanded an extension to Control Lyapunov Functions to accommodate the minimization of the input signal when hard restrictions were not active. Such extension, on the other hand, is general and allows Control Lyapunov Functions that influence the state, something unused in this text but potentially necessary in other applications.

The first proposal had a shortcoming, the chance of leaving the safe set—even if with zero probability. Another deficiency was employing a safe set that was conservative in the

sense of preventing impossible situations. In addition, the test maneuver we used to compare the results with those previously presented in the literature was less challenging than standardized maneuvers already in use in the industry and by control agencies. Finally, both the work we have extended and our first implementation omitted the longitudinal dynamics in the simulated vehicle, even though it has an effect taken into account by standard tests and consists of an advantage of differential-braking ESCs.

The second AFS proposal addressed these shortcomings. Another extension to safety-critical control was necessary, this time to include higher-order exponential control barrier functions that depend on the control input. We used more descriptive vehicle models: an in-house model that added combined slip and commercial model from CarSim. A similar CLF extension is possible but was not necessary for our application.

Finally, we mention that nowhere in this text have we considered road bank and grade, which affect lateral stability. We have also not contemplated large model or parameter errors nor failsafe situations such as sudden friction losses. Moreover, we focused on passenger cars, whereas race or off-road cars would have other design objectives and restrictions. Hence these are definitely not conclusive results in terms of exhausting lateral stability. On the contrary, other control methods remain viable, including alternative safety-critical control methods such as (CHINELATO; ANGÉLICO, 2021).

Active steering is an efficient ESC method but has limited stability recovery ability if the vehicle leaves the safe set. In addition to it, it is possible that there is enough room to recover stability if the vehicle decreases its longitudinal speed. This speed reduction is not as pronounced with AFS, compared to commercial ESC systems, which use differential braking. Finally, we wished to use our development of improved stability regions in Chapter 5 in yaw stability control. Chapter 7 discusses this possibility and the aforementioned aspects.

7 YAW STABILITY CONTROL

In Chapter 6, electronic stability control systems using active front steering have been proposed. On the other hand, most ESC devices use differential braking as their actuation method. In truth, standard ESC tests go as far as defining ESC as lateral stability control devices that use differential braking as actuators, e.g., (NHTSA, 2001, 2018, 2008, 2009). This is not to say that AFS systems are not useful, but by the time those regulations were being designed, a) commercial AFS systems were new, b) only one tested vehicle had it, c) its response was inferior to the differential-braking ESC vehicles, and d) the standard designers felt that the efficacy of other ESC technologies had not yet been demonstrated. Refer to (NHTSA, 2008), Final Rule, Chapter IV, Section C2 for the full discussion.

In this chapter, we assess the applicability of the current safety-critical control theory based on control barrier functions to the vehicle lateral stability control problem when using the brake system as input. After concluding that the current tools are not sufficient, we propose the necessary extension to the theory and apply it. The proposal is validated by our relatively simple combined slip and rigid mass model and by using the realistic vehicle models from CarSim.

Let us consider the desired yaw rate $\dot{\psi}_d$, as defined in Section 3.2 and given by (3.1). It can be obtained by considering a wheeled vehicle moving with a null side-slip angle, which is not a realistic situation for road vehicles at moderate-to-high speeds. At very low speeds, a vehicle has either negligible or low wheel slip angles, which result in vehicle side-slip angles pointing inwards, in curves. As the speed increases, so do the lateral forces and tire slip angles, which lead to the vehicle side-slip angle eventually pointing outwards. Hence β goes from negative to positive, for positive δ and increasing longitudinal speeds. However, would we consider equal tire slip angle increases at all wheels, from those which would result from a null side-slip angle, the yaw rate would be unchanged in steady-state if the slip angles are also constant. As a result, the desired yaw rate is still a viable reference for stable vehicles, when we consider lateral stability.

In this sense, let us consider a quadratic control barrier function candidate

$$h_{cand}(\mathbf{x}, \delta) = -(\dot{\psi} - \dot{\psi}_d - d_\psi)(\dot{\psi} - \dot{\psi}_d + d_\psi), \tag{7.1}$$

which is positive for yaw rate errors that do not exceed d_ψ in magnitude. For simplicity, let us consider the simple linear lateral model given by the extension of the bicycle model with the external moment input M_ψ, given by (2.124)–(2.125), and see if the default safety-critical control formulation from Section 4.3 can be applied. We conclude that the first formulation cannot be applied, since (7.1) depends on the driver's input δ. This means we cannot consider higher-order exponential control barrier functions as presented in Section 4.3.1 either, due to the same reason.

Next, let us assess the control-dependent barrier functions, presented in (HUANG; LIANG; CHEN, 2017; HUANG; CHEN, 2017) (Section 6.1). Two problems arise: first, (7.1) has a relative degree of 1 with respect to M_ψ. The second problem is that there is another input, the steering angle from the driver. Hence we must consider two inputs: a control input, for the control system, and either a measured disturbance input or an external input. From a theoretical point of view, they are indistinguishable, so we shall refer to it as an external input, which is the case here.

Since the exponential barrier function theory for higher relative degrees includes the case when the relative degree is zero, we shall omit this last case, and present general exponential barrier functions for any relative degree, in Section 7.1.

7.1 Control-dependent exponential barrier functions with external inputs

Let us consider a nonlinear system described by

$$\dot{\mathbf{x}} = f(\mathbf{x}) + g_e(\mathbf{x})\mathbf{u}_e + g_c(\mathbf{x})\mathbf{u}_c, \tag{7.2}$$

where $f(\cdot)$, $g_e(\cdot)$ and $g_c(\cdot)$ are Lipschitz continuous; $\mathbf{x} \in \mathcal{D} \subset \mathbb{R}^n$, $\mathcal{D}$ the set of possible state vectors; $\mathbf{u}_e \in \mathcal{U}_e \subset \mathbb{R}^{m_e}$, $\mathcal{U}_e$ encompassing the possible disturbances or external input vectors; and $\mathbf{u}_c \in \mathcal{U}_c \subset \mathbb{R}^{m_c}$, $\mathcal{U}_c$ consisting of the admissible control input vectors. Assume $\mathbf{u}_e$ is measurable and both $\mathbf{u}_e$ and $\mathbf{u}_c$ are, in the respective order, r_{me} and r_{mc} times differentiable—we shall define r_{me} and r_{mc} soon enough—and $\mathbf{u}_c$ is a function of $\mathbf{x}$ and $\mathbf{u}_e$.

Let $h(\mathbf{x}, \mathbf{u}_e, \mathbf{u}_c)$ be a concave function with respect to $\mathbf{x}$ and the safe set [(4.14)–(4.16)]

be extended as

Definition 8 (Control-disturbance-dependent safe set)**.** *Let* $\mathcal{C}(\mathbf{u}_e, \mathbf{u}_c)$ *satisfy*

$$\mathcal{C}(\mathbf{u}_e, \mathbf{u}_c) = \{\mathbf{x} \in \mathcal{D} \subset \mathbb{R}^n : h((x), \mathbf{u}_e, \mathbf{u}_c) \geq 0\} \tag{7.3}$$

$$\text{fr}\left(\mathcal{C}(\mathbf{u}_e, \mathbf{u}_c)\right) = \{\mathbf{x} \in \mathcal{D} \subset \mathbb{R}^n : h(\mathbf{x}, \mathbf{u}_e, \mathbf{u}_c) = 0\} \tag{7.4}$$

$$\text{Int}\left(\mathcal{C}(\mathbf{u}_e, \mathbf{u}_c)\right) = \{\mathbf{x} \in \mathcal{D} \subset \mathbb{R}^n : h(\mathbf{x}, \mathbf{u}_e, \mathbf{u}_c) > 0\}. \tag{7.5}$$

Then $\mathcal{C}$ *is the* control-disturbance-dependent safe set *(CDD safe set).*

Assume $h(\mathbf{x}, \mathbf{u}_e, \mathbf{u}_c)$ may have a higher-than-1 relative degree, thus Definition 4 cannot be generalized to consider CDD safe sets at all times. In particular, let r_{me} be the relative degree of h with respect to $\mathbf{u}_e$ and r_{mc} the relative degree of h with respect to $\mathbf{u}_c$. We define $r = \max\{r_{me}, r_{mc}\}$, and proceed as (4.22)–(4.24) or (6.35)–(6.36), i.e.,

$$\dot{\eta}_b(\mathbf{x}, \mathbf{u}_e, \mathbf{u}_c) = \bar{\mathbf{F}}\eta_b(\mathbf{x}, \mathbf{u}_e) + \bar{\mathbf{G}}\mu_i \tag{7.6}$$

$$h(\mathbf{x}, \mathbf{u}_e, \mathbf{u}_c) = \bar{\mathbf{C}}\eta_b(\mathbf{x}, \mathbf{u}_e, \mathbf{u}_c), \tag{7.7}$$

with

$$\eta_b(\mathbf{x}, \mathbf{u}_e, \mathbf{u}_c) \triangleq \begin{bmatrix} h(\mathbf{x}, \mathbf{u}_e, \mathbf{u}_c) \\ \dot{h}(\mathbf{x}, \mathbf{u}_e, \mathbf{u}_c) \\ \vdots \\ \mathbf{h}^{(r-1)}(\mathbf{x}, \mathbf{u}_e, \mathbf{u}_c) \end{bmatrix}$$

$$\bar{\mathbf{F}} = \begin{bmatrix} \mathbf{0}_{(r-1)\times 1} & \mathbf{I}_{r-1} \\ 0 & \mathbf{0}_{1\times(r-1)} \end{bmatrix} \qquad \bar{\mathbf{G}} = \begin{bmatrix} \mathbf{0}_{(r-1)\times 1} \\ 1 \end{bmatrix}$$

$$\bar{\mathbf{C}} = \begin{bmatrix} 1 & \mathbf{0}_{1\times(r-1)} \end{bmatrix} \qquad \mu_i = h^{(r)}(\mathbf{x}, \mathbf{u}_e, \mathbf{u}_c).$$

As in Sections 4.3.1 and 6.3.1, $\bar{\mathbf{F}}$ is a companion matrix. Therefore, if μ_i is a polynomial $\mathbf{K}\eta_b$ on the linearized state variables, the characteristic polynomial $\sigma(\bar{\mathbf{F}} + \bar{\mathbf{G}}\mathbf{K})$ of the closed-loop system can be arbitrarily assigned. Consequently, we use μ_i to extend the Nagumo invariance principle to (7.6). Hence let $P_{\zeta r}$ be a r-degree Hurwitz polynomial given by (6.39). Then its coefficients are given by (6.41), and we can define a control-disturbance-dependent exponential barrier function as

Definition 9 (Control-disturbance-dependent exponential control barrier function)**.** *Let* $\mathcal{C} \in \mathcal{D} \subset \mathbb{R}^n$ *be a superlevel set of an* r*-times differentiable function* $h\colon \mathcal{D} \to \mathbb{R}$ *with respect to* t *for known (and, possibly, time-varying)* $\mathbf{u}_e$ *and* $\mathbf{u}_c$*. Then* $h(\mathbf{x}, \mathbf{u}_e, \mathbf{u}_c)$ *is a* control-disturbance-dependent exponential control barrier function *(CDDEBF) if there*

exists $\mathbf{K}_\zeta$, $\Re\{\sigma(\bar{\mathbf{F}} - \bar{\mathbf{G}}\mathbf{K}_{\zeta r})\} < 0$, *such that for* $\dot{\mathbf{x}} = f(\mathbf{x}) + g(\mathbf{x})\mathbf{u}$,

$$\sup_{\mathbf{u}\in\mathcal{U}} h^{(r)}(\mathbf{x}, \mathbf{u}_e, \mathbf{u}_c) \geq \mathbf{K}_{\zeta r}\eta_b(\mathbf{x}, \mathbf{u}_e, \mathbf{u}_c), \tag{7.8}$$

any $\mathbf{x} \in \operatorname{Int}\mathcal{C}$ *results in* $h(\mathbf{x}(t), \mathbf{u}_e, \mathbf{u}_c) \geq \bar{\mathbf{C}}e^{(\bar{\mathbf{F}}-\bar{\mathbf{G}}\mathbf{K}_{\zeta r})t}\eta_b(\mathbf{x}(0), \mathbf{u}_e, \mathbf{u}_c) \geq 0$ *if* $h(\mathbf{x}(0), \mathbf{u}_e, \mathbf{u}_c) \geq 0$.

If (7.8) holds, the CDD safe set can be satisfied by the CDDEBF QP problem

$$\dot{\mathbf{u}}^\star = \underset{\dot{\mathbf{u}}_f\in\mathbb{R}^{m+1}}{\arg\min} \frac{1}{2}\dot{\mathbf{u}}_f^{\mathrm{T}}\mathbf{H}_{qp}\dot{\mathbf{u}}_f + \mathbf{F}_{qp}^{\mathrm{T}}\dot{\mathbf{u}}_f, \tag{7.9}$$

subject to

$$h^{(r)}(\mathbf{x}, \mathbf{u}_e, \mathbf{u}_c) + \mathbf{K}_{\zeta r}\eta_b(\mathbf{x}, \mathbf{u}_e, \mathbf{u}_c) \geq 0.$$

Let us also extend exponential control Lyapunov functions to depend on $\mathbf{u}_e$ and $\mathbf{u}_c$. Proceeding with the Lyapunov-Nagumo analogy in mind, we obtain the CDDELF-CDDEBF QP problem

$$\dot{\mathbf{u}}_\mathbf{f}^\star = \underset{\dot{\mathbf{u}}_f\in\mathbb{R}^{m+1}}{\arg\min} \frac{1}{2}\dot{\mathbf{u}}_f^{\mathrm{T}}\mathbf{H}_{qp}\dot{\mathbf{u}}_f + \mathbf{F}_{qp}^{\mathrm{T}}\dot{\mathbf{u}}_f, \tag{7.10}$$

subject to

$$V^{(r)}(\mathbf{x}, \mathbf{u}_e, \mathbf{u}_c) + \mathbf{K}_{\gamma r}\eta_b(\mathbf{x}, \mathbf{u}_e, \mathbf{u}_c) \geq \delta_s$$
$$h^{(r)}(\mathbf{x}, \mathbf{u}_e, \mathbf{u}_c) + \mathbf{K}_{\zeta r}\eta_b(\mathbf{x}, \mathbf{u}_e, \mathbf{u}_c) \geq 0,$$

where, as in Section 6.2, $\dot{\mathbf{u}}_f \triangleq [\dot{\mathbf{u}} \;\; \delta_s]$ and $\mathbf{K}_{\gamma r}$ is given by (6.40). We can have different relative degrees for V and h, but we leave the restrictions as-is for the sake of simplicity.

We can now apply CDDELFs and CDDEBFs to the yaw stability control problem. Whatever the case, we have that

$$\mathbf{u}_e = u_e = \delta, \tag{7.11}$$

i.e., the uncontrolled input vector is a scalar, namely the front wheels' steering angle. Since differential braking generates a yaw moment on the vehicle, we can consider $\mathbf{u}_c = u_c = M_\psi$ as the control system input. It shall have two different effects: to cause the yaw rate to change, and to reduce the longitudinal speed, since braking whatever wheels reduce vehicle speed. Both effects are interesting to either regain or maintain lateral stability.

First, let us consider the stability regions from Chapter 5. Assuming the steering wheel inputs from the Sine with Dwell test, it follows that (7.8) does not hold. Therefore CDDEBFs do not exist. The geometrical explanation is that the harsh steering moves the control-dependent safe set away from the state, while the external yaw moment input

direction and maximum magnitude are such that the state moves in a different direction ($\dot{\psi}$ and null lateral speed, for M_ψ; and the shifting vector $\mathbf{s}$, for δ) at a limited rate. Hence the task at hand is to recover lateral stability, and safety-critical control based on stability regions as safe sets is not feasible. We are forced to pursue a different strategy from what was used for AFS.

Section 7.1.1 investigates an alternative: using the desired yaw rate $\dot{\psi}_d$, seen in Chapter 3.

7.1.1 Desired Yaw Rate Reference

We propose the use of the desired yaw rate as a relaxed set point. In fact, several ESC systems use $\dot{\psi}_d$ as a reference (XU; WANG; LI, 2014; MAGALHÃES JÚNIOR, 2019; MIRZAEI, 2010; MIRZAEINEJAD; MIRZAEI; RAFATNIA, 2018; BASLAMISLI; KÖSE; ANLAÇ, 2011; CHO et al., 2008). Hence we assess the feasibility of using safety-critical control based on CBFs to relax the use of this variable as a reference, similarly to the on-off control strategies used in the industry for both ESC and ABS. Let us consider a maximum deviation d_ψ which is to be safeguarded by the YSC system. Then we define

$$h_1(v_{gx}, \dot{\psi}, \delta) = k_r(\dot{\psi} - \dot{\psi}_d + d_\psi), \tag{7.12}$$

$$h_2(v_{gx}, \dot{\psi}, \delta) = -k_r(\dot{\psi} - \dot{\psi}_d - d_\psi) \tag{7.13}$$

as the control barrier functions, which are positive for any yaw rate error $\dot{\psi}_d - \dot{\psi} \in (-d_\psi, d_\psi)$.

We realized the yaw rate error d_ψ by considering a maximum steering angle error d_δ that would be added to the steering angle δ. Consequently, we have

$$d_\psi = \frac{v_{gx} d_\theta}{l + k_{st} v_{gx}^2}, \tag{7.14}$$

so the yaw rate error is proportional to the steering angle error.

The desired yaw rate, as defined by (3.5), is not differentiable everywhere, however. This makes (7.1) an inconvenient barrier function since it is not differentiable where it needs the most, i.e., at the vehicle's maximum lateral accelerations, when the wheels must provide forces to both generate lateral force and yaw moment. Hence we introduce hard barrier functions

$$h_3(v_{gx}, \dot{\psi}) = k_r(\dot{\psi} + \dot{\psi}_{\max}) \tag{7.15}$$

and

$$h_4(v_{gx}, \dot{\psi}) = -k_r(\dot{\psi} - \dot{\psi}_{\max}), \tag{7.16}$$

with $\dot{\psi}_{\max}$ given by (3.4), which are positive for $\dot{\psi} - \dot{\psi}_d \in \{-\dot{\psi}_{\max}, \dot{\psi}_{\max}\}$, and make (7.12)–(7.13) soft by defining $\dot{\psi}_d$ as (3.1), which is continuous in δ.

The dependency of h_1 and h_2 in δ is due to $\dot{\psi}_d$, which depends on the longitudinal speed and the steering angle [see (3.1)]. As a consequence, h_1 and h_2 depend directly on the uncontrolled input, and indirectly on the control input, since braking reduces v_{gx}. This last aspect, however, is not described when using (2.124)–(2.125), since the bicycle model does not include the longitudinal motion, assuming constant longitudinal speed. When using the extended linear model with v_{gy} and $\dot{\psi}$ as state variables, we have

$$f(\mathbf{x}) = \mathbf{A}\mathbf{x}, \qquad g_e = \mathbf{B}_e, \qquad g_c = \mathbf{B}_c, \tag{7.17}$$

with

$$\mathbf{A} = \begin{bmatrix} -\frac{C_{\alpha f}+C_{\alpha r}}{m_b v_{gx}} & -\frac{C_{\alpha f} l_1 - C_{\alpha r} l_2}{m_b v_{gx}} - v_{gx} \\ -\frac{C_{\alpha f} l_1 - C_{\alpha r} l_2}{I_z v_{gx}} & -\frac{C_{\alpha f} l_1^2 + C_{\alpha r} l_2^2}{I_z v_{gx}} \end{bmatrix} \qquad \mathbf{B}_e = \begin{bmatrix} \frac{C_{\alpha f}}{m_b} \\ \frac{C_{\alpha f} l_1}{I_z} \end{bmatrix}$$

$$\mathbf{B}_c = \begin{bmatrix} 0 \\ \frac{1}{I_z} \end{bmatrix}$$

We can state the quadratic problem with relaxed control barrier functions by using a relaxation variable, as previously done in (4.21) or (6.27). The relaxed barriers h_1 and h_2 depend on the external control variable $\mathbf{u}_e = u_e \triangleq \delta$, the steering angle from the driver; but not on the control input $\mathbf{u}_c = u_c \triangleq M_\psi$, the correcting yaw moment. As a consequence, higher-order barrier functions on u_c are not necessary and only the first time derivatives of h_1 and h_2 are needed. Additionally, the hard barriers h_3 and h_4 do not depend on either u_e or u_c. Hence these can be described by the usual inequalities from Chapter 4. Then $\dot{h}_i$, $i \in \{1, 2\}$, is obtained as

$$\dot{h}_i(\mathbf{x}, u_e) = L_f h_i(\mathbf{x}, u_e) + L_{g_e} h_i(\mathbf{x}, u_e) u_e + L_{g_c} h_i(\mathbf{x}, u_e) u_c + \frac{\partial h_i}{\partial u_e} \dot{u}_e \tag{7.18}$$

while $\dot{h}_j$, $j \in \{3, 4\}$ is

$$\dot{h}_j(\mathbf{x}, u_e) = L_f h_j(\mathbf{x}, u_e) + L_{g_e} h_j(\mathbf{x}, u_e) u_e + L_{g_c} h_j(\mathbf{x}, u_e) u_c. \tag{7.19}$$

The quadratic problem takes the form

$$\mathbf{u}_f^\star = \arg\min_{\mathbf{u}_f \in \mathbb{R}^2} \frac{1}{2} {\mathbf{u}_f}^{\mathrm{T}} \mathbf{H} \mathbf{u}_f + \mathbf{F}^{\mathrm{T}} \mathbf{u}_f, \tag{7.20}$$

subject to

$$\begin{aligned}
L_f h_1(\mathbf{x}, u_e) + L_{g_e} h_1(\mathbf{x}, u_e) u_e + \frac{\partial h_1(\mathbf{x}, u_e)}{\partial u_e} \dot{u}_e + L_{g_c} h_1(\mathbf{x}, u_e) u_c + \zeta_1 h_1(\mathbf{x}, u_e) + \delta_s \geq 0 \\
L_f h_2(\mathbf{x}, u_e) + L_{g_e} h_2(\mathbf{x}, u_e) u_e + \frac{\partial h_2(\mathbf{x}, u_e)}{\partial u_e} \dot{u}_e + L_{g_c} h_2(\mathbf{x}, u_e) u_c + \zeta_2 h_2(\mathbf{x}, u_e) + \delta_s \geq 0 \\
L_f h_3(\mathbf{x}, u_e) + L_{g_e} h_3(\mathbf{x}, u_e) u_e + L_{g_c} h_3(\mathbf{x}, u_e) u_c + \zeta_3 h_3(\mathbf{x}, u_e) \geq 0 \\
L_f h_4(\mathbf{x}, u_e) + L_{g_e} h_4(\mathbf{x}, u_e) u_e + L_{g_c} h_4(\mathbf{x}, u_e) u_c + \zeta_4 h_4(\mathbf{x}, u_e) \geq 0,
\end{aligned}$$

where $\mathbf{u}_f \triangleq [\mathbf{u}_c \;\; \delta_s]^{\mathrm{T}}$, $\mathbf{H} = \mathrm{diag}\{p_u, p_\delta\}$, and $\mathbf{F} = [0 \;\; 0]^{\mathrm{T}}$. The control parameters are listed in Table 6. The block diagram is similar to the general ESC system, shown in Figure 20, Section 3.2. The vehicle outputs are the lateral and longitudinal speeds and the yaw rate; the control system inputs are the vehicle outputs and the steering angle from the driver; and the control system outputs are either the correcting yaw moment, for Matlab results, or the individual brake pressures, for the CarSim implementation.

Table 6: Yaw Control parameters

Parameter	Value
ζ_1	200
ζ_2	200
ζ_3	200
ζ_4	200
p_u	1
p_δ	20 000
k_r	10
d_θ	$\pi/600$ rad

We first validate the YSC system by considering a linear vehicle, described by (7.17). To better illustrate the behavior of the closed-loop system, we present two steering inputs from the Sine with Dwell test ensemble in Figure 69, $\delta_{d\max} = 1.5A$ and $\delta_{d\max} = 7.5A$: the first and last inputs for each steering wheel direction. The first input does not saturate the desired yaw rate, while the second one does.

The desired yaw rate and the actual yaw rate on the simulated vehicle are displayed in Figure 70. The figure shows that the maximum value of the yaw rate coincides with the saturated value from $\dot{\psi}_d$, for $\delta_{d\max} = 7.5A$. When $\delta_{d\max} = 1.5A$, only the continuous reference is followed, i.e., (3.1).

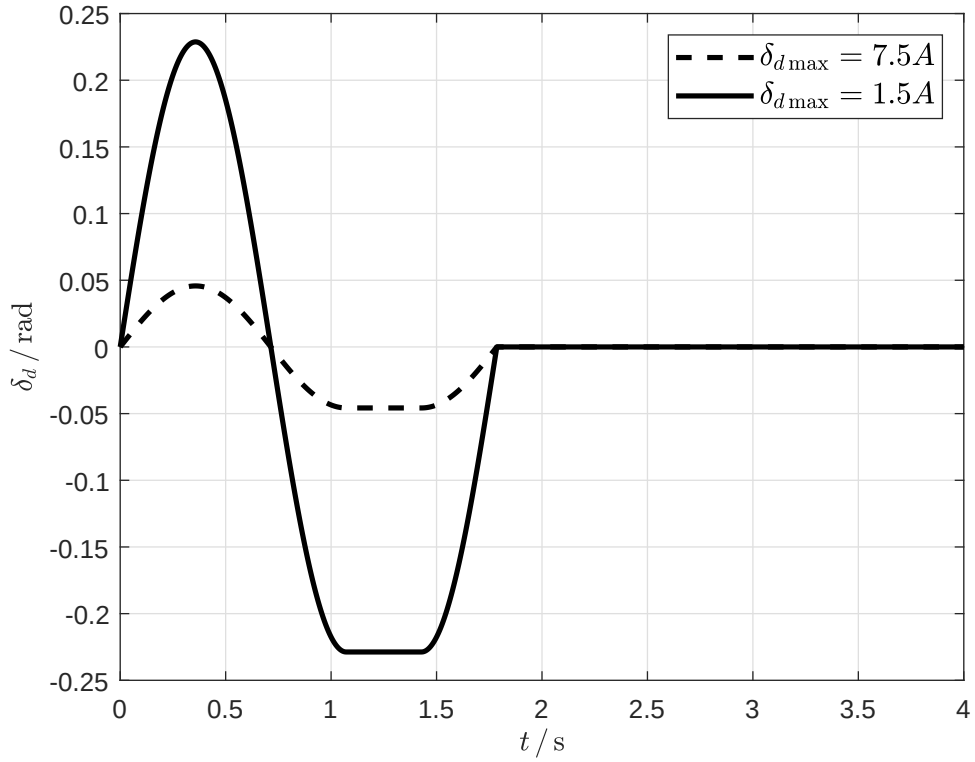

Figure 69: Front steering angle for the Sine with Dwell test. Continuous line: $\delta_{d\max} = 7.5A$. Dashed line: $\delta_{d\max} = 1.5A$.

Figure 71 depicts the control inputs. They tend to counteract the steering wheels' movements, providing a negative (i.e., clockwise) moment when the steering angle is positive, and a positive one when the steering wheels' angles are negative. When the steering input does saturate the yaw rate (Figure 71a), it is only nonzero when necessary to follow the relaxed reference. Since the Sine with Dwell test induces oversteering, one would expect the vehicle to exhibit yaw rates of larger than expected magnitude, which is avoided by the aforementioned control inputs.

The hard constraints are related to h_3 and h_4. Figure 72 shows that both are non-negative throughout the maneuver. On the other hand, h_1 and h_2 become negative when the yaw rate saturates during both the first and second sine half cycles, if $\delta_{d\max} = 7.5A$ (see Figure 72b). Consequently, the hard constraints are always satisfied. Alternatively, Figure 72a depicts the barrier functions for $\delta_{d\max} = 7.5A$, when only the relaxed barriers become active. In this case h_1 and h_2 can be respected without detriment of the hard barriers h_3 and h_4.

Figure 73 presents the trajectories of the state after using the shifting vector $\mathbf{s}$ to compare them with the conservative stability region from Figure 54a, previously used to

design the AFS system with CDEBF in Section 6.3.1.1. We observe that for $\delta_{d\max} = 1.5A$ the trajectory remains inside the stable region. When the magnitude of the input increases, the desired yaw rate saturates and the hard constraints restrict $\dot{\psi}$. The lateral speed, in turn, still increases in magnitude. We have already established that differential braking cannot render stability sets safe for harsh maneuvers at high speeds: Figure 73 is an instance of how the state can escape the safe set when a control system tries to restrict the yaw rate. Similar results would apply in case we used the side-slip angle as a reference but in another direction.

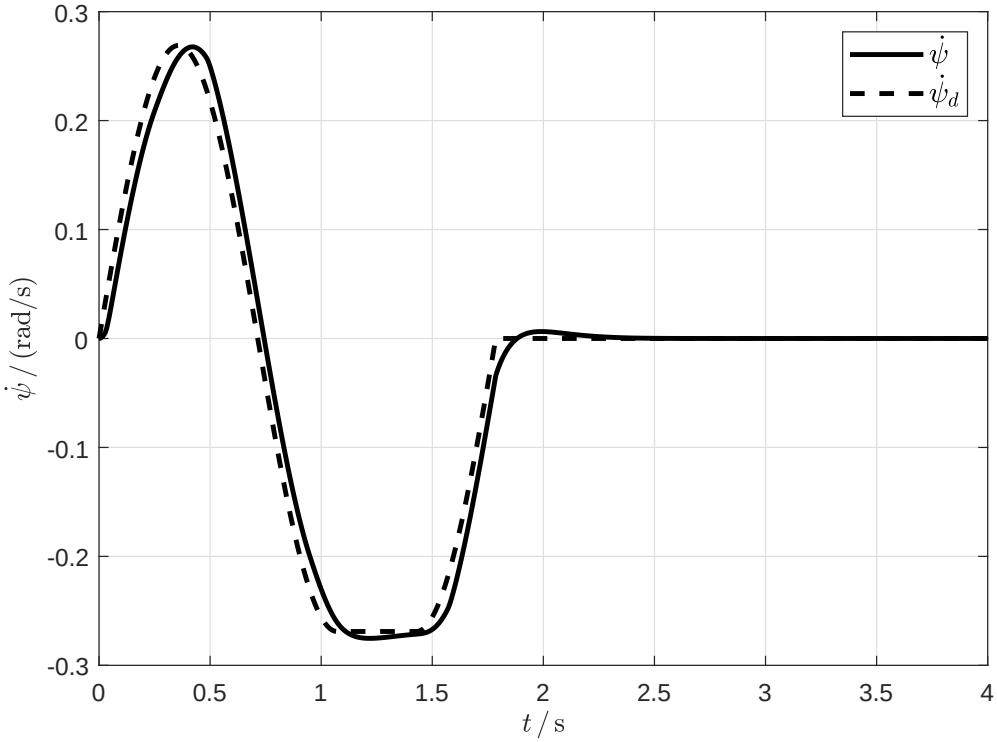

(a) Continuous line: vehicle yaw rate for $\delta_{d\,\max} = 1.5A$. Dashed line: desired yaw rate for $\delta_{d\,\max} = 1.5A$.

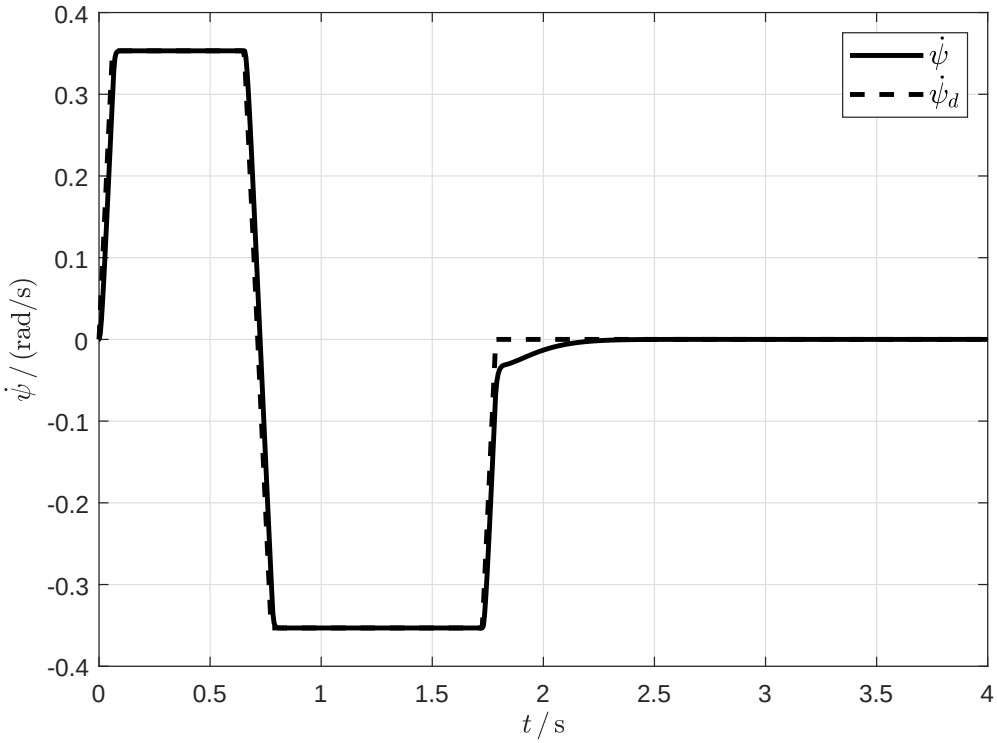

(b) Continuous line: vehicle yaw rate for $\delta_{d\,\max} = 7.5A$. Dashed line: desired yaw rate for $\delta_{d\,\max} = 7.5A$.

Figure 70: Yaw rate of the vehicle with a linear model and YSC considering the desired yaw rate as a relaxed reference, when subject to the Sine with Dwell test, for different steering inputs.

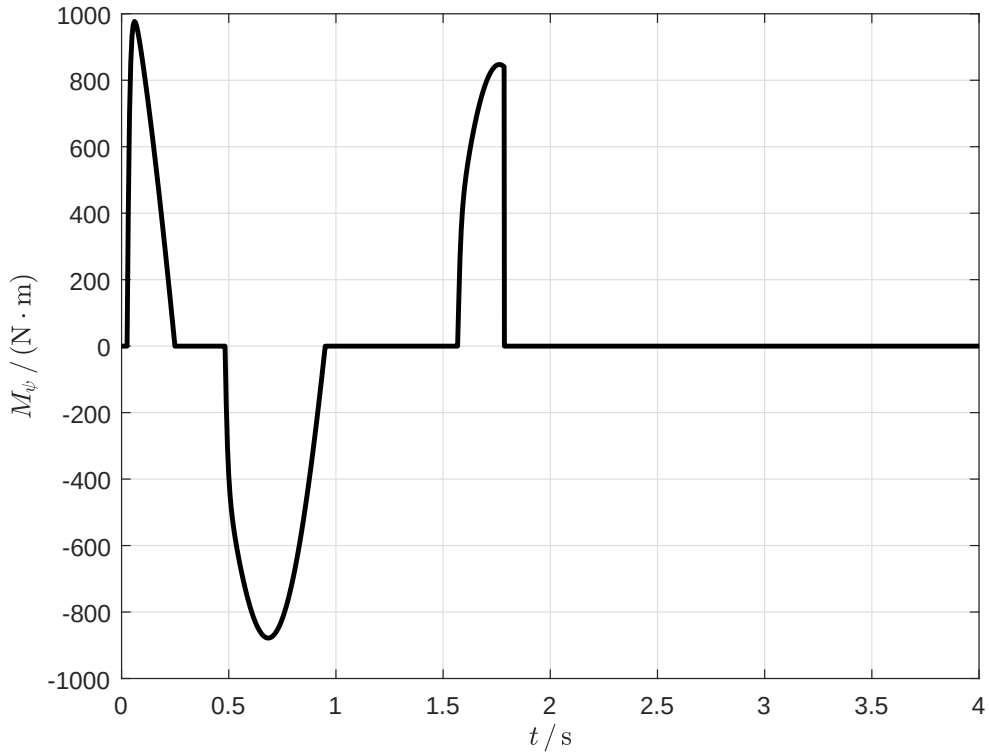

(a) Correcting yaw moment for $\delta_{d\,\max} = 1.5A$.

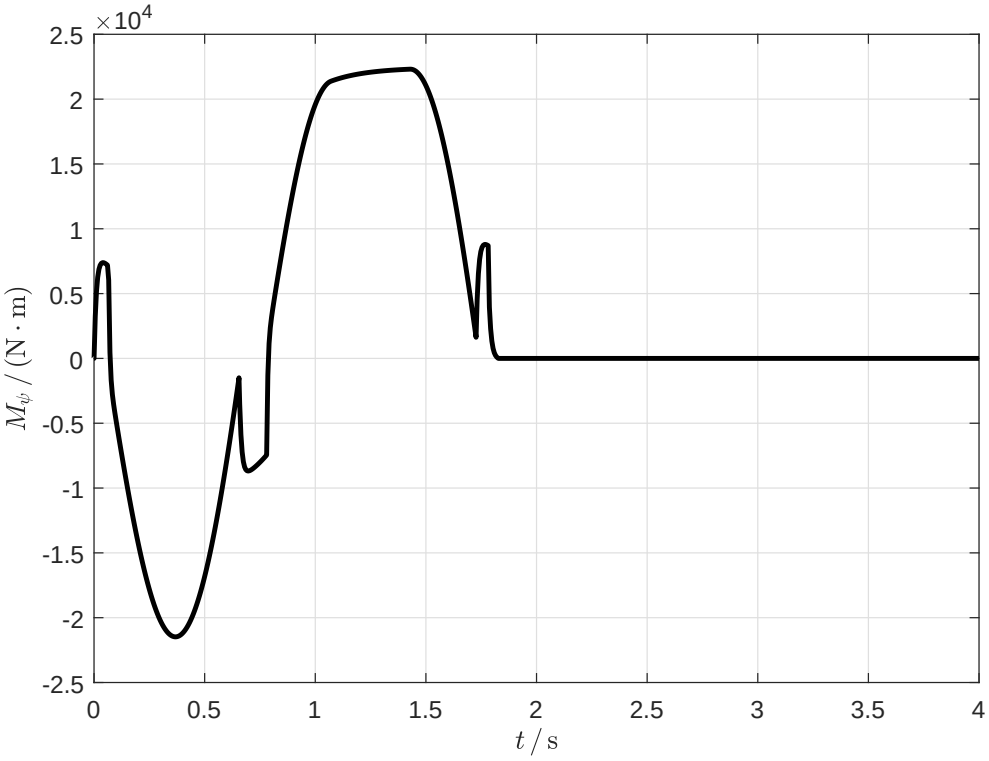

(b) Correcting yaw moment for $\delta_{d\,\max} = 7.5A$.

Figure 71: Correcting yaw moment on the vehicle with YSC considering a linearized model and the desired yaw rate as reference, when subject to the Sine with Dwell test.

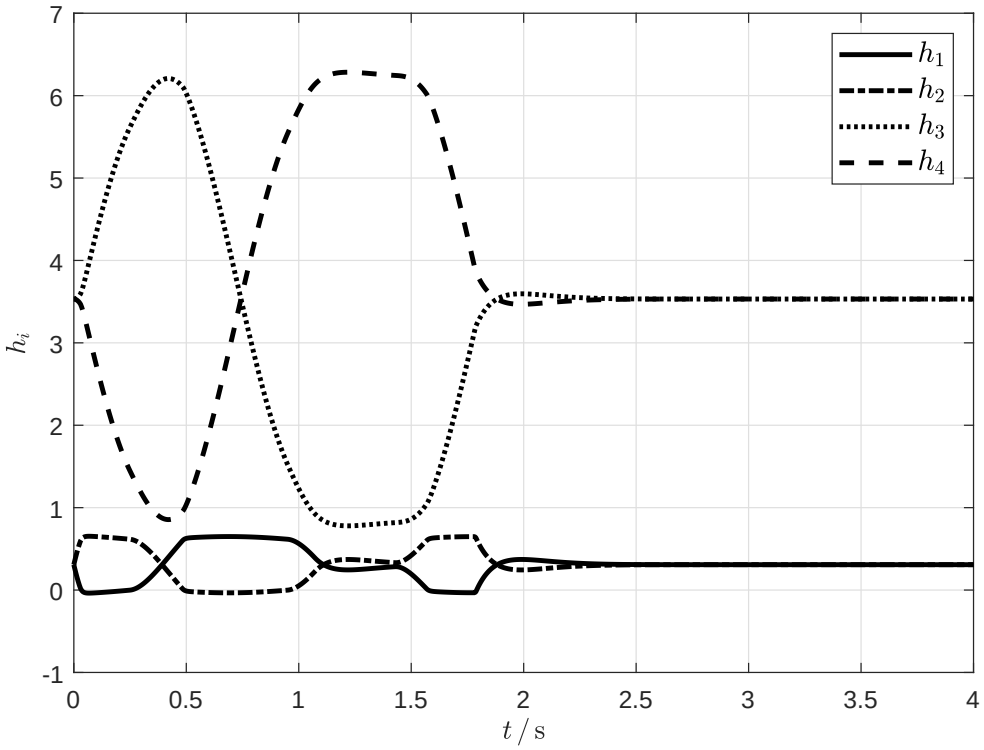

(a) Continuous line: h_1 for $\delta_{d\max} = 1.5A$. Dash-dot line: h_2 for $\delta_{d\max} = 1.5A$. Dotted line: h_3 for $\delta_{d\max} = 1.5A$. Dashed line: $h4$ for $\delta_{d\max} = 1.5A$.

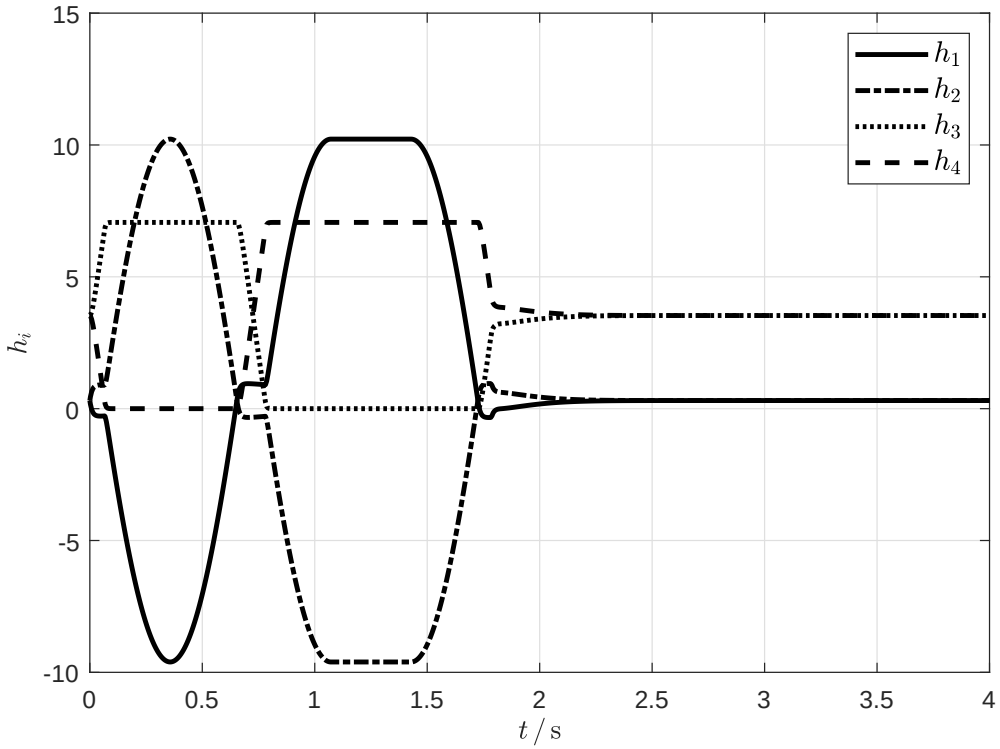

(b) Continuous line: h_1 for $\delta_{d\max} = 7.5A$. Dash-dot line: h_2 for $\delta_{d\max} = 7.5A$. Dotted line: h_3 for $\delta_{d\max} = 7.5A$. Dashed line: $h4$ for $\delta_{d\max} = 7.5A$.

Figure 72: Relaxed and hard control barrier functions for YSC considering a linearized model and the desired yaw rate as reference, when subject to the Sine with Dwell test.

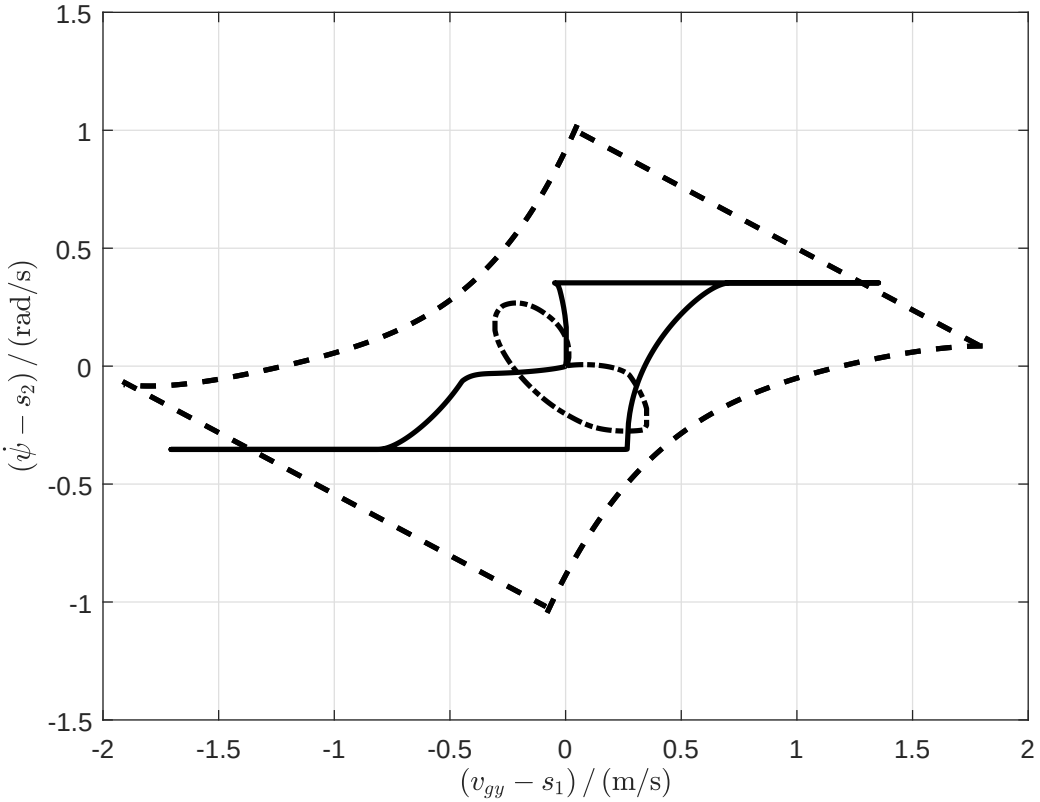

Figure 73: Lateral speed and yaw rate of vehicle over the conservative stability region on the shifted space $(v_{gy} - s_1) \times (\dot{\psi} - s_2)$. Vehicle with YSC considering a linearized model and the desired yaw rate as reference, when subject to the Sine with Dwell test. Conservative stability region for minimum $v_{gx} = 80$ km/h, minimum $\mu \geq 0.85$, and maximum $\delta = 5\pi/36$ rad (25°). Continuous line: trajectory for $\delta_{d\max} = 7.5A$. Dash-dot line: trajectory for $\delta_{d\max} = 1.5A$. Dashed line: conservative stability region.

Actual vehicles are not described by linear models, as seen in Chapter 2. Hence the consideration of a realistic vehicle model from CarSim; again, the C-class Hatchback model. When tested as model-in-the-loop with CarSim, the ESC system became too intrusive with the parameter set from Table 6, however, exhibiting chattering. This phenomenon happens because the models from CarSim are of a much higher order than the ones we used so far. Moreover, they consider compliances for the several subsystems that the models we implemented did not account for. In addition, the tire model is dynamic, whereas we implemented steady-state tire models.

Consequently, we changed the parameters to make the system less responsive during the transient dynamics. We achieve this by reducing the relaxation variable weight p_δ and increasing the maximum allowable steering angle error d_θ. So far, we have used $p_\delta = 20\,000$ and $d_\theta = \pi/600$ rad, or a mere 0.3°. A high p_δ means the designer is unwilling to sacrifice the hard constraints (the maximum yaw rate) in favor of the soft ones (yaw rate error), while a small d_θ means the system is more intrusive when the hard constraints are not active. This worked because the control design and system validation models were identical or similar. Consequently, we decreased p_δ to 1000 and increased d_θ to $\pi/90$ rad (2.0°). The full Sine with Dwell input ensemble is shown in Figure 63 (Section 6.3.1.1). The vehicle passes the test by large margins, as before.

Figure 74 depicts the yaw rate on the C-class Hatchback. There is no prominent yaw rate peak before ESC intervention and barely any yaw rate reminiscent at $t = 2.53$ s, or 600 ms after the end of steering. We recall from Section 3.3 that reductions of 65 % and 80 % of the peak yaw rate are to be verified only 1.00 s and 1.75 s, in the respective order, after the end of steering.

The responsiveness is assessed by the lateral displacement of the vehicle at $t = 1.07$ s. This lateral displacement has to exceed 1.83 m in magnitude if the peak steering angle is $\delta_{d\max} = 5.0A$ or greater. This maneuver is the 8th in the ensemble. However, the condition is already satisfied for $\delta_{d\max} = 2.5A$, the third maneuver.

Figure 76 presents the respective barrier functions. The relaxed barriers (h_1 and h_2) reach large negative values, while h_3 and h_4, the hard ones, are kept at positive or small negative numbers.

The signals in Figure 76 may be too cluttered to be distinguished. Hence we will select signals from single maneuvers to better describe the closed-loop system behavior. In particular, Figure 77 shows the barrier functions for $\delta_{d\max} = 7.5A$, which is the second-largest steering wheel movement for the vehicle model. The barrier function h_3 vehicle

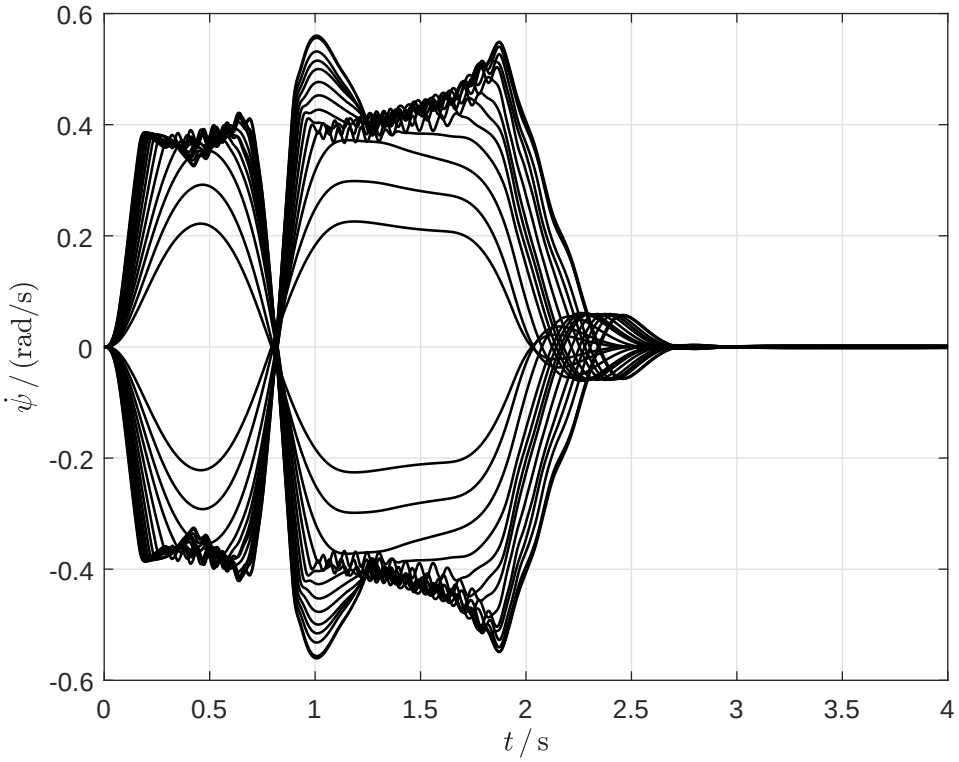

Figure 74: Yaw rate of the C-class Hatchback CarSim vehicle model, YSC considering the desired yaw rate as a relaxed reference, when subject to the Sine with Dwell test.

exhibits a negative peak at the beginning of the dwell time, but quickly recovers non-negative values. This is expected, since the vehicle model is much more complex than the linearized model used in the control design, and there is input saturation in practice, since brake forces are limited by the normal forces on the tires, further factored by the friction coefficient.

The high-level controller outputs a correcting yaw moment, which is displayed in Figure 78. There is a saturation for $t \in \{0.910\ \text{s}, 1.235\ \text{s}\}$, which considers the maximum possible correcting yaw moment magnitude. This results from the maximum brake forces on each wheel, factored by their distance to the vehicle's center of mass and the friction coefficient between the tires and the track.

The signal in Figure 78 is much noisier than that from Figure 71b. This is explained by the much more detailed model, which can describe vibrations from the vehicle structure, drive train, eventual gear switches, and tire dynamics. In addition to it, we have implemented a simple open-loop brake controller which outputs brake pressures for each wheel. The sudden brakes also cause vibrations that propagate themselves throughout the vehicle.

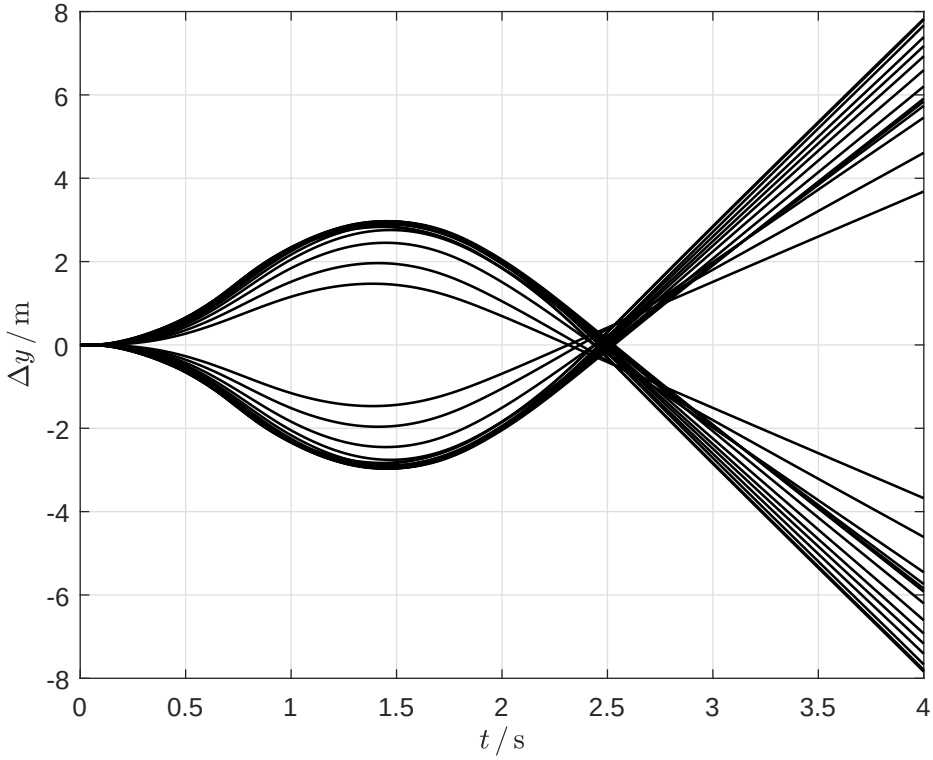

Figure 75: Lateral displacement of the C-class Hatchback CarSim vehicle model, YSC considering the desired yaw rate as a relaxed reference, when subject to the Sine with Dwell test.

The brake pressures P_{bi}, $i \in \{1, 2, 3, 4\}$ for the front left, front right, rear left, and rear right wheels, in the respective order, obtained as

$$P_{bi} = \frac{r_{ei}}{k_{bf\,i}} F_{bi}, \tag{7.21}$$

where r_{ei} is the effective rolling radius of the ith wheel, $k_{bf\,i}$ is the ratio of the braking force and moment on said wheel, and F_{bi} is the target braking force which is to be achieved. The obtention of r_{ei} is rather convoluted for the magic formula model and has been done as presented in (PACEJKA, 2012), Appendix 3.

The correcting yaw moment and the brake forces are approximately related by

$$M_\psi = F_{b1} l_{w1} + F_{b3} l_{w2} \tag{7.22}$$

for small steering angles. The brake forces are obtained as a ratio of them and the maximum brake force each wheel is able to provide, according to the combined slip equations from Appendix A, which is the same as the required and maximum correcting yaw moments.

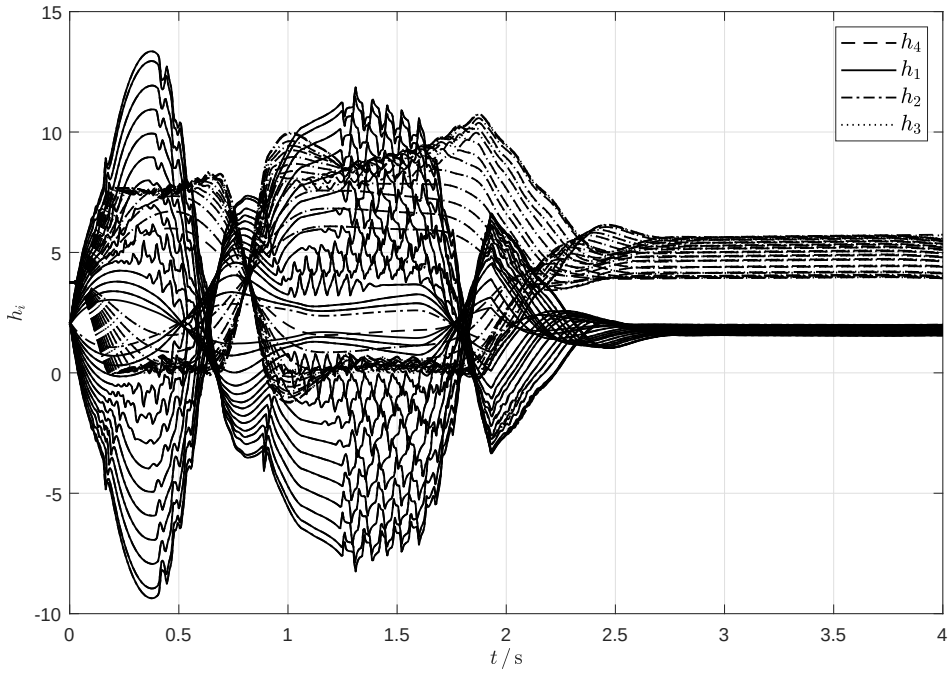

Figure 76: Barrier functions for the Sine with Dwell test, YSC with relaxed barriers, C-class Hatchback CarSim vehicle model. Continuous line: h_1. Dash-dot line: h_2. Dotted line: h_3. Dashed line: h_4.

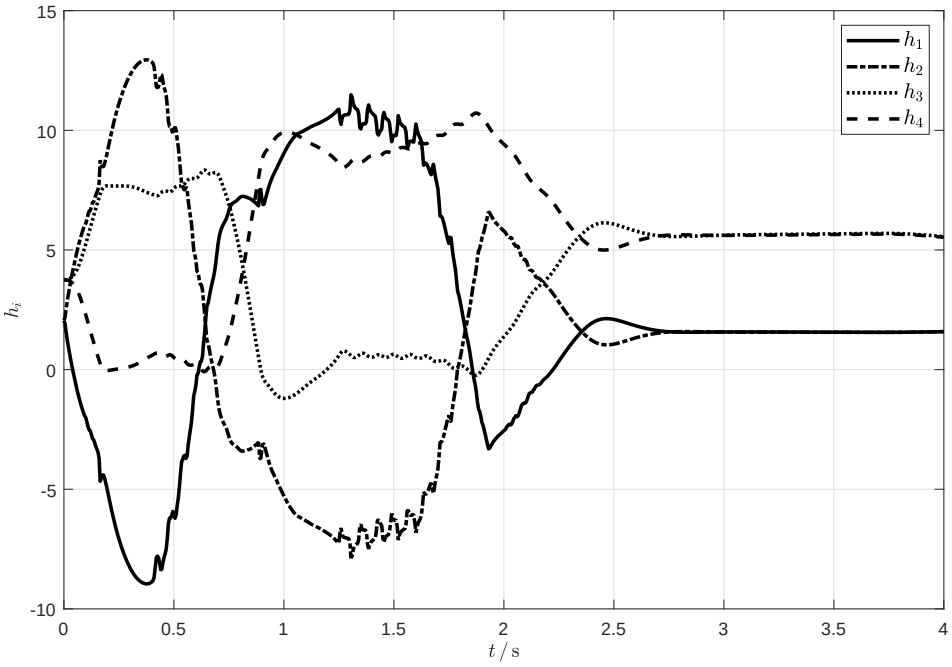

Figure 77: Barrier functions for the Sine with Dwell test, YSC with relaxed barriers, C-class Hatchback CarSim vehicle model, $\delta_{d\max} = 7.5A$. Continuous line: h_1. Dash-dot line: h_2. Dotted line: h_3. Dashed line: h_4.

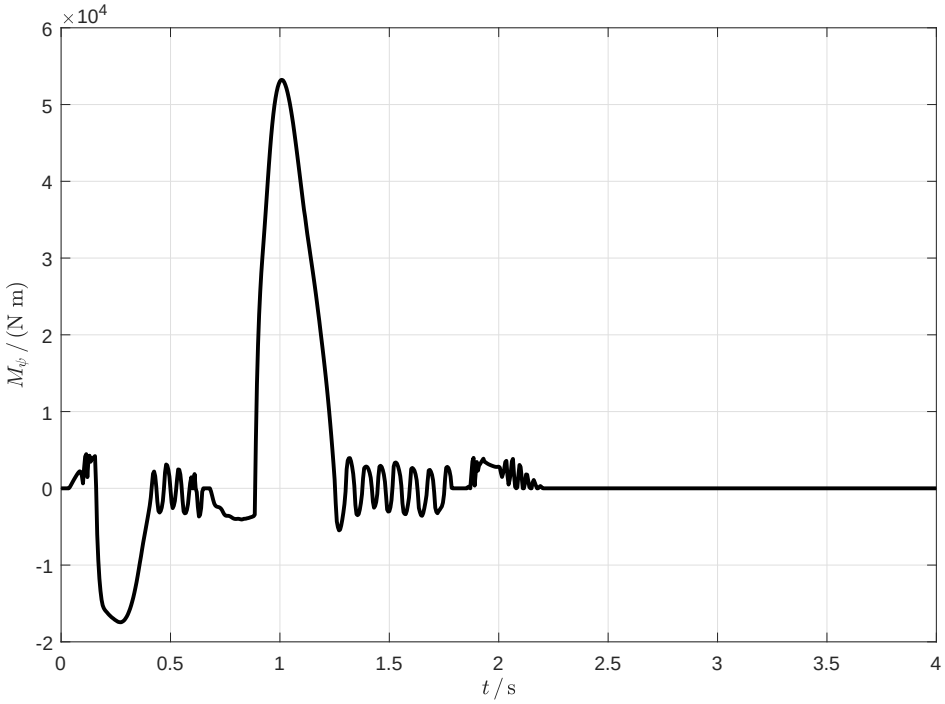

Figure 78: Correcting yaw moment for the Sine with Dwell test, YSC with relaxed barriers, C-class Hatchback CarSim vehicle model, $\delta_{d\max} = 7.5A$.

Figure 79 depicts the individual brake pressures on each wheel, again for the 13th maneuver from the Sine with Dwell test for the C-Class Hatchback model, i.e., $\delta_{d\max} = 7.5A$. The first part of the maneuver is a curve to the left, when the vehicle exhibits oversteering of positive sign. The right wheels, or Wheels 2 and 3, brake in that situation. After that, the vehicle turns to the right and initiates the dwell time, which induces negative oversteering. In this case, both left brakes activate (P_{b1} and P_{b3}).

Consequently, the YSC system with safety-critical control based on control-disturbance-dependent control barrier functions is validated with both simple and complex vehicle models. The simplest model, which is linear on both the driver and control inputs, was used to design the high-level controller. The second model, provided by CarSim, describes a realistic vehicle.

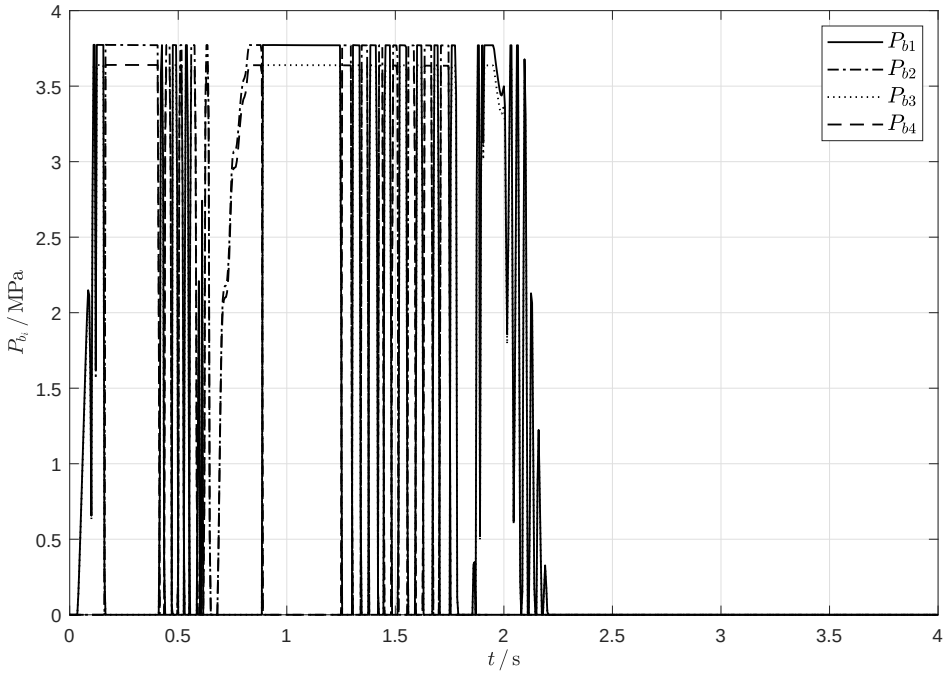

Figure 79: Brake pressures for the Sine with Dwell test, YSC with relaxed barriers, C-class Hatchback CarSim vehicle model. Continuous line: P_{b1}. Dash-dot line: P_{b2}. Dotted line: P_{b3}. Dashed line: P_{b4}.

7.2 YSC conclusions

We have extended the safety-critical control theory to accommodate known disturbances or external measurable control inputs. Also, we have considered relaxed conditions based on the Nagumo invariance principle, instead of only Lyapunov control. The latter allows for hard safety conditions, which must always be secured, and soft safety conditions, which can be sacrificed in favor of the first ones.

We have shown that YSC can be implemented using safety-critical control, after those extensions. We have validated the proposal using a simple linear model, which shows how the closed-loop system would operate in ideal conditions; and using CarSim, when a vehicle with a much larger set of realistic parameters is considered, which lets us observe that there is a degree of robustness to the system. This is, naturally, desirable, since is not practical to use a complex model such as the one CarSim uses for control design. As safety-critical control based on control barrier functions depends on the derivatives of the state variables from the system, it is expected that limited barrier violations occur, when harsh maneuvers are used.

One particular limitation of the validation method that we have employed is that it is limited to oversteer intervention. More specifically, by the time this work was under

development, standardization institutions or regulatory agencies had been unable to develop a maneuver that would reliably induce understeer (NHTSA, 2008). So far, vehicle manufacturers submit documentation that describes how the vehicle is supposed to intervene in order to mitigate understeer, but there is no objective criterion that the vehicles must satisfy (NHTSA, 2009). For the proposed YSC system, it is easy to understand that understeer would also induce barrier violations, causing the respective restrictions to become active and yielding a correcting yaw moment that brakes the inner wheels, instead of the ones from the outer side of the curve, which happens when oversteering.

8 CONCLUSION

Safety-critical control can be an efficient method to design and implement ESC systems. We presented AFS and differential braking systems, but it is safe to assume that AWS and electric motors (i.e., accelerating or braking each wheel) would be equally viable, as they include the first methods. One obtains AFS by disabling rear steering in AWS, much like one obtains differential braking by disabling driving wheels in electric vehicles.

Safety-critical control is a trending research topic. The academic community foresees many interesting contributions in this field shortly (ANNASWAMY; JOHANSSON; PAPPAS, 2023). We have proposed and validated several extensions to its theory:

- control-dependent control Lyapunov functions;
- control-dependent exponential control Lyapunov and barrier functions;
- control-disturbance-dependent exponential control Lyapunov and barrier functions.

During our investigation of electronic stability control, we also identified a deficiency in the area of stability regions. We suggested a method to generate higher-definition regions for ranges of parameters, which were successfully validated by a control application. The respective proposal was also published in (ALVES; CHINELATO; ANGELICO, 2022).

This work leaves several research opportunities for the ones interested in vehicle dynamics and control, electronic stability control, and safety-critical control. We can identify open problems in vehicle dynamics, state estimation, parameter identification, validation and design methods, and low-level brake system control. Additionally, the proposals can be adapted or extended to other vehicle types or other control problems.

Vehicles are complex systems, with several internal dynamics. In particular, the modeling of parts with diverse mass values causes the system model to become ill-conditioned. To circumvent this problem, we can avoid including those parts in the model, especially those whose influence can be further described by another quantity. For instance, since the drivetrain takes the motor torque as an input, we can try and avoid including the motor's internal parts, such as pistons and camshafts.

Unfortunately, the inclusion of wheels cannot be avoided. Their masses and rubber deformations are closely related to how a vehicle is propelled, so they must be well described. However, since the vehicle mass is much greater than the wheels', the body dynamics is much slower, in comparison. As a result, numerical errors while simulating wheels cause a noticeable impact of the forces which act on the body, and the simulation steps must accommodate their behavior. On the other hand, studies in numerical analysis may be able to circumvent or mitigate the problem and allow for the use of more complex models in control design or vehicle simulation.

A complete model of a moving vehicle has infinite dimension not only because the vehicle has deformable parts, but because the environment can never be fully described (THRUN; BURGARD; FOX, 2005). This environment includes the road surface, other vehicles, wind, road and air temperature, and various materials—such as sand, water, oil, or mud—which may be either clustered or outspread over the road.

The aforementioned environmental aspects are not only hard to model but also to measure. For instance, road and air temperature will influence rubber stiffness and inflating pressure, which, in turn, influence tire stiffness (see Section 2.2.2). The road surface may be modeled by road bank and grade if it is smooth enough. Else, each tire will be subject to different camber and a different angle in relation to gravity (which, both, generate noticeable lateral forces). Computer vision can help detect many of the aforementioned aspects before the vehicle comes into contact with them.

Since any model-based control strategy depends on an available model, the necessary parameters must be obtained. Possible parameters or states include road bank and grade, road friction coefficient, vehicle speed and acceleration, and angular speeds. A few of those quantities have affordable commercial sensors which directly measure them. Some demand estimators, while others demand extra sensors. These sensors operate in a noisy and harsh environment. Hence, the development of affordable and reliable automotive sensors remains an open problem. This includes any necessary devices and methods to accurately detect and describe the road ahead. For the sake of simplicity and time constraints, this work has left the important topic of estimation aside.

Manufacturers use more scenarios to tune their ESC systems. For instance, low friction surfaces due to frozen roads are considered in countries where the climate conditions are colder. Hence the proposed systems may be improved by fiction coefficient detection or simply the consideration of a lower friction coefficient. One can also study how a human driver interacts with the proposed system. ESC systems may cause the driver–vehicle

loop to become unstable, depending on the driver's skill and open-loop transport delay and response time (MAGALHÃES JÚNIOR; MURILO; LOPES, 2022).

This study has implemented a limited brake control function for its model-in-the-loop validation through CarSim. We considered an open-loop function that did not measure or estimate the vertical load on each wheel and did not track the actual slip ratio on the wheels. Hence low-level brake controllers can be included or developed in order to improve the system. These may be further improved by estimated variables from the vehicle or the environment, which we have already mentioned as a research opportunity.

The control method is related to the available actuators which can be controlled. An inherent property of control systems is that the more control inputs are available, the more freedom the designer has to manipulate the closed-loop dynamics, a fact that can be made analogous to the linear case, where more control inputs eventually allow the designer to not only manipulate close-loop eigenvalues but also change the related node eigenvectors or focus frequencies. Such analysis was briefly presented in Section 3.2, in which, in essence, it is explained that, in the face of side-slip or yaw rate errors, it is impossible to assign an eigenvector that takes the state directly to the reference. Moreover, more control objectives can be achieved with more input options, e.g., roll and pitch angle control, or tire camber and normal force. In other words, the proposed safety-critical formulations can be tested for these extra input methods.

Additionally, this work focused on passenger cars. This design decision impacted every aspect of this text, to some extent. As a consequence, stability regions and ESC systems may be obtained or investigated for race cars, off-road vehicles, commercial sports cars, or even adapted to vehicles with a higher center of mass, such as SUVs, buses, or trucks.

Also concerning passenger cars, the proposed ESC systems completed the Sine with Dwell test with ease. Since the standard only takes the total mass of the vehicle (i.e., the GVWR), but not the center of mass location, SUVs and passenger cars are treated equally. As a consequence, the requirements are relaxed so that SUVs can meet them, whereas passenger cars could be made more stable—at the cost of fuel consumption and tire deterioration. It is unknown how many lives could be saved compared to the direct and environmental costs.

Another possibility that arises from this study is its validation though hardware-in-the-loop and full implementations on actual vehicles. Some of these were previously planned for but had to be postponed due to difficulties outside our control, e.g., the COVID-19 pandemic.

Finally, the proposed safety-critical control formulations may be applied elsewhere. As an example, we have only needed control barrier functions that depend on disturbances or external control inputs for relative degree 1. Moreover, the YSC proposal did not require a control Lyapunov function. Most certainly higher-order barrier functions or Lyapunov functions shall be required by other systems.

REFERENCES

ALVES, J. A. V.; CHINELATO, C. I. G.; ANGELICO, B. A. Vehicle lateral stability regions for control applications. **IEEE Access**, v. 10, p. 87787–87802, 2022.

AMES, A. D.; COOGAN, S.; EGERSTEDT, M.; NOTOMISTA, G.; SREENATH, K.; TABUADA, P. Control barrier functions: Theory and applications. In: **European Control Conference (ECC)**. Piscataway, NJ: IEEE, 2019. v. 18, p. 3420–3431. Available from Internet: <https://ieeexplore.ieee.org/document/8796030>.

AMES, A. D.; GALLOWAY, K.; SREENATH, K.; GRIZZLE, J. W. Rapidly exponentially stabilizing control lyapunov functions and hybrid zero dynamics. **IEEE Transactions on Automatic Control**, IEEE, Piscataway, NJ, v. 59, n. 4, p. 876–891, 2014. Available from Internet: <https://ieeexplore.ieee.org/document/6709752>.

AMES, A. D.; XU, X.; GRIZZLE, J. W.; TABUADA, P. Control barrier function based quadratic programs for safety critical systems. **IEEE Transactions on Automatic Control**, IEEE, Piscataway, NJ, v. 62, n. 8, p. 3861–3876, 2017. Available from Internet: <https://ieeexplore.ieee.org/document/7782377>.

ANNASWAMY, A. M.; JOHANSSON, K. H.; PAPPAS, G. J. **Control for Societal-Scale Challenges**. Piscataway, NJ, 2023.

ARIPIN, M. K.; SAM, Y. M.; DANAPALASINGAM, K. A.; PENG, K.; HAMZAH, N.; ISMAIL, M. F. A review of active yaw control system for vehicle handling and stability enhancement. **International Journal of Vehicular Technology**, v. 2014, p. 1–15, jun 2014. Available from Internet: <https://doi.org/10.1155/2014/437515>.

BASLAMISLI, S. Ç.; KÖSE, I. E.; ANLAÇ, G. Handling stability improvement through robust active front steering and active differential control. **Vehicle System Dynamics**, Taylor & Francis, v. 49, n. 5, p. 657–683, 2011. Available from Internet: <https://doi.org/10.1080/00423111003671900>.

BLANCHINI, F. Set invariance in control. **Automatica**, v. 35, n. 11, p. 1747–1767, 1999. ISSN 0005-1098. Available from Internet: <https://www.sciencedirect.com/science/article/pii/S0005109899001132>.

BOYD, S.; VANDENBERGHE, L. **Convex Optimization**. Cambridge University Press, 2004. ISBN 780521833783. Available from Internet: <https://web.stanford.edu/~boyd/cvxbook/>.

BRASIL, Ministério da Infraestrutura. **Frota de Veículos 2020**. Braília, DF, 2020. Available from Internet: <https://antigo.infraestrutura.gov.br/component/content/article/115-portal-denatran/9484-frota-de-ve{\'i}culos-2020.> Accessed: 19 August 2020.

BUEHLER, M.; IAGNEMMA, K.; SINGH, S. (Ed.). **Journal of Field Robotics**: Special issue on the 2007 DARPA urban challenge, part 1. Hoboken, NJ: John Wiley & Sons, 2008. v. 25, n. 8. ISSN 1556-4967.

BUEHLER, M.; IAGNEMMA, K.; SINGH, S. (Ed.). **Journal of Field Robotics**: Special issue on the 2007 DARPA urban challenge, part 2. Hoboken, NJ: John Wiley & Sons, 2008. v. 25, n. 9. ISSN 1556-4967.

CADILLAC MOTOR CAR DIVISION. **2020 Cadillac XT5**. 2020. Available from Internet: <https://www.cadillac.com/suvs/xt5>. Accessed: 31 August 2020.

CAMPION, G.; BASTIN, G.; D'ANDRÉA-NOVEL, B. Structural properties and classification of kinematic and dynamic models of wheeled mobile robots. **IEEE Transactions on Robotics and Automation**, v. 12, n. 1, p. 47–62, 1996.

CHEN, K.; PEI, X.; MA, G.; GUO, X. Longitudinal/lateral stability analysis of vehicle motion in the nonlinear region. **Mathematical Problems in Engineering**, Hindawi Publishing Corporation, aug 2016. ISSN 1024-123X. ID 3419108. Available from Internet: <https://doi.org/10.1155/2016/3419108>.

CHESTERTON, A. **How many cars are there in the world?** 2018. Available from Internet: <https://www.carsguide.com.au/car-advice/how-many-cars-are-there-in-the-world-70629>. Accessed: 19 August 2020.

CHIANG, H.-D.; HIRSCH, M.; WU, F. Stability regions of nonlinear autonomous dynamical systems. **IEEE Transactions on Automatic Control**, v. 33, n. 1, p. 16–27, 1988.

CHINELATO, C. I. G.; ANGÉLICO, B. A. Robust exponential control barrier functions for safety-critical control. In: **American Control Conference (ACC)**. Piscataway, NJ: IEEE, 2021. p. 2342–2347.

CHO, W.; YOON, J.; KIM, J.; HUR, J.; YI, K. An investigation into unified chassis control scheme for optimised vehicle stability and maneuverability. **Vehicle System Dynamics**, Taylor & Francis, v. 46, n. sup1, p. 87–105, 2008. Available from Internet: <https://doi.org/10.1080/00423110701882330>.

CHOI, M.; CHOI, S. B. Model predictive control for vehicle yaw stability with practical concerns. **IEEE Transactions on Vehicular Technology**, v. 63, n. 8, p. 3539–3548, 2014.

CONTRAN. Resolução no 799, de 22 de outubro de 2020. **Diário Oficial [da] República Federativa do Brasil**, Brasília, DF, 2020. Available from Internet: <https://www.gov.br/infraestrutura/pt-br/assuntos/transito/conteudo-contran/resolucoes/Resolucao7992020.pdf>. Accessed: 19 December 2020.

DRAKUNOV, S.; OZGUNER, U.; DIX, P.; ASHRAFI, B. Abs control using optimum search via sliding modes. **IEEE Transactions on Control Systems Technology**, IEEE, Piscataway, NJ, v. 3, n. 1, p. 79–85, 1995.

DRAKUNOV, S. V.; ASHRAFI, B.; ROSIGLIONI, A. Yaw control algorithm via sliding mode control. In: **Proceedings of the 2000 American Control Conference (ACC)**. Piscataway, NJ: IEEE, 2000. v. 1, n. 6, p. 580–583 vol.1.

DUGOFF, H.; FANCHER, P. S.; SEGEL, L. An analysis of tire traction properties and their influence on vehicle dynamic performance. In: **International Automobile Safety**

Conference. SAE International, 1970. ISSN 0148-7191. Available from Internet: <https://doi.org/10.4271/700377>.

ERKE, A. Effects of electronic stability control (ESC) on accidents: A review of empirical evidence. **Accident Analysis & Prevention**, v. 40, n. 1, p. 167 – 173, 2008. ISSN 0001-4575. Available from Internet: <http://www.sciencedirect.com/science/article/pii/S0001457507000851>.

EURO NCAP. **The Dynamic Test of Car Electronic Stability Control (ESC) Systems Protocol**. Leuven, Belgium, 2020. Available from Internet: <https://www.latinncap.com/po/nossos-testes>. Accessed: 16 February 2023.

EURO NCAP ESC Dynamic Test Protocol. Leuven, Belgium, 2011. Available from Internet: <https://www.latinncap.com/data/protocolos/testing/EuroNCAP-ESCDynamicTestProtocolv1.2Jun2011.pdf>.

EUROPEAN UNION. Regulation (ec) no 661/2009 of the european parliament and of the council. **Official Journal of the European Union**, jul 2009. Available from Internet: <https://eur-lex.europa.eu/legal-content/EN/ALL/?uri=celex\%3A32009R0661>. Accessed: 23 July 2021.

EUROPEAN UNION. Regulation no 13-h of the economic commission for europe of the united nations — uniform provisions concerning the approval of passenger cars with regard to braking [2015/2364]. **Official Journal of the European Union**, v. 335, dec 2015. Available from Internet: <https://eur-lex.europa.eu/legal-content/EN/TXT/PDF/?uri=CELEX:42015X1222(01)>. Accessed: 8 November 2022.

FENG, J.; CHEN, S.; QI, Z. Coordinated chassis control of 4wd vehicles utilizing differential braking, traction distribution and active front steering. **IEEE Access**, v. 8, p. 81055–81068, 2020. Available from Internet: <https://ieeexplore.ieee.org/document/9079515>.

FORD, T. **I Swear, I'm Stable!: Ford's AdvanceTrac Electronic Stability Control**. 2018. Available from Internet: <https://www.teamford.ca/2018/10/10/fords-advancetrac-electronic-stability-control/>. Accessed: 31 August 2020.

GILLESPIE, T. D. **Fundamentals of vehicle dynamics**. Society of Automotive Engineers, 1992. (Electronic publications). ISBN 9780768023336. Available from Internet: <http://gen.lib.rus.ec/book/index.php?md5=ecb320e8268ac0198df5823e34a8bde6>.

GILLULA, J. H.; KAYNAMA, S.; TOMLIN, C. J. Sampling-based approximation of the viability kernel for high-dimensional linear sampled-data systems. In: **Proceedings of the 17th international conference on Hybrid systems: computation and control**. New York: ACM, 2014. p. 173–182.

GREEN, P. E.; WOODROOFFE, J. The estimated reduction in the odds of loss-of-control type crashes for sport utility vehicles equipped with electronic stability control. **Journal of Safety Research**, v. 37, n. 5, p. 493 – 499, 2006. ISSN 0022-4375. Available from Internet: <http://www.sciencedirect.com/science/article/pii/S0022437506001071>.

GUIZZO, E. **How Google's Self-Driving Car Works**. 2011. Available from Internet: <https://spectrum.ieee.org/automaton/robotics/artificial-intelligence/how-google-self-driving-car-works>. Accessed: 27 August 2020.

GUO, N.; ZHANG, X.; ZOU, Y.; LENZO, B.; ZHANG, T.; GÖHLICH, D. A fast model predictive control allocation of distributed drive electric vehicles for tire slip energy saving with stability constraints. **Control Engineering Practice**, v. 102, p. 104554, 2020. ISSN 0967-0661. Available from Internet: <http://www.sciencedirect.com/science/article/pii/S0967066120301519>.

GURRIET, T.; MOTE, M.; SINGLETARY, A.; NILSSON, P.; FERON, E.; AMES, A. D. A scalable safety critical control framework for nonlinear systems. **IEEE Access**, v. 8, p. 187249–187275, 2020.

GÜVENÇ, B. A.; BÜNTE, T.; ODENTHAL, D.; GÜVENÇ, L. Robust two degree-of-freedom vehicle steering controller design. **IEEE Transactions on Control Systems Technology**, v. 12, n. 4, p. 627–636, 2004.

HADT, H. S.; MILLIKEN, W. F. Non-dimensionalizing tyre data for vehicle simulation. **Road Vehicle Handling**, Institution of Mechanical Engineers, p. 229–240, 1983.

HADT, H. S.; PACEJKA, H. B. Analysis of the steady-state turning behaviour of an automobile. In: **Proceedings of the Symposium on Control of Vehicles**. London: Institution of Mechanical Engineers, 1963. p. 66–79.

HILDRETH, C. A quadratic programming procedure. **Naval Research Logistics Quarterly**, v. 4, n. 1, p. 79–85, mar 1957. Available from Internet: <https://onlinelibrary.wiley.com/doi/abs/10.1002/nav.3800040113>.

HO, N.; SADLER, G. G.; HOFFMANN, L. C.; ZEMLICKA, K.; LYONS, J.; FERGUESON, W.; RICHARDSON, C.; CACANINDIN, A.; CALS, S.; WILKINS, M. A longitudinal field study of auto-gcas acceptance and trust: First-year results and implications. **Journal of Cognitive Engineering and Decision Making**, SAGE Publications Sage CA: Los Angeles, CA, v. 11, n. 3, p. 239–251, 2017.

HØYE, A. The effects of electronic stability control (ESC) on crashes—an update. **Accident Analysis & Prevention**, v. 43, n. 3, p. 1148 – 1159, 2011. ISSN 0001-4575. Available from Internet: <http://www.sciencedirect.com/science/article/pii/S0001457510004021>.

HUANG, Y.; CHEN, Y. Estimation and analysis of vehicle lateral stability region with both front and rear wheel steering. In: **Dynamic Systems and Control Conference**. New York: ASME, 2017. v. 3. V003T33A004. Available from Internet: <https://doi.org/10.1115/DSCC2017-5154>.

HUANG, Y.; LIANG, W.; CHEN, Y. Estimation and analysis of vehicle lateral stability region. In: **American Control Conference (ACC)**. Piscataway, NJ: IEEE, 2017. p. 4303–4308.

HUANG, Y.; YONG, S. Z.; CHEN, Y. Guaranteed vehicle safety control using control-dependent barrier functions. In: **2019 American Control Conference (ACC)**. Piscataway, NJ: IEEE, 2019. p. 983–988.

HUANG, Y.; YONG, S. Z.; CHEN, Y. Stability control of autonomous ground vehicles using control-dependent barrier functions. **IEEE Transactions on Intelligent Vehicles**, v. 6, n. 4, p. 699–710, 2021.

IAGNEMMA, K.; BUEHLER, M. (Ed.). **Journal of Field Robotics**: Special issue on the DARPA grand challenge, part 1. Hoboken, NJ: John Wiley & Sons, 2006. v. 23, n. 8. ISSN 1556-4967.

IAGNEMMA, K.; BUEHLER, M. (Ed.). **Journal of Field Robotics**: Special issue on the DARPA grand challenge, part 2. Hoboken, NJ: John Wiley & Sons, 2006. v. 23, n. 9. ISSN 1556-4967.

IBGE. **Frota de Veículos**. 2020. Available from Internet: <https://cidades.ibge.gov.br/brasil/pesquisa/22/28120?tipo=grafico>. Accessed: 27 April 2022.

INAGAKI, S.; KUSHIRO, I.; YAMAMOTO, M. Analysis on vehicle stability in critical cornering using phase-plane method. In: **Proceedings of the International Symposium on Advanced Vehicle Control 1994 (AVEC '94)**. Tokyo, Japan: JSAE Review, 1994. p. 287–292.

JALALI, M.; KHOSRAVANI, S.; KHAJEPOUR, A.; CHEN, S. ken; LITKOUHI, B. Model predictive control of vehicle stability using coordinated active steering and differential brakes. **Mechatronics**, v. 48, p. 30 – 41, 2017. ISSN 0957-4158. Available from Internet: <http://www.sciencedirect.com/science/article/pii/S0957415817301411>.

JARAŠŪNIENE, A.; JAKUBAUSKAS, G. Improvement of road safety using passive and active intelligent vehicle safety systems. **Transport**, Taylor & Francis, v. 22, n. 4, p. 284–289, 2007.

JAZAR, R. N. **Vehicle Dynamics: Theory and Application**. Boston, MA: Springer, 2008. 1015 p. ISBN 978-0-387-74243-4. Available from Internet: <https://link.springer.com/book/10.1007/978-0-387-74244-1>.

JOCHEM, T.; POMERLEAU, D.; THORPE, C. Vision guided lane transition. In: **Proceedings of 1995 IEEE Symposium the Intelligent Vehicles**. Piscataway, NJ: IEEE, 1995. p. 30–35.

KHALIL, H. K. **Nonlinear Systems**. 3. ed. Hoboken, NJ: Prentice Hall, 2002. 750 p. ISBN 9780130673893.

KINJAWADEKA, T. S. **Model-based Design of Electronic Stability Control System for Passenger Cars Using CarSim and Matlab-Simulink**. Thesis (Master's) — The Ohio State University, Columbus, OH, USA, 2009.

LACERDA, L. Jovens são as maiores vítimas do trânsito no mundo. **Folha de São Paulo**, 29 June 2019. Available from Internet: <https://www1.folha.uol.com.br/seminariosfolha/2019/06/jovens-sao-as-maiores-vitimas-do-transito-no-mundo.shtml>. Accessed: 19 August 2020.

LATIN NCAP. **Testing Protocol – Moose Test**. Montevideo, Uruguay, 2020. Available from Internet: <https://www.latinncap.com/po/nossos-testes>. Accessed: 16 February 2023.

LENZO, B.; ZANCHETTA, M.; SORNIOTTI, A.; GRUBER, P.; NIJS, W. D. Yaw rate and sideslip angle control through single input single output direct yaw moment control. **IEEE Transactions on Control Systems Technology**, v. 29, n. 1, p. 124–139, 2021.

LIU, J.; CHEN, P.; LI, D.-F. Vehicle stability control based on phase-plane method. **Chinese Journal of Engineering Design**, Springer, v. 23, n. 5, p. 409–416, 2016. ISSN 1006-754X. Available from Internet: <http://www.zjujournals.com/gcsjxb/CN/abstract/article_1533.shtml>.

LOPEZ, B. T.; HOW, J. P. Aggressive 3-d collision avoidance for high-speed navigation. In: **2017 IEEE International Conference on Robotics and Automation (ICRA)**. Piscataway, NJ: IEEE, 2017. p. 5759–5765.

MAGALHÃES JÚNIOR, Z. R. **Vehicle Stability Controller Based On Model Predictive Control**. Thesis (Master's) — Universidade de Brasília, Brasília, DF, Brazil, dec 2019.

MAGALHÃES JÚNIOR, Z. R.; MURILO, A.; LOPES, R. V. Vehicle stability upper-level-controller based on parameterized model predictive control. **IEEE Access**, v. 10, p. 21048–21065, 2022. Available from Internet: <https://ieeexplore.ieee.org/document/9698140>.

MATHWORKS, I. T. **Vehicle Dynamics Blockset v. 1.4**. Natick, MA, USA, 2020. Available from Internet: <https://www.mathworks.com/help/vdynblks/index.html>.

MIRZAEI, M. A new strategy for minimum usage of external yaw moment in vehicle dynamic control system. **Transportation Research Part C: Emerging Technologies**, v. 18, n. 2, p. 213–224, 2010. ISSN 0968-090X. Available from Internet: <https://www.sciencedirect.com/science/article/pii/S0968090X09000795>.

MIRZAEINEJAD, H.; MIRZAEI, M.; RAFATNIA, S. A novel technique for optimal integration of active steering and differential braking with estimation to improve vehicle directional stability. **ISA Transactions**, v. 80, p. 513–527, 2018. ISSN 0019-0578. Available from Internet: <https://www.sciencedirect.com/science/article/pii/S0019057818302167>.

MITCHELL, I.; BAYEN, A.; TOMLIN, C. A time-dependent hamilton-jacobi formulation of reachable sets for continuous dynamic games. **IEEE Transactions on Automatic Control**, v. 50, n. 7, p. 947–957, 2005.

NAGAI, M.; SHINO, M.; GAO, F. Study on integrated control of active front steer angle and direct yaw moment. **JSAE Review**, v. 23, n. 3, p. 309–315, 2002. ISSN 0389-4304. Available from Internet: <https://www.sciencedirect.com/science/article/pii/S0389430402001893>.

NAGUMO, M. Uber die lage der integralkurven gew ohnlicher differentialgleichungen. **Proceedings of the Physico-Mathematical Society of Japan. 3rd Series**, v. 24, p. 551–559, 1942. Available from Internet: <https://www.jstage.jst.go.jp/article/ppmsj1919/24/0/24_0_551/_article>.

NATIONAL HIGHWAY TRAFFIC SAFETY ADMINISTRATION. **FMVSS Rollover Resistance**. Washington, D.C., 2001. Available from Internet: <https://www.nhtsa.gov/sites/nhtsa.gov/files/fmvss/RolloverResistance.pdf>. Accessed: 16 February 2023.

NATIONAL HIGHWAY TRAFFIC SAFETY ADMINISTRATION. **Federal Motor Vehicle Safety Standards; Electronic Stability Control Systems**. Washington, D.C., 2008. Available from Internet: <https://www.nhtsa.gov/fmvss/federal-motor-vehicle-safety-standards-electronic-stability-control-systems-0>. Accessed: 23 July 2021.

NATIONAL HIGHWAY TRAFFIC SAFETY ADMINISTRATION. **FMVSS No 126 Electronic Stability Control Systems**. Washington, D.C., 2009. Available from Internet: <https://www.nhtsa.gov/sites/nhtsa.gov/files/fmvss/ESC_FRIA_\%252003_2007_0.pdf>. Accessed: 8 November 2022.

NATIONAL HIGHWAY TRAFFIC SAFETY ADMINISTRATION. **FMVSS No 136 Electronic Stability Control Systems for Heavy Vehicles**. Washington, D.C., 2018. Available from Internet: <https://www.nhtsa.gov/sites/nhtsa.gov/files/documents/tp-136-01_tag.pdf>. Accessed: 16 February 2023.

PACEJKA, H. B. **Study of the lateral behavior of an automobile moving upon a flat level road**. Ithaca, NY, 1958.

PACEJKA, H. B. **Tire and Vehicle Dynamics**. Elsevier, 2012. 675 p. ISBN 9780080970165. Available from Internet: <https://www.sciencedirect.com/book/9780080970165/tire-and-vehicle-dynamics>.

PAPELIS, Y. E.; WATSON, G. S.; BROWN, T. L. An empirical study of the effectiveness of electronic stability control system in reducing loss of vehicle control. **Accident Analysis & Prevention**, v. 42, n. 3, p. 929 – 934, 2010. ISSN 0001-4575. Assessing Safety with Driving Simulators. Available from Internet: <http://www.sciencedirect.com/science/article/pii/S0001457509000967>.

PASSENGER cars – Steady-state circular driving behaviour – Open-loop test methods. Geneva, CH, 2021. v. 2021. Available from Internet: <https://www.iso.org/standard/81710.html>.

PILUTTI, T.; ULSOY, G.; HROVAT, D. Vehicle steering intervention through differential braking. In: **Proceedings of 1995 American Control Conference - ACC'95**. Piscataway, NJ: IEEE, 1995. v. 3, p. 1667–1671.

ROBERT BOSCH GMBH. **Electronic Stability Program**. 2020. Available from Internet: <https://www.bosch-mobility-solutions.com/en/products-and-services/passenger-cars-and-light-commercial-vehicles/driving-safety-systems/electronic-stability-program/>. Accessed: 30 August 2020.

SAVA, D.; COPAE, I. Control and stability of the lateral dynamics of the vehicle to avoid road accidents. **Global Journal of Engineering and Technology Advances**, Global Scholarly communication, v. 6, n. 2, p. 159–168, 2021. ISSN 2582-5003. Available from Internet: <https://doi.org/10.30574/gjeta.2021.6.2.0029>.

SHIBAHATA, Y.; SHIMADA, K.; TOMARI, T. Improvement of vehicle maneuverability by direct yaw moment control. **Vehicle System Dynamics**, Taylor & Francis, v. 22, n. 5-6, p. 465–481, 1993. Available from Internet: <https://doi.org/10.1080/00423119308969044>.

SLOTINE, J.; LI, W. **Applied Nonlinear Control**. Hoboken, NJ: Prentice Hall, 1990. 352 p. ISBN 9780130408907.

STATISTA. **Number of vehicles in use worldwide 2015**. 2020. Available from Internet: <https://www.statista.com/statistics/281134/number-of-vehicles-in-use-worldwide/>. Accessed: 19 August 2020.

STEADY-STATE Circular Test Procedure for Trucks and Buses. Warrendale, PA, USA, 1998. Available from Internet: <https://www.sae.org/standards/content/j2181_199812/>.

SUBROTO, R. K.; WANG, C. Z.; LIAN, K. L. Four-wheel independent drive electric vehicle stability control using novel adaptive sliding mode control. **IEEE Transactions on Industry Applications**, v. 56, n. 5, p. 5995–6006, 2020. Available from Internet: <https://ieeexplore.ieee.org/document/9019598>.

SUN, W.; TIAN, J.; LI, S.; YANG, Z.; MA, Z. Stability analysis of vehicle negotiating a curve in the plane. **Advances in Mechanical Engineering**, v. 5, p. 893835, jan 2013. Available from Internet: <https://doi.org/10.1155/2013/893835>.

THRUN, S.; BURGARD, W.; FOX, D. **Probabilistic Robotics**. Cambridge, MA: The MIT Press, 2005. 672 p. (Intelligent Robotics and Autonomous Agents series). ISBN 9780262201629.

TOYOTA MOTOR CORPORATION. **When should I use the VSC Off button in my vehicle?** 2022. Available from Internet: <http://toyota.custhelp.com/app/answers/detail/a_id/7879/~/when-should-i-use-the-vsc-off-button-in-my-vehicle\%3F>. Accessed: 26 April 2022.

TSENG, H.; ASHRAFI, B.; MADAU, D.; BROWN, T. A.; RECKER, D. The development of vehicle stability control at ford. **IEEE/ASME Transactions on Mechatronics**, v. 4, n. 3, p. 223–234, 1999.

U.S. DEPARTMENT OF TRANSPORTATION. **Rollover Causes**. 2020. Available from Internet: <https://www.safercar.gov/Vehicle-Shoppers/Rollover/Causes>. Accessed: 18 November 2020.

U.S. DEPARTMENT OF TRANSPORTATION. **Rollover Fatalities**. 2020. Available from Internet: <https://www.safercar.gov/Vehicle-Shoppers/Rollover/Fatalities>. Accessed: 18 November 2020.

U.S. DEPARTMENT OF TRANSPORTATION. **Rollover Types**. 2020. Available from Internet: <https://www.safercar.gov/Vehicle-Shoppers/Rollover/Types-of-Rollovers>. Accessed: 1 December 2020.

VAN PUTEN, B. J. S. **Design of an Electronic Stability Program for vehicle simulation software**. Eindhoven, 2008.

VU, V. T.; SENAME, O.; DUGARD, L.; GASPAR, P. The design of an H_∞/LPV active braking control to improve vehicle roll stability. **IFAC-PapersOnLine**, v. 52, n. 17, p. 54 – 59, 2019. ISSN 2405-8963. 7th IFAC Symposium on System Structure and Control SSSC 2019. Available from Internet: <http://www.sciencedirect.com/science/article/pii/S2405896319309619>.

WANG, L. **Model Predictive Control System Design and Implementation Using MATLAB**. London: Springer, 2009. 378 p. (Advances in Industrial Control). ISBN 9781848823310.

WHEALS, J.; DEANE, M.; DRURY, S.; GRIFFITH, G. et al. Design and simulation of a torque vectoring™ rear axle. In: **SAE Technical Paper 2006-01-0818**. SAE International, 2006. Available from Internet: <https://doi.org/10.4271/2006-01-0818>.

WIELAND, P.; ALLGÖWER, F. Constructive safety using control barrier functions. **IFAC Proceedings Volumes**, v. 40, n. 12, p. 462–467, 2007. ISSN 1474-6670. 7th IFAC Symposium on Nonlinear Control Systems. Available from Internet: <https://www.sciencedirect.com/science/article/pii/S1474667016355690>.

WORLD HEALTH ORGANIZATION. **Global status report on road safety 2018**. Geneva, 2018. Available from Internet: <https://www.who.int/violence_injury_prevention/road_safety_status/2018/en/>. Accessed: 25 August 2020.

WORLD HEALTH ORGANIZATION. **The top 10 causes of death**. Geneva, 2018. Available from Internet: <https://www.who.int/news-room/fact-sheets/detail/the-top-10-causes-of-death>. Accessed: 27 April 2022.

XIANG, W.; RICHARDSON, P. C.; ZHAO, C.; MOHAMMAD, S. Automobile brake-by-wire control system design and analysis. **IEEE Transactions on Vehicular Technology**, v. 57, n. 1, p. 138–145, 2008.

XU, W.; WANG, D.; LI, Y. The lateral stability control of vehicles based on sliding mode method. In: **Proceedings of the 2014 IEEE International Conference on Information and Automation (ICIA)**. Piscataway, NJ: IEEE, 2014. p. 1312–1317.

XU, X.; TABUADA, P.; GRIZZLE, J. W.; AMES, A. D. Robustness of control barrier functions for safety critical control. **IFAC-PapersOnLine**, v. 48, n. 27, p. 54–61, 2015. ISSN 2405-8963. Analysis and Design of Hybrid Systems ADHS. Available from Internet: <https://www.sciencedirect.com/science/article/pii/S2405896315024106>.

YAMAKADO, M.; TAKAHASHI, J.; SAITO, S. Comparison and combination of direct yaw-moment control and g-vectoring control. **Vehicle System Dynamics**, Taylor & Francis, v. 50, n. sup1, p. 111–130, 2012. Available from Internet: <https://doi.org/10.1080/00423114.2012.679283>.

ZANTEN, A. T. van; ERHARDT, R.; PFAFF, G. VDC, the vehicle dynamics control system of Bosch. In: **SAE Technical Paper**. SAE International, 1995. Available from Internet: <https://doi.org/10.4271/950759>.

ZHAI, L.; SUN, T.; WANG, J. Electronic stability control based on motor driving and braking torque distribution for a four in-wheel motor drive electric vehicle. **IEEE Transactions on Vehicular Technology**, v. 65, n. 6, p. 4726–4739, 2016.

ZHANG, H.; LI, X.-S.; SHI, S.-M.; LIU, H.-F.; GUAN, R.; LIU, L. Phase plane analysis for vehicle handling and stability. **International Journal of Computational Intelligence Systems**, Taylor & Francis, v. 4, n. 6, p. 1179–1186, 2011. Available from Internet: <https://doi.org/10.1080/18756891.2011.9727866>.

ZHANG, J.; SUN, W.; FENG, Z. Vehicle yaw stability control via H_∞ gain scheduling. **Mechanical Systems and Signal Processing**, v. 106, p. 62 – 75, 2018. ISSN 0888-3270. Available from Internet: <http://www.sciencedirect.com/science/article/pii/S0888327017306702>.

ZHANG, X.; WANG, P.; LI, Z.; WANG, F.; CHEN, H. Estimation and analysis of vehicle stability region under complex road conditions. In: **2020 Chinese Automation Congress (CAC)**. Piscataway, NJ: IEEE, 2020. p. 3036–3041.

ZHOU, H.; LIU, Z. Vehicle yaw stability-control system design based on sliding mode and backstepping control approach. **IEEE Transactions on Vehicular Technology**, v. 59, n. 7, p. 3674–3678, 2010.

APPENDIX A – MAGIC FORMULA EQUATION SET

The combined slip equation set from the magic formula model (excluding aligning moment and turn slip) is presented here. It includes the longitudinal and lateral equation sets, adding factors and shifts to adapt those when both the slip ratio and slip angle are not zero.

The general variables that are used throughout the equation set are

$$F'_{zo} = F_z \lambda_{Fzo} \tag{A.1}$$

$$df_z = \frac{F_z - F'_{zo}}{F'_{zo}} \tag{A.2}$$

$$dp_i = \frac{p_i - p_{io}}{p_{io}} \tag{A.3}$$

$$\alpha^* = \tan\alpha \,\mathrm{sign}(v_{cx}) \tag{A.4}$$

$$\kappa = \frac{v_{sx}}{|v_{cx}| + \epsilon_x} = -\frac{v_{cx} - r_e\omega}{|v_{cx}| + \epsilon_x} \tag{A.5}$$

where v_{cx} is the longitudinal speed of the tire (v_x in Section 2.2.1) and $\epsilon_x \in \mathbb{R}$ is a small quantity to avoid singularities due to division by zero.

The pure longitudinal slip equations are

$$F_{xo} = D_x \sin\Big\{C_x \arctan\Big[B_x\kappa_x - E_x\big(B_x\kappa_x - \arctan(B_x\kappa_x)\big)\Big]\Big\} + S_{Vx} \tag{A.6}$$

$$C_x = p_{Cx1}\lambda_{Cx} \tag{A.7}$$

$$D_x = \mu_x F_z \zeta_1 \tag{A.8}$$

$$\mu_x = (p_{Dx1} + p_{Dx2}df_z)(1 + p_{px3}dp_i + p_{px4}dp_i^2)(1 - p_{Dx3}\gamma^2)\lambda^*_{\mu x} \tag{A.9}$$

$$E_x = (p_{Ex1} + p_{Ex2}df_z + p_{Ex3}df_z^2)[1 - p_{Ex4}\,\mathrm{sign}(\kappa_x)]\lambda_{Ex} \tag{A.10}$$

$$B_x = \frac{K_{x\kappa}}{C_x D_x + \epsilon_x} \tag{A.11}$$

$$K_{x\kappa} = F_z(p_{Kx1} + p_{Kx2}df_z)e^{p_{Kx3}df_z}(1 + p_{px1}dp_i + p_{px2}dp_i^2)\lambda_{Kx\kappa} \tag{A.12}$$

$$\kappa_x = \kappa + S_{Hx} \tag{A.13}$$

$$S_{Hx} = (p_{Hx1} + p_{Hx2} df_z)\lambda_{Hx} \tag{A.14}$$

$$S_{Vx} = F_z(p_{Vx1} + p_{Vx2} df_z)\lambda_{Vx}\lambda'_{\mu x}\zeta_1. \tag{A.15}$$

The pure lateral slip equations are

$$F_{yo} = D_y \sin\Big\{C_y \arctan\Big[B_y\alpha_y - E_y\big(B_y\alpha_y - \arctan(B_y\alpha_y)\big)\Big]\Big\} + S_{Vy} \tag{A.16}$$

$$C_y = p_{Cy1}\lambda_{Cy} \tag{A.17}$$

$$D_y = \mu_y W \zeta_2 \tag{A.18}$$

$$\mu_y = (p_{Dy1} + p_{Dy2} df_z)(1 + p_{py3} dp_i + p_{py4} dp_i^2)(1 - p_{Dy3}{\gamma^*}^2)\lambda^*_{\mu y} \tag{A.19}$$

$$E_y = (p_{Ey1} + p_{Ey2} df_z)\left[1 + p_{Ey5}{\gamma^*}^2 - (p_{Ey3} + p_{Ey4}\gamma^*)\operatorname{sign}(\alpha_y)\right]\lambda_{Ey} \tag{A.20}$$

$$\alpha_y = \alpha^* + S_{Hy} \tag{A.21}$$

$$B_y = \frac{K_{y\alpha}}{C_y D_y + \epsilon_y} \tag{A.22}$$

$$\begin{aligned} K_{y\alpha} &= p_{Ky1} W_o (1 + p_{py1})(1 - p_{Ky3}|\gamma^*|) \\ &\quad \sin\left\{p_{Ky4} \arctan\left[\frac{W/W_o}{(p_{Ky2} + p_{Ky5}{\gamma^*}^2)(1 + p_{py2} dp_i)}\right]\right\} \\ &= C_{F\alpha} \end{aligned} \tag{A.23}$$

$$S_{hy} = (p_{Hy1} + p_{Hy2} df_z)\lambda_{Hy} + \frac{K_{y\gamma 0}\gamma^* - S_{Vy\gamma}}{K_{y\alpha} + \epsilon_K}\zeta_o + \zeta_4 - 1 \tag{A.24}$$

$$S_{Vy} = W(p_{Vy1} + p_{Vy2} df_z)\lambda_{Vy}\lambda'_{\mu y}\zeta_2 + S_{Vy\gamma} \tag{A.25}$$

$$S_{Vy\gamma} = W(p_{Vy3} + p_{Vy4} df_z)\gamma^*\lambda_{Ky\gamma}\lambda'_{\mu y}\zeta_2 \tag{A.26}$$

$$\begin{aligned} K_{y\gamma o} &= W(p_{Ky6} + p_{Ky7} df_z)(1 + p_{py5} dp_i)\lambda_{Ky\gamma} \\ &= C_{F\gamma}. \end{aligned} \tag{A.27}$$

The combined slip equations for longitudinal force are

$$F_x = G_{x\alpha} F_{xo} \tag{A.28}$$

$$G_{x\alpha} = \cos\Big\{C_{x\alpha} \arctan\Big[B_{x\alpha}\alpha_S - E_{x\alpha}\big(B_{x\alpha}\alpha_S - \arctan(B_{x\alpha}\alpha_S)\big)\Big]\Big\}/G_{x\alpha o} \tag{A.29}$$

$$G_{x\alpha o} = \cos\Big\{C_{x\alpha} \arctan\Big[B_{x\alpha}S_{Hx\alpha} - E_{x\alpha}\big(B_{x\alpha}S_{Hx\alpha} - \arctan(B_{x\alpha}S_{Hx\alpha})\big)\Big]\Big\} \tag{A.30}$$

$$\alpha_S = \alpha^* + S_{Hx\alpha} \tag{A.31}$$

$$B_{x\alpha} = (r_{Bx1} + r_{Bx3}{\gamma^*}^2)\cos[\arctan(r_{Bx2}\kappa)]\lambda_{x\alpha} \tag{A.32}$$

$$C_{x\alpha} = r_{Cx1} \tag{A.33}$$

$$E_{x\alpha} = r_{Ex1} + r_{Ex2} df_z \tag{A.34}$$

$$S_{Hx\alpha} = r_{Hx1}. \tag{A.35}$$

Finally, the lateral force equations for combined slip are

$$F_y = G_{y\kappa} F_{yo} + S_{Vy\kappa} \tag{A.36}$$

$$G_{y\kappa} = \cos\Big\{ C_{y\kappa} \arctan\Big[B_{y\kappa}\kappa_S - E_{y\kappa}\big(B_{y\kappa}\kappa_S - \arctan(B_{y\kappa}\kappa_S)\big)\Big]\Big\} / G_{y\kappa o} \tag{A.37}$$

$$G_{y\kappa o} = \cos\Big\{ C_{y\kappa} \arctan\Big[B_{y\kappa} S_{Hy\kappa} - E_{y\kappa}\big(B_{y\kappa} S_{Hy\kappa} - \arctan(B_{y\kappa} S_{Hy\kappa})\big)\Big]\Big\} \tag{A.38}$$

$$\kappa_S = \kappa + S_{Hy\kappa} \tag{A.39}$$

$$B_{y\kappa} = (r_{By1} + r_{By4}\gamma^{*2}) \cos[\arctan(r_{By2}(\alpha^* - r_{By3}))] \lambda_{y\kappa} \tag{A.40}$$

$$C_{y\kappa} = r_{Cy1} \tag{A.41}$$

$$E_{y\kappa} = r_{Ey1} + r_{Ey2} df_z \tag{A.42}$$

$$S_{Hy\alpha} = r_{Hy1} + r_{Hy2} df_z \tag{A.43}$$

$$S_{Cy\alpha} = D_{Vy\kappa} \sin[r_{Vy5} \arctan(r_{Vy6}\kappa)] \lambda_{Vy\kappa} \tag{A.44}$$

$$D_{Vy\kappa} = \mu_y F_z (r_{Vy1} + r_{Vy2} df_z + r_{Vy3}\gamma^*) \cos[\arctan(r_{Vy4}\alpha^*)] \zeta_2. \tag{A.45}$$